To the Graduate Council:
I am submitting herewith a dissertation written by Peter Nikolaivich Yaron entitled "Adsorption of Small Molecules on MgO and Graphite" I have examined the final paper copy of this dissertation for form and content and recommend that it be accepted in partial fulfillment of the requirements for the degree of Doctor of Philosophy, with a major in Chemistry.

John Z. Larese

John Z. Larese, Major Professor

We have read this dissertation
and recommend its acceptance:

Takeshi Egami

Ffrancon Williams

Frank Vogt

Accepted for the Council:

Linda Painter

Vice Chancellor and Dean of
Graduate Studies

(Original signatures are on file with official student records.)

# Physical Adsorption of Small Molecules on MgO and Graphite: The Study of Molecular and Surface Symmetry on Adsorption

A Dissertation
Presented for the
Doctor of Philosophy
Degree
The University of Tennessee, Knoxville

Peter N. Yaron
Dec 2006

# Dedication

To my mother who has been the embodiment of perseverance and resolve and demonstrates to me a daily work ethic in every facet of her life which I can only strive to attain. Thank you for driving an an hour each way to work for the past twenty years in rush hour traffic on Long Island all while obtaining two masters degrees, teaching full time and being a wonderful mother. No one ever asked you to do these things, you just did.

To my father who first introduced me the joy of what I now get to do everyday and who has always been there for me no matter what the circumstances. My time here would not have been possible without the sacrifice you made of giving up an academic life in physics to raise a family. This degree is as much yours as it is mine. I hope I have made you proud.

To Nicole, thanks for all your advice over the years which was invaluable for helping through this experience and for your countless selfless acts you have done not only for me but for the rest of the family. I feel like I owe you so much I don't know how I can repay you for everything.

To Nadia, whom I hope I can only emulate in success someday. You have showed me that I can be the best at anything I put my mind to and to take chances once in a while if you truly believe in them. I would still be in New York working a boring job if it wasn't for the example you set.

To my grandparents Eric and Adele Caira, and the rest of my family Lesley, Gerhard, Alexis and Kyle Sogl all whom I miss dearly and can't wait to see them again.

To all my friends in whom have been there in any capacity through this time, especially my friends in knoxville and my former and current roommates who all have had to put up with me.

And to John Z. Larese who has taught me the most important lesson of my academic life which has been to take full responsibility of my education and career because no one else is responsible for it but yourself and that your career path is only limited by how big you dream and the effort you put into attaining that dream.

"Choose a job you love, and you will never have to work a day in your life."
—Confucius

# Acknowledgments

To my group my fellow Larese group members both past and present Tom Arnold, Rick Cook, Lillian Frazier, Michael Felty, Sami Chanaa, Andi Barbour, Paige Landry and David Cañoto. Thank you for all your help over the years. To the chemistry department staff particularly Gary Wynn, Art Pratt and Tim Free for all their help. To the instrument scientists and technical staff who has provided assistance at the ISIS facility. NSF, DOE and the Chemical Physics program at the University of Tennessee, Knoxville who have kindly provided funding for conferences and some experiments over the years.

# Abstract

The physical adsorption of molecules on metal oxide surfaces has direct implications in a number of industrial applications such as; catalysis, electronics, and fuel cells to name a few. Despite the large number of adsorption studies to date, only a small number of systems can be explained with the most advanced *ab initio* calculations currently available.

One of the simplest metal oxide systems to study is magnesium oxide due to its simple cubic rock-salt structure. Using a patented method, nearly defect-free MgO cubes can be synthesized with a narrow size distribution exposing exclusively the (100) equilibrium crystal face. The use of this material minimizes the heterogeneity of adsorption sites due to surface defects and edge effects and allows for comparison with theoretical calculations. This study is a continued work on various homologous groups of normal alkanes and cyclic molecules. The study of *n*-hexane, cyclohexane, benzene, and pyridine were conducted in this work. These molecules in were chosen because of their molecular symmetry and are physically well-characterized. These systems are experimentally studied using high-resolution adsorption isotherms and neutron diffraction techniques. The results of these experiments are then matched with theoretical calculations. Analogous adsorption experiments and calculations were also conducted on graphite. Graphite is a physically well-defined surface and provides comparison with MgO. In understanding more ideal systems one can attempt to better understand more complex metal oxide surfaces.

Another facet of this study is the role molecular and surface symmetry have on the adsorption characteristics of the system. Adsorbing molecules of different molecular symmetry onto surfaces of different symmetry one can better determine the importance symmetry considerations play in the adsorption characteristics of the system. Results indicate both symmetry properties drastically affect the wetting properties of these systems.

# Contents

# List of Tables

# List of Figures

# Chapter 1

# Introduction

Although we live in a three-dimensional world, the interfaces between three-dimensional objects comprise of two-dimensions. Many two-dimensional (2D) systems exhibit different physical behaviors than their three-dimensional counterparts warrant further investigation. The study of surfaces provides the opportunity to not only study systems with many direct industrial applications but to also experimentally study the fundamental physics of two-dimensional systems. Topics such as surface melting, phase transitions, and the evolution of three-dimensional properties from two-dimensional properties are intensively studied topics in that involve physics and mathematics. This importance of this field may best be illustrated by realizing that 2006 Fields medal winners were all involved in the development of various theories involving 2D systems. In 1982, Kenneth G. Wilson won the Nobel Prize for introduction of the concept of 'universality'. his study of physical systems near their critical point. He proposed that systems though very different in appearance would behave in similar ways and used his elegant mathematics to illustrate this point. Experimental models of two-dimensional systems can be used to shed light on whether this 'universality' concept can be extended to different dimensions near their critical points as well.

The study of how surface and molecular symmetry affect adsorption is important to the layering properties of the particular system studied. The study of adsorption involves a

delicate interplay between between molecules and surfaces in how to establish the most favorable interaction not only between each atom of the molecule and surface with each other but with neighboring adsorbed atoms and as well. In process of a minimizing all atom-atom interactions molecules can change conformation, reorient, perturb molecular orbitals and can alter the properties of the substrate effecting the band gap of a surface, change its local electric field, alter its surface structure, and change its reactivity. Slight changes in molecular symmetry can drastically affect the adsorption properties of a system and is an important factor to take into account in the growth of thin films. This effect becomes even more pronounced in the production of physically adsorbed multi-layer thin films where the stability of the film is intimately dependent on the match of the adsorbed molecule with the lattice of the substrate. Surface symmetry plays a role by altering the number of adsorption sites available for molecules. The increase in potential adsorption sites can alter the configuration a adsorbed molecule might take on a surface due to the increase in multiply coordinated interactions to create the lowest energy configuration.

The modern study of adsorption onto surfaces has matured dramatically in both its theory and experimental techniques and can be roughly divided roughly into three periods. The first period of study was based mostly on the theories of Langmuir and Brunauer, Emmet, and Teller (BET) formalism. At that time the above theories and equations of adsorption isotherms were extensively verified experimentally and improved theoretically. In spite of many refinements of the Langmuir and BET equations, the fitting of these equations to experimental data remains inaccurate. These inaccuracies persist because of the equations inability to accurately explain factors such as, adsorbate-adsorbate interactions, heterogeneity of surfaces, and the behavior of adsorbed films near the saturated vapor pressure. The saturated vapor pressure is defined as the pressure where a liquid and vapor in a vessel are in equilibrium with each other, and is dependent on temperature.

The second period of adsorption theory began in the 1960's by Steele who abandoned the kinetic based theories of Langmuir and BET in favor of theory grounded in Statistical Mechanics and utilizing potential theories based on the work Lennard-Jones, Morse, Buckingham, and other similar potentials. In 1974, Steele published *The Interaction of Gases with Solid Surfaces* which investigated the nature of solid-gas interactions in terms of a two-dimensional virial formalism. The numerical values of the second, third, and fourth two-dimensional virial coefficients give qualitative information on the interactions between adsorbed molecules and adsorption sites as well as on the interactions among suitable numbers of adsorbates.

Experimentally, a variety of new methods were produced during this period which allowed for the studies of thin film adsorption on surfaces. The most important of these was the development of high vacuum equipment which allowed for the production and characterization of surfaces with little to no degradation. With the ability to create high vacuum and Ultra High Vacuum (UHV) environments, a variety of surface characterization methods followed such as: Infrared (IR), Raman, Neutron, X-ray photoelectron spectroscopy (XPS), Auger, High Energy Electron Energy Loss Spectroscopy (HREELS), Electron Energy Loss Spectroscopy (EELS), Helium Atom Scattering (HAS), and Low Energy Electron Diffraction (LEED), to name a few. Another important development which facilitated the study of adsorbed molecules on surfaces was the ability to create highly controllable, ultra low-temperature environments. This came about by the ability to use liquid helium or use helium gas expansions to lower temperatures down to the boiling point of helium (4.2 K) and below. From these ideas, equipment such as closed-cycle helium cryostats and open-flow helium cryostats came to existence. This equipment along high precision temperature controllers allowed for the control of sample environment temperature. This allowed for first characterization studies of simple atoms and molecules such as argon, nitrogen, and methane to name a few.

More recently, the theoretical framework developed by Steele and others has been adapted for use in computational simulations. This development has been ushered in by the reduction of costs and increased speed of computers. The availability of large-scale computing power has allowed for the simulations of large, complicated systems more resembling real experimental environments. With this increase in computing power, the variety of methods to simulate these systems blossomed. Based directly on a microscopic model of the adsorption system, both Monte Carlo (MC) as well as molecular dynamics (MD) can provide an exact numerical solution to a system being modeled. The sophistication in theory of these codes vary in complexity and are highly specialized in determining certain physical parameters. The most important input for computer simulation methods are suitable potentials representative of all atomic interactions in the system. In terms of MC and MD approaches, it is possible to carry out computational measurements of adsorption isotherms to calculate many thermodynamic and quantum mechanical values in addition to the ability model experimental spectroscopic data such as, IR, Raman, X-ray, and Neutrons to name a few. Thermodynamic experiments can also be modeled such as heat capacity and volumetric isotherm measurements.

Experimentally, the affordability and availability of high vacuum, and UHV components with high precision temperature controllers, reliable low-temperature cryostats, well-defined characterization methods, along with simple computer interfacing of all of the above has lead to readily available methods to conduct high quality surface science experiments. These methods can then be matched with computational simulations of comparable scale to provide an analytical comparison to experimental results.

These above mentioned breakthroughs have highlighted the delicate interplay between molecule-molecule and molecule-substrate interactions which intimately affects the layering and phase properties of alkane thin films. The use of volumetric adsorption isotherms as the primary method to study the thermodynamics of thin film alkane adsorption on

graphite and MgO is primarily due to the ease in the ability of this group to conduct high-resolution volumetric isotherms which can be remotely controlled via a computer interface. This differs drastically from most current volumetric isotherm setups which need to be operated by a user which introduces an additional error and bias of measuring the initial and final pressures of each point and determining when equilibrium conditions are met, etc.. The use of a computer controlled algorithm [Mursic et al., 1996] allows for an unbiased measurement, and the ability to use small doses of adsorbate throughout the isotherm measurement. Volumetric isotherms also allow for the study of these systems in more realistic environments which more closely resemble real-world applications.

One experimental technique which has proven to be invaluable for studying alkane thin films on a variety of substrates is elastic neutron scattering. Elastic neutron scattering complements other scattering techniques such as x-ray and electron scattering. The latter two methods rely on electron scattering from the electron clouds of the atoms. Scattering from electrons of atoms makes determination of LEED patterns difficult to interpret the spot intensities. This makes interpretation of molecular orientation on the surface difficult. X-ray scattering is complicated by the scattering cross-section which is dependent on the magnitude of the scattering vector. This results in weak scattering at high angles. X-rays are also dependent on the atomic scattering amplitude which is directly related to the size of the electron 'cloud' around the nucleus.

Neutron scattering techniques are the primary method used for the determination of the structure and dynamics of a particular system. Neutrons provide the ideal probe due lack of dependence on electron density allows for the interrogation of small atoms normally 'invisible' to other techniques. Neutrons are primarily a nuclear scatterer which makes it independent of the magnitude of the scattering vector. Neutron diffraction is only limited by the intensity of the instrument and the resolution of the detectors.

The use of volumetric isotherms coupled with neutron scattering measurements allows one to map out the phase diagram and structure of a thin film on a particular substrate. Experimental results from volumetric isotherms and neutron scattering measurement can be corroborated with theoretical predictions of structures and phase transitions.

This study contributes to a growing body of information on the systematic study of small alkane adsorption on MgO (100) surfaces. The ability of this group to synthesize large quantities of homogenous, nearly defect-free MgO coupled with the ability to conduct high-resolution volumetric isotherms and neutron scattering studies using *in-situ* volumetric isotherms allows for the study of the interaction potentials involved in the physical adsorption of alkanes on surfaces. Alkanes are chosen primarily because they are the simplest molecules to study both experimentally and in simulations. Alkanes are relatively inexpensive and easy to purify and distill to the very high purities. All alkanes condense at temperatures above 20 K which allows for their study in isotherm and neutron studies without the use of exotic cryogenic equipment. The potential energy surfaces of alkane molecules are the most well known of any structures due to the amount of previous studies conducted, simplistic bonding scheme and size.

MgO has been chosen because of the relative dearth of information known about the interaction potentials of metal oxides. MgO the simplest structure of the metal oxides with a simple rock salt cubic structure. Our group is able to produce large quantities of this material for use in isotherm and neutron studies. A better understanding of MgO will provide a framework to better understand more complex metal oxide surfaces.

The results from this and previous work can provide empirical parameters to generate better theoretical interaction potentials to use in future modeling packages. Current modeling packages do a poor job in modeling thin film alkane structures and thus provide little hope

in the modeling of larger or more complicated molecules. This work can also provide empirical data to better study topics in two-dimensional physics such as, phase transitions, surface melting, and critical points.

The remainder of this thesis is organized into 5 chapters.

- Chapter 2 is concerned with the theory behind thin film adsorption and discusses the various theoretical models developed and the derivation of the thermodynamic quantities from volumetric adsorption isotherms and how these values are used as a guide for our neutron diffraction studies. The theory behind diffraction is then discussed in general as it is applied to x-rays, neutrons, and TOF neutron experiments.

- Chapter 3 discusses the details of the various experimental set-ups used, along with sample preparation, data collection, and data analysis.

- Chapter 4 reports the thermodynamic results obtained from volumetric isotherm measurements and from temperature programmed desorption (TPD) results. Layering transitions are identified along with monolayer capacities, area per molecule (APM) calculations, differential enthalpy and entropy, heat of adsorption, isosteric heats of adsorption, and two-dimensional compressibility are discussed.

- Chapter 5 reports the neutron diffraction results and interpretation of $n$-hexane adsorbed on MgO as well as the results of force field calculations performed on each of the adsorbates and substrates.

- Chapter 6 compares and contrasts each of the systems studied and attempts to develop a systematic look at how the substrates and adsorbates affect thin film growth

and propose future work that needs to be conducted.

# Chapter 2

# Background Theory

The theory of various adsorption phenomena and the experimental techniques used to interrogate them are varied and numerous. Presented below is a summary of the theory behind the systems of interest and experiments conducted to observe them. A much larger body of work exists in all these following subjects whose complexities and depth extend far beyond the scope of this work.

## 2.1 Adsorption

Adsorption can take place in a variety of methods and is dependent on a large number of factors. A broad classification of adsorption can separate adsorption into two categories: chemisorption and physisorption.

### 2.1.1 Chemisorption

When the adsorption energy is comparable to the bond energies in a molecule, chemisorption may take place. Chemisorption involves the formation of a chemical bond (an exchange of electron) between the surface and the adsorbate. Chemisorption may be irreversible and once bonded to the surface the adsorbate may undergo dissociation. Chemisorption can take place at virtually any temperature adsorption takes place. Chemisorption is crystallographically specific and often shows variation in binding energy depending on what face

adsorption takes place [Adamson and Gast, 1996], [Somorjai, 1994]. There have been many studies illustrating such behavior like the adsorption of $N_2$ and $O_2$ on different crystallographic faces of Tungsten [Somorjai, 1994]. This plays an important role in catalysis using metals, especially metal nanoclusters which exhibit a variety of crystal faces [Richards, 2006].

Chemisorption of molecules proceeds in two stages. In the first stage, the molecule may re-evaporate, or it may stay on the surface as a physisorbed molecule. In the second stage, the molecule overcomes the physisorbed energy barrier and proceeds closer to the substrate by donation or acquisition of an electron to transform irreversibly into a chemisorbed state. This transition can result in the splitting of the molecule and adsorption of the fragments which is referred to as dissociative chemisorption. The adsorption energies for the precursor phase are similar to physisorption of rare gases, but may contain additional contributions from the dipole, quadrapole, and higher moments of the molecules [Boinovich and Emelyanenko, 2004].

### 2.1.2 Physisorption

All gases near their respective critical temperature adsorb to a surface. The critical temperature is defined as the temperature where the properties of gas and liquid phases become indistinguishable [Klein and Cole, 1985]. Physical adsorption occurs at energies on the order of their bulk enthalpies and are reversible. Van der Waals, dipole-dipole, and ionic interactions dictate interactions with the substrate by slightly distorting the electron density of substrate and adsorbate, however no electron transfer takes place in this interaction. Physisorption is not crystallographically specific, but will show slight variations in structure. An illustration of this relationship between the energy scales of physisorption and chemisorption can be seen in Figure 2.1 and quantified in Table 2.1. Physisorption is important in applications such as hydrogen storage where hydrogen binds to high surface area materials, but no chemical reaction occurs, so desorption occurs without any reaction with

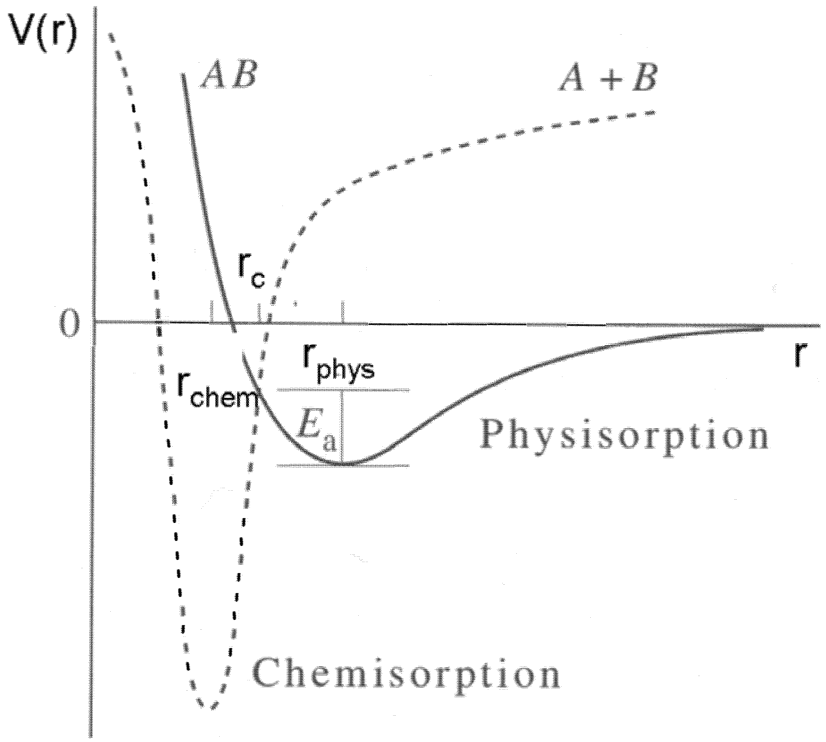


Figure 2.1: One-dimensional potential energy curve for the physisorption of a molecule and dissociative chemisorption of a molecule. The value $r$ is the distance from the substrate. Points $r_{chem}$ and $r_{phys}$ are the equilibrium distances of a chemisorbed and physisorbed molecule respectively. The two potential energy curves cross at $r_c$ which is the point at which a physisorbed molecule becomes chemisorbed. Adapted from [McQuarrie and Simon, 1997].

Table 2.1: Typical heat of adsorption ($Q_{ads}$) values, for physisorbed and chemisorbed molecules. Adapted from [Adamson and Gast, 1996].

| | $Q_{ads}$ [J/mol] |
|---|---|
| physisorption | $6 \sim 40$ |
| chemisorption | $80 \sim 400$ |

the surface [Somorjai, 1994]. The focus of this research is based primarily on physisorbed systems and the distinction between physisorbed and chemisorbed systems.

### 2.1.3 Surface Wetting

When a vapor is physisorbed onto a substrate, the strength of interaction it has with the surface will dictate how the adsorbate covers the surface. Surface wetting is dependent on the magnitude of the adsorbate-substrate versus the adsorbate-adsorbate interaction [Dash, 1975]. A comparison of the relative strengths of these interactions creates a broad classification system based on the behavior of the adsorbate on the substrate.

The wetting classifications in section 2.1.5 are generalizations of a much more complex phenomena. A more detailed description is beyond the scope of this thesis. More in depth theory behind these classifications and the forces that drive them can be found in the following texts and papers [Dash, 1975], [Fisher and Pandit, 1983], [Thomy and Duval, 1990], [Pandit et al., 1982], and [Schick, 1990].

### 2.1.4 Contact Angle

When a vapor condenses onto a substrate, the interaction with the surface can be measured by observing the angle made by the condensed droplet on the surface. Interfacial tension between the surface and adsorbate can be used to describe the contact angle (see Figure 2.2). Using Young's equation this can be calculated as follows,

$$\gamma_{lg}\cos(\theta) = \gamma_{sl} = \gamma_{sg}, \tag{2.1}$$

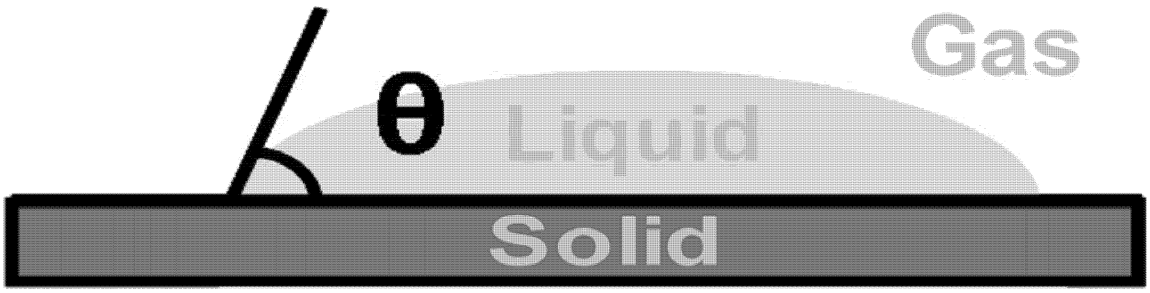


Figure 2.2: Illustration of the contact angle made by a liquid drop on a surface

where $\gamma_{lg}$ is the liquid-gas interfacial tension, $\gamma sl$ is the solid-liquid interfacial tension, and $\gamma_{sl}$ is the solid-gas interfacial tension. Surface contact angle can be vastly altered by surface roughness and exposed crystallographic face [Adamson, 1967]. Contact angle can be measured on powdered samples by compressing the sample to a cylindrical plug so that the capillary pressure required to pass a non-wetting liquid through the sample can be calculated [Adamson and Gast, 1996].

### 2.1.5 Classifications of Wetting

Wetting behavior can be roughly classified into three different types depending on the contact angles of wetting. Beyond classifying wetting strictly in terms of contact angle Wortis et. al. [Pandit et al., 1982] have developed a classification system based on relative strengths of the adsorbate-adsorbate adsorbate-substrate interactions. The different classifications of wetting as well as the relative strengths of interactions will be described below. A much more involved description of these phenomena in two-dimensions can be found in [Fisher and Pandit, 1983], [Dash, 1977], [Kjems et al., 1976], [Schick, 1990], and [Bretz et al., 1973].

#### Non-Wetting

Non-Wetting or also known as 'Volmer-Weber' [Volmer and Weber, 1926] or 'Type III' behavior by Dash [Dash, 1975]. The macroscopic classification of a non-wetting surface is when a droplet forms a 180° contact angle with the surface. This angle means the droplet is only in contact with the substrate at one point. This occurs because of a weak adsorbate-substrate interaction relative to the adsorbate-adsorbate interaction. The isotherms in this classification show no layering characteristics and form only bulk-like droplets when the saturated vapor pressure is reached.

#### Incomplete Wetting

Incomplete wetting, also known as 'Stranski-Krastanov' [Stranski and Krastanow, 1937] or 'Type II' behavior by Dash [Dash and R.D., 1981] is macroscopically defined as when the

contact angle of a droplet of adsorbate molecules makes an angle with surface between 0 and 180° degrees. This is the most prevalent type of wetting phenomena. Incomplete wetting is described as an intermediate adsorbate-substrate interaction which falls off quickly $r^{-3}$ as a function of distance. As distance $r$ is increased and the saturated vapor pressure approached, the adsorbate-adsorbate interaction dominates. The definition of incomplete wetting can be expanded in terms of the temperature region of the isotherm relative to the roughening temperature, $T_R$, and the wetting temperature, $T_W$ [Pandit et al., 1982]. The roughening temperature is the temperature at which the surface of the adsorbed film develops kinks and defects to the point where it is no longer considered a flat surface. The wetting temperature is defined as the temperature at which film thickness builds up to a finite value as saturation is approached. Above this temperature coexistence is complete.

In the region where the wetting temperature is less than the roughening temperature ($T_W < T_R$), as temperature is increased the number steps increases until becoming infinite at $T_W$. In the region where $T_R$ is less than $T_W$, the layering transitions have disappeared leaving a finite thin-film to thick-film transition in the neighborhood of bulk coexistence referred to as pre-wetting. Pre-wetting can also be interpreted as the continuation of coexistence of the wetting transition. The corresponding surface area is finite rather than infinite. Surface coverage changes from a thin film to a thick liquid film as you approach the critical temperature $T_c$. In the region where $T_R$ is much less than $T_W$ pre-wetting disappears and only a transition to bulk coexistence occurs [Nakanishi and Fisher, 1982].

**Complete Wetting**

Complete wetting, also known as 'Frank-van der Merwe' [Frank and van der Merwe, 1949] growth or 'Type I' behavior by Dash [Dash and R.D., 1981] is macroscopically defined as when the contact angle formed by the adsorbate with the surface is 0°. Complete wetting occurs when the adsorbate-substrate interaction is strong and the lattice parameters of the substrate surface match well with the adsorbate dimensions. When the interaction is

Table 2.2: Residence times of adsorbates versus the strength of interaction with the substrate

| $Q$ [J/mol] | $Q$ [kcal/mol] | $\tau$ at 25° [sec$^{-1}$] | Regime |
|---|---|---|---|
| 0.4 | 0.1 | $10^{-13}$ | No Adsorption |
| 6.3 | 1.5 | $10^{-12}$ | Region of Physisorption |
| 14.6 | 3.5 | $4 \times 10^{-11}$ | |
| 37.0 | 9.0 | $4 \times 10^{-7}$ | Unity |
| 83.6 | 20.0 | 100 | Chemisorption |
| 167.3 | 40.0 | $10^{17}$ | |

strong the thin film builds up in layer-by-layer fashion by a series of discrete steps when it is below $T_R$ and smoothly at higher temperatures. Only rare gases and small spherical molecules exhibit complete wetting, all which exhibit bulk crystal unit cell structures similar to the two-dimensional thin-film unit cell parameters formed upon adsorption onto the substrate [Bienfait, 1985].

## 2.2 Desorption

Desorption is the amount of energy needed for an adsorbate molecule to be removed from the potential well in the surface potential. The residence time in the potential well is proportional to,

$$\tau_0 e^{(E/RT)}, \tag{2.2}$$

where $\tau_0$ is the characteristic time which is dependent on the molecule adsorbed and E is the energy of adsorption. A table of typical residence times can be found in Table 2.2.

### 2.2.1 Redhead Equation

Analysis of the desorption process of a substrate was first given by Redhead [Redhead, 1962]. The assumptions made by Redhead in the desorption process are that the desorption energy is independent of time and concentration and takes the form for a zero-order desorption

process,

$$\frac{E_0}{R} = \frac{\nu_0}{\sigma\alpha} e^{\left(-\frac{E_0}{RT_p}\right)}, \tag{2.3}$$

for a first-order desorption process,

$$\frac{E_1}{RT_p^2} = \frac{\nu_1}{\alpha} e^{\left(-\frac{E_1}{RT_p}\right)}, \tag{2.4}$$

and for a second-order process,

$$\frac{E_2}{R} = \frac{\nu_2}{\alpha} e^{\left(-\frac{E_2}{RT_p}\right)}, \tag{2.5}$$

where $T_p$ is the temperature of the desorption peak, $\sigma$ is the initial adsorbate concentration, and $\alpha$ is the constant of proportionality relating the rise in temperature with time. The temperature rise is linear with time. If sensitivity and resolution of the TPD apparatus is high enough, TPD can be used to identify the heats of adsorption of different types of sites as well as the relative number of each type of adsorption site.

A general form of the equation can be arrived at by simple kinetic analysis [Adamson and Gast, 1996] where a rate $R$ can be expressed as,

$$R = -\frac{d\theta}{dt} = A\theta e^{\left(\frac{-E}{RT}\right)}, \tag{2.6}$$

where $A$ is a frequency factor, $E$ is the desorption energy, and $\theta$ is the coverage. If a uniform rate of heating is assumed the differentiation of equation 2.6 yields,

$$\frac{dR}{dt} = A - \frac{d\theta}{dt} e^{\left(\frac{-E}{RT}\right)} + (A\theta)\, e^{\left(\frac{-E}{RT}\right)} \left(-\frac{E}{R}\right) \left(-\frac{\beta}{T^2}\right), \tag{2.7}$$

setting $dR/dt = 0$ gives,

$$\frac{E}{RT^2} = \frac{A}{\beta} e^{\left(\frac{-E}{RT_m}\right)}, \tag{2.8}$$

where $T_m$ is the temperature of the maximum desorption rate. $E$ can thus be calculated once a value for $A$ is chosen (typically $A \sim 10^{-13}$ sec$^{-1}$). If TPD experiments are run

at multiple rates, an approximate value of $A$ can be determined by calculating the slope of a plot of $\ln \beta/T_m^2$ versus, $1/T_m$ [Adamson and Gast, 1996]. The maximum desorption energy can be determined from the following equation which can derived from the redhead equation,

$$\ln\left(\frac{\beta}{T_m^2}\right) = -ln\left(\frac{E_d}{k_B\nu}\right) - \frac{E_d}{k_B}\frac{1}{T_m}, \tag{2.9}$$

where $\beta$ is the heating rate, and $\nu$ is the pre-exponential factor which quantifies average residence time and usually varies from $10^{12.2} - 10^{16}$ sec$^{-1}$. Simplifying yields,

$$E_d = k_B T_{max} \ln\left(\frac{T_{max}}{\beta}\right) - 3.64. \tag{2.10}$$

Tait et. al. derived a modified coverage dependent desorption energy $E_d(\theta)$ that is derived and modified from the Redhead equation,

$$E_d(\theta) = E_0 + \gamma\theta + E_{def} e^{\left(\frac{-\theta}{\theta_{def}}\right)}, \tag{2.11}$$

where $E_0$ is an empirically derived energy term from the linear portion of the linear region of the coverage-dependent energy term. $\gamma$ is the increase in desorption energy per $\theta$ increase in coverage due to the lateral interactions between adsorbates. $E_{def}$ is the energy difference between $E_0$ and the measures desorption energy at zero coverage. $\theta_{def}$ corresponds to the rate at which the influence of defects sites with increasing coverage. This modified equation yields more accurate results but requires the use of empirical terms which requires background work to determine reliable values.

## 2.3 Surface Structure

In order to properly define the surface structure of an adsorbed thin film, a two-dimensional analog to defining three-dimensional structures needs to be described. Adsorbed thin films can be described by two-dimensional unit cells which represent the smallest repeatable pattern adopted by the thin film relative to the underlying substrate.

### 2.3.1 Miller Indices

The substrate is composed of a three-dimensional system of atoms which can be expressed in terms of a unit cell which describes the smallest repeatable unit of the crystal [Sands, 1993]. The periodicity of the three-dimensional cell can be related through the use of Miller indices. Miller indices are represented as $h$, $k$, and $l$ values which correspond to the inverse of $x$, $y$, and $z$ coordinates in a cartesian system. Miller indices relate the lattice spacings of a cell in terms of whole numbers. This notation can be utilized in the determination of inter-planar lattice spacings within a lattice by the relation to inter-planar spacing $d$,

$$d = \left[ \left(\frac{h}{a}\right)^2 + \left(\frac{k}{b}\right)^2 + \left(\frac{l}{c}\right)^2 \right]^{\frac{1}{2}} \tag{2.12}$$

where $a$, $b$, and $c$ are the unit cell parameters (see Figure 2.3).

### 2.3.2 Surface Coordination

Actual crystal planes are incomplete and contain defects. There are a variety of dislocations which can alter the surface coordination of an atom. The surface coordination number of an atom on the surface also changes if it resides on an edge of a crystal. The reduction in the surface coordination number of an atom on the surface increases the surface free energy of the crystal and therefore increases the binding energy between the surface and an adsorbate molecule [Mutaftschiev, 2001]. An image of the types of surface dislocations is shown in Figure 2.4. The reduced surface coordination number of dislocation sites makes them the first adsorption sites due to their low energy barrier to adsorption. The number of defects on a surface can therefore drastically affect the adsorption properties of a system. To experimentally study an adsorbate-substrate system, care must be taken to ensure that the substrate contains as few defects and impurities as possible to properly quantify values such as the binding energy of the predominantly exposed crystallographic surface.

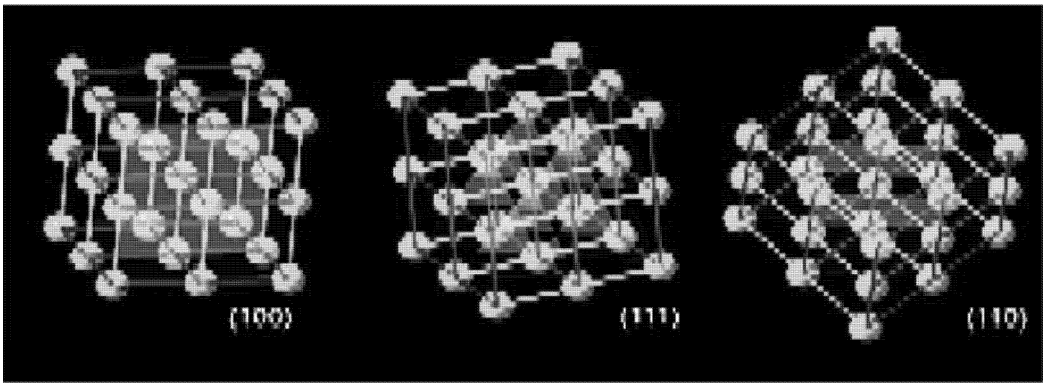


Figure 2.3: Illustration of Miller indices nomenclature used to describe different crystallographic faces of a crystal.

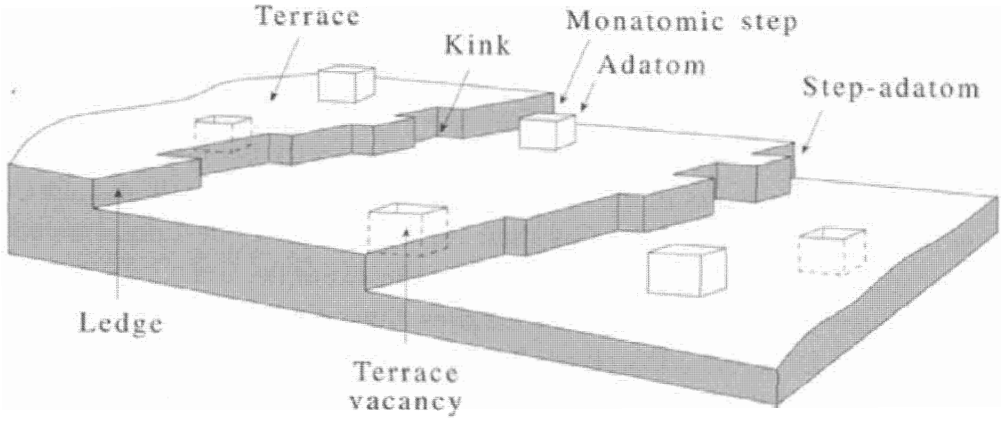


Figure 2.4: An illustration of the different types of surface dislocations present on a typical surface. Image from [McQuarrie and Simon, 1997].

### 2.3.3 Crystal Defects

Crystal defects differ from surface defects and affect the entire crystal. Crystal defects are lattice imperfections in the crystal, created during the nucleation process. Defects typically involve an extra or intersticial atom in the lattice known as a Frenkel defect, or as a vacancy in the lattice known as a Schottky defect [Mutaftschiev, 2001]. There are also translational defects where the lattice is shifted in a particular direction or angle. An edge defect occurs when a shift in the lattice is made by the crystal during nucleation to remove a series of vacant or interstitial sites within the lattice. A slip in a particular direction can move a series of atoms off line which affects all atoms grown above this slip plane. This type of dislocation is called a screw dislocation.

### 2.3.4 Surface Relaxation and Reconstruction

Reconstruction of the surface occurs when any surface is created. The dangling bonds at the surface restructure in order to increase their surface coordination number which maximizes the number of interactions between other atoms thereby lowering the surface free energy of the atom [Somorjai, 1994]. Relaxation and reconstruction assume a surface structure different than the bulk structure of the substrate. Restructuring occurs several layers into the substrate until the bulk lattice resumes. Typically, the outer layer relaxes into the substrate, decreasing the interatomic distance between the layers [Somorjai, 1994]. Reconstruction can be adsorbate induced or can occur on its own. The structural relaxation of an MgO (100) surface is shown in Figure 2.5.

### 2.3.5 Adsorption Sites

Adsorption sites differ slightly depending on type of crystal facet exposed. In these studies we are primarily concerned with the (100) face of magnesium oxide and the (0001) face or basal plane of graphite. On a (100) face of an f.c.c. crystal, a surface exhibits four-fold symmetry which can be separated into two orthogonal modes. On this potential energy surface there are three primary adsorption sites which correspond to the various potential

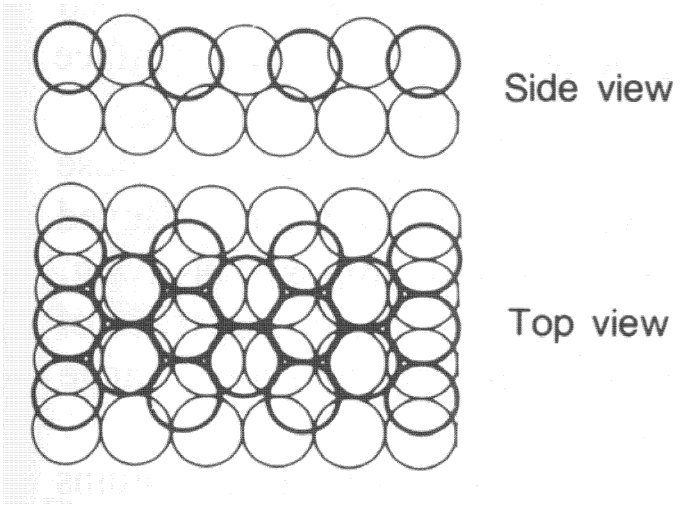


Figure 2.5: The side view illustrates the inward relaxation of the surface creating a corrugation in the surface. The top view shows the translational restructuring of the surface during reconstruction. Image from [Somorjai, 1994].

energy minima of the surface (see Figure 2.6) [Steele, 1974]. The saddle point or 'bridge' lies in between two atoms on the saddle point of the potential energy surface. As is characteristic with any saddle point this is a local minimum and not the global minimum of the system. At the center of four atoms on the surface the potential energy surface experiences a dip from all directions and is the global minimum of the system this site is called the 'hollow' site. The third type of site is the potential directly above an atom, called the 'atom' or 'a-top' site. Although this site is not located at a potential energy minima, it is an adsorption site because of its proximity to four hollow sites surrounding it due to the four-fold symmetry of the system. This allows for an adsorbate molecule to exploit the four-fold symmetry of the hollow sites and saddle points and configure on top of this site.

The sites on the (0001) face like graphite form a three-fold symmetric surface and thus has a different potential energy surface with different adsorption locations (see Figure 2.7). At the center of three atoms lies the three-fold 'hollow' point adsorption site. The 'center' adsorption site lies at the center of a graphene hexagon which forms the surface. This site lies above an atom in the $B$ layer beneath it (shown in red). The 'bridge' site lies in between two atoms at a saddle point of the potential energy surface similar to MgO. The 'a-top' site lies above a surface atom and can access both the six-fold symmetry of the hollow sites and the six-fold symmetry of the saddle points [Steele, 1974].

### 2.3.6 Surface Acidity

The reactivity of a surface can be determined using the Lewis definition of acidity and basicity. The Lewis acidity or basicity of a surface is based on whether it is an electron donor or acceptor and forms a coordinated covalent bond. The procedure used to study the acidity of a surface or surface site is to use a probe molecule that is classified as a strong base. One very commonly used probe molecule is pyridine. Pyridine is a strong base ($pK_B$=8.75) and is routinely used as a surface probe [Travert et al., 2006]. Pyridine easily gives rise to the formation of H-bonded and pyridinium species. Pyridine is routinely used

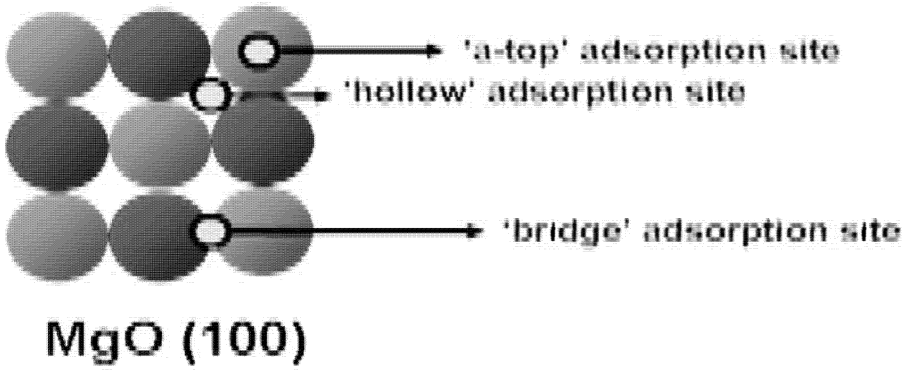


Figure 2.6: An illustration of different adsorption sites on MgO corresponding to minimums in the corrugation of the surface potential.

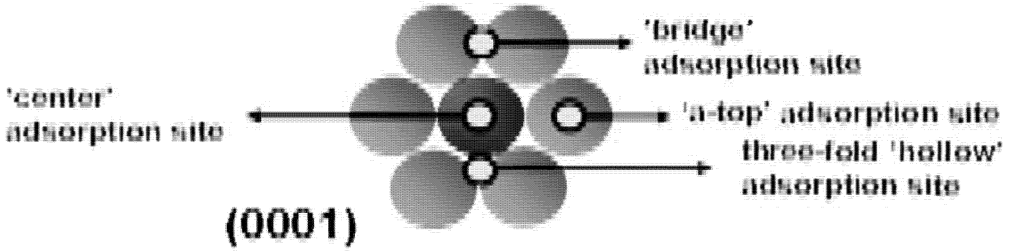


Figure 2.7: An illustration of different adsorption sites on graphite corresponding to minimums in the corrugation of the surface potential. The red atom represents a carbon atom in the layer beneath the blue layer in the *AB* stacking sequence.

because of the lone pair of electrons it possesses at the nitrogen atom site. These electron can participate in forming a covalently bonded species. The IR spectrum of pyridine can also be readily distinguished to determine the nature of the acidic site from the change of the $\nu$(C=C) ring vibrational modes. The nature of surface species formed can be determined from analysis of the spectra from 1400 - 1700 $cm^{-1}$ range. In this region of the spectra are various ring puckering and breathing modes which become hindered upon adsorption to the surface. The hindering of these vibrational modes can shift, broaden, and split peaks which can readily be identified.

### 2.3.7 Commensurability

When an atom or molecule is adsorbed to a surface, its interaction with the surface (adsorbate-substrate) interaction relative to the interactions it experiences from other adsorbate atoms or molecules (adsorbate-adsorbate) is an important consideration on how the surface structure aligns itself relative to the surface atoms of the substrate. When the thin film atoms or molecules adsorbed onto the substrate are aligned with the surface atoms, a similar crystal structure is formed. When this occurs the surface structure is said to be commensurate. Conversely, if the adsorbed thin-film has a weak adsorbate-substrate interaction relative to the adsorbate-adsorbate interaction then the adsorbate molecules may ignore the symmetry of the surface and form an incommensurate structure relative to the surface.

To quantify the surface structure formed by the thin-film on the substrate a set of vectors, $\vec{a}'$, and $\vec{b}'$, can be used referencing the coordinates of the surface structure of the substrate. This can be expressed as,

$$\vec{a}' = m_{11}\vec{a} + m_{12}\vec{b}, \tag{2.13}$$

$$\vec{b}' = m_{21}\vec{a} + m_{22}\vec{b}, \tag{2.14}$$

where $\vec{a}$ and $\vec{b}$ are the unit vectors of the substrate surface and $m_{ij}$ are the coefficients to the matrix $\mathbf{M}$ that define the surface unit cell of a substrate [Somorjai, 1994],

$$\mathbf{M} = \begin{bmatrix} m_{11} & m_{12} \\ m_{21} & m_{22} \end{bmatrix}. \tag{2.15}$$

This notation can be expressed in a short-hand notation where the unit cell of the surface structure is designated with respect to the bulk unit cell. So, for a surface structure that is commensurate with the surface at every site, then the notation would be $(1 \times 1)$, corresponding to one adsorbed atom for every surface substrate atom. This short hand notation is useful if the surface thin film is in registry with the surface but can be complicated slightly by non-integer multiples and rotated unit cells. For rotated structures the designation of an angle $R$ is added to notation to describe the rotation of the surface lattice unit cell from the surface substrate unit cell. For example on a (100) cubic crystal face, if adsorption occurs at every other site excluding the central atom site at the center then a $\sqrt{2} \times \sqrt{2}\ R45^\circ$ can be observed. A rotation can also be observed in Figure 2.8, if the third lattice site on a hexagonal face is occupied then a commensurate $\sqrt{3} \times \sqrt{3}\ R30^\circ$ surface structure would arise.

## 2.4 Physics of Adsorption

Adsorption onto a substrate can be approached from a variety of viewpoints all with their own distinct advantages and disadvantages. The end result of these models all draw the same conclusions. The variety of derivations arises from the need to describe adsorption of molecules in different areas of study and illustrates the importance of isotherm models.

### 2.4.1 Kinetics and Thermodynamics of Adsorption

The kinetics of adsorption relate to the relative rates of adsorption, retention time, diffusion, and desorption of a particular adsorbate-substrate interaction. Adsorption in kinetic

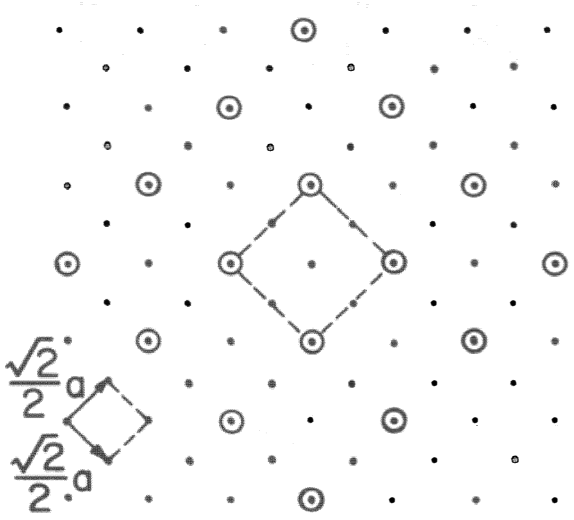


(a)

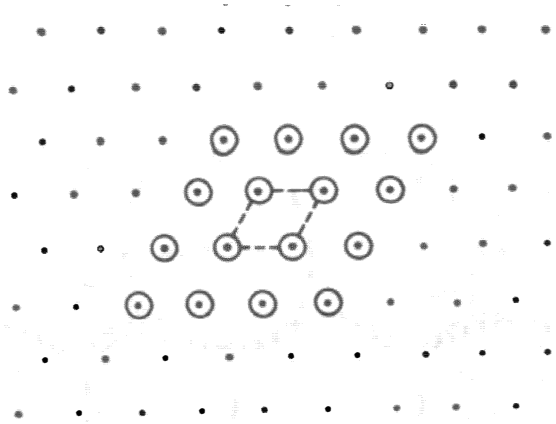

(b)

Figure 2.8: This is an illustration of a surface structure on a MgO (100) surface and on a graphite (0001) surface. (a) $\sqrt{2} \times \sqrt{2}$ $R45°$ structure characteristic of $CH_4$ adsorption on MgO (100) surface. (b) $\sqrt{3} \times \sqrt{3}$ $R30°$ structure characteristic of $CH_4$ adsorption on graphite (0001) surface. Image from [Somorjai, 1994].

terms refers to the steady-state equilibrium maintained by these competing phenomena.

When a molecule or atom approaches a surface each atom or molecule encounters an attractive potential. If the parameters are appropriate, the adsorbate molecule is 'trapped' by the surface potential in a process called adsorption. Adsorption is an exothermic process releasing energy so that the atom or molecule and surface reside in a lower energy state favorable to both the adsorbate and the surface. This can be recognized in the basic thermodynamic equation,

$$\Delta G = \Delta H - T\Delta S, \tag{2.16}$$

where $\Delta G$ is the change in the Gibbs free energy, $\Delta H$ is the change in enthalpy of adsorption, $\Delta S$ is the change in entropy, and $T$ is the temperature. The process of adsorption lowers the free energy and entropy making the change negative thereby favoring adsorption at a certain temperature. The rate of adsorption onto the surface depends on the kinetic parameters of the vapor above the surface and can be expressed as a kinetic equation,

$$\frac{dn_{ads}}{dT} = Ae^{(-\frac{E_a}{RT})}, \tag{2.17}$$

where $E_a$ is the activation energy, $T$ is the temperature required for adsorption to occur, and $A$ is the arrehenius pre-exponential factor which relates to the frequency of collisions with the surface. If expressed as a flux (rate of molecules colliding with a surface of dimensions x by y per unit of time), then the rate of adsorption can be expressed as,

$$\frac{dn_{ads}}{dT} = S \cdot F, \tag{2.18}$$

where $S$ is the sticking probability and $F$ is the incident flux of atoms or molecules. The incident flux of molecules is derived from the kinetic theory of gases and is expressed as,

$$F = \frac{P}{\sqrt{2\pi mkT}}, \tag{2.19}$$

where $P$ is the gas pressure, $m$ is the mass of the atom or molecule and $T$ is the temperature. The sticking probability of a molecule is dictated by the adsorbate and substrate chosen and their subsequent interactions with each other. The sticking probability is also affected by the existing coverage of adsorbed molecules and can be generally expressed as,

$$S = f(\theta)e^{(-\frac{E_a}{RT})} \tag{2.20}$$

where $f(\theta)$ is the function relating sticking probability to the existing coverage of adsorbed molecules. Coverage, $\theta$, is defined to be the number of occupied adsorption sites over the total number of available adsorption sites or,

$$\theta = \frac{S_{occupied}}{S_{total}}, \tag{2.21}$$

Combining equations 2.18 and 2.20 yields,

$$\frac{dn_{ads}}{dT} = \frac{f(\theta)}{\sqrt{2\pi mkT}}e^{(-\frac{E_a}{RT})}. \tag{2.22}$$

This equation takes in many assumptions; the activation energy is not dependent on coverage, the sticking probability is directly proportional to the number of vacant adsorption sites, the surface is perfect with similar adsorption sites, and adsorption is non-dissociative [Adamson and Gast, 1996]. Another factor determining adsorption is residence time of a molecule on the substrate adsorption site. This can also be expressed in a kinetic arrenhius form as,

$$\tau = \tau_0 e^{(\frac{Q}{RT})}, \tag{2.23}$$

where $\tau_0$ is the characteristic residence time of the particular adsorbate substrate interaction, $Q$ is the heat of adsorption which is defined as the amount of energy needed to bring a molecule from the vapor to the substrate adsorption site [Pan et al., 1998], [Sircar and Cao, 2002]. A typical residence time of a physisorbed atom or molecule depends on the strength of the interaction between the adsorbate and substrate and is shown in Table 2.2.

### 2.4.2 Statistical Thermodynamics of Adsorption

The statistical thermodynamic model of adsorption can be viewed as a adiabatic vessel containing adsorbate molecules and substrate material. Adsorbate in this context refers to the vapor in the vessel and the adsorbed film of adsorbate on the substrate. The mixed system is in equilibrium with the vessel at temperature T. The canonical partition function for the systems total number of accessible states is,

$$Z = \sum_{n} e^{(-\beta E_n)}, \tag{2.24}$$

where $\beta = (kT)^{-1}$, and $E_n$ is the energy of state $n$. This partition can now be written to represent all phases of the adsorbate and substrate,

$$Z_{tot} = Z_{film} Z_{vapor} Z_{substrate}. \tag{2.25}$$

The thermodynamic properties such as energy, entropy, free energy of the vapor, film, and substrate can be derived from the above partition functions. The difference from the adsorbed film and the vapor can be discerned in the three-dimensional to two-dimensional analogs to pressure [Dash, 1975]. In a three-dimensional system, pressure is defined as,

$$P = -\left(\frac{\partial F}{\partial V}\right)_{T,V}, \tag{2.26}$$

where $F$ is the Helmholtz free energy, and $V$ is the volume and $T$ and $V$ are held constant. The two-dimensional analog to equation 2.26 is,

$$\phi = -\left(\frac{\partial F}{\partial A}\right)_{T,V}, \tag{2.27}$$

where $\phi$ is the spreading pressure, $A$ is the area and $T$ and $V$ are held constant. The difference between equations 2.26 and 2.27 is that in the three-dimensional pressure the area is held constant while there is a change in volume and free energy. In the two-dimensional

analog, the volume and temperature is held constant with a change in area and free energy.

In an adsorption system, equilibrium must be established between the vapor, adsorbed film, and substrate. This can be viewed in different ways depending on the type of ensemble of variables utilized. The microcanonical, canonical, and grand canonical ensembles all yield the same equilibrium properties but differ in what properties fluctuate to maintain equilibrium [Hill, 1986]. All ensembles will achieve the same equilibrium in an adsorption system where,

$$\mu_{film} = \mu_{adsorption}. \tag{2.28}$$

Chemical potential $\mu$, is related to entropy and energy of the system as follows,

$$\mu = \left(\frac{\partial E}{\partial N}\right)_{S,A,V} = T\left(\frac{\partial S}{\partial N}\right)_{E,A,V}, \tag{2.29}$$

where $N$ is the number of particles in a particular phase. From the energy and entropy one can establish connections to other thermodynamic variables using,

$$F = E - TS, \tag{2.30}$$

$$G = F + \sum_n X_n x_n, \tag{2.31}$$

$$H = E + \sum_n X_n x_n, \tag{2.32}$$

$$\Omega = F - G. \tag{2.33}$$

Taking the total differential of each of these functions gives,

$$dH = -SdT - \phi dA - PdV + \sum \mu_i dN_i, \tag{2.34}$$

$$dG = -SdT + Ad\phi + VdP + \sum \mu_i dN_i, \tag{2.35}$$

$$dF = TdS + Ad\phi + VdP + \sum \mu_i dN_i, \tag{2.36}$$

$$d\Omega = -Ad\phi - \phi dA - VdP - PdV. \tag{2.37}$$

where $\Omega$ is the thermodynamic potential. The chemical potentials are related to the above equations [Dash, 1975],

$$\mu = (\frac{\partial H}{\partial N})_{T,A,V} = (\frac{\partial G}{\partial N})_{T,\phi,P} = (\frac{\partial H}{\partial N})_{S,\phi,P}. \tag{2.38}$$

It can now be shown that the chemical potential is just equal to the Gibbs free energy per particle [Mutaftschiev, 2001]. Gibbs free energy is an extensive variable and is proportional to the total number of particles $N$. The variables related to G are intensive variables so for each component,

$$G_i = N_i \mu_i. \tag{2.39}$$

### 2.4.3 Potential Theory of Adsorption

Potential theory of adsorption is predicated on all interactions within a system being compromised of attractive and repulsive interactions describing the adsorbate-adsorbate interaction and the adsorbate-substrate interaction. The most basic interaction describing this attractive and repulsive interactions between atoms and molecules is the van der Waals interaction.

### 2.4.4 Adsorbate-Substrate Potentials

The following models refer to the use of inter-atomic potentials to describe all interactions in the system. Although these methods are more difficult to solve analytically, they provide a more accurate description of the adsorbate-adsorbate and adsorbate-substrate interactions. Potential models play a central role in theory and computer simulations of adsorption. One of the simplest potential forms is the Lennard-Jones potential,

$$U(r) = 4\varepsilon \left( \left[\frac{\sigma}{r}\right]^{12} - \left[\frac{\sigma}{r}\right]^{6} \right), \tag{2.40}$$

where $r$ is the distance between particles, $\varepsilon$ is the potential energy well depth and $\sigma$ is the zero-potential point of the potential energy curve or the hard-sphere diameter. The first term is a repulsion force which scales as $1/r^{12}$, the result of nuclear-nuclear repulsion between atoms and from overlapping electron orbitals which violates Pauli's exclusion principle of electrons occupying the same orbital. The second term an attractive term which scales as $1/r^6$, the result of an attractive van der Waals force,

$$U(r) = 4\varepsilon \int \left( \left[\frac{\sigma}{r}\right]^{12} - \left[\frac{\sigma}{r}\right]^{6} \right) dr. \tag{2.41}$$

To apply a potential model to a adsorbate-substrate interaction modifications must be made to account for the multiple interactions the adsorbate atoms 'feels' from the surface. The simplest potential model of adsorption is to model the surface as a two-dimensional structureless plane with spherically symmetric adsorbate molecules [Steele, 1974]. This replaces the sum of interaction energies of all the substrate atoms with a constant distribution. This allows the sum to be replaced by an integral. To obtain the result for this first potential a general set of coordinates must be constructed to relate the adsorbate to the surface an example of this is illustrated in Figure 2.9. In Figure 2.9, $x$, $y$, and $z$ are the coordinates of the surface, and $Z$ is the perpendicular distance above the surface,

$$r = \sqrt{(z+Z)^2 + X^2 + Y^2}, \tag{2.42}$$

inserting into equation (2.41) gives,

$$U(z) = 4\varepsilon \int^{x}\int^{y}\int^{z} \left( \left[\frac{\sigma}{((z+Z)^2+x^2+z^2)^{1/2}}\right]^{12} - \left[\frac{\sigma}{((z+Z)^2+x^2+z^2)^{1/2}}\right]^{6} \right) dxdydz, \tag{2.43}$$

this can be simplified by setting $S = X^2 + Y^2$,

$$U(z) = 4\varepsilon n \int_0^{\infty}\int_0^{\infty} \left( \frac{\sigma^{12}}{[(z+Z)^2+S^2]^6} - \frac{\sigma^6}{[(z+Z)^2+S^2]^3} \right) \pi dSdZ, \tag{2.44}$$

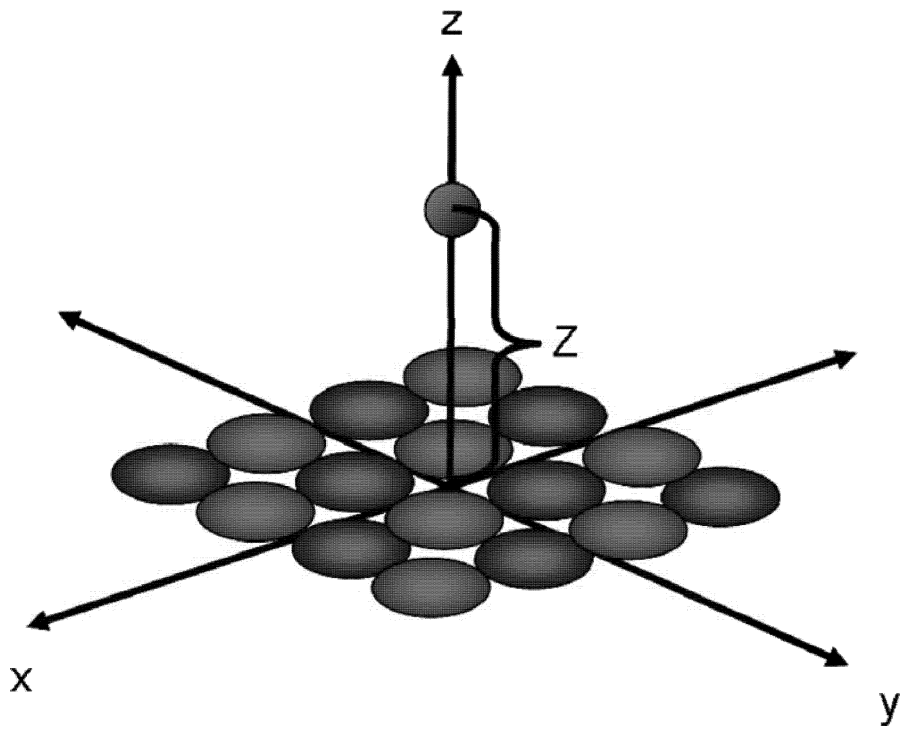


Figure 2.9: A description of the nomenclature used by Steele in the development of the $\sum$ (10-4) potential.

integrating over S gives,

$$U(z) = 2\pi n\varepsilon \int_0^\infty \left( \frac{2\sigma^{12}}{5(z+Z)^{10}} - \frac{\sigma^6}{(z+Z)^4} \right) dZ. \tag{2.45}$$

When the above solution is summed over the the substrate surface vectors, it gives the solution is known as the $\sum$(10–4) potential. This model first proposed by William Steele, represents the interaction potential after integration over a plane of atoms parallel to the surface. The $\sum$(10–4) potential cannot show variations as the atoms move parallel to the surface but shows a significant improvement over the (9-3) potential [Steele, 1974] without necessitating the lengthy computations to evaluate three-dimensional summations. The (9–3) potential is expressed as,

$$U(z) = \frac{2}{3}\pi n\sigma^3\varepsilon \left( \frac{2}{15} \left[\frac{\sigma}{z}\right]^9 - \left[\frac{\sigma}{z}\right]^3 \right) \tag{2.46}$$

It physically represents a flat-feature surface which is an over generalization of the substrate-adsorbate interaction and does not produce accurate results. It fails to capture surface features such as corrugation of atoms of different sizes, ionic or charge nature of the constituent atoms of the substrate, and effects of multiple substrate layers [Steele, 1974].

Using the $\sum$(10–4) potential as a starting point one can increase the level of sophistication of the calculation by relating it to the symmetry properties of the surface and adding pair-wise interactions and taking into consideration the effects of ionic substrates and multi-pole moments of adsorbate molecules. Explicit derivations for adsorbate-substrate interactions with graphite and simple cubic ionic solids like MgO can be found in [Steele, 1974].

### 2.4.5 Adsorbate-Adsorbate Potentials

To fully obtain an accurate potential model describing all interactions in the system one must also account for adsorbate-adsorbate interactions. These models are based on the

same potentials used for adsorbate-substrate interactions but are more grounded in semi-empirical results calculated from the interactions of molecules. The simplest interaction to theoretically model is the two-body problem where two particles interact with each other. Experimental data for this particular type of interaction is primarily obtained through gas-phase data which assumes implicity that the gases are near-ideal and when dilute do not interact with other particles [Axelrod, 1951a]. This is primarily based on the same Lennard-Jones interaction as described in equation 2.40. The experimental data obtained from gas-phase interactions potentials is used to find the $\sigma$ and $\varepsilon$ parameters. The solution to a two-body problem is exactly solvable but does not represent a realistic model of the system. To properly assess this problem one needs to solve for a three-body interaction. Axelrod first demonstrated that the interaction of three particles can be approximated by a sum of pair-wise interactions between the three atoms [Axelrod, 1951b]. If a third order pertubation is applied to the calculation the third term corresponds to the interactions between the three atoms. The resulting magnitude of the interaction is,

$$\frac{V\alpha^3}{r_{12}^3 r_{23}^3 r_{31}^3}, \tag{2.47}$$

where $r_{12}^3$, $r_{23}^3$, and $r_{31}^3$ are the distances between the atoms. The Lennard-Jones interaction potential depends on the shape of the triangle created by the three atoms. The dependence of the interaction potential on the shape of the triangle is due to a inverse dependence on distance in the third order interaction energy term of the pertubation and to the dipole-dipole orientation of the atoms relative to each other. The solutions of the third term yielding the interaction potential is,

$$W_0^{(3)} = C\frac{3\cos\gamma_1\cos\gamma_2\cos\gamma_3 + 1}{r_{12}^3 r_{23}^3 r_{31}^3}, \tag{2.48}$$

where $C$ is the constant of integration and $\gamma_1$, $\gamma_2$, and $\gamma_3$ are the angles formed by the triangle of the three interacting atoms. When solved for a variety of configurations (see Figure 2.10) it can be shown that when three atoms form a triangle where a third atoms

distance is less than the distance between the two other atoms the interaction potential is repulsive. In all other cases the interaction is attractive.

### 2.4.6 Rotational Motion of Molecules

The rotational motion of a molecule are is an important parameter which can determine the translational and rotational freedom a molecule possesses at a particular temperature and coverage. The rotational motion for any collection of atoms can be described by,

$$\mathbf{L} = \mathbf{I}\omega, \tag{2.49}$$

where $\mathbf{I}$ is the moment of inertia tensor, and $\omega$ is the angular velocity. Solutions of $\mathbf{I}$ can be classified on the basis of the values of the three principle moments of inertia, $I_A$, $I_B$, and $I_C$. In naming the moments of inertia $I_C$ is always the largest moment of inertia and $I_A$ is always the smallest. The five classes are as follows:

- Linear Molecules, $I_B = I_C$, $I_A = 0$
- Spherical Tops, $I_A = I_B = I_C$
- Prolate Symmetric Tops, $I_A < I_B = I_C$
- Oblate Symmetric Tops, $I_A = I_B < I_C$
- Asymmetric Tops, $I_A < I_B < I_C$

group theory can also be used to classify the rotational properties of molecules. All spherical top molecules have a high degree of symmetry and have point group assignments such as $O_h$, $T_d$, and $I_h$. Linear molecules have point groups like $C_{\infty v}$ and $D_{\infty h}$. Symmetric tops all have a $C_n$-axis with $n$ greater than 2. The symmetry properties of a molecule are also useful in locating the principle axes of rotation [Bernath, 1995].

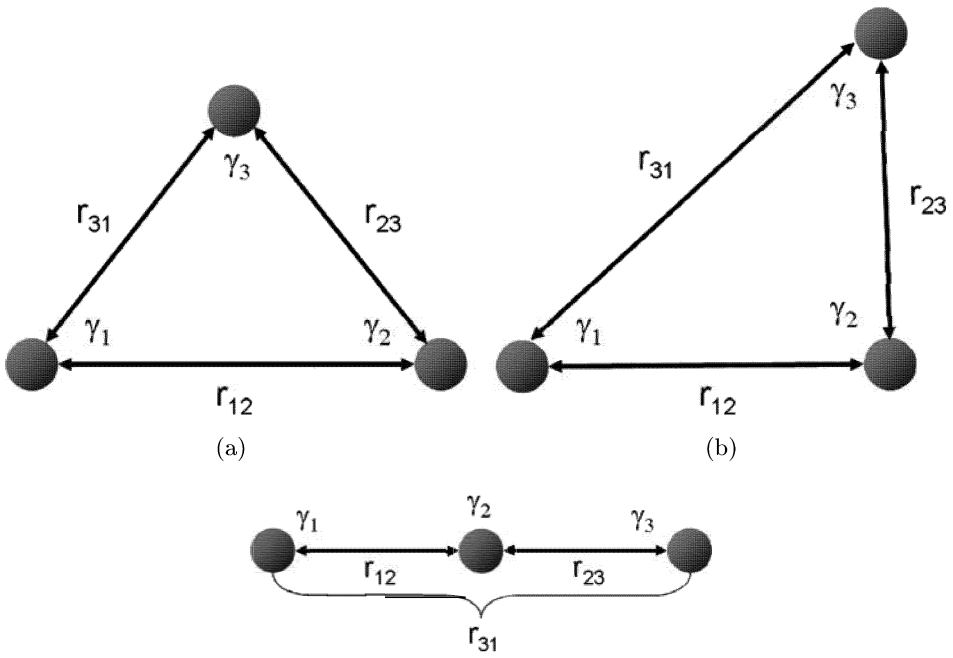


Figure 2.10: Interactions between atoms or molecules can be categorized in to three basic types: (a) When $\gamma_1 = \gamma_2 = \gamma_3$ the interaction energy is positive so the interaction is repulsive. (b) When $\gamma_2 = 90^\circ$ the interaction is positive and the interaction is repulsive. (c) When $\gamma_1 = \gamma_2 = 0^\circ$ and $\gamma = 180^\circ$ the interaction potential is negative which indicates attraction.

### 2.4.7 Conformation of Molecules

In larger alkane molecules, rotation about the $sp^2$ carbon-carbon bonds results in a structural change in the molecule. Conformers can interconvert by rotation around single bonds, without breaking chemical bonds. The relative populations of various conformations follows a Boltzmann distribution and is dependent on the $kT$,

$$\frac{N_i}{N_j} = \frac{g_i}{g_j} \exp\left(-\frac{E_i - Ej}{RT}\right), \tag{2.50}$$

where $N_i$ and $N_j$ represent the number in the highest and lowest energy conformation, $g$ is the number of conformations found at that particular energy, and $E_i$ and $E_j$ are the energies of each conformation.

In the case of $n$-hexane this results in three possible molecular conformations, the linear *trans*, and folded *cis* and *gauche* conformations. In the case of cyclohexane the bond rotation allows for the inter-conversion between its chair, boat, and twist conformations. Multiple effects can account for the conformation of alkane molecules such as; bond interaction with the back lobes of orbitals on adjacent atoms which is possible only when atoms are staggered thereby making this conformation energetically favorable, steric repulsion between atoms favors the maximum distance between atoms [Battezzati et al., 1975]. The relatively low energy needed for conformation to inter-convert allows molecules to undergo rapid conformational change and can reach frequencies of $10^8$ sec$^{-1}$ [Leventis et al., 1997].

## 2.5 Two-Dimensional Thermodynamics

A volumetric isotherm is an experimental method to study the the number of molecules adsorbed as a function of pressure. Thermodynamically, this can be expressed as the equilibrium of chemical potentials between the adsorbate and substrate and the three-dimensional bulk vapor above the adsorbate molecules. The two-dimensional spreading pressure of the

adsorbed film can be measured indirectly through its interaction with the three-dimensional bulk vapor pressure above it.

### 2.5.1 Definitions of Two-Dimensional Phases

Surfaces can exist in three phases which are analogs to the three-dimensional solid, liquid, and vapor phases. The definitions of these phases differ from their three-dimensional counterparts and deserve explanation. A two-dimensional vapor can be considered to be a transactionally disordered film which has a constant density throughout the film [Lee and Kosterlitz, 1990]. The melting process occurs in a random fashion where at random spots in the film dislocations occur which desorb off the surface.

A two-dimensional liquid can be defined as translationally disordered as well but melts in an orderly fashion. Desorption in a two-dimensional liquid film occurs at the domain wall of the droplet and proceeds inwards. This forms cleavage locations which eventually split the large drop into smaller droplets increasing the exposed surface area where the process continues.

A two-dimensional solid can be defined as translationally ordered where the adsorbate atom or molecule is firmly locked into the adsorption site potential. Melting occurs in a similar fashion as in a liquid where dislocations occur in the two-dimensional film which creates translational disorder and locations for other adsorbate atoms to migrate to. A two-dimensional hypercritical fluid can be defined as the continuous growth at the growth front and no condensation occurs. Growth occurs in a monotonic fashion and proceeds smoothly to the saturated vapor pressure [Larese and Lee, 1997], [Phillips and Larese, 1997].

### 2.5.2 Two-Dimensional Melting

The melting of any material regardless of dimensionality is still a debated topic as to what are the mechanism(s) are involved. One major difference between a two-dimensional system and a three-dimensional system are the energetics need to melt the structures. In two-dimensions the number of nearest-neighbor interactions is reduced because of the predominant interactions which occur between the surface and adsorbed molecule and between other neighboring adsorbed molecules [Steele, 1996]. If all the interacting molecules can be approximated by perfect spheres the number of nearest-neighbor interactions in a two-dimensional system would be 2/3 or 0.66 the amount as in a three-dimensional system [Bienfait, 1985]. The different interaction energies can be represented by the critical temperature of a 2D Ising-model versus a 3D Ising-model [Stanley, 1971]. This reduced number of interactions reduces the amount of energy needed to affect a molecule on a surface. This affect can be seen in analagous effects such as the melting temperature of a two-dimensional film versus a three-dimensional bulk structure. Typically, the two-dimensional melting temperature of a substance is also about 0.66 the temperature of the analagous bulk value. This value is a broad approximation and can vary drastically from molecule to molecule because not all molecules can be approximated as spheres which alters the number of nearest-neighbor interactions and changes the energetics of the system.

### 2.5.3 KTHNY Theory of Melting

The theory of two-dimensional melting predicated on the creation of dislocations was developed by Kosterlitz, Thouless, Halperin, Nelson, and Young in a series of publications [Strandburg, 1988], [Ostlund and Halperin, 1981], [Thouless, 1978], [Young and Crowell, 1962], suggested that melting of a two-dimensional solid to a liquid occurs via a two-step process where the unbinding of pairs of surface crystal defects occurs via a two-step transition separated by a nearest-neighbor-bond orientationally ordered fluid termed a '*hexatic*' phase. The process first involves the positional order being disrupted by free dislocations in a dislocation-unbinding transition. A dislocation is defined as a pair of disclinations which

Table 2.3: Various predictions made by the KTHNY theory are summarized for the melting mechanism of a two-dimensional film.

| Mechanism | Solid | *Hexatic* | Liquid |
|---|---|---|---|
| Dislocations | Bound in Pairs | Free | Liquid |
| Disclinations | Bound in Quartets | Bound in Pairs | Free |
| Positional Correlations | Quasi Long-Range | Short Range | Short Range |
| Bond-Oriented Correlations | Long-Range | Quasi Long-Range | Short Range |

is characterized by a mismatch in the number of nearest neighbors and can be thought of as the junction of distinct walls [Fisher and Pandit, 1983]. Dislocation pairs are lower energy defects in two-dimensions and can drastically affect the stability of adsorbed thin films [Larese et al., 1988a]. The creation of a dislocation can be caused by a variety effects such as molecular flipping or conformation.

Solids in this theory are characterized by two types of ordering. Quasi-long-range positional order and orientations of nearest-neighbor bonds. Quasi-long-range positional order refers to the presence of long-range order of atoms or molecules on the surface without vacant sites, defects, or dislocations. Orientation of nearest neighbor bonds refers to the long-range order of the orientation of atoms or molecules relative to each other. Long-range-orientational order implies the existence of adsorbate molecules being oriented in the same pattern or direction over long-ranges The dissociation of dislocation pairs in the two-dimensional solid destroys the long-range positional order. This leaves a fluid which is only characterized by long-range order in the nearest-neighbor bond-orientations. A summary of the predictions made by KTHNY theory for two-dimensional melting can be seen in Table 2.3.

The melting mechanism of a three-dimensional crystal is still a debated subject. The melting temperature of a three-dimensional crystal can be estimated using the Lindermann criterion described in [Lindermann, 1910]. One proposed mechanism is when a phonon mode is softened by an increase in temperature so an instability in the crystal phase takes

place leading to a phase change. This mechanism is not valid in two-dimensions. Recent work [Gomez et al., 2001] has been conducted to determine if the KTHNY theory of defect-mediated melting occurs in three dimensions as well.

### 2.5.4 Two-Dimensional Critical Point

The definitions of a two-dimensional critical points differ in the physical attribute of the critical temperature they concentrate on. A two-dimensional critical temperature refers to the temperature at which a phase transition is continuous or pseudo-second order. At this point there is no distinction between phases and only a hypercritical fluid is present.

## 2.6 Isotherm Models

The variety of approaches used to describe adsorption has yielded a variety of isotherm models. These models vary greatly in complexity and each have their own distinct set of advantages and disadvantages characteristic to them. The models described below are the most commonly used isotherms to describe different adsorption phenomena the assumptions, the information they give, as well as advantages and disadvantages of each is also described.

### 2.6.1 Gibbs Isotherm

The simplest thermodynamic model of adsorption is based on the consideration of thermodynamic equilibrium. Gibbs isotherm is an equation which could be considered an adsorption isotherm that connects surface tension of a solution with the concentration of the solute and thus the extent of adsorption [Hill, 1986]. Gibbs proved that surface tension and concentration are linked through surface concentration, which represents excess of solute per unit area of the surface over what would be present if the bulk concentration prevailed all the way to the surface, it can be positive, negative or zero [Mutaftschiev, 2001]. In other words it gives the difference in concentration of adsorbate if it is different from the bulk all

the way to the surface. $G$ can be expressed as,

$$G = F + TS, \tag{2.51}$$

or replacing $F$ by using the Helmholz free energy relationship,

$$F = U + PV, \tag{2.52}$$

giving,

$$G = U - TS + PV. \tag{2.53}$$

For a small change in a two-dimensional system, U can be expressed in total differential form as,

$$dU = TdS + \sum_{i}^{N} \mu_i dn_i + \gamma dA, \tag{2.54}$$

G can also be simplified assuming a two-dimensional system, (where $V = 0$) and shown in total differential form as,

$$dG = -SdT + \sum_{i}^{N} \mu_i dn_i + \gamma dA, \tag{2.55}$$

when $V = 0$ as in the two-dimensional case, the Gibbs free energy and the Helmholtz free energy H are equal,

$$G = F = U - TS, \tag{2.56}$$

at constant temperature yields,

$$d\gamma = -\sum_{i} \Gamma_i d\mu_i^{(S)}, \tag{2.57}$$

this is the solution to the Gibbs isotherm and shows that the negative of the change in surface tension is related to the spreading pressure, $\phi$ [Mutaftschiev, 2001].

The two-dimensional spreading pressure of a system can best be described in physical terms as a cylinder filled by the adsorbate gas at pressure $p$ which pushes a piston out, increasing the area underneath the piston (see Figure 2.11). An arbitrarily thin drawer is then introduced through a leak-tight slot that allows the substrate to slide without any leakage of gas molecules. Introduction of the thin drawer reduces the surface tension and reduces the pressure due to the introduction of new surfaces for molecules to adsorb to and 'pulls' in the drawer into the cylinder. Equilibrium is established when the pressure of the system is equilibrated. The spreading pressure is the work needed to push the drawer out from the piston. So an increase in the external pressure of the cylinder would increase the pressure inside the area beneath the piston which if kept at the same temperature will increase the spreading pressure of the molecules adsorbed on the surface.

### 2.6.2 Langmuir Isotherm

The simplest situation is when adsorption is limited to a single adsorbed monolayer on the solid surface. The Langmuir isotherm model makes the following assumptions. The substrate surface is perfect and uniform, the molecules are adsorbed to definite adsorbate sites, atoms do not diffuse over the surface, and each adsorption site can only accommodate one adsorbate particle. The original derivation by Langmuir [Langmuir, 1918] was based on kinetic theory but since has derived in a statistical thermodynamic viewpoint by Fowler and Guggenheim [Fowler and Guggenheim, 1949]. The kinetic derivation is based on a dynamic equilibrium between the vapor above the adsorbate and the adsorbate in the adsorbed layer. The statistical thermodynamic derivation does not suffer from the generalizations made by the kinetic derivation in that the adsorbate on the surface and the adsorbate vapor above the surface are equivalent. Both derivations are important to adsorption theory because they are different approaches which yield the same result. The statistical thermodynamic viewpoint is of particular importance because it gives the ability to link the macroscopic observable measurable properties of the isotherm to its microscopic properties.

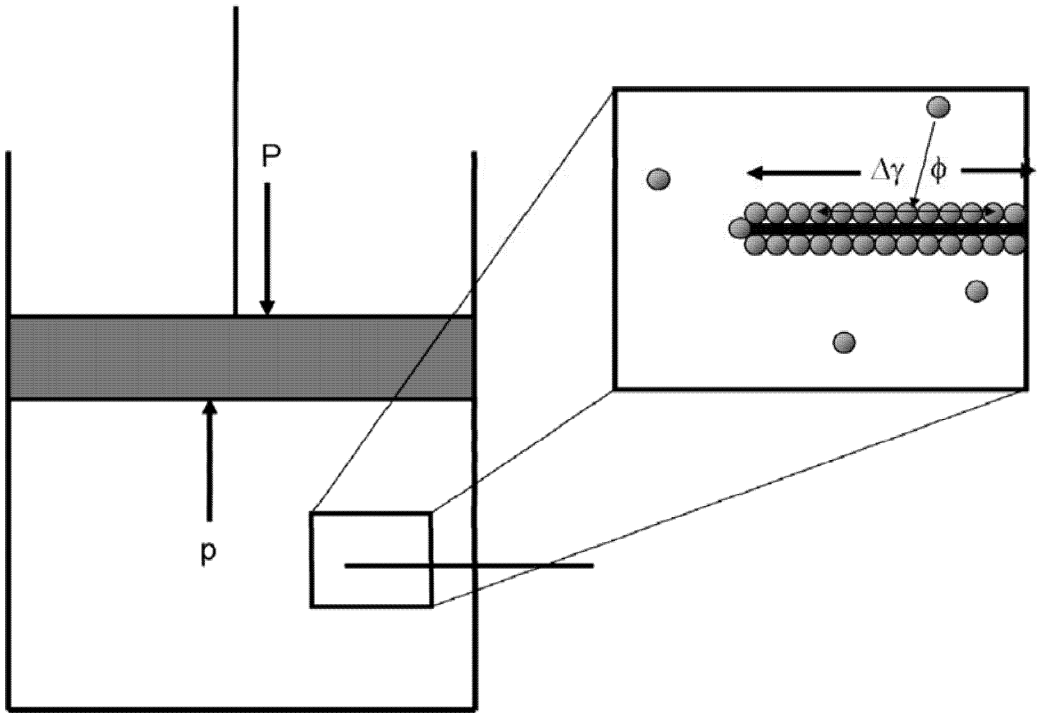


Figure 2.11: The physical interpretation of a Gibbs isotherm can be shown as a piston pushing down on a volume of a pressure $P$. Inside the volume a infinite one-dimensional plate of negligible mass can be pushed in and out of the volume by the addition or reduction of molecules adsorbed on the plate. Adsorption of molecules increases the spreading pressure on the surface and decreases the surface tension.

### Kinetic Derivation of Langmuir Isotherm

The rate of adsorption on to the substrate is dependent on the pressure of gas and the number of available sites on the substrate. Using the definition of coverage, $\theta$, from equation (2.21) can be shown as,

$$R_{adsorption} = k_{ads}[A](1-\theta), \tag{2.58}$$

where $[A]$ is the gas concentration and $(1-\theta)$ is the number of vacant adsorption sites on the substrate where $\theta$ is the total number of adsorption sites. The rate of desorption from the substrate depends on the amount of adsorbed gas on the surface and an activation energy,

$$R_{desorption} = k_{des}\theta, \tag{2.59}$$

at equilibrium the rates of adsorption and desorption are equal

$$k_{ads}[A](1-\theta) = k_{des}\theta, \tag{2.60}$$

this can be re-arranged in terms of coverage to yield,

$$\frac{\theta}{1-\theta} = \frac{k_{ads}}{k_{des}}[A], \tag{2.61}$$

if,

$$K[A] = \frac{k_{ads}}{k_{des}}, \tag{2.62}$$

then $K$ can be viewed as an equilibrium constant whose value dictates the strength of the interaction with the surface and,

$$\theta = \frac{K[A]}{1+K[A]}. \tag{2.63}$$

Figure 2.12 shows the variation in the $b$ parameter. At large values of $b$, an inflection point in the isotherm develops. This corresponds to the completion of a monolayer. From this

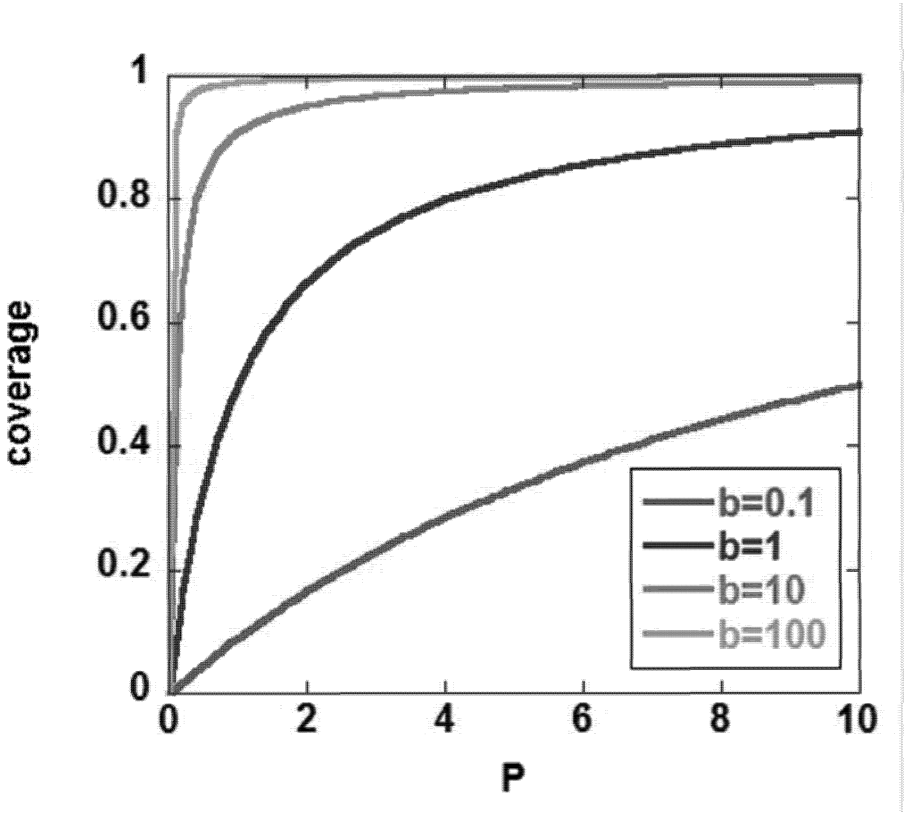


Figure 2.12: An illustration of the effect different values of $b$ has on the profile of the Langmuir isotherm.

point it can be re-arranged into a linear form,

$$\frac{P}{n} = \frac{1}{Kn_m} + \frac{P}{n_m}, \tag{2.64}$$

where $n_m$ is the amount of adsorbate needed for monolayer completion. This can be put into the more familiar form,

$$\frac{\theta}{1-\theta} = bP. \tag{2.65}$$

**Statistical Thermodynamic Derivation of Langmuir Isotherm**

The statistical thermodynamic model proposed originally by Fowler and Guggenheim [Fowler and Guggenheim, 1949] is based on the assumption that the adsorbed molecules are considered to differ from vapor phase molecules and thus have a representative partition function to describe them. In this assumption, adsorption is localized and the surface is regarded as an array of identical adsorption sites. The occupancy of any adsorption site is treated as independent of any other. Each adsorbed molecule is also considered to be an adsorption site for the next layer. All the molecules in layers above the first layer are assumed to have the same partition function as in the bulk liquid.

The internal energy and entropy of a molecule should be different in the adsorbed state than in the gas phase. The adsorbed molecule loses some of its rotational and vibrational freedom upon adsorption. The partition function for the adsorbed state of a molecule is,

$$Z^s = Z^s_{site} Z^s_{internal} e^{(Q/RT)}, \tag{2.66}$$

where the partition function is broken into an internal energy component comprised of its available vibrational and rotational energy states and the site adsorption partition function which can be described by the partition function of available positions in a three-dimensional particle in a box of area $a^3$, and the partition function of the available energy states in a

harmonic oscillator.

$$Z^s_{site} = Z^s_{translation} Z^s_{vibration}. \tag{2.67}$$

For a three-dimensional particle in a box the solution can be arrived at by separating the variables into their $x$, $y$, and $z$ components and solving for the Schrödinger equation.

$$\psi(x, y, z) = X(x)Y(y)Z(z), \tag{2.68}$$

solving for $\psi$ and separating yields,

$$\frac{1}{X}\frac{d^2X}{dx^2} = \frac{-2mE_x}{\hbar^2}, \frac{1}{Y}\frac{d^2Y}{dy^2} = \frac{-2mE_y}{\hbar^2}, \frac{1}{Z}\frac{d^2Z}{dz^2} = \frac{-2mE_z}{\hbar^2}, \tag{2.69}$$

the energy of the system is then,

$$E = E_x + E_y + E_z. \tag{2.70}$$

Since we are finding the solution of a box, ($x = y = z = a$) the solution to $E$ gives the following allowed energy states,

$$E = \left(\frac{n^3h^2}{8a^3m}\right). \tag{2.71}$$

The allowed energy states are inserted into a three-dimensional partition function which yields,

$$Z^s_{translation} = \left(\frac{2\pi mkT}{\hbar^2}\right)^{3/2} \frac{kT}{P}, \tag{2.72}$$

the volume, $a^3$, is replaced by volume in terms of $kT/P$. The available vibrational energy states in a harmonic oscillator are,

$$E_n = (n + \frac{1}{2})h\nu, \tag{2.73}$$

and the corresponding harmonic oscillator partition function is,

$$Z_{vibration} = \sum_{n} e^{(-\frac{E_n}{kT})} = \frac{e^{\frac{h\nu}{2kT}}}{e^{\frac{h\nu}{kT}} - 1}. \tag{2.74}$$

If $(\frac{h\nu}{kT}) \ll 1$, which occurs when the adsorption bond between the substrate and adsorbate is weak, then the vibrational partition function is just $kT/h\nu$. When combining the solutions of both partition functions this yields,

$$Z^s_{site} = \frac{2\pi mKT}{h^2} a^3 \frac{kT}{h\nu}. \tag{2.75}$$

The kinetic and statistical thermodynamic derivations can now be brought together by using the linear form of the Langmuir equation where,

$$\frac{\theta}{1-\theta} = \left( \frac{\frac{h^2}{2\pi mkT^{3/2}}}{kT} \right) \frac{Z^s_{site} Z^s_{internal}}{Z^g_{internal}} e^{(\frac{Q}{RT})} P, \tag{2.76}$$

where $K$ from (2.62) gives,

$$K = \frac{k_{ads}}{k_{des}} = \frac{Na^3 e^{\frac{Q}{RT}}}{\sqrt{2\pi, MRT\nu}} \tag{2.77}$$

inserting into equation (2.76) yields the familiar solution,

$$\frac{\theta}{1-\theta} = KP. \tag{2.78}$$

The assumptions that internal partition functions are the same for the adsorbed state and the vapor state is incorrect because upon adsorption molecules lose some degrees rotational and vibrational freedom.

### 2.6.3 Henry Isotherm

Henry isotherm model is a good indicator of substrate uniformity where at very low coverage adsorbate-adsorbate interactions can be neglected [Adamson and Gast, 1996] in this pressure

regime only the adsorbate-substrate interactions is present and forms a linear relationship relationship with pressure and the amount adsorbed.

$$kP = \theta. \tag{2.79}$$

Generally this can be assumed at very low coverage of less than 0.1 monolayers. A heterogeneous surface would give a non-linear relationship due to the non-uniform surface giving a distribution of sites with different binding energies. This model is mainly used to attempt to quantify the adsorbate-substrate heat of adsorption and an approximate binding energy.

### 2.6.4 Brunauer Emmett Teller, (BET) Isotherm

The derivation of the BET isotherms stems from the Langmuir isotherm of unimolecular adsorption [Brunauer, 1945]. It utilizes the same forces responsible for condensation on the surface for the binding energy to multi-layer adsorption. The assumptions of the BET model are that: all adsorption sites are equivalent, there is no limit to the amount of layers that can be formed, the Langmuir equation applies to each layer, adsorption and desorption only occur at exposed surfaces. The distribution of adsorbate between the different adsorption layers is constant. The similarities of the BET isotherm to the Langmuir isotherm allows for both a statistical thermodynamic and kinetic solution.

#### Kinetic Derivation of BET the Isotherm

The kinetic derivation of the BET equation follows the kinetic solution of the Langmuir isotherm of balancing rates of reaction between the different states of adsorbate molecules to produce a steady-state equilibrium. The rate of adsorption can be written as,

$$R_{adsorption} = a_1 p A_0, \tag{2.80}$$

where $a_1$ is the adsorption factor for the first layer and differs from system to system, $p$ is the pressure, and $A_0$ is the area on the substrate not covered by molecules. The rate of

adsorption is in equilibrium with the rate of desorption written as,

$$R_{desorption} = b_1 A_1 e^{\left(-\frac{E_1}{RT}\right)}, \tag{2.81}$$

where $b_1$ is the desorption factor of the first layer, $A_1$ is the area of the surface covered by one molecule, and the last term is the activation energy needed for desorption to occur, where $E_1$ is the enthalpy of desorption. At equilibrium $A_1$ remains constant therefore the rate of adsorption onto $A_1$ plus the rate of desorption from $A_1$ is equal to the rate of desorption from $A_2$ plus the rate of adsorption on $A_0$.

$$a_2 p A_1 + b_1 A_1 e^{\left(-\frac{E_1}{RT}\right)} = b_2 p A_2 e^{\left(-\frac{E_2}{RT}\right)} + a_1 p A_0, \tag{2.82}$$

where $a_2$ is the second layer adsorption factor, $b_2$ is the desorption factor of the second layer, combining equations (2.81) and (2.82) yields,

$$a_2 P A_1 = b_2 A_2 e^{\left(-\frac{E_2}{RT}\right)}, \tag{2.83}$$

this can be written as a general expression for any layer as,

$$a_i p A_{i-1} = b_i A_i e^{\left(-\frac{E_1}{RT}\right)}. \tag{2.84}$$

From this general statement the total amount of gas adsorbed and the surface area of the substrate can be found by the following assumptions: the enthalpy of vaporization of each layer is equal to the bulk enthalpy of vaporization, the adsorption and desorption factors are equal for each layer and form a constant $c$, above the first layer adsorption and desorption is equivalent to condensation and evaporation [Brunauer, 1945]. Equations can now be formed relating the amount of each area, $A_i$, covering the surface,

$$\frac{n_{ads}}{n_{monolayer}} = \frac{cP}{(P_0 - P)(1 + (c-1)(P/P_0)}, \tag{2.85}$$

where $n_{ads}$ is the number of moles adsorbed, $n_{monolayer}$ are the number of moles needed to complete a monolayer, and $c$ is,

$$c = e^{\left(\frac{(E_1 - E_v)}{RT}\right)}, \tag{2.86}$$

the first term is the coverage on the surface, $c$, is the change in the enthalpy of desorption between the first layer and the bulk enthalpy of vaporization and $P_0$ is the saturated vapor pressure of the isotherm. This can be re-arranged into the more familiar linear form by setting $P/P_0$ equal to $x$,

$$\frac{x}{n_{ads}(1-x)} = \frac{1}{cn_{monolayer}} + \frac{(c-1)x}{cn_{monolayer}}, \tag{2.87}$$

by varying the value of $c$ in the equation one arrives at the five different isotherms (see Figure 2.13) profiles as defined by [Brunauer, 1945].

### Statistical Thermodynamic Derivation of the BET Isotherm

The derivation of the BET isotherm using statistical thermodynamics uses the same assumptions used in the statistical derivation with the inclusion that each 'stack' of molecules is treated as a separate system and that no lateral interactions take place [Hill, 1949]. The partition functions used in the derivation are assumed to be the same the bulk liquid of the system. The full derivation of this isotherm can be found in Hill [Hill, 1946] and Adamson and Gast [Adamson and Gast, 1996]. The harmonic oscillator partition function function for the first adsorbed and higher layers is described as,

$$Z_{solid} = \frac{A_{tot}!}{(A_{tot} - A_1)!(A_1!)}(j_s e^{\left(\frac{E_1}{kT}\right)})^{A_1}, \tag{2.88}$$

$$Z_{liquid} = \frac{((A_1 + A_2) - 1)!}{(A_2)!(A_1 - 1)!}(j_s e^{\left(\frac{E_1}{kT}\right)})^{A_2}, \tag{2.89}$$

where $A$ is the total number of sites, $A_1$ is the number of sites occupied by molecules in the first layer, and $A_2$ is the number of sites occupied by molecules that have been adsorbed on

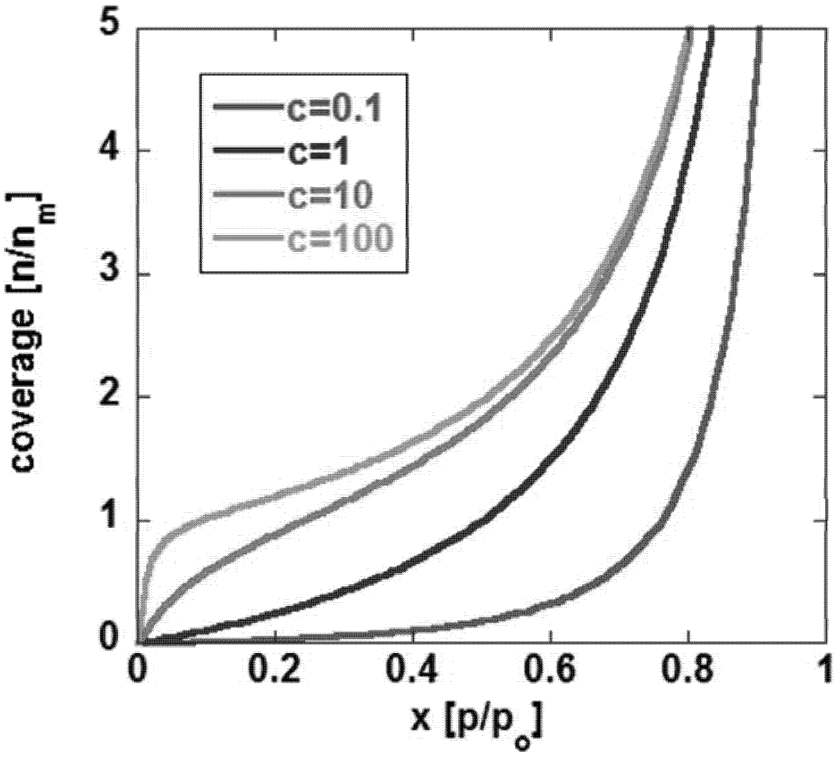


Figure 2.13: An illustration on the effect of varying the values of $c$ has on the profile of the BET isotherm model.

top of $A_1$ molecules. The complete partition function of the entire system is,

$$Z_{total} = \sum_{A_1=1}^{k} Z_{solid} Z_{liquid}. \tag{2.90}$$

The assumption can be made of setting $\log Z$ equal to the largest term in the sum. The value of $A_1$ which satisfies this is found by differentiating with respect to $A_1$ giving,

$$(A_2)(A_{tot} - A_1) = \beta A_1^2. \tag{2.91}$$

The chemical potential can then be obtained from equation (2.91) and an expression for $P/P_0$ obtained,

$$\frac{P}{P_0} = \frac{(A_1 + A_2)}{A_2}. \tag{2.92}$$

Combining equations (2.91) and (2.92) you obtain the familiar BET equation,

$$\frac{A_1 + A_2}{A_1} = \frac{cx}{(1-x)(1-x+cx)}, \tag{2.93}$$

where $c = 1/\beta$ and $x = P/P_0$. The problem with BET models are that it assumes all adsorption sites to be equal as in the case of a Langmuir isotherm. The model neglects horizontal interactions between adsorbate molecules and only considers lateral substrate-adsorbate interactions [Halsey Jr., 1948]. It also treats the molecules in the second layer identically to the first layer and assumes the same amount of adsorption sites as the first layer. Another problem with the Langmuir isotherm is the inability to the model to accurately portray Type II isotherms which show incomplete wetting behavior which make up a majority or adsorbate-substrate interactions.

### 2.6.5 Frenkel Halsey Hill, (FHH) Isotherm

A major shortcoming of all the above models is the inability to model adsorption at high coverage near the saturated vapor pressure and the lack of accounting for any lateral adsorbate-adsorbate interactions. The FHH isotherm employs the use of an van der Waal interaction

potential between the adsorbate and substrate as well as between adsorbate-molecules which is dependent on distance [Halsey Jr., 1948]. As the coverage reaches saturation, the potential felt by an adsorbate molecule from the surface decreases while the adsorbate-adsorbate potential is constant. At the point where the substrate-adsorbate interaction is less than the adsorbate-adsorbate interaction the isotherm reaches a saturation and bulk habitat behavior begins to prevail. The equation takes the form,

$$\left(\frac{n}{n_m}\right)^n = \frac{A}{\ln\left(P/P_0\right)}, \tag{2.94}$$

where $n$ is a empirical parameter taken from the integration of the $r^{-6}$ repulsive term in the Lennard-Jones potential model and varies from 2-3 [Frenkel, 1946], $n_m$ is the number of molecules required to complete a monolayer, and $A$ is defined as,

$$A = \frac{U_0}{x_m^n RT}, \tag{2.95}$$

where $x_m^n$ is the film thickness of the monolayer, and $U_0$ is a coefficient of the potential. Although the FHH model takes into account A-A interactions, the model does not accurately portray experimental isotherm data for the first few layers of a multilayer film [Adamson and Gast, 1996].

### 2.6.6 Lattice-Gas Model

The lattice-gas model is the representation of an adsorbed film as a combination of an Ising ferromagnet and a fluid system. A lattice-gas confined to a volume $V$ can be represented by a array of cells $v$ each representing the volume of an adsorbate molecule. The adsorbate molecules are not restricted to single cells but can migrate to any unoccupied cell. The equivalence to the Ising model was demonstrated by Stanley who showed that the canonical partition function of the lattice-gas model can be shown to be proportional to the grand canonical partition function of the Ising model [Stanley, 1971].

The disadvantages to using the lattice-gas model is that it omits all quantum effects, lacks degrees of freedom, and cannot accurately model phase changes of adsorbed layers going through orientational transitions nor can it model of adsorbed layers passing in and out of registry with the substrate [Adamson and Gast, 1996].

## 2.7 Isotherm Thermodynamics

The thermodynamic data compiled by our groups high-resolution volumetric isotherms record the results of the equilibration points as the final pressure versus the summation of the change in initial pressure and final pressure of all equilibration points $i$. From this data all other thermodynamic quantities may be calculated.

### 2.7.1 Molecules Adsorbed

The number of molecules adsorbed onto the substrate during a volumetric isotherm can be extrapolated from the summation of the change in initial pressure and final pressure of all equilibration points or 'sum of the delta P's' ($\sum \Delta P$). Calculation of the number of molecules adsorbed can be calculated as follows. Using the ideal gas equation and assuming the vapor phase of the adsorbate behaves ideally solve for $n$ you obtain,

$$n_i = \frac{P_i V_i}{R T_{calvol}}. \tag{2.96}$$

$P_i$ is the initial pressure in the calibrated volume which consists of the calibrated volume on the gas handling system and the calibrated volume of the tube connecting the calibrated volume to the sample cell. $V_i$ is the calibrated volume prior to opening the valve to the sample cell. $T_{calvol}$ is the temperature of the gas handling system. When the valve to the sample is opened the adsorbate vapor expands into the sample cell where it adsorbs on the substrate and creates a vapor pressure above the substrate at a temperature $T_{sample}$. The vapor above the substrate at temperature $T_{sample}$ must be subtracted from the total number adsorbed. This 'effective deadspace volume', $V_{deadspace}$, above the substrate is calculated

using a Helium expansion prior to the adsorption isotherm and changes as a function of temperature. A schematic of a volumetric isotherm can be seen in Figure 2.14. The number of molecules in the deadspace volume within the sample cell is then,

$$n_{deadspace} = \frac{P_f V_{deadspace}}{RT_{deadspace}}, \tag{2.97}$$

the final calculation for the number adsorbed is then,

$$n_{ads} = n_{icalvol} - n_{deadspace} - n_{fcalvol}, \tag{2.98}$$

where $n_{fcalvol}$ is,

$$n_{fcalvol} = \frac{P_f V_f}{RT_{calvol}}, \tag{2.99}$$

where $P_f$ is the final pressure at equilibrium, and $V_f$ is the volume of the calibrated volume plus dead space in the sample cell. When combined and simplified the solution gives the number of moles adsorbed in a single equilibration point,

$$n_{ads} = \frac{V_i(P_i - P_f)}{RT_{calvol}} - \frac{P_f V_{deadspace}}{RT_{calvol}}. \tag{2.100}$$

when summed over all equilibration points of the high resolution isotherm yields,

$$n_{ads} = \frac{V_i(\sum_i^n \delta P)}{RT_{calvol}} - \frac{P_f V_{deadspace}}{RT_{calvol}}, \tag{2.101}$$

where $i$ is the initial number and $n$ is the total number of points.

### 2.7.2 Chemical Potential

A more useful thermodynamic quantity to use in analyzing volumetric isotherms is the chemical potential which can be derived from the final pressures of the equilibration points. Chemical potential is defined as,

$$\mu = k_B T ln(P), \tag{2.102}$$

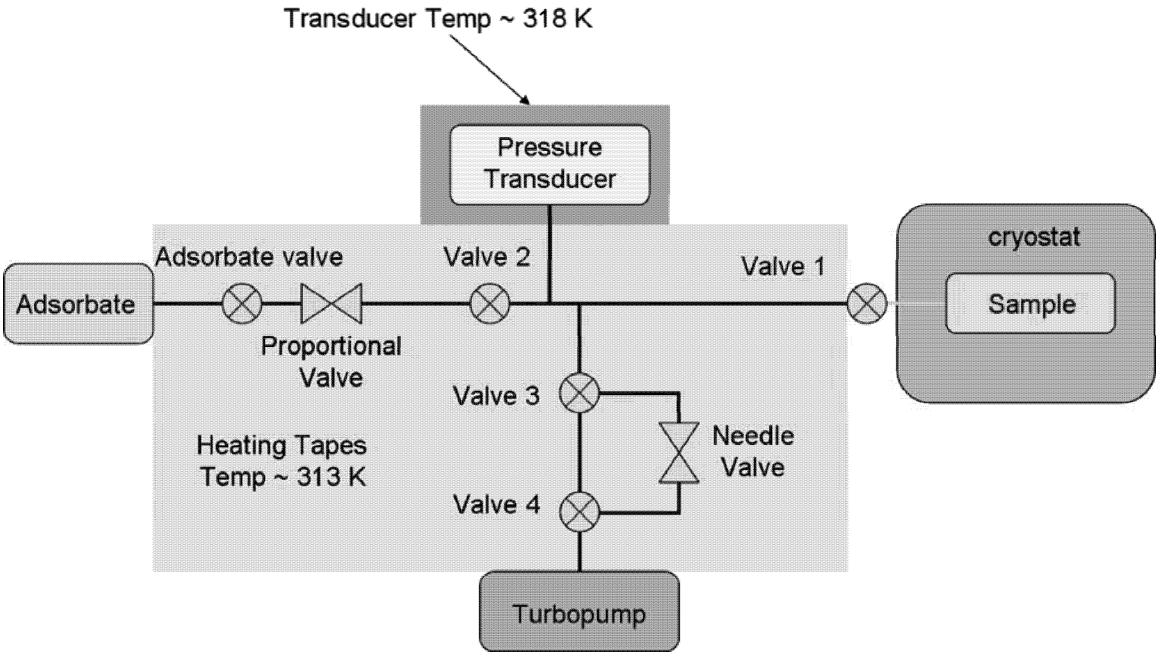


Figure 2.14: An schematic of a volumetric isotherm.

where $k_B$ is the boltzmann constant. When systems with corresponding chemical potentials are in contact and in equilibrium, the difference between them is zero [Steele, 1993]. In a volumetric isotherm this occurs when the isotherm reaches its saturated vapor pressure $P_0$. This can be expressed as a difference in chemical potentials,

$$\mu - \mu_0 = k_B T ln(P) - k_B T ln(P_0). \tag{2.103}$$

As a extensive variable, the chemical potential is a calculable thermodynamic quantity from the isotherm data and can thus be related to other thermodynamic variables [Steele, 1993].

### 2.7.3 Layering Transition

A layering transition in the isotherm data can be identified by taking the derivative $dN/dP$ of the isotherm and locating the peaks of the derivative. The peaks correspond to the change of the number adsorbed versus the change in pressure (see Figure 2.15). When the change in the number adsorbed is large relative to the change in pressure then the value of the derivative is large and vice versa.

### 2.7.4 Clausius-Clapeyron Equation

When two large three-dimensional phases are in equilibrium the Clausius-Clapeyron equation can relate the temperature, pressure, volume and entropy of the system [Mutaftschiev, 2001]. The traditional form of the equation takes on the form of,

$$\left(\frac{d \ln P}{dT}\right) = \frac{\Delta H_{ads}^{diff}}{RT^2}. \tag{2.104}$$

The equation assumes that the enthalpy of a phase transition is independent of temperature over small ranges. If the locations of layering transitions in the isotherms are plotted as $\log(P)$ versus $1/T$, a linear form of the Clausius-Clapeyron equation can be cast,

$$\log(P_f) = B^{(n)} - \frac{A^{(n)}}{T}, \tag{2.105}$$

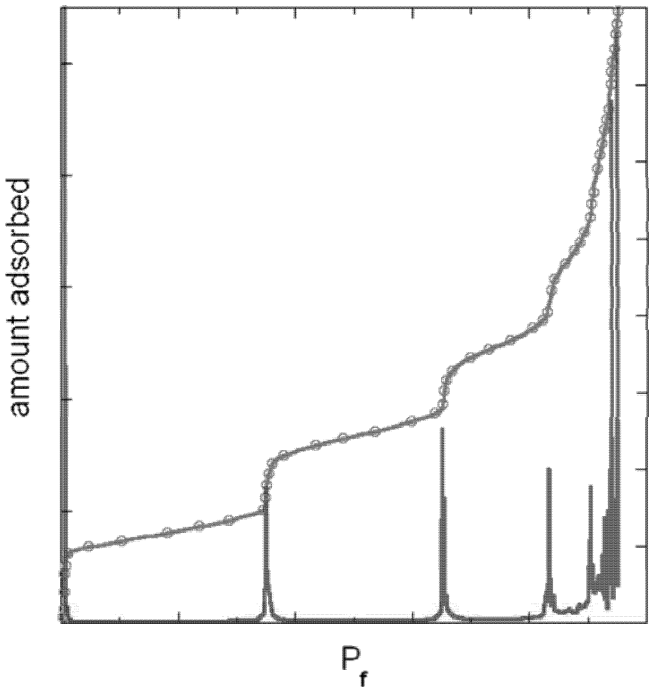


Figure 2.15: A layering transition can be defined as a peak of the numerical derivative ($dN/dp$) in a volumetric isotherm experiment. This figure shows the raw data from a methane isotherm (blue) and its associated numerical derivative (red).

where the $n$ superscript refers to the particular layering transition of the isotherm [Larher, 1967].

### Heat of Adsorption

From the Clausius-Clapeyron plot Lahrer has shown that a variety of thermodynamic variables can be calculated using the slope $A^{(n)}$ and the intercept as $B^{(n)}$ from the linear form of the Clausius-Clapeyron equation parameters along with the assumption that the slope of the lines plotted of the layering transitions versus the inverse temperature gives the enthalpy of adsorption. The heat of adsorption of each layer can thus be extrapolated from the linear Clausius-Clapeyron plot,

$$Q_{ads}^{(n)} = A^{(n)} \cdot R, \tag{2.106}$$

this quantity is the heat of adsorption at the $n^{th}$ layer [Madih, 1986].

### Enthalpy

The enthalpy of each layer can be calculated using the expression,

$$\Delta H^{(n)} = -R(A^{(n)} - A^{(\infty)}), \tag{2.107}$$

where $B^{(\infty)}$ is the intercept value of the saturated vapor pressure plotted using the linear Clausius-Clapeyron equation. $\Delta H^{(n)}$, gives the difference in enthalpies from the bulk to the $n^{th}$ layer [Larher, 1967]. These values should approach zero as the difference between the $n^{th}$ layer and the bulk value approach zero.

**Entropy**

The change in entropy can be calculated in the same manner as the enthalpy using the $B$ intercept values [Larher, 1967],

$$\Delta S^{(n)} = -R(B^{(n)} - B^{(\infty)}). \tag{2.108}$$

The values of $\Delta S$ should converge to zero indicating that the formation of bulk crystals are entropically favored.

### 2.7.5 Two-Dimensional Compressibility, $K_{2D}$

For each three-dimensional thermodynamic variable there exists a two-dimensional analog. The three-dimensional compressibility measures the change in pressure as change in volume.

$$K_{3D} = -\frac{1}{V}\left(\frac{\partial V}{\partial P}\right). \tag{2.109}$$

In the two-dimensional compressibility, the volume is replaced by a area and the pressure which in three-dimensions is defined as the amount of force applied per unit area is replaced by a two-dimensional quantity called the spreading pressure. The spreading pressure $\phi$ can be defined as the pressure need to maintain a saturated vapor of the liquid around the solid and is defined in the one-dimensional units $m/N$ [Phillips and Larese, 1997],

$$K_{2D} = -\frac{1}{\sigma}\left(\frac{\partial \sigma}{\partial \phi}\right), \tag{2.110}$$

where $\sigma$ is the molecular area of the adsorbate. The molecular area of the individual adsorbate atom or molecule can be calculated taking the total surface area over the number of moles adsorbed. The chemical potential similarly has a two-dimensional analog [Dash, 1977],

$$d\mu_{2D} = -SdT + \sigma d\phi. \tag{2.111}$$

Differentiating at constant temperature gives,

$$A = \left(\frac{\partial \mu}{\partial \phi}\right). \tag{2.112}$$

The chemical potential of the film is assumed to be in equilibrium with the vapor above the film,

$$\mu_f = \mu_v = k_B T ln\left(\frac{k_B T}{\lambda^3 P}\right), \tag{2.113}$$

where $\lambda$ is the De Broglie wavelength of the gas. Differentiating $\mu$ gives,

$$d\mu_f = d\mu_v = k_B T \frac{1}{P} dP. \tag{2.114}$$

Combining equations (2.113) and (2.114) gives,

$$K_{2D} = \frac{AP}{k_B T n^2 N_A}\left(\frac{dn}{dP}\right), \tag{2.115}$$

where $n$ is the number of moles adsorbed and $N_A$ is Avogadro's number. The two-dimensional compressibility is the measure of the change in the spreading pressure of an adsorbed film as a function of chemical potential [Mutaftschiev, 2001].

### 2.7.6 Phase Transitions

The two-dimensional compressibility ($K_{2D}$) in equation (2.115), can also give information of the locations of possible phase transitions as a function of temperature. Larher has shown that by taking the Full Width at Half Maximum (FWHM), you can locate regions of possible phase transitions.

The compressibility of an experimental adsorbed film can be thought of as being comprised of the combined compressibilities of all layers. The top layer of film is undergoing the most dramatic changes in compressibilities can be a sensitive indicator of a two-dimensional phase change in the growth front of the film [Phillips and Larese, 1997]. A large FWHM value

of a particular $K_{2D}$ peak indicates a broad peak which is characteristic of a liquid-like state [Larher, 1979]. As you reach a liquid-like state the compressibility versus the chemical potential should show a decrease and broadening of the peak due to the amount of pressure needed to adsorb another atom or molecule is lower due to the adsorbate molecules in the thin film ability to translationally relocate to another adsorption site on the lattice and accommodate the incoming molecule. The broadening of the peak is due to the ability of the liquid to compress slightly as it approaches the layering transition as a function of chemical potential.

In a similar method, Larher has shown that by calculating the critical exponent of a series of isotherms and calculating its value one can quantify and locate phase transitions. The value of the critical exponent $\beta$ shows the two-dimensional character of the transition thus giving information about the dimensionality of the system and thus information about its wetting properties [Larher, 1979]. The critical exponent can be calculated by,

$$\frac{N'' - N'}{N_0} = B\left(\frac{T_C - T}{T_C}\right)^{\beta}, \tag{2.116}$$

where $N'' - N'$ is the change in the adsorbed quantity during the transition as a function of $T - T_C$, $T_C$ is the critical temperature, and $B$ is an integration constant. For a purely two-dimensional transition the critical exponent value should have a value near the solution of the two-dimensional Ising model solution of 1/8 or 0.12. A value which deviates from this indicates that the transition has some three-dimensional component due to interactions between layers.

### 2.7.7 Isosteric Heat of Adsorption, $Q_{st}$

The isosteric heat of adsorption is defined as the amount of work needed to adsorb an atom or molecule onto the surface at a constant coverage. The heat of adsorption is equal to the binding energy of the adsorbate to the substrate. In its differential form the isosteric heat

can be calculated as a function of coverage [Pan et al., 1998],

$$Q_{st} = RT^2 \left(\frac{\partial P}{\partial T}\right)_n . \tag{2.117}$$

With a series of isotherms, one can calculate the isosteric heat of adsorption by taking an isostere between two closely spaced isotherms, $\sim 1$ K apart. Under these conditions, the derivative of equation (2.117) can be defined as,

$$\left(\frac{\partial P}{\partial T}\right)_n \cong \left(\frac{\Delta \ln P}{\Delta T}\right)_n . \tag{2.118}$$

The resulting plot gives the isosteric heat of adsorption as a function of coverage. As the coverage reaches it saturation point the value of the isosteric heat should converge to the bulk enthalpy of vaporization of the adsorbate.

Use of the isosteric heat of adsorption from the neccessitates two assumptions: the bulk gas phase of the adsorbate is considered ideal, and the volume of the adsorbed phase in neglected [Pan et al., 1998]. Both of these assumptions have been experimentally proven by Balbuena et. al. to be valid except at very low pressures.

### 2.7.8 Determination of Surface Area

The surface area of the substrate which adsorption isotherms are being performed on is an important measurement because a relation of the number of moles of adsorbate adsorbed onto the surface versus the surface area can give information about the relative surface area a single molecule occupies at monolayer completion. The methods described are some of the most commonly used methods of determining surface area of a substrate. Both methods necessitate the use of a molecule which its molecular area is well-known and characterized. This value can then be correlated to the amount of moles adsorbed to determine the total surface area of the sample. The molecule traditionally used has been $N_2$ which has a calculated molecular surface area of 16.2 $Å^2$ [Gregg and Sing, 1982]. The disadvantage to using

$N_2$ is the assumption that when adsorbed onto a substrate the $N_2$ adsorbs perpendicular to the substrate. It also makes the assumption that the surface is completely covered by the $N_2$ atoms irrespective of the substrate being adsorbed onto which may not be necessarily true. The value being calculated using the thermodynamic measurements is dependent on coverage and is therefore not a molecular area calculation but a molecular 'footprint' or projection on a surface therefore a calculation of the molecular area would not suffice.

**Point-B method**

The monolayer capacity of 'Type II', BET isotherms (see Figure 2.16) that describe the adsorption of gases on non-porous solids can be determined by extrapolating a line from the point at which the layering transition is completed indicated by the region immediately after a peak in a plot of the derivative $dN/dP$ versus pressure. The point at which the line fitted to the horizontal portion of an isotherm departs from the isotherm plot is called the '$B$' point. The point-$B$ method works best for isotherms with $c$ value from the BET equation greater than 20 [Gregg and Sing, 1982]. Under this value the infection point of the layering transition becomes rounded and the accuracy of the point-$B$ method suffers. The point-$B$ method was tested by Morrison using low temperature isotherms of $N_2$. The results show that the point-$B$ method works as well as the using the BET equation [Gregg and Sing, 1982].

To determine the surface area of the substrates used in the experiments performed, methane ($CH_4$) isotherms were performed on the samples. Methane was chosen because previous studies by a number of groups have determined the surface structure on graphite to be $\sqrt{3} \times \sqrt{3}\ R30^\circ$ with a molecular area of 17.74 $Å^2$ [Beaume et al., 1984], [Yang et al., 2006] [White et al., 1978]. Methane on MgO forms $\sqrt{2} \times \sqrt{2}\ R45^\circ$ surface structure with a molecular area of 17.74 $Å^2$ [Larese et al., 1991]. The use of methane as a fiducial is a superior method to the use of nitrogen because methane is very near spherical in nature

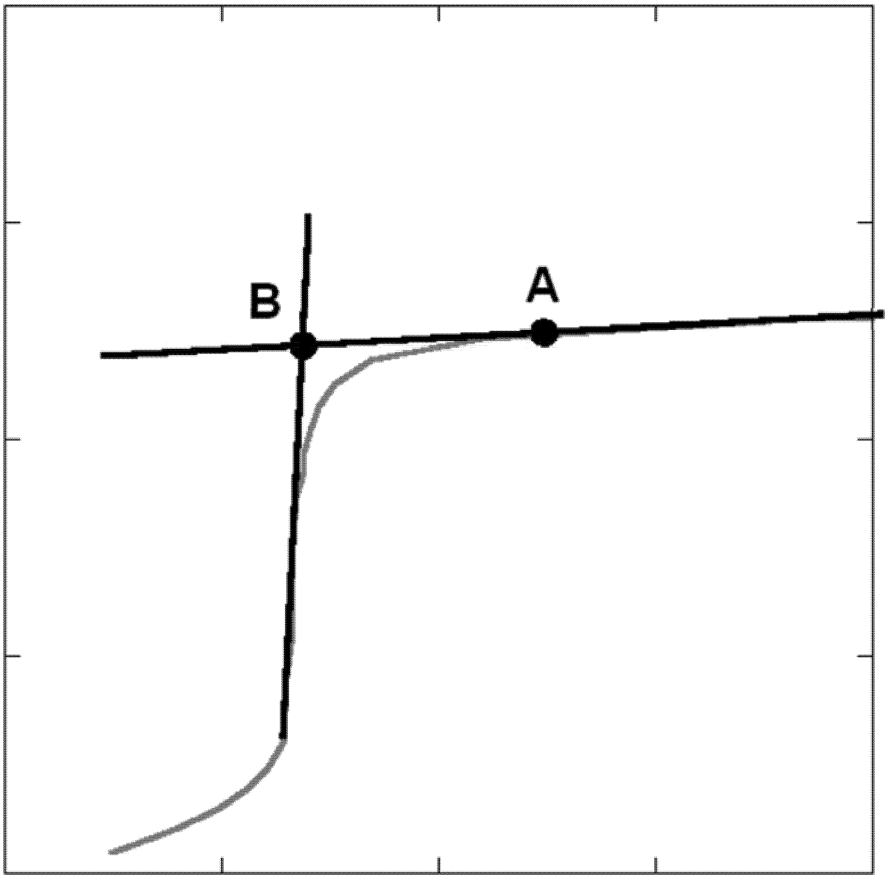


Figure 2.16: An illustration of the point-B method and the location of $B$ point used to determine surface area of a sample.

and therefore there is no possibility of the orientation affecting the surface area occupied by the molecule.

## 2.8 Neutron Scattering

By exploiting the wave-particle duality of the neutron coupled with the highly penetrating nature of neutrons through materials neutron powder diffraction is a useful to tool to determine the structures and magnetic properties of materials. The wave-particle duality means that a neutron traveling at a certain velocity should have a corresponding wavelength given by the de Broglie relationship,

$$\lambda = \frac{h}{mv}, \tag{2.119}$$

where $h$ is Planck's constant, and $m$ and $v$ are the mass and velocity of the neutron respectively.

The use of neutrons for scattering has the following properties which make it advantageous to use:

- Neutrons interact primarily with the atomic nucleus and with the spins of unpaired electrons. As a result the scattering of neutrons has no dependence on the number of electrons surrounding the nucleus. This is particularly advantageous in the study of light atoms.

- The scattering of neutrons is at much lower energies and is on the order of elementary excitations in atoms and molecules. Therefore neutrons not only probe the structure of atoms and molecules but the dynamics.

- Neutrons interact weakly with matter and only via a nuclear spin interaction with the nucleus of the scatterer neutrons are therefore highly penetrating. The weak interaction also means that there is little radiation damage.

- Neutrons have a magnetic moment and therefore interact with magnetic structures whose properties can be probed.

Neutron diffraction is a complementary method to x-ray diffraction and the same basic scattering theory can be applied to both. Neutron scattering is a complementary method to x-ray scattering because the nucleus and surrounding electrons are correlated by the Born-Oppenheimer approximation which states that the motion of electrons around the nucleus does not alter the position of the nucleus because the nucleus is so much heavier than the electrons around it ($\sim$1800$\times$). This approximation breaks down when larger atoms are taken into consideration [Boni and Furrer, 2000]. The scattering of neutrons occurs at much lower energies than x-rays of the same wavelength and is on the order of elementary excitations in atoms and molecules [Squires, 1978]. Therefore neutrons can not only probe the structure of atoms and molecules but also dynamics.

A neutron is a fermion with a nuclear spin ($s = 1/2$), and magnetic moment ($\mu = -1.913$ magnetons), where a nuclear magneton is equivalent to,

$$\mu_N = 5.051 \times 10^{-27} JT^{-1}, \tag{2.120}$$

and a mass of $1.67493 \times 10^{-27}$ kg. Neutrons are neutral particles and have no nuclear charge thus a neutron interacts with matter via its nuclear and magnetic interactions [Rauch and Waschkowski, 2003]. This interaction of a neutron with the nucleus of an atom is weak and therefore neutrons are highly penetrating. When a neutron does interact with matter, it can either be absorbed or scattered from the atoms. If no energy is exchanged in the interaction of the neutron with the atom, then the interaction is said to be elastic and the neutron is diffracted and travels as a spherical wave away from the atom. If there is energy exchanged with the atom the neutron is either absorbed or inelastically scattered from the atom. When absorbed, the atom goes under a process of neutron capture and is incorporated into the nucleus of the atom [Bacon, 1977]. Upon absorption, the atom is in an excited state and

to return to a ground state emits excess energy in the form $\gamma$ radiation or as $\alpha$ or $\beta$ particles.

X-ray radiation is comprised of high energy photons and because of their electromagnetic field, interact with the negatively charged electrons of an atom. The impinging x-rays interact with the electrons of an atom inducing a perturbation in the electron wavefunction of the electrons. This interaction results in the re-emission of the photons as spherical waves as the electron returns to its ground state. The interactions of neutrons and x-rays with an atom can be described by an atomic scattering amplitude [IUC, 1952]. This is a measure of how strongly an x-ray photon or neutron interacts with an particular atom. The scattering amplitude is represented analytically by real and imaginary portion [Bacon, 1977]. The real portion describes the scattering which can be positive or negative depending on whether the interaction with the atom is attractive or repulsive. The imaginary portion describes absorption of an x-ray or neutron. X-ray scattering amplitudes vary linearly with atomic number while the values with neutrons vary randomly. This is true because the scattering amplitude of x-rays is dependent on the electron density of the atoms which increases as the atomic number gets larger. The scattering amplitudes with neutrons are random due to the complex nature of the Coulomb screening potentials functions of atoms and don't follow any systematic pattern correlating to atomic number.

The random variation in scattering cross-sections is particularly useful for neutron scattering with hydrogenous materials. Hydrogen has a large incoherent neutron scattering cross-section which is particularly useful for studying the dynamics of systems where as deuterium has a large coherent scattering cross-section which is useful in studying the structure of systems. Information on structure and dynamics is generated from pair-correlation function and the self-correlation functions which can be derived from the scattering data. Isotopic substitution of deuterium for hydrogen is in most cases relatively simple and therefore makes an excellent method to study both the structure and dynamics of these particular systems.

Table 2.4: Neutron scattering cross-sections of some relevant atoms. 1 barn = $1 \times 10^{-28}$ $m^2$. Values from [IUC, 1952].

| Atom | I (nuclear spin) | $b_c$ (fm) | $\sigma_{coh}$ (barn) | $\sigma_{inc}$ (barn) | $\sigma_{tot}$ (barn) |
|---|---|---|---|---|---|
| $H^1$, $H^3$ | 1/2 | -3.74 | 1.758 | 80.26 | 82.03 |
| $H^2$ | 1 | 6.674 | 5.592 | 2.05 | 7.65 |
| $C^{12}$ | 0 | 4.792 | 2.89 | 0.14 | 3.03 |
| $N^{14}$ | 1 | 9.37 | 11.03 | 0.50 | 11.53 |
| $O^{16}$ | 0 | 5.805 | 4.232 | 0 | 4.232 |
| $Mg^{24}$ | 0 | 5.49 | 4.03 | 0 | 4.03 |
| $Mg^{25}$ | 5/2 | 3.62 | 1.65 | 0.28 | 1.93 |
| $Al^{27}$ | 5/2 | 3.449 | 1.495 | 0.082 | 1.503 |
| $Ar^{36}$ | 0 | 24.9 | 77.9 | 0 | 77.9 |
| $Ar^{40}$ | 0 | 1.7 | 0.421 | 0 | 0.421 |
| $V^{51}$ | 7/2 | -0.402 | 0.0203 | 5.07 | 5.09 |

Details of this phenomena will be discussed in greater detail later.

Neutrons are generated by either nuclear fission reactors or by the bombardment of neutron rich metal targets by accelerated protons in a process called 'spallation'. Spallation is a process in which accelerated protons bombard a neutron-rich metal target. This liberates neutrons from the metal which can then be harnessed in a collector ring. The neutrons escaping the target are released at a variety of energies and therefore velocities and wavelengths [Squires, 1978]. A list of typical spallation targets and their respective neutron counts can be found in Table 2.4.

### 2.8.1 Scattering Theory

Considered here is the scattering of a monochromatic beam of neutrons or x-rays. The kinetic energy of an incoming beam is,

$$E = k_B T = \frac{mv^2}{2} = \frac{p^2}{2m} = h\omega, \tag{2.121}$$

with momentum,

$$\vec{p} = \hbar\vec{k} = \frac{h}{\lambda}, \tag{2.122}$$

where $\vec{k}$ is the incoming wavevector. The incident beam interaction with the sample can then be described with the an incoming and outgoing wavevector $\vec{k}'$ with momentum $\vec{p}'$. The momentum transfer of the incident and scattered wavevectors can be described as,

$$\vec{Q} = \vec{k} - \vec{k}', \tag{2.123}$$

where $\vec{Q}$ is the momemtum transfer vector. Figure 2.17, illustrates the relationship between the magnitudes of the incoming and outgoing wavevectors and $\vec{Q}$. The wavevector can be related to the wavelength by,

$$k = \frac{mv}{h2\pi} = \frac{2\pi}{\lambda}. \tag{2.124}$$

The energy transfer of the interaction can be described as,

$$E = \hbar\omega = E - E_0 = \frac{\hbar^2}{2m}(k - k'), \tag{2.125}$$

where $E$ and $E_0$ are the final and initial energies of the scattered photon or neutron. When there is no energy transfer and the difference between the initial and final energies are zero the scattering event is known as elastic scattering. A non-zero energy transfer is known as inelastic scattering. These different types of neutron scattering events yield different information.

Neutrons spallated from a target travel at a distribution of velocities between $v$ and $dv$, and follow a Maxwell-Boltzmann distribution where the probability of traveling at a velocity $v$ is,

$$P(v)dv = 4\pi \left(\frac{m}{2\pi k_B T}\right)^{(3/2)} v^2 e^{\left(-\frac{mv^2}{k_B T}\right)} dv, \tag{2.126}$$

where $m$ is the mass of the neutron, and $T$ is the temperature of the moderator. The temperature of the moderator therefore dictates the velocities and wavelengths of the outgoing

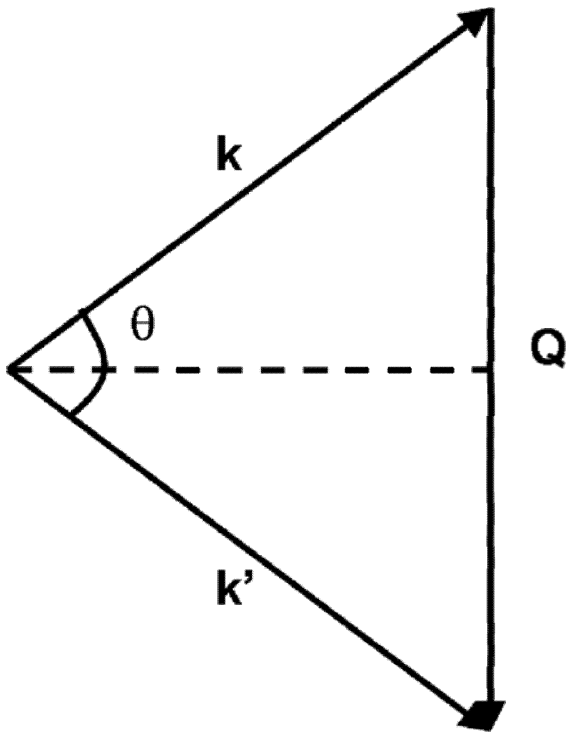


Figure 2.17: Construction of the scattering vector $\vec{Q}$ from the incoming wave vector $\vec{k}$ and the outgoing wavevector $\vec{k}$'. When scattering is elastic in reciprocal space $k = k$' gives an isosceles triangle where $Q = 2k \sin\theta$.

neutrons. 'Cold' neutrons refer to neutrons which have traveled through a liquid deuterium moderator which is maintained at 30 K [Bacon, 1977]. The wavelength of the out coming cold neutrons have spectral peak at 3.5 Å. 'Hot' neutrons refer to neutrons that have passed through a graphite block maintained at 2000 K. The spectral peak of hot neutrons is at 0.5 Å [Squires, 1978]. For the diffraction experiments on the OSIRIS beam line at ISIS spallation neutron source the moderator seen by the detector is a liquid hydrogen moderator maintained at 22 K which produces neutrons with a maximum at 3 Å. Further details on this particular instrument can be found in [Andersen et al., 2002].

The quantity measured during a neutron experiment is the partial differential scattering cross-section,

$$\frac{\partial^2\sigma}{\partial\Omega\partial E} \equiv \frac{1}{\hbar}\frac{\partial^2\sigma}{\partial\Omega\partial\omega}, \tag{2.127}$$

and is defined as the fraction of incident neutrons or photons scattered by a solid angle, $d\Omega$, where,

$$d\Omega = \sin\theta d\theta d\phi, \tag{2.128}$$

with energy range $E$ to $E+dE$, $\phi$ is the total scattering cross-section and is the total fraction of the incident flux that is scattered by the sample, and $d\sigma$ is the number of neutrons or photons scattered over an angle $d\Omega$ and is expressed as,

$$\frac{d\sigma}{d\Omega}. \tag{2.129}$$

The intensity of neutrons scattered by an assembly of atoms is represented by an intensity function. The general expression for intensity was first derived by Van Hove and takes into account two assumptions which makes the derivation possible [Boni and Furrer, 2000]. The first assumption is that the probability of an interaction of a plane wave of neutrons with a potential $V(r)$ can be represented by the perturbation expansion of the wavefunction

solution for the scattering off a weak potential [Boni and Furrer, 2000],

$$\left| \int e^{i\mathbf{k}\cdot r} V(\mathbf{r}) e^{-i\mathbf{k'}\cdot r} d^3r \right|^2 = \left| \int e^{i\mathbf{Q}\cdot r} V(\mathbf{r}) d^3r \right|^2. \tag{2.130}$$

The second assumption replaces the potential interaction between a neutron and nucleus is replaced by a weaker Fermi pseudo-potential. The Fermi pseudo-potential between a plane wave of neutrons and an assembly of nuclei is represented by,

$$V(\mathbf{r}) = \sum_j b_j \delta(\mathbf{r} - \mathbf{r}_j), \tag{2.131}$$

where $b_j$ is the scattering length of a particular nucleus at a position $\mathbf{r}_j$, and $\delta$ is the Dirac delta function which is zero unless $\mathbf{r} = \mathbf{r}_j$, where it is equal to one. Replacing the potential with the Fermi pseudo-potential allows for the analytic solution of the perturbation expansion derived by Born [Squires, 1978].

This approximation is only valid when multiple scattering processes are ignored and scattering off the sample occurs at an angle of incidence above the critical angle. At the critical angle neutrons are perfectly reflected from the surface which the Born approximation of a weak interaction cannot be applied [Squires, 1978]. Combining equations (2.130) and (2.131) you get the number of intensity of scattered neutrons as a function of momentum transfer $\mathbf{Q}$ energy transfer $\epsilon$,

$$I(\mathbf{Q}, \epsilon) = \frac{1}{h} \frac{k'}{k} \sum_{j,k} b_j b_k \int_{-\infty}^{\infty} \langle e^{i\mathbf{Q}\cdot r_k(t)} e^{-i\mathbf{Q}\cdot r_k(0)} \rangle e^{-i\epsilon t} dt, \tag{2.132}$$

where $i$ is the complex conjugate, $j$ and $k$ is a nucleus at position $\mathbf{r}_j$ at time $t$ and position $\mathbf{r}_k$ at time 0. This is summed over all pairs of nuclei and averaged for all particular times $t$.

If there is no correlation between the scattering amplitudes of the atoms in an lattice of atoms, then the partial differential cross-section can be split into two parts that correspond

to coherent and incoherent scattering,

$$\frac{\partial^2\sigma}{\partial\Omega\partial E} = \left(\frac{\partial^2\sigma}{\partial\Omega\partial E}\right)_{coherent} + \left(\frac{\partial^2\sigma}{\partial\Omega\partial E}\right)_{incoherent} \tag{2.133}$$

Where the coherent and incoherent portions are equivalent to,

$$\sigma_{coherent} = \sum_{j,k}(\bar{b})^2 I_{jk} \tag{2.134}$$

$$\sigma_{incoherent} = \sum_{j}(\bar{b^2} - (\bar{b})^2) I_{jj} \tag{2.135}$$

where $(\bar{b})^2$ is the spin averaged sum of the scattering lengths and $\bar{b^2}$ is the average area for a scattering event to occur. $I_{jk}$ and $I_{jj}$ are the intensity functions summed over $j, k$ nuclei for coherent scattering to discern the structure of the material by correlating the positions of the atoms relative to each other, and summed over $j, j$ nuclei for incoherent scattering to relate positions of the same nucleus at different positions and times.

The scattering lengths $b$ depend on the element but also on the isotope which affects the angular momentum quantum number of the atom. When a scattering event occurs, the spin 1/2 neutron interacts with the spin of atom. The interaction with the atom causes the outgoing neutrons to travel at different phases and amplitudes and do not interfere constructively. From the expressions above it is possible to define the coherent and incoherent scattering lengths as,

$$b_{coherent} = \bar{b}, \tag{2.136}$$

$$b_{incoherent} = \sqrt{\bar{b^2} - (\bar{b})^2}. \tag{2.137}$$

Coherent scattering processes include Bragg scattering and inelastic scattering from phonons or other collective excitations. This can be further separated into coherent elastic and inelastic scattering processes. These studies focus on the structure of adsorbed hydrocarbon

thin films and therefore coherent elastic scattering is used. In coherent elastic scattering experiments it is advantageous to isotopically replace hydrogen with deuterium because deuterium is a weak incoherent scatterer. Deuterium does not have degenerate spin nuclear spin states which can create different scattering lengths depending on the state of the atom (see Table 2.4). This allows for the collection of data which relies on the direction of the scattering vector $\vec{Q}$ which gives information on the correlations of atomic positions relative to each other.

Incoherent scattering measures the atomic motions of atoms by calculating the probability of finding a particle at a position $\vec{r}$, at time $t$ when there is a particle at $\vec{r}$=0 and $t$=0. Incoherent scattering can also be further separated into incoherent elastic scattering and inelastic scattering. Inelastic coherent scattering measures the correlated motions of atoms in concert, while incoherent inelastic scattering measures the self-correlated motions of atoms (i.e. the probability of finding the same nucleus at a position $r$ and time $t$ from a position $r$=0 and $t$=0).

## 2.9 Neutron Diffraction

Although neutron diffraction is primarily an elastic process, neutron diffractometers actually integrate over the energies of the scattered neutrons [Boni and Furrer, 2000]. By integrating over the energies of scattered neutrons this allows for the inclusions of thermodynamic effects such atomic vibrations. These factors are also introduced by the addition of the Debye-Waller factor. With these factors taken into consideration equation (2.132) can now be expressed as,

$$I(\mathbf{Q}) = b_{coherent} \sum_{j,k} e^{i\mathbf{Q}(\mathbf{r}_j - \mathbf{r}_k)} e^{\frac{1}{2}Q^2\langle u^2\rangle} \equiv S(\mathbf{Q}), \tag{2.138}$$

where $\langle u^2\rangle$ is the average square displacement of an atom from its equilibrium position and $S(\mathbf{Q})$ is the structure factor. For coherent scattering $S(\mathbf{Q})$ is proportional to the Fourier

transform of the probability to find a particle at a position $\vec{r}$ at a time $t$ when there was another particle $\vec{r} = 0$ at $t = 0$.

### 2.9.1 Time-of-Flight (TOF) Neutron Diffraction

In a pulsed accelerator based facility the pulse of neutrons travel at a range of velocities described in equation (2.126) towards the instrument. As the neutrons travel towards the instrument, the range of velocities and directions due to steering of the neutrons and the use of focussing mirrors and bending magnets cause the pulse to lengthen and expand. To further monochromate the pulse of neutrons, a mechanical chopper and collimators are used to cut portions of the pulse before entering the detector. Improved monochromatization of the pulse allows narrowed well defined incoming and outgoing energies and wavelengths of the neutrons.

After diffracting off the sample, the neutrons will be traveling at a variety of velocities which will hit the detector banks at different angles and times which can be discerned by the detector. This location where the neutron hits the detector and time of flight of a known distance from the sample to the detector gives information about the final energy of the neutron. The wavelength and time-of-flight are then related by the following expression,

$$\lambda = \frac{ht}{mL}, \tag{2.139}$$

where $t$ is the time-of-flight and $L$ is the total flight path. This can be further related to the $d$-spacing by,

$$t = \frac{mL2d\sin\theta}{h} \tag{2.140}$$

where $m$ is the mass of the neutron, $\theta$ is the scattering angle. Which can then be related to $\vec{Q}$.

The resolution of a TOF diffraction instrument is the $\Delta d/d$ of a diffraction pattern measured at a given angle. In pulsed detectors the resolution is nearly flat over $2\theta$. In diffraction instruments this value is constant over the entire diffraction pattern and can be improved by increasing the length of the instrument from the spallation source thereby narrowing the allowed energies of neutrons into the instrument [Squires, 1978]. The total $d$-range of the instrument depends on the TOF and wavelength of the neutrons. To access lower $d$-spacings instruments with high energy neutrons and short TOF should be used and vice versa for high $d$-spacings.

### 2.9.2 Backscattering TOF diffraction

TOF diffraction in the backscattering mode is method used to record the neutron data for these experiments. Experiments were performed on the OSIRIS TOF backscattering diffractometer were coherent elastic scattering experiments which well suited to calculate the structure of thin films of isotopically deuterated alkanes. The theory and principle of operation for these particular experiments and a description of greater detail can be found in [Andersen et al., 2002].

### 2.9.3 Neutron Powder Diffraction

A powder sample consists of a large number of randomly oriented single crystals which diffract according to Braggs law. The random orientation of the crystals cause the incident neutron beam to be diffracted as Debye-Scherrer cones at an angle of $2\theta$ from the incident beam [Warren, 1990]. Figure 2.18 illustrates these 'scattering cones', a cone is produced for all the possible lattice planes of reflection. Since the chromatization of the incoming neutrons is not perfect there is a distribution of wavelengths which results in the cones having a finite thickness [Sprung, 2001]. Another potential problem is the preferred orientation a powder sample might take on. Every powder has some degree of orientation which manifests itself in the diffraction pattern by altering the intensities of some peaks and causing some peaks to be missing all together [Guinier, 1994].

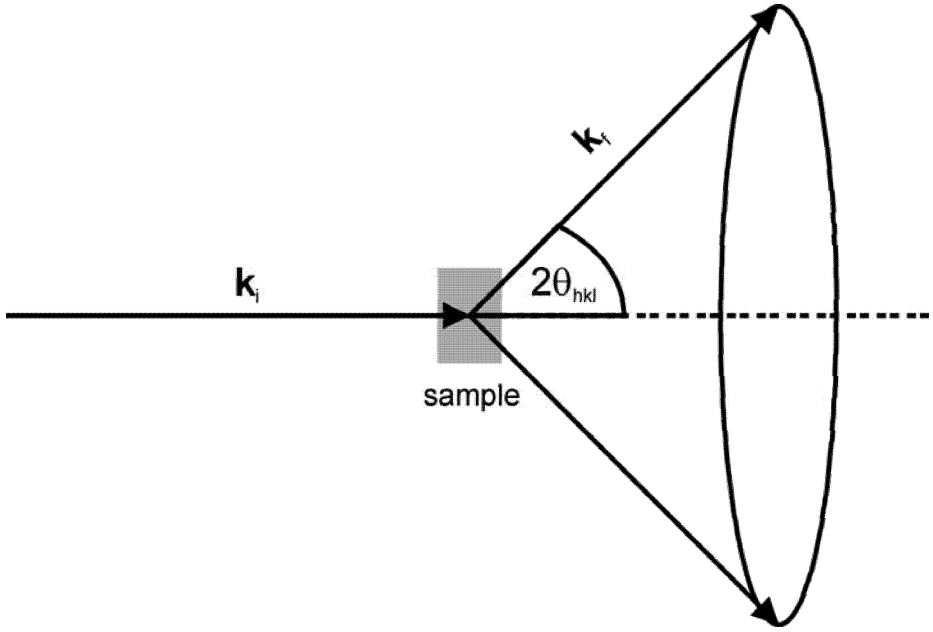


Figure 2.18: Debye-Scherrer cones produced by x-ray diffraction from a powder. Scattering from a powder sample occurs in all directions. Each scattering peak produces a scattering cone which subtends an angle of $2\theta$ from the incoming wave vector. Image from [Sprung, 2001].

## 2.10 Position and Intensity of Diffraction Peaks

### 2.10.1 Position of Diffraction Peaks

The position of peaks in a diffraction experiment can be determined using a variety of methods which will be described in short. A more detailed description of these methods can be found in [Warren, 1990], [Guinier, 1994], [Sands, 1993], and [Atkins and de Paula, 2002]. The positions of the diffraction peaks can be rationalized using Bragg's law, Laue's conditions of diffraction, or by Ewald's construction. In all constructions the sample is considered to be a collection of lattice planes stacked on top of each other with an interplanar distance $d_{hkl}$, where $h$,$k$, and $l$ are the miller indices in the $x$,$y$, and $z$ directions.

#### Laue Equations

The Laue method is the oldest method to interpret diffraction patterns. The diffraction of x-rays from a sample is analogous to the diffraction of light through a grating where only certain allowed combinations of wavelengths and lattice spacing will produce constructive interference. To describe this in three dimensions three equations are needed,

$$a(\cos\alpha_0 - \cos\alpha) = h\lambda, \tag{2.141}$$

$$b(\cos\beta_0 - \cos\beta) = k\lambda, \tag{2.142}$$

$$c(\cos\gamma_0 - \cos\gamma) = l\lambda, \tag{2.143}$$

where $a$, $b$, and $c$ are the unit cell axes and $\alpha$, $\beta$, and $\gamma$ are the the incoming and outgoing angles of the x-ray or neutron beam. Diffraction is an elastic scattering process and can be defined as when the incoming wavevector is equal in magnetude to the outgoing wavevector, ($\vec{k} = \vec{k}'$). When this condition is met, the following relations can be made about the resultant scattering vector can be expressed as,

$$Q = 2k\sin\theta = \frac{4\pi\sin\theta}{\lambda}. \tag{2.144}$$

Constructive interference will only occur when the $h$, $k$, and $l$ values are integer values.

**Bragg's Law**

A two-dimensional array of points is known as a crystal plane. These planes show long-range order in the sample to diffract protons or neutrons. A crystal can be thought of as comprised of many lattice planes and thus all can diffract protons or neutrons. Scattering off lattice planes is known as Bragg's law and it's derivation and further explanation can be found in these texts [Atkins and de Paula, 2002], and [Sands, 1993].

$$n\lambda = 2d\sin\theta, \tag{2.145}$$

where $\lambda$ is the wavelength of the incoming photon or neutron, $d$ is the inter-lattice plane spacing, $\theta$ is the scattering angle from the lattice plane (see Figure 2.19). This can be related to $d$ and the reciprocal lattice spacing $\vec{Q}$ by,

$$d = \frac{2\pi}{Q} = \frac{\lambda}{2\sin\theta}. \tag{2.146}$$

If an incident x-ray or neutron makes an angle $\theta$ with the sample, the diffracted beam also makes an angle $\theta$ with the sample giving a total angle of $2\theta$. Since a sample is a large collection of lattice planes reflections from successive planes will produce waves that with interfere constructively and destructively with each other. Bragg's law gives the same information as solving for the Laue equations with the exception of only angle being measured. Using the Bragg equation one can calculate the interplanar spacing of a sample using the following relation for a general orthorhombic cell [Atkins and de Paula, 2002],

$$\frac{1}{d_{hkl}^2} = \frac{h^2}{a^2} + \frac{k^2}{b^2} + \frac{l^2}{c^2} \tag{2.147}$$

the locations of peaks can also be determined using the bragg equation and indexed to a diffraction pattern with only an assumption of the type of unit cell.

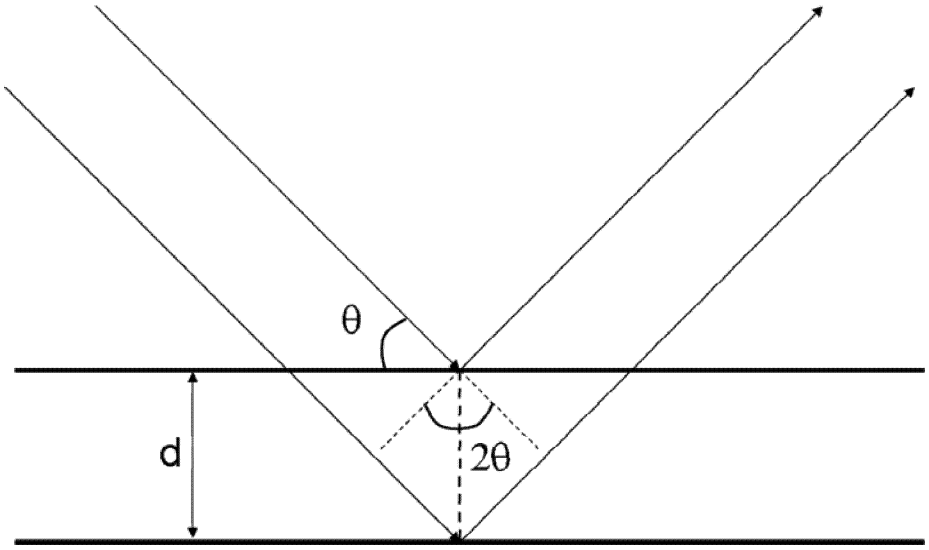


Figure 2.19: An illustration of bragg scattering off a series of planes. The *d*-spacing represents the distance between two adjacent planes of reflection.

**Ewald Construction**

Another way to conceptualize the diffraction process off a sample is by the use of the Ewald construction. This method brings together both the Bragg and Laue concepts in its explantation of diffraction. The Ewald construction utilizes the reciprocal lattice of the unit cell. P. P. Ewald was responsible for interpreting Laue's results in terms of reciprocal lattices. He separated the origins of direct and reciprocal space placing the crystal at the center of a sphere of radius $1/l$. The origin of reciprocal space is placed on the surface of the sphere where the incident beam exits the sphere. Figure 2.20, illustrates the concept of an Ewald sphere and how it relates to the lattice spacing of the sample.

### 2.10.2 Symmetry Considerations

In powder diffraction it is possible that some peaks might be systematically absent due to the symmetry of the crystal. The symmetry of three-dimensional and two-dimensional crystals can be categorized into space groups which are categorized in books such as, [IUC, 1952]. Each kind of symmetry system have there own distinct set of absences which are defined by the kind of symmetry operations that can be performed on them. Of particular importance in these experiments are the space groups two-dimensional thin films organize into. There are 17 possible two-dimensional plane-groups that the alkane thin films can organize into.Conversely to systematic absences, there can also be multiplicity in diffraction peaks due to equivalent reflections which increase the intensity of certain peaks. Multiplicity result from lattice planes which are equivalent in $d$-spacing.

### 2.10.3 Intensities of Peaks

The intensities of diffraction peaks depend on several factors which differ from x-rays from neutrons. The ability of atoms to diffract depends on a variety of factors such as crystal size and orientation, reflection angle of the x-ray of the crystal, strongly on whether neutrons of x-rays (photons) are being used because or the $Z = r^2$ dependence of x-ray scattering versus the variable dependence on $Z$ for neutrons, where $Z$ is the atomic number of an

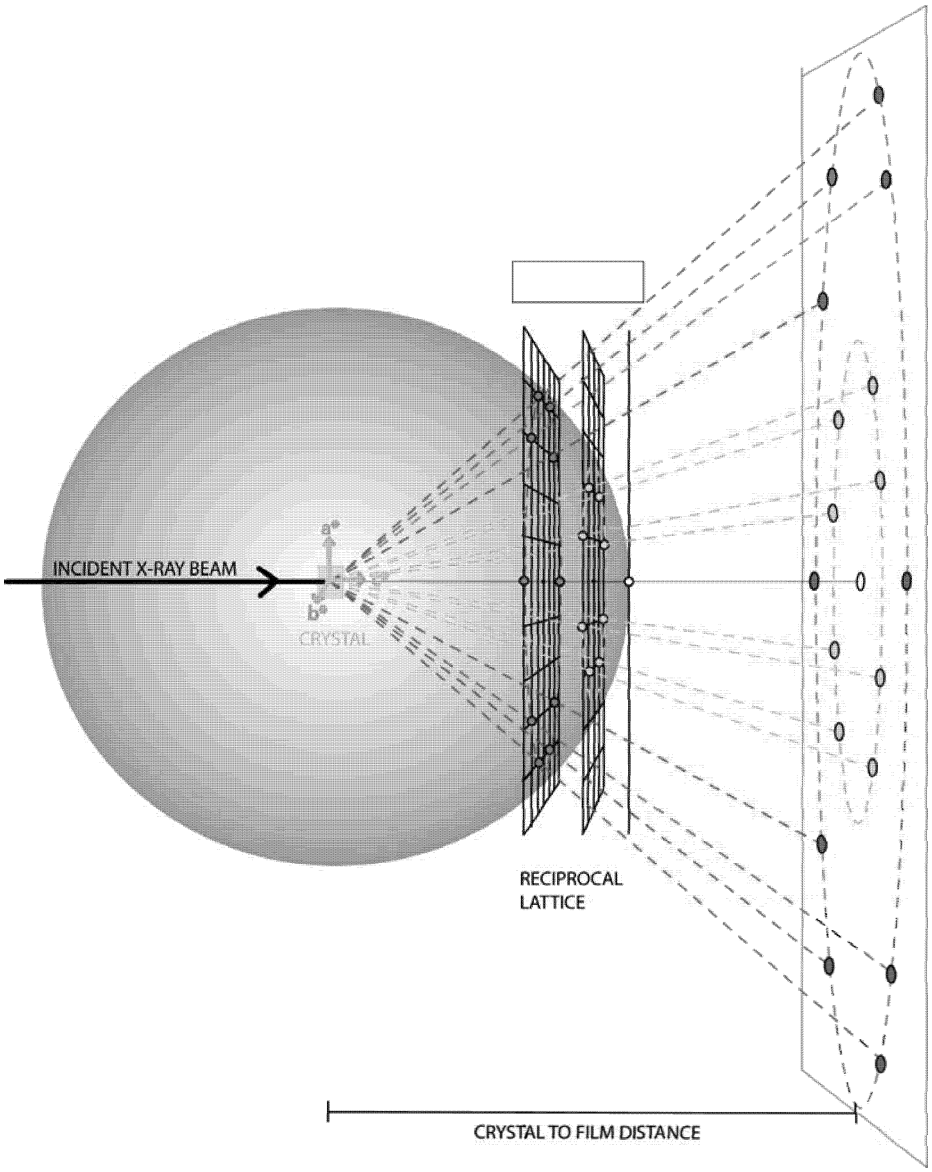


Figure 2.20: An illustration of the Ewald conceptualization of diffraction. Each reciprocal lattice point that is located on the Ewald sphere of reflection, the Bragg condition is satisfied and diffraction arises. Image from [http://www.doe mbi.ucla.edu/, 2006].

atom. This effect is particularly important when considering crystals composed of only one element. If scattering off a series of lattice planes of all the same atoms with the same structure factor this will cause complete destructive interference of the outgoing spherical waves and no diffraction peak. The intensity of a diffraction peak can be determined using the square of the scattering amplitude factor,

$$F_{hk} = \sum_n f_n e^{2\pi i(\frac{hx}{a}+\frac{ky}{b})}, \tag{2.148}$$

where $h$ and $k$ are Miller indices, $x/a$ and $y/b$ are the fractional coordinates of the atoms in the unit cell, and $f_n$ is the atomic scattering factor.

### 2.10.4 Peak Shapes

The peak shapes of diffraction peaks can be affected by factors such as crystal size in the powder, imperfections in the crystal, thermal motion of atoms, and multiple scattering of neutrons from the sample.

The Scherrer equation describes the effect of peak broadening due to small particle size ($\leq 1000\mathring{A}$) [Warren, 1990] and can be described using the following equation,

$$B(2\theta) = \frac{2[(\ln 2)/\pi]^{1/2}\lambda}{Na\cos\theta}, \tag{2.149}$$

where $Na$ are the dimensions for a cubic crystal. When $L = Na$ the equation reduces to,

$$B(2\theta) = \frac{0.94}{L\cos\theta}. \tag{2.150}$$

In the Scherrer equation, $B(2\theta)$, is the full-width-half-maximum of the peak in $2\theta$. The effects of peak broadening due to crystal size become more pronounced at larger values of $2\theta$ [Warren, 1990].

Imperfections in the crystal cause broadening of peaks due to the creation of other diffraction planes which create peaks slightly shifted from the diffraction peaks of the predominant 'perfect' crystal face. There are a variety of expressions which can account for this type of broadening and can be found in [Guinier, 1994]. The thermal motion of atoms about there mean position means their positions are not perfectly defined. This leads to a reduction in scattering intensity and broadening of diffraction peaks as temperature increases. Broadening due to temperature can be accounted for using the Debye-Waller factor,

$$e^{(-2W)} = e^{(-Q^2\langle u^2\rangle)}, \tag{2.151}$$

where $Q$ is the momentum transfer, and $\langle u^2\rangle$ is the mean vibrational displacement about its equilibrium position [Warren, 1990].

## 2.11 Two-Dimensional Diffraction

Diffraction in two-dimensions varies from three-dimensional diffraction due to the need for only two Laue conditions to be satisfied. The result of this relaxation of conditions results in a reciprocal lattice composed of lattice rods corresponding to the reflections of the two-dimensional symmetry planes illustrated in Figure 2.21. The bragg rods produced diffracted when observed on a debye-scherrer scattering cone would appear as a series of lines distributed onto tangents off the cone. The integration of intensity across the lattice rods leads to a characteristic 'Warren' profile in $Q$ space named after Warren who first developed a comprehensive analytic method of quantifying two-dimensional (2D) diffraction off randomly oriented graphene sheets shown in reflections of the 2D symmetry planes. As you begin to move from a 2D system to a three-dimensional (3D) system, modulation of the bragg rods occurs (see (c) in Figure 2.21). These modulations become more pronounced until each modulation becomes its own bragg spot which is indicative of a 3D system (see (d) in Figure 2.21) [Larese et al., 1988b]. In infinite systems, the 2D bragg rods and 3D bragg spots would be represented by delta functions. For finite systems in reciprocal space however, the

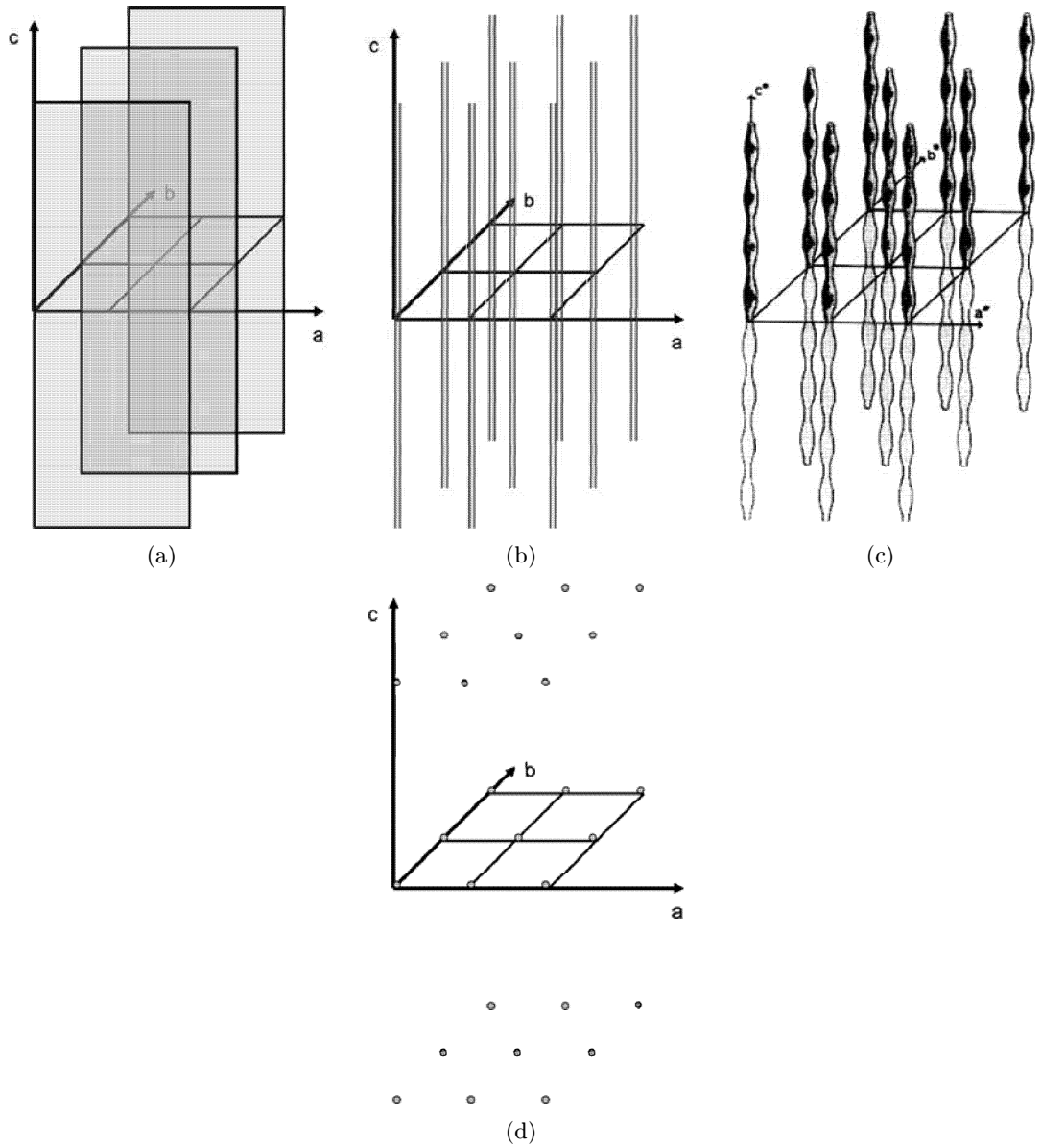


Figure 2.21: This illustration shows the evolution of a diffraction signal as a system evolves from a 1D system to a 3D system. (a) 1D diffraction. Diffraction from a one-dimensional system. (b) 2D diffraction. Diffraction from a finite 2D system. (c) 2D to 3D diffraction. As a system moves from a 2D system to a 3D system the bragg rods begin to modulate. Image from [Larese et al., 1988b]. (c) 3D diffraction. As the modulation becomes more pronounced they form bragg spots.

bragg rods and spots would have finite thickness. Analytic solutions to two-dimensional diffraction has been expanded to include diffraction off a variety two-dimensional thin films adsorbed onto powder samples including effects such as preferred orientation [Ruland and Tompa, 1967], incommensurate overlayers [Weling and Griffin, 1981], multilayers [Imry and Gunther, 1971] [Larese et al., 1988b], and domain structures [Dutta and Sinha, 1982].

A more rigorous mathematical fitting equation to the intensity function utilizing multiple functions for line-shape fitting was developed by Lauter and Schildberg [Schildberg and Lauter, 1989] and extended by Strezelczyk [Strzelczyk et al., 1997] and is expressed as,

$$I(\theta) \propto \frac{|F_{hk}|^2 e^{-2W}}{(sin\theta)^{3/2}} \left(\frac{L}{\pi\lambda}\right)^{1/2} F(a), \tag{2.152}$$

where $F_{hk}$ is the two-dimensional structure factor, $L$ is the correlation length of the structure, $\lambda$ is the incoming wavelength, and $F(a)$ is the characteristic functional form of the lineshape. This functional form of the scattered intensity has been incorporated into a program originally developed by J.C. Newton which can index and fit two-dimensional diffraction patterns [Newton, 1989]. Traditional diffraction software is designed to resolve three-dimensional structures use primarily Rietveld refinement technique (described elsewhere [Rietveld, 1967]) which is predicated on the satisfaction of all three Laue conditions which cannot be satisfied in a two-dimensional system.

## 2.12 Data Treatment and Fitting

The collected coherent neutron diffraction patterns of thin films adsorbed on MgO and graphite have very low intensity due to the small amount of atoms to scatter from. To partially rectify this, large samples with high specific surface areas are required. This allows for the maximum amount of adsorbed molecules to be diffracted from. This problem can also be reduced by using diffraction instruments with high flux so to improve counting statistics of the diffraction pattern. A subtraction method is employed where a diffraction

pattern is collected of the substrate which is subtracted from the diffraction pattern of the thin film adsorbed onto the substrate. This allows for better resolution of the diffracted peaks from the thin film.

# Chapter 3

# Experimental Setup

## 3.1 Adsorbates

The adsorbates molecules employed in this study are all small hydrocarbon molecules. This is part of an ongoing systematic study of the homologous series of alkanes, cycloalkanes, and hetrocyclic aromatic hydrocarbons on magnesium oxide and graphite surfaces. It is aimed at providing a more complete understanding of adsorbate-adsorbate, adsorbate-substrate interactions with the goal of developing more accurate interatomic and intermolecular interactions. These more accurate model potentials will lead to improved computational modeling and a better understanding of the role surface and molecular symmetry plays in the adsorption of molecules.

### 3.1.1 *n*-Hexane

*n*-Hexane is the sixth member of the normal alkane family of hydrocarbons with the empirical formula $C_nH_{2n+2}$. It is a highly flammable, colorless liquid with a petrol-like odor. *n*-Hexane is non-polar and is often used as a cleaning agent and laboratory chemical. *n*-Hexane is most often used as a mixture with other hexane isomers. Hexanes are mainly used for: the extraction of oil from soybeans, flaxseed, peanuts, safflower, corn germ, and

Table 3.1: *n*-Hexane forms a triclinic crystal structure with $P\bar{1}$ symmetry at 178 K. The unit cell contains one molecule. *a*, *b*, and *c* values are in Å. $\alpha$, $\beta$, and $\gamma$ in deg. Adapted from [Boese et al., 1999].

| a | b | c | $\alpha$ | $\beta$ | $\gamma$ |
|---|---|---|---|---|---|
| 4.1309 | 4.6963 | 8.8392 | 83.398 | 87.265 | 75.172 |

cottonseed [Merck, 2004], as solvents in industrial processes, such as rubber polymerization [Wade, 1995]. Isomerization and cycloaddition catalytic reactions use *n*-hexane as a precursor material [Richards, 2006].

*n*-Hexane is a linear carbon chain molecule, consisting of two methyl ($CH_3$) groups at either end joined by four methylene ($CH_2$) groups (see Figure 3.1). In the gas phase it has three possible conformations; a linear *trans* and folded *cis* and *gauche* conformations. *n*-Hexane has $C_{2v}$ symmetry in its lowest energy *trans* conformation. It can exist in the above mentioned conformations by rotation of its interior methyl groups. The $CH_2$–$CH_2$ conformational barrier is 3 kcal/mole due to steric hinderance. This barrier increases as a result of torsional strain as the hydrogens become eclipsed [Wade, 1995]. Staggered conformations of small hydrocarbons are more stable than eclipsed conformations and therefore predominate at equilibrium.

Solid *n*-Hexane forms a triclinic crystal structure with $P\bar{1}$ symmetry at 178 K. The unit cell contains one molecule. Illustration of its unit cell and table of the unit cell parameters can be seen in Figure 3.2 and Table 3.1 [Boese et al., 1999]. The center of mass of the molecule can be found at the midpoint of the carbon–carbon bond of the third and fourth carbon atoms.

Vapor pressure studies of *n*-hexane in the temperature range of this study have been performed previously. Coefficients for Antoine's equation can be extracted which related vapor

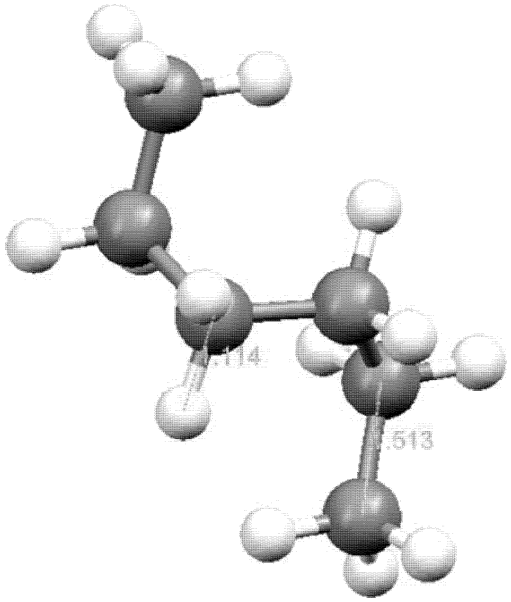

Figure 3.1: An illustration and dimensions of a single minimized gas phase *n*-hexane molecule. The calculated C–C bond distance is 1.513 Åand the C–H bond distance is 1.114 Å.

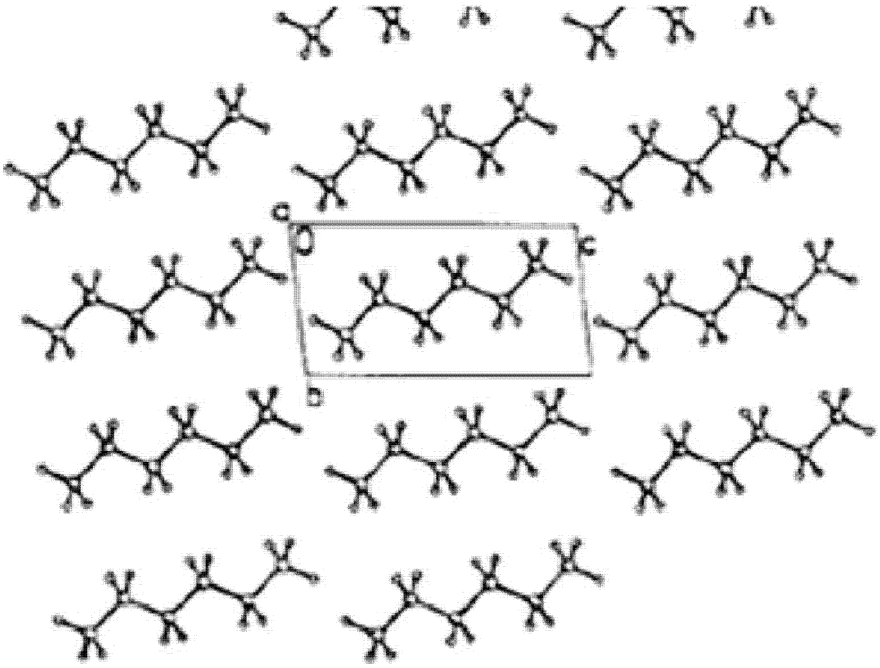


Figure 3.2: Bulk crystal phase of $n$-hexane viewed along the $a$-axis. $n$-Hexane forms a triclinic unit cell with $P\bar{1}$ space group symmetry and one molecule per unit cell . Image from [Boese et al., 1999]

.

Table 3.2: Some important physical and thermodynamic values relevant to bulk $n$-hexane. Adapted from [http://webbook.nist.gov, 2006].

| | |
|---|---|
| Mol. Weight | 86.18 |
| Symmetry | $C_{2h}$ |
| $T_{boil}$ | 341.9 ± 0.3 K |
| $T_{fusion}$ | 178 ± 1 K |
| $T_{triple}$ | 178.0 ± 0.5 K |
| $\Delta_{vap}H$ | 31.73 kJ/mol |
| Antoine Parameters | (177.70 - 264.93 K) |
| A | 3.45604 |
| B | 1044.038 |
| C | -53.893 |

pressure to temperature. A table of $n$-hexanes physical and thermodynamic characteristics can be found in Table 3.2.

$$\log_{10}(p) = A - \frac{B}{T[K] + C} \tag{3.1}$$

### 3.1.2 Cyclohexane

Cyclohexane, $C_6H_{12}$ is a non-polar saturated hydrocarbon where the carbon backbone forms a six-membered ring illustrated in Figure 3.3. Cyclohexane is a colorless liquid at room temperature with a petrol-like odor. It is most commonly used as a reactant in the production of adipic acid and caprolactan both precursors in the production of nylon [Merck, 2004]. Cyclohexane is commercially produced by the hydrogenation of benzene over a metal catalyst [Land et al., 1989].

Cyclohexane exists in a variety of structural conformations (see Figure 3.4) whose ratios depend on temperature. The partition function is shown in equation (2.50). The lowest energy configuration of cyclohexane is the 'chair' conformation as a consequence of the reduction in the steric hinderance of the six axial and six equatorial hydrogens. The 'twist' conformation is the next lowest energy conformation which does not suffer from angle strain

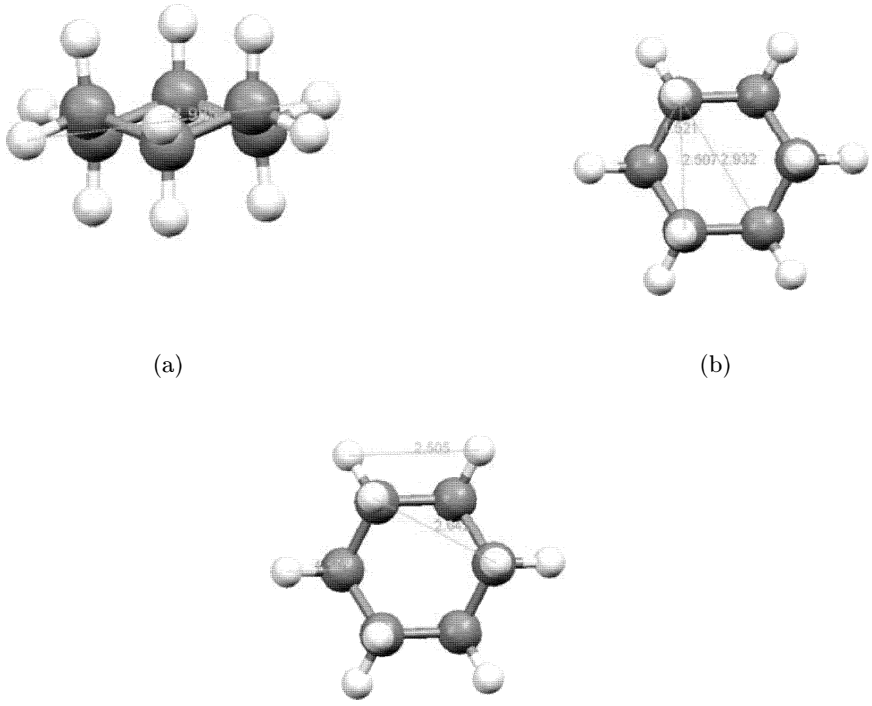


(a) (b)

(c)

Figure 3.3: Bond distances of single minimized gas phase cyclohexane molecule. (a) gives the diameter of a cyclohexane molecule as 4.985 Å. (b) gives the values of various C–C distances of the 6-membered ring, the next-neighbor C–C distance is 1.521 Å. (c) gives the various H–H distances on the molecule.

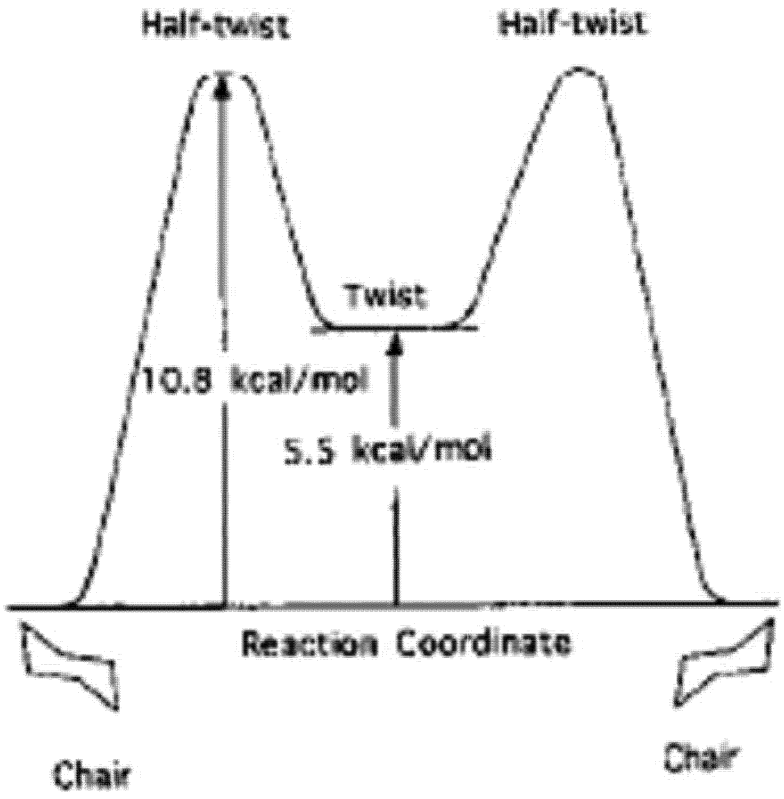


Figure 3.4: Cyclohexane can undergo a variety of conformations all which depend need a certain energy to overcome an activation barrier. Image from [Leventis et al., 1997].

Table 3.3: Cyclohexane forms two different bulk crystal structures with a transition temperature of 186 K. Above 186 K, the 'Phase I' crystal forms a cubic unit cell with $Fm\bar{3}m$ symmetry. The unit cell contains four molecules. Below 186 K cyclohexane forms a monoclinic unit cell with $C_{2c}$ symmetry and four molecules per unit cell. $a$, $b$, and $c$ values are in Å. $\alpha$, $\beta$, and $\gamma$ in deg. Adapted from [Kahn et al., 1972].

| Phase | a | b | c | $\alpha$ | $\beta$ | $\gamma$ |
|---|---|---|---|---|---|---|
| I | 8.61 | – | – | 90 | 90 | 90 |
| II | 11.23 | 6.44 | 8.20 | – | 108.83 | – |

but has a higher energy than the chair form as a result of the steric strain introduced by the two axial hydrogen atoms. The energy barrier between the chair and twist states is 5.5 kcal/mol, so inter-conversion between the two conformations takes place rapidly at room temperature. The 'boat' conformation is the highest energy conformation, which exists only as a transitional state because of its steric and torsional strain and cannot be isolated experimentally. The torsional strain in the boat conformation is a maximum because all the carbon bonds in the ring are eclipsed. The interatomic distances in cyclohexane differ slightly from the linear saturated hydrocarbons and exhibit a weak dependence on conformation.

Solid cyclohexane forms two bulk structures dependent on the temperature. The high temperature phase termed 'Phase I' with $Fm\bar{3}m$ symmetry with 4 atoms per unit cell, exists above 186 K. Below 186 K, the monoclinic 'Phase II' structure with $C_{2c}$ symmetry forms. Illustrations and parameters of the unit cells can be found in Figure 3.5 and Table 3.3 [Kahn et al., 1972].

Vapor pressure measurements of bulk cyclohexane were not available in the temperature region of the volumetric isotherm data. Antoine parameters for the accessible pressure and temperature regions were extrapolated from existing data [http://webbook.nist.gov, 2006] at higher temperatures and were found to correspond well. A summary of some common parameters of cyclohexane can be found in Table 3.4.

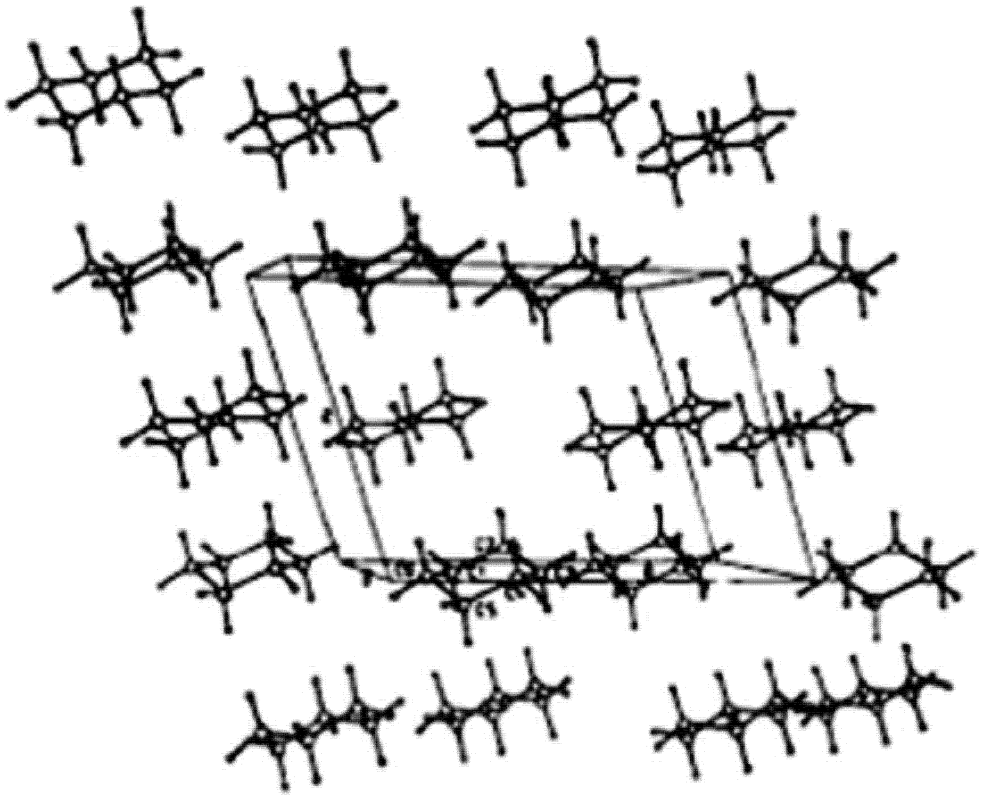

Figure 3.5: Bulk crystal 'Phase II' of cyclohexane at 115 K. At 115 K cyclohexane forms a monoclinic crystal with $C_{2c}$ symmetry. The unit cell contains 4 molecules per unit cell. At temperatures above 186 K the undergoes an isothermal transition and forms the 'Phase I' bulk structure. Above 186 K cyclohexane forms a cubic unit cell with $Fm\bar{3}m$ symmetry and 4 molecules per unit cell. Image from [Kahn et al., 1972].

Table 3.4: Some important physical and thermodynamic values relevant to bulk cyclohexane. Adapted from [http://webbook.nist.gov, 2006].

| | |
|---|---|
| Mol. Weight | 84.16 |
| Symmetry | $D_{3H}$ (chair); $C_{2v}$ (boat) |
| $T_{boil}$ | 353.9 ± 0.2 K |
| $T_{fusion}$ | 279.6 ± 0.3 K |
| $T_{triple}$ | 279.7 ± 0.4 K |
| $\Delta_{vap}H$ | 32 ± 2 (kJ/mol) |
| $\Delta_{sub}H$ | 37.7 (kJ/mol) |
| Antoine Parameters | (293.06 - 354.73 K) |
| A | 3.96988 |
| B | 1203.526 |
| C | -50.287 |

### 3.1.3 Pyridine

Pyridine is a heterocyclic aromatic hydrocarbon, structurally similar to benzene with the exception of one C-H group replaced by a nitrogen atom with a lone pair of electrons (see Figure 3.6). At room temperature is is a clear liquid with a strong, putrid, fish-like odor. Pyridine is carcinogenic and extremely harmful if inhaled, ingested, or absorbed through the skin and is known to reduce male fertility and is carcinogenic [http://webbook.nist.gov, 2006]. Pyridine has $C_{2v}$ symmetry. The physical size dimensions of pyridine differs slightly from benzene due to the replacement of a carbon atom with a nitrogen atom. The molecule is slightly distorted due to a decrease in the C–N bond distance. This shortened bond length can also be attributed to the lack of a hydrogen bonded to the nitrogen atom. Hydrogen atoms are slightly electronegative and only weakly draw electrons towards them. The missing hydrogen atom at the nitrogen site allows for a lone pair of electrons to be in a non-bonding configuration which are less attracted to the nucleus and can therefore participate in the aromatic $\pi$-bonding scheme of the molecule. Pyridine is obtained naturally from coal tar or can be synthesized from acetylaldehyde, formaldehyde, and ammonia [Merck, 2004]. Pyridine is used as a solvent and reagent in organic chemistry and used as a starting

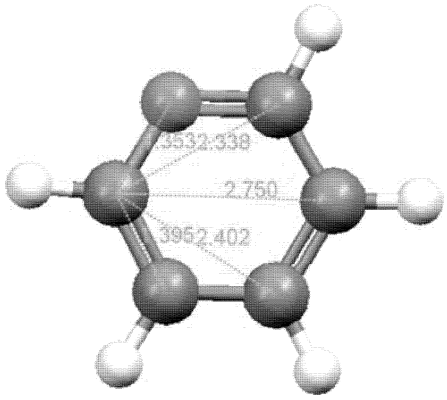


(a)

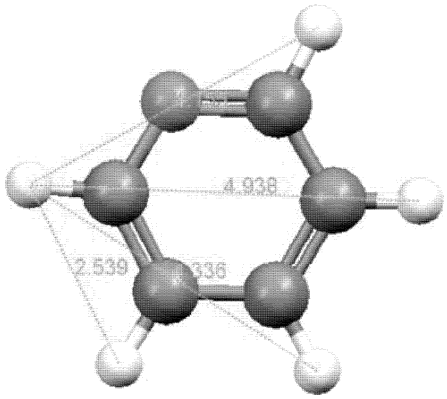


(b)

Figure 3.6: An illustration of a single molecule of pyridine minimized in the gas phase. (a) is an illustration of the various C–C and C–N distances. The C–N distance in pyridine is slightly shorter than the C–C distance in benzene. (b) is an illustration of the various H–H distances including the diameter of pyridine molecule calculated to be 4.928 Å.

Table 3.5: Experimental results show pyridine forms a rhombohedral asymmetric unit cell with $Pna2_1$ space group symmetry. The unit cell is comprised of four asymmetric cells each with four molecules. The lowest energy theoretical structure with the same symmetry is also shown. $a$, $b$, and $c$ values are in Å. $\alpha$, $\beta$, and $\gamma$ in deg. Adapted from [Anghel et al., 2002].

| results | a | b | c | $\alpha$ | $\beta$ | $\gamma$ |
|---|---|---|---|---|---|---|
| experiment | 17.524 | 8.969 | 11.340 | – | – | – |
| theory | 18.32 | 9.40 | 11.04 | – | – | – |

material in insecticides, pharmaceuticals, dyes, adhesives,and explosives [Partal et al., 2000].

In the solid state, pyridine forms an asymmetric unit cell of rhombohedral symmetry with $Pna2_1$ space group symmetry at 153 K. There are four molecules in each asymmetric cell and thus 16 molecules in the unit cell [Anghel et al., 2002]. Crystal structures with lower energy configurations have been theoretically predicted, but these structure have yet to be observed (illustrated in Figure 3.7). Unit cell dimensions for both the experimentally determined and theoretically predicted structure can be found in Table 3.5. The crystal structure of pyridine is very different from geometrically similar molecules like benzene.

Vapor pressure studies have not been performed in the temperature regions of the volumetric isotherms measurements therefore antoine parameters are extrapolated to the temperature range of the study. The results of our adsorption measurements can possibly be used for the antoine parameters within the temperature range of the study. Other useful parameters can be found in Table 3.6.

### 3.1.4 Benzene

Benzene, $C_6H_6$, is a planar aromatic hydrocarbon where each member of the six-carbon ring backbone has one hydrogen attached (see Figure 3.8). Benzene is a colorless and flammable liquid with a sweet smell and a relatively high melting point. It is carcinogenic and is an important industrial solvent and precursor in the production of drugs, plastics, synthetic rubber, and dyes. Benzene is a natural constituent of crude oil, but it is usually synthesized

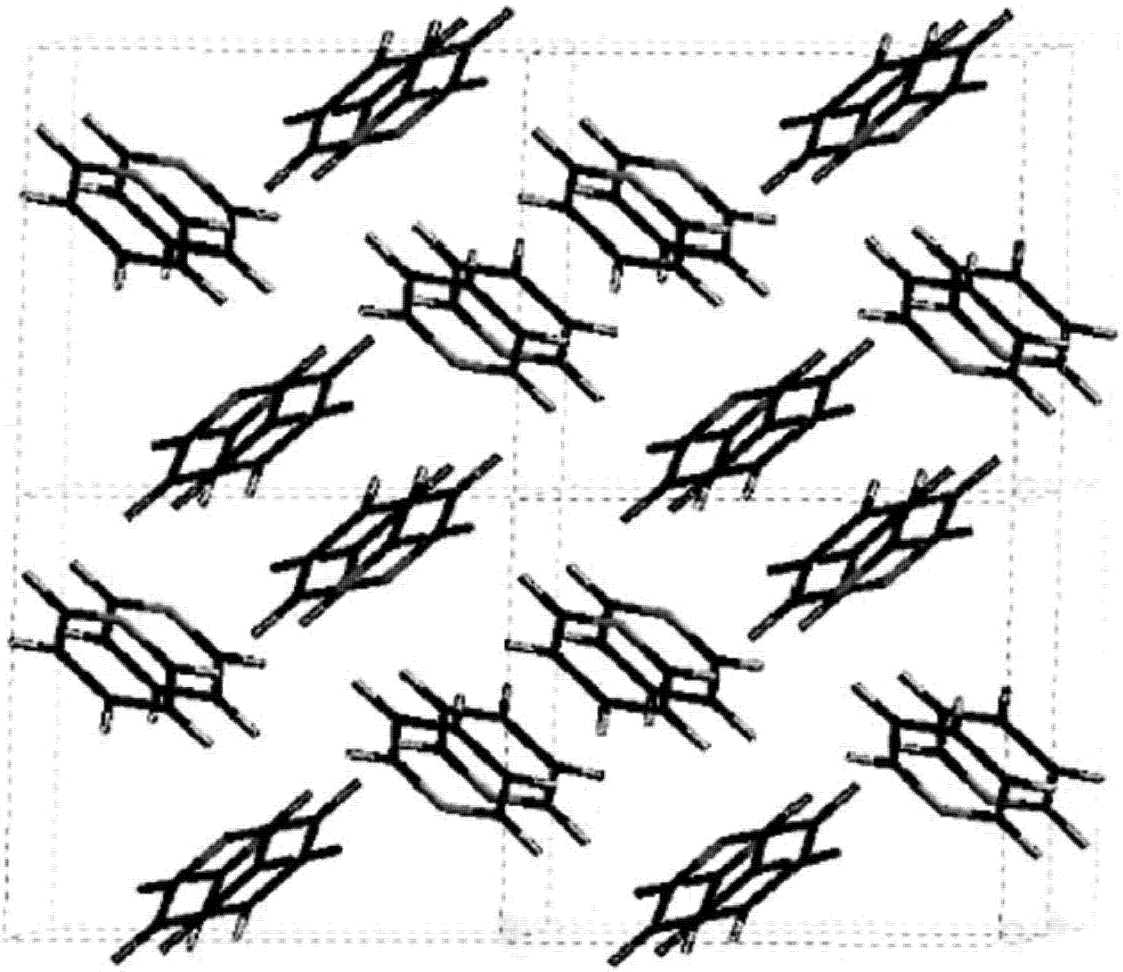

Figure 3.7: Pyridine forms an asymmetric unit cell of rhombohedral symmetry with $Pna2_1$ space group symmetry at 153 K. The unit cell contains 16 molecules which consists of 4 molecules in each of the 4 asymmetric cells which make up the unit cell. Illustrated above is the lowest energy calculated theoretical structure of bulk pyridine. Its lattice parameters can be found in Table 3.5. Images from [Anghel et al., 2002].

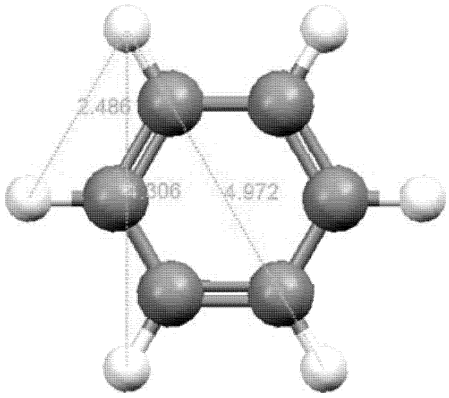


(a)

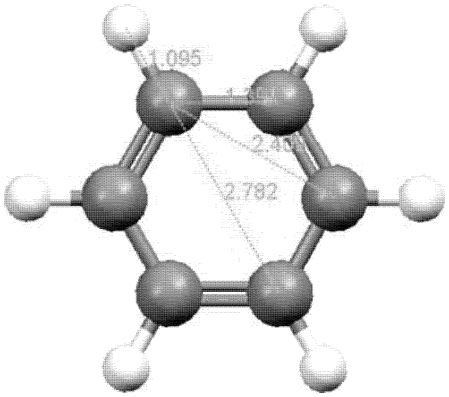


(b)

Figure 3.8: Illustrations of a single gas phase minimized single molecule of benzene. (a) illustrates the diameter of benzene of 4.972 Å and other H–H distances. (b) shows the different C–C bond distances on the carbon ring and the C–H bond distance. The C–C bond distance is calculated as 1.391 Å and the C–H bond distance is calculated as 1.095 Å.

Table 3.6: Some important physical and thermodynamic values relevant to bulk pyridine. Adapted from [http://webbook.nist.gov, 2006].

| | |
|---|---|
| Mol. Weight | 79.10 |
| Symmetry | $C_{2V}$ |
| $T_{boil}$ | 388.5 ± 0.6 K |
| $T_{fusion}$ | 232 ± 2 K |
| $T_{triple}$ | 231.5 ± 0.6 K |
| $\Delta_{vap}H$ | 40.21 (kJ/mol) |
| Antoine Parameters | (320 - 426 K) |
| A | 4.16272 |
| B | 1371.358 |
| C | -58.496 |

from other compounds present in petroleum. The aromaticity of benzene due to conjugated $\pi$-bonding stabilizes the molecule and affects many of its physical and thermodynamic properties.

The physical size of benzene differs from that of other alkane molecules due to its aromaticity of its carbon backbone created by its conjugated $\pi$-bonding scheme. The C–C distance in benzene (1.391 Å) is slightly shorter than a typical alkane molecule (1.513 Å). This shorter distance results from the resonant structure brought about by the conjugated $\pi$-bonding system. This shorter C–C bond length imparts additional strength to the molecule which alters many of its physical properties (see Table 3.7). Crystalline bulk benzene adopts a orthorhombic structure with *Pbca* symmetry and 4 molecules per unit cell (see Figure 3.9). The dimensions of the unit cell can be found in Table 3.8.

## 3.2 Purification of Adsorbates

Prior to their use in the adsorption experiments each of the sample gases undergo a distillation procedure to minimize the amount of contaminants.

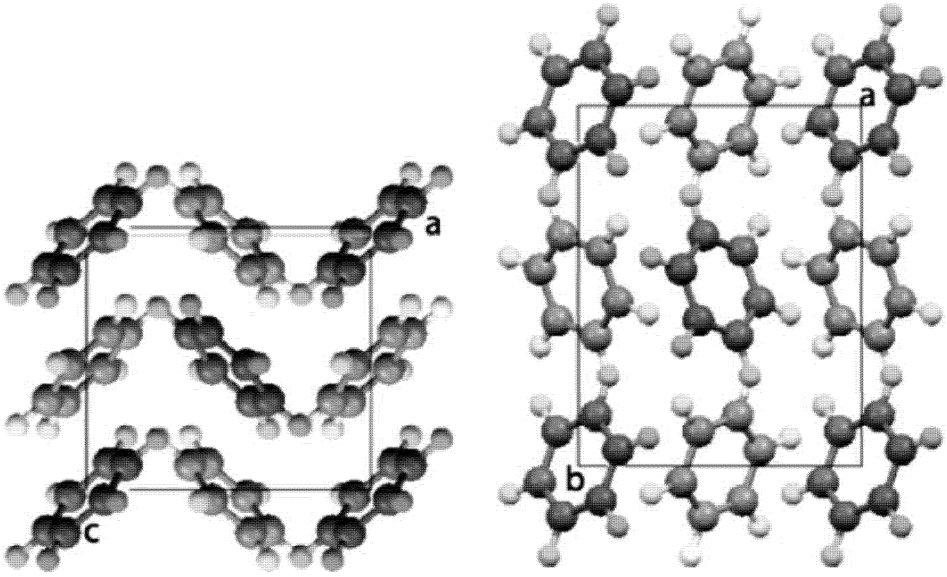


(a) (b)

Figure 3.9: Crystalline benzene adopts a orthorhombic unit cell with *Pbca* symmetry and 4 molecules per unit cell. (a) viewed along the *ac* plane. (b) viewed along the *ab* plane. Images from [Schweizer and Dunitz, 2006].

Table 3.7: Some important physical and thermodynamic values relevant to benzene. Adapted from [http://webbook.nist.gov, 2006].

| Mol. Weight | 78.11 |
|---|---|
| Symmetry | $D_{6H}$ |
| $T_{boil}$ | 353.3 ± 0.1 K |
| $T_{fusion}$ | 278.64 ± 0.8 K |
| $T_{triple}$ | 278.5 ± 0.6 K |
| $\Delta_{vap}H$ | 33.92 (kJ/mol) |
| $\Delta_{sub}H$ | 44.4 (kJ/mol) |
| Antoine Parameters | (287.70 - 354.07 K) |
| A | 4.01814 |
| B | 1203.835 |
| C | -53.226 |

### 3.2.1 *n*-hexane Distillation Procedure

*ReagentPlus®, ≥99%* *n*-hexane was purchased from Sigma-Aldrich because it contained the highest percentage of normal hexane. Although the water content is slightly higher ($\sim$ 0.05 %) than other available types the percentage of structural isomers is the lowest. Isomers of *n*-hexane can be difficult to extract and were therefore avoided. To remove the 0.05% water a distillation was performed.

The hexane was transferred into a round-bottom flask filled with a small quantity Linde® 4A activated molecular sieve and then attached to the distillation apparatus shown in Figure 3.10. The hexane is then refluxed over sodium metal within a dry $N_2$ atmosphere. It is then boiled through a distillation column and condensed into a round bottom flask outfitted with a septum and filled with a small amount of activated molecular sieve. The dried hexane was then removed from the round-bottom flask through the septum using a syringe. The syringe was then placed into a $N_2$ glove bag and transferred into a stainless steel Swagelok® vessel which had been evacuated with a turbomolecular pump and heated with heating tapes for 72 hours until the base pressure of the pump was reached.

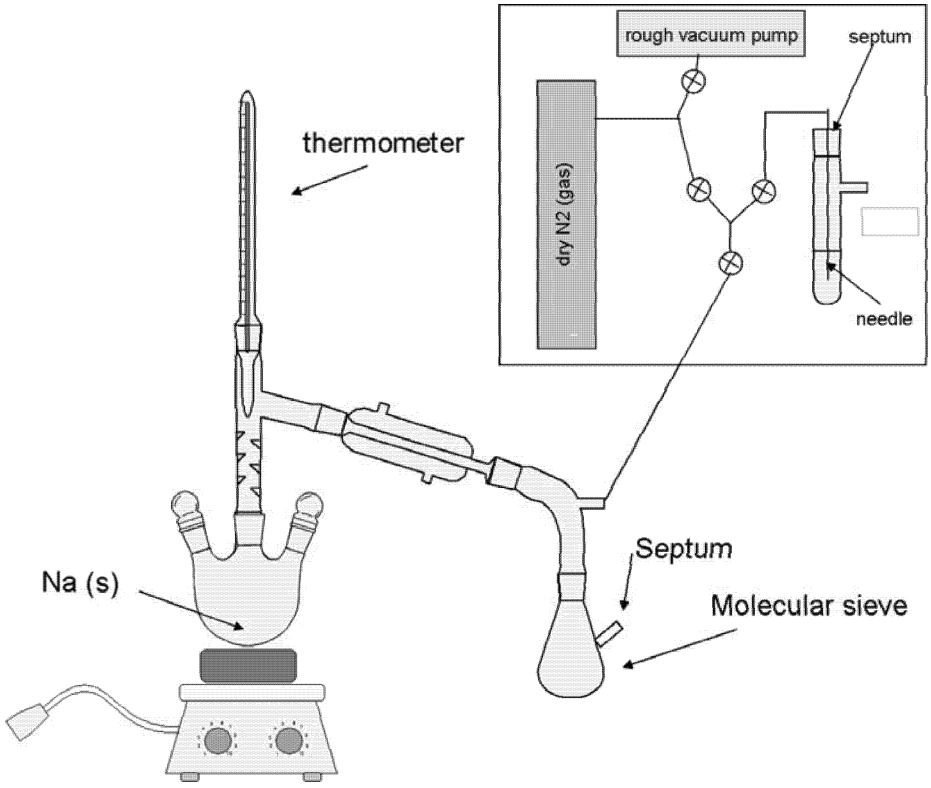


Figure 3.10: Schematic of the distillation setup used for the distillation of *n*-hexane. Image from [Cook, 2006].

Table 3.8: Benzene forms an orthorhombic cell with *Pbca* space group symmetry. The unit cell contains 4 molecules. $a$, $b$, and $c$ values are in Å. $\alpha$, $\beta$, and $\gamma$ in deg. Adapted from [Cox, 1958].

| a | b | c | $\alpha$ | $\beta$ | $\gamma$ |
|---|---|---|---|---|---|
| 7.39 | 9.42 | 6.81 | – | – | – |

### 3.2.2 Cyclohexane Distillation Procedure

The distillation of cyclohexane differs from the distillation of $n$-hexane and was changed to reduce the amount of transfers and exposure to different atmospheres. *CHROMASOLV® Plus for HPLC ≥ 99.9%* from Sigma-Aldrich was chosen because of its isomeric purity. The cyclohexane was transferred into a three-necked round bottom flask that contained activated 4A moleculaer sieve and was allowed to sit overnight in the flask. The cyclohexane was then transferred into a round bottom flask loaded with a generous sized chunk of sodium metal in a $N_2$ glove bag. The flask containing the cyclohexane and sodium metal and was then attached to a high vacuum (base pressure $\sim 1 \times 10^{-5}$ torr), schlenk line. The cyclohexane was then refluxed gently for 8 hours then transferred directly to the stainless steel container using a 1/4" tube graded seal blown onto a size 24 glass female vacuum seal. The liquid was transferred to the stainless steel container by gently boiling the cyclohexane and submerging the stainless steel container in liquid nitrogen creating a cold trap where the cyclohexane would condense.

### 3.2.3 Pyridine Distillation Procedure

The distillation of pyridine followed the same procedure and used the same apparatus as the distillation of cyclohexane outlined above except that potassium metal was used instead of sodium to reflux the pyridine. Potassium was employed because of the higher boiling point of pyridine ($T_{boil}$ = 388.5 K). *CHROMASOLV® Plus for HPLC, ≥99.9%* was purchased from Sigma-Aldrich. This was chosen because it had the highest isomeric purity and the lowest impurity content including water.

### 3.2.4 Freeze-Thaw Distillation

In addition to the distallation procedures outlined above, all adsorbates used in these studies underwent a freeze-pump-thaw distillation process to remove any remaining impurities including, $N_2$, $H_2O$ or argon gas used in the transfer process. This works under the premise that the boiling point of the impurities in the sample are different from the adsorbate. This brings about the process of Ostwald ripening where impurities in a nearly homogeneous crystal migrate to the surface to minimize the free energy of the crystal [Burkalov, 2006]. The liquid is frozen by submerging the stainless steel cylinder into a liquid nitrogen bath. While submerged, the liquid is pumped on using a turbo pump equipped with an ion gauge. The sample is pumped on in the submerged bath until the base pressure of the of the system is reached ($\sim 1 \times 10^{-7}$ torr). Once base pressure is reached the liquid nitrogen bath is removed and the sample is thawed using a water bath while being pumped on. Once pressure in the system reaches $\sim 1 \times 10^{-4}$ torr. The container is then re-submerged into the liquid nitrogen bath. This freeze-pump-thaw process is repeated 4-5 times.

## 3.3 Substrates

The substrates were chosen because of their structural simplicity, homogeneity, and lack of defects. Powders with high surface to volume ratios are ideal for use in adsorbed film neutron experiments because a reliable scattering signal can be obtained after subtraction of the large background signal from the substrate. Metal oxide powders have been avoided in the past because of the difficulty in producing large quantities of pure hyroxyl-free, homogeneous powders. Even the best material has special handling procedures because it is air and water sensitive. Graphite has traditionally been used because it is commercially available and easy to handle prepare with clean surfaces. The adsorption properties of the molecules on these two substrates were chosen to make a comparison of how substrate or molecular symmetry affects the adsorption properties.

### 3.3.1 Magnesium Oxide

Magnesium oxide is comprised of magnesium and oxygen atoms in a cubic rocksalt structure with alternating atoms at each corner of the cube. The ideal geometry of the rocksalt surface is with the (100) face of the crystal of the crystal exposed (see Figure 3.11). MgO is an insulator with an experimental band gap of 7.8 eV. MgO forms a cubic unit cell with *Fm3m* space group symmetry and 4 atoms per unit cell. The unit cell has a dimension of 2.98 Å.

Metal Oxides (MO) are typically ionic in nature where electron charge is localized near the more electronegative oxygen atoms and very little electron charge distribution is between the atoms. The ionic nature of these bonds creates a strong surface electric field. In the case of Metal Oxides (MO), the oxygen cation radii is the larger than the metal anion radii. This slight difference in atomic size can create a slight corrugation on the surface of the crystal. In the case of magnesium oxide, the oxygen is approximately twice the size of the magnesium anion [Cox and Hendrich, 1994]. When atomically perfect, a slab of crystal has no net dipole moment. Non-polar surfaces such as the (100) face are the equilibrium faces of the crystal. If a polar surface is created, they are never truly stable since long-range electrostatic interactions drive the reconstruction of the surface to minimize the polar surface [Mutaftschiev, 2001].

All exposed surfaces experience some variation of relaxation or reconstruction depending on the exposed facet and the constituent atoms of the crystal. MgO (100) experiences an inward relaxation of the surface plane and a rumpling of the surface where the $O^{2-}$ anions move away from the surface and the Mg cations move towards. The rumpling of the top layer is repeated in lower layers but with a decreasing amplitude. This is thought to occur up to 8-10 layers below the surface layer [Somorjai, 1994].

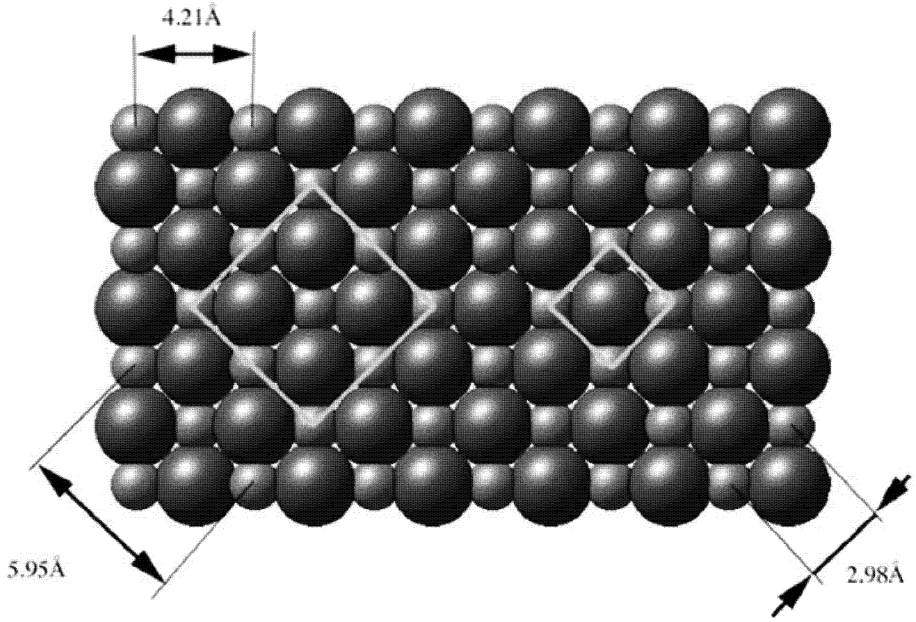


Figure 3.11: Magnesium oxide (100) crystallographic face illustrated. Magnesium oxide forms a cubic unit cell with *Fm3m* symmetry and four atoms per unit cell. The unit cell length is 2.98 Å.

The primary defect on the MgO (100) surface are point defects and vacancies of the $\overline{O}^{2-}$ cation sites [Hendra et al., 1971], [Cox and Hendrich, 1994]. These defects are typically formed when samples are heated or remain from synthesis in an oxygen deficient environment. The acid-base properties of MgO is based on its Brönstead acidity and Lewis basicity. Brönstead acidity is the availability of $H^+$ ions from water and $OH^-$ groups already adsorbed on the surface. Stable (100) surfaces show very weak acidity because of the relatively low cation charge and large bandgap [Iizuka and Tanabe, 1975]. Empty orbitals at the surface are too high in energy to interact effectively with donors. Lewis basicity on MgO is related to the availability of a pair of $2p$ electrons from oxygen anions. Low anion charge and large anion radius lead to weaker bonding and hence more basic $O^{2-}$ anions. The coordination number of the surface atoms also play a role in acidity or basicity. Surface defects create sites where surrounding ions have lower coordination number and thus may be more active acidic or basic centers.

Bulk defects in MgO are important because they generally give rise to electronic levels within the bandgap of the solid. The electronic properties associated with defects depend on both the energies relative to the band edges of a perfect crystal and the number of electrons occupying defect levels. Two types of structural defects which occur on MgO are the $O^{2-}$ vacancy or, '$F$' center, and the Mg cation vacancy, or '$V$' center. A neutral oxygen vacancy must have two electrons remaining which may be trapped by the unbalanced coulomb potential. Removing one of these electrons gives the $F^+$ center. Conversely a magnesium atom removed takes an electron with it giving a $V^+$ center [Cox and Hendrich, 1994].

### 3.3.2 Graphite

Graphite can be found in a variety of polymorphs all which have slightly different physical properties due to the amount perfect graphite crystals displaying long-range order. Perfect graphite forms a hexagonal unit cell with $P6_{3/mmc}$ space group symmetry and 4 atoms per unit cell. The unit cell has dimensions of $a = 2.4612$ Å and $c = 6.7079$ Å (see Figure

3.12) [Reynolds, 1968]. The interatomic distances between carbons are 1.415 Å along the basal plane and 3.35 Å between basal planes. Perfect graphite is defined when a well-developed layer structure is formed in which the atoms are arranged in open hexagons and layers show an $ABAB$ stacking sequence.

Imperfections in graphite are typically due to dislocations between the basal planes [Robertson and O'Reilly, 1987]. This is due to the large difference between atoms in the basal plane which are covalently bonded to each other. Bonds between the planes are much weaker than covalently bonded atoms. This makes the preferential type of dislocation a glide dislocation between basal planes.

Graphite is a semi-metal and is a conductor. In graphite there are three co-planar bonds of type $sp^2$ and the length of 1.54 Å with electron available for the mixed role of co-planar and interplanar binding as well as electrical conduction. The strongly $sp^2$ bonded hexagonal lattice which forms the basal plane of graphite makes electrical conductivity highest in the basal plane direction.

The type of graphite used in these studies is classified as vermicular graphite. Vermicular graphite is made by the Union Carbide corporation (a subsidiary of Dow Chemical), and is a loosely packed powdery substrate with a quoted surface coherence length of $\sim$ 500 Å [Dow, 2000].

## 3.4 Substrate Synthesis and Preparation

### 3.4.1 Magnesium Oxide

The synthesis of Magnesium Oxide powder used in our studies is produced by a patented method [Lar, 2001] which involves heating Mg metal mixed with high purity graphite pieces

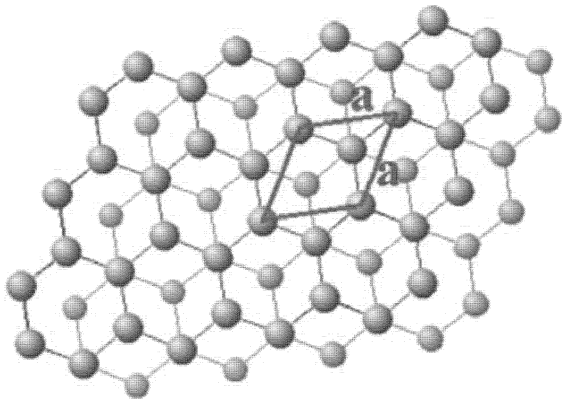


(a)

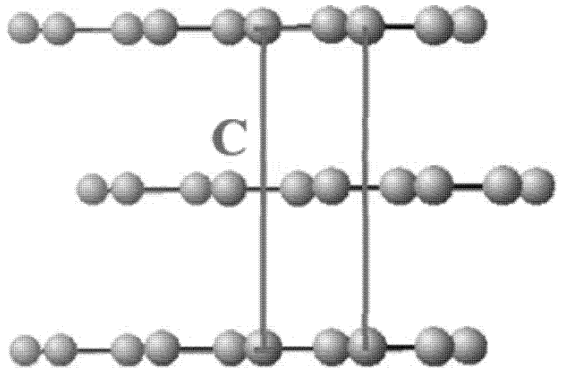


(b)

Figure 3.12: Unit cell of graphite shown from the $a$-axis and $c$-axis where $a = 2.4612$ and $c = 6.7079$ Å. (a) shows the graphite unit cell along the $a$-axis. (b) illustrated the unit cell along the $c$-axis. Images from [http://invsee.asu.edu, 2006]

in a graphite crucible of the same graphite with an induction furnace in an inert gas atmosphere while flowing oxygen gas. Using this method we are able to produce cubic MgO particles with tunable mean size and size distribution. The particles show almost exclusive (100) face exposure and exhibit nearly defect-free long range surface homogeneity.

The operating principle of an induction furnace is as follows. A solid state RF power supply sends an AC current through a copper coil. The coil serves as a transformer primary and the component that becomes heated becomes a short circuit secondary. When a conductive piece is placed within the coil, circulating eddy currents are induced around the piece. Ohmic losses from the eddy currents generate thermal heat. If the material is magnetic, heat is also created through a hysteresis effect in which during induction the magnetic field offers resistance to the AC electrical fields [Diefenderfer and Holton, 1994]. This effect causes enough friction to heat the piece. This affect dissipates at the curie point of the material. The induction heating effect occurs on the surface of the piece. Pieces with higher surface to volume ratios heat quicker.

The argon used as an inert atmosphere and as a carrier gas is Ultra High Purity (UHP) grade which is passed through a drying column containing Dririte®, 4A molecular sieve, and dried calcium oxide powder, in that order. The oxygen used in the reaction is typical compressed oxygen tank and is not purified further.

Controlling the heating, oxygen, and argon flow allows for the tuning of the magnesium oxide powder particles mean size and size distribution. The graphite crucible and chunks interspersed with the Mg metal are both high purity graphite. The highest possible purity of graphite is desirable to minimize impurities entering the powder and to withstand heating by the induction furnace since it is a conducting material. The chunks of graphite are produced by chiseling rods down to a mean size of 5 mm $\pm$3 mm chunks.

The Mg metal is a high purity (*Alfa Aesar 99.9%*) ingot. The predominant impurity present in the ingot is manganese and chromium which are present at levels of 4 ppm as seen by Electron Spin Resonance (ESR) and flame Atomic Absorption (AA) spectroscopies [Arnold et al., 2006]. Magnesium ingot is cut to 6-10 mm cubes with a band saw and cleaned to remove any oils and impurities introduced by the saw. This metal is dispersed in the graphite crucible with graphite chunks.

The loaded graphite crucible is then placed on top of a smaller diameter perforated quartz tube which acts as a stand to hold the graphite crucible inside the coil. Quartz is used so to not conductively couple to the electric field. An insulating tube of alumina and tube of quartz of larger diameter are placed around the crucible. This aids in the flow of argon by the crucible and as a measure of protection.

Around the heating coil a quartz chimney is placed to collect the powder from the reaction. At the top of the chimney are a series of stainless steel baffles designed to slowly constrict the flow of gas through to the exhaust. Slowly constricting the flow deposits lighter particles on baffles as you travel farther from the crucible. The exhaust of the reactor is attached to a fume hood to pull a slight vacuum on the chimney thereby allowing for the flow of gas through the system.

The procedure for preparation of the crucible used in the reaction of the reaction is a follows. Cubed Mg metal is first submerged in a dilute solution of hydrochloric acid to clean the surfaces of any impurities. The Mg metal is then weighed and carefully interspersed in the graphite crucible with the graphite chunks so to have as much graphite as possible near each Mg metal cube. The chimney and baffles are then cleaned with a minute amount of ethanol and dried with a heat gun to remove any remaining ethanol or water. The crucible is then placed on the quartz stand inside the alumina tube and quartz tube. The chimney is then placed around the entire setup and covered with the baffles setup and attached to

the exhaust of the fume hood. The argon is then flowed slowly usually 8 hours prior to the reaction. This is done to slowly displace the air present inside the chimney by utilizing that argon is slightly heavier than air (argon $\sim$ 40 g/mol, air $\sim$ 28.8 g/mol). Once purged for a few hours, the oxygen flow is turned on briefly to purge out stainless steel gas lines leading to the reactor.

The induction furnace is then turned on. The argon flow is left on as a carrier gas to carry the particles away from the crucible. The crucible is heated slowly up to the melting point of the magnesium metal ($T_{vap}$= 923 K) [http://webbook.nist.gov, 2006]. Once $T_{vap}$ has been reached the synthesis of MgO proceeds as follows,

$$Mg_{(s)} + C_{(s)} \xrightarrow{\Delta H} Mg_xC_{y(g)}, \tag{3.2}$$

$$Mg_xC_{y(g)} \rightarrow Mg_{(g)} + C_{(s)}, \tag{3.3}$$

$$M_{(g)} + O_{2(g)} \rightarrow MgO_{(s)}. \tag{3.4}$$

The oxygen flows over the crucible where the evaporated magnesium complex is traveling. The complex then reacts with the oxygen to produce MgO powder. The powder is then entrained in the carrier gas flow of argon and transported away from the furnace and to the chimney. The powder produced deposits on the chimney and the baffles of the apparatus. Once the furnace is turned off the powder is collected and transferred into desiccants until used. Each batch that is produced is tested by taking a sample immediately after synthesis and transferred into a quartz tube which is leak tested then heat treated under vacuum to a base pressure of $\sim 1 \times 10^{-7}$ torr for a minimum of 36 hours but not exceeding 72 hrs. at 950°C. It has been shown that heat treatment at this temperature homogenizes the surface structure of the MgO and ensures that all the exposed facets are the (100) equilibrium face [Cox and Hendrich, 1994]. Upon heating, water and some small hydrocarbons evolve from the surface as can be seen by a TPD.

The primary defect of the MgO (100) surface is an oxygen vacancy. Prolonged exposure to air allows adsorption of molecules at these sites so exposure is always kept at a minimum. Our method enables us to produce extremely pure MgO with impurities below 1 ppm with the exception of manganese which was found using Electron Spin Resonance (ESR) spectroscopy and Atomic Absorbtion spectroscopy (AA) to be ∼4 ppm. The impurities present in the MgO are primarily due to the impurities present in the original magnesium ingot.

### 3.4.2 Graphite

The vermicular graphite used in these experiments was synthesized by the Union Carbide Corporation (a subsidiary of Dow Chemical). Preparation of the graphite before use follows a similar procedure as the MgO. First the graphite is cut into small cylinders in order to fit within the copper sample cells. The pieces are then weighed and put into a large quartz tube which is sealed with by a compression fitting and a swagelok valve. The setup is then leak checked using a helium leak detector. The sample is then put into a furnace and attached to a turbomolecular pump with an ultimate pressure of $\sim 1 \times 10^{-7}$ torr and baked out at a temperature of 900°C for a minimum of 24 hours. Once completed the sealed quartz tube is removed from the pump and furnace and transferred into an Argon glove box and sample cell both described in section 3.6. The graphite is then transferred into the cell and sealed using an indium seal. The sample cell is then removed from the glove box and leak tested with a helium leak detector. The sample is then attached to the gas handling system described in section 3.5.1.

## 3.5 Experimental Equipment

Described below is the equipment used in the groups isotherm and neutron studies.

### 3.5.1 Gas Handling System

A variety of thermodynamic quantities can be derived from a set of adsorption isotherms recorded over a temperature region. The only restriction to these experiments is the accessible pressure range which can be accurately read by the pressure transducer. To perform isotherm experiments one only needs a constant temperature bath to house the sample, a gas handling system of known volume, and some method to record the pressure in the volume.

The Gas Handling System (GHS) used for our groups volumetric isotherms is comprised of a calibrated volume with pressure transducer manometer and an arm connecting the calibrated volume to the sample cell. The GHS is constructed from 1/4" stainless steel tubing and swagelok B-4HK valves. The calibrated volume and arm is wrapped in resistive wire heating tapes and serve to facilitate the transport of the adsorbates with low vapor pressures to the sample cell and to keep the temperature of the GHS constant which dampens the the effects of temperature fluctuations in the room. The heating tapes are held at a temperature of 313 K ( $\sim 40^{\circ}$C), which is slightly below the temperature of the pressure transducer.

The pressure is read using an MKS® 120A High Accuracy Pressure Transducer. The appropriate transducer is chosen based on the range of saturated vapor pressures of the isotherms being studied. Transducers range from 0.1 torr to 5000 torr maximum pressures. The pressure in the transducer is read by variable capacitance diaphragm sensor which is housed within a controlled temperature chamber which is maintained at 45°C [MKS, 2002]. When pressure is applied to the diaphragm, its deflection creates a change in the distance between the electrode and diaphragm and produces a capacitance change. This change in capacitance is then changed to an AC voltage by a bridge circuit. The AC output is then demodulated and converted to a DC voltage. The pressure reading of the transducer is read externally as a voltage that varies proportionally with the full-scale pressure reading and varies from 0 V to 10.4 V. The voltage output from the transducers is fed to a 16-bit

analog-to-digital board in the control box.

The resolution of the pressure transducer is dependent on the translation of the analog-to-digital signal through the 16-bit A-to-D converter. The number of discrete points possible through the A-to-D conversion is equal to,

$$2^{16} = 65,536. \tag{3.5}$$

When this value is divided by the 10.4 volt range of the transducer, it gives a resolution of limit .001587 torr on a 100 torr transducer. This value is incrementally changed by a factor of 10 depending on the pressure limit of the pressure limit of the transducer. So, for a 1 torr transducer, the resolution limit is a factor of 100 smaller than for a 100 torr transducer and has a resolution limit of $1.587\times10^{-5}$ torr. Zeroing of the voltage signal against the base pressure of the system is accomplished using a multimeter that is connected in parallel to the voltage signal received from the torr head. This is done prior to the start of each isotherm experiment and is compared to the base pressures achieved before the start of other isotherms.

The precise volume of the calibrated volume with manometer is determined using Boyle's Law corresponding change in pressure and change in volume. A glass bulb is used to calibrate the volume whose volume has been determined with purified water gravimetrically to less than 1% error. Gas expansions into the bulb or out of the bulb are then performed with (UHP) helium to calculate the volume the unknown value. UHP helium is used because at room temperature it behaves as an ideal gas which allows the use of the Boyle's Law relation. Once the calibrated volume is known to a precise value, the volume of the arm and sample cell can be calculated. The GHS system is attached to a turbomolecular pumping system with a backing pump which reaches a base pressure of $\sim 1 \times 10^{-7}$ torr. To perform high-resolution volumetric isotherms, a LabVIEW® driven system which is described in [Mursic et al., 1996]. This program integrates the reading of the pressure manometer,

the actuation of the valves and regulation of the sample cell temperature.

The program algorithm is illustrated in Figure 3.13 and works as follows. A known quantity of gas is administered from a reservoir to the calibrated volume which is specified at the start of the program and can be adjusted as the program runs. This gas is slowly delivered to the calibrated volume using an MKS® type 248 solenoid control valve which is driven with a type 1249A solenoid driver housed in a control box. The valve can be incrementally opened and closed using an algorithm which generates proportional, integrative, and differential (PID) values. The controller takes a measured value from a process or other apparatus and compares it with a reference setpoint value. The difference (or "error" signal) is then used to adjust some input to the process in order to bring the process' measured value to its desired setpoint. Larger 'P' values typically means faster response since the larger the error, the larger the feedback to compensate. Smaller 'I' values imply steady state errors are eliminated quicker. The tradeoff is larger overshoot because any negative error integrated during response must be integrated away by positive error before a steady state is reached. Larger 'D' values decreases overshoot, but slows down transient response [Lewis, 1992]. In this application PID values dictate how fast or slow the valve closes and opens depending on the pressure read from the manometer. The proportional valve is housed in-line behind a swagelok BH4-K valve (valve 2) which is driven by a pneumatic solenoid and actuator which are driven by the program. The pneumatic valve is controlled via a control box which provides the 24 V signal needed to actuate the solenoid. If the quantity of gas allowed into the gas handling volume is higher than the specified pressure a valve (valve 3) to the turbomolecular pump is opened with a small leak valve housed in-line after the pneumatic valve which allows for the slow evacuation of adsorbate gas from the calibrated volume. The valve to the sample is opened and the adsorbate is allowed to expand into the sample cell and adsorb onto the substrate once the specified pressure is reached in the calibrated volume. For the program to accept the point as equilibrated, a timer records the change in pressure versus the change in time and calculates a numerical derivative. Once

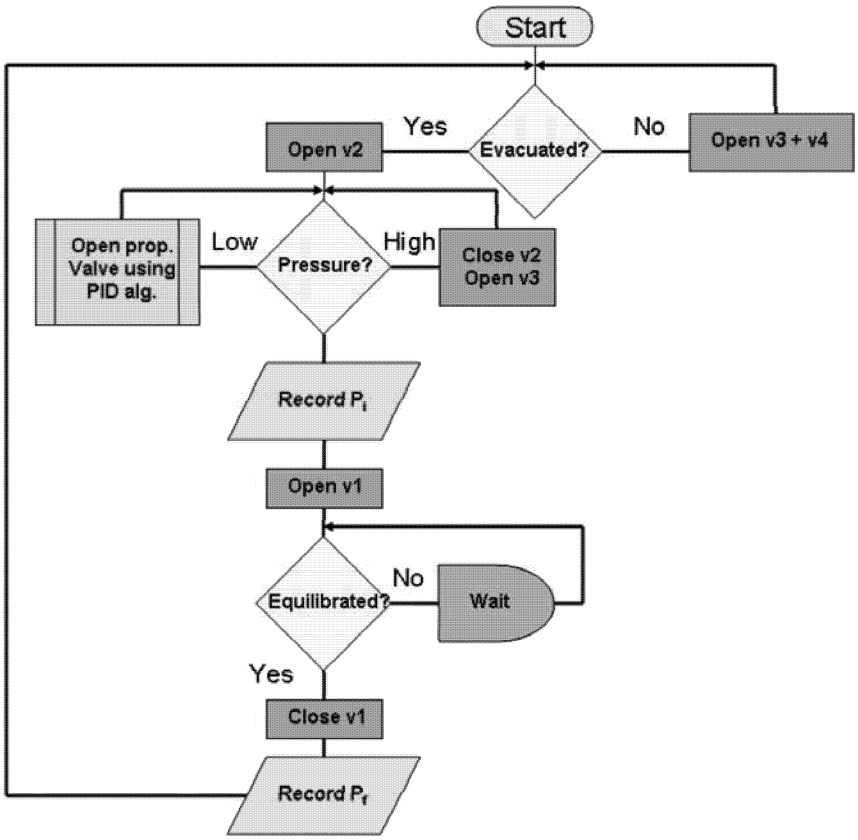


Figure 3.13: Each data point of an isotherm reaches equilibration using this algorithm.

this numerical derivative matches the value specified by the user the system is considered in equilibrium and the point is accepted. The process is repeated for the number of points specified by the user. When the isotherm program is not running by-pass valves (valve 4) are available to expedite evacuation of the sample in preparation for the next isotherm.

The program records in a spreadsheet the initial pressure of the point ($P_i$), the final pressure ($P_f$), a summation of the change in pressures from all the points ($\Sigma\Delta P$), as well as the maximum, minimum, average, standard deviation of the temperature at each point.

### 3.5.2 Glove Box

Once the sample has been baked out following the procedure outlined in section 3.4, the sample is then transferred to a (UHP) argon glove box where it is loaded into a sample cell. The glove box has only trace amount of impurities $\leq 1$ ppm $H_2O$ and $O_2$ as detected using a method outlined in [Shriver and Drezdzon, 1986], where the time elapsed of an exposed 25 W light bulb filament can be related to the concentration of impurities in the atmosphere. The light bulb filaments in our glove typically last on the order of 1–2 months which is far beyond the values extrapolated by Shriver and Drezdzon which describes the duration of a exposed 25 watt filament is related to the number of impurities of $O_2$ and $H_2O$.

## 3.6 Sample Cells

Our groups efforts span a variety of experimental techniques which require specialized sample cells some which are described below.

### 3.6.1 Gas Handling System Sample Cell

The sample cells used for our isotherm experiments are constructed out of a Oxygen Free High Conductivity (OFHC) copper and the supporting ring stand which attaches to the two-stage closed cycle helium expander 'displex' from APD Cryogenics®. The copper cell holds the MgO sample and is sealed using an indium compression seal using small screws

to compress the seal. From the bottom of the copper cell, a small stainless steel capillary is attached which allows for the flow of the adsorbate gas into the cell. This capillary is attached to the outside of the displex via a soldered adapter to a swagelok valve. For the experiments using room temperature liquid adsorbates, the capillary leading to the OFHC copper cell is wrapped in a resistive wire which has been treated with a electrically insulated GE® varnish. To prevent the entrance of MgO powder into the gas handling system and capillary, quartz wool is placed in the capillary which allows for the flow of gas through.

The sample cell mounted on the displex is attached to an APD cryogenics HC-2 closed cycle helium compressor [APD, 1988]. The compressor serves to drive the expander piston which cools the sample utilizing the Joule-Thompson effect where the compressed Helium gas is compressed then expanded by a piston and the change in pressure and volume in an adiabatic system lowers the temperature of the space through each successive compression and expansion [APD, 1988]. Once mounted to the sample stage on the displex, the inner-vacuum shroud and outer shroud are mounted and the interior of the displex is evacuated with a turbomolecular pump. This creates an isolated environment with minimal thermal contact to the outside environment.

The temperature of the closed-cycle helium refrigerator is regulated using a Neocera® LTC-10 temperature controller. A platinum resistance thermometer and silicon diode are mounted at the end of the cold head and on top of the sample cell respectively. Each thermometer has a calibration table which relates temperature to resistance or voltage depending on type of thermometer. Two 25 $\Omega$ carbon resistance heaters mounted in series are glued with epoxy in a OHFC copper block and mounted underneath the sample stage. The resistance heater can be run at three different outputs (0.5 W, 5 W, and 50 W) depending on the cooling power of the displex. Control of the temperature is regulated by PID settings automatically generated by the LTC-10 controller which regulates the voltage to the heater. Temperature control can be regulated to $\pm$ 0.002 K over the entire operating range

of the closed-cycle refrigerator provided proper PID settings are input or generated by the controller.

### 3.6.2 Neutron Sample Cell

All neutron sticks share the same basic features but differ slightly in length and electronic connections which differ from neutron instruments and are described elsewhere [Koehler III et al., 2000]. The neutron sample cell described below is for the OSIRIS beam line at ISIS, Rutherford Appleton Lab (Chilton, UK).

The MgO sample is sealed with an indium wire o-ring to a vanadium or aluminium can depending on the type of neutron experiment being performed. The dimensions of the sample cell used on the OSIRIS beamline are 20 mm by 50 mm (0.787 in. by 1.96 in.) which coincide with the incident neutron beam dimensions. The sample cans typically hold 10-15 grams of MgO. The sample cells are then inserted into an open-cycle liquid helium cryostat ILL 'orange cryostat' constructed by AS Scientific®. The cryostat is lowered into the beam line and its surroundings evacuated to reduce amount of scattering from the air between the cryostat and neutron beam aperture. Adsorbate gases are delivered to the sample cell in the cryostat via a long capillary to the top of the cryostat. The capillary is terminated by a valve and is connected to a GHS with a tube of known volume. To ensure no condensation within the capillary, a varnished non-inductive resistance wire heater is used. The capillary is thermally shielded from the cryostat by housing the capillary in a vacuum shroud and centered in the shroud with teflon spacers. The vacuum shroud is evacuated using a valve at the top of the stick. Two thermometers are attached to the stick to read the temperature of the capillary and the sample itself. One mounted near the top of the sample can within the vacuum shroud and one on the outside of the sample.

### 3.6.3 Quartz Tube Sample

The quartz tube sample cell consists of a 11 mm OD by 8 mm ID quartz tube which is blown onto a quartz to borosilcate graded adapter from Duniway®. This is blown onto a borosilicate to 1/4" or 3/8" Kovar® graded seal. The sample tubes are made to a length so to allow the baking of the sample in a furnace without exposing the borosilicate (M.P. $\sim 450°$) to the furnace. The Kovar seal can then be attached to a swagelok BH4-K valve and sealed.

## 3.7 Experimental Procedure

### 3.7.1 Isotherm Experiments

To obtain an accurate thermodynamic picture of the studied system, a series of 20–50 isotherms are run. This is done to capture the changes in layering, phases, and behavior as a function of temperature. Before starting each isotherm heating tapes around the calibrated volume of the GHS and the capillary heater on the sample are allowed to sit for a few hours to evenly heat the stainless tubing and reach equilibrium at the desired temperature. A typical experiment can last from 6 hours to 36 hours depending on the adsorbate, substrate, temperature, and algorithm parameters that the isotherm is being run at. After each isotherm, the sample cell is warmed to room temperature and evacuated for at least 8 hours. At the conclusion of each isotherm to obtain the most accurate saturated vapor pressure (SVP) and temperature offset from the temperature controller, the sample cell is filled with the equivalent of 30–40 layers of adsorbate. According to Dash, [Dash, 1977] 30–40 equivalent layers of adsorbate molecules the bulk properties of materials can be observed. The SVP of the isotherm is then related to temperature using the semi-empirical Antoine equation.

A temperature dependent dead space correction is then applied over the entire range of the isotherm study using helium expansions. This expansion calculates the amount of adsorbate

molecules that occupy the sample cell but are not adsorbed onto the substrate. This value is subsequently subtracted from the total amount of moles adsorbed.

### 3.7.2 Neutron Scattering Experiments

The neutron experiments described were all performed on the OSIRIS beam line at the ISIS pulsed neutron source located in the Rutherford Appelton Laboratory in Oxford, UK. The experiments performed on the instrument were conducted in the backscattering diffraction mode. OSIRIS can probe $Q$-ranges from to with a resolution of 1% or 6 $\times 10^{-3}$ $\Delta d/d$. A detailed explanation of instrument can be found elsewhere [Andersen et al., 2002] and [Telling and Andersen, 2005]. First the sample is inserted into an 'orange' cryostat and the temperature dropped to 4.2 K. The diffraction pattern is then taken for as much time as possible to ensure high quality counting statistics. The cryostat is then removed from the beamline and allowed to warm up and connected to the evacuated GHS via a calibrated tube. An isotherm is run to the appropriate coverage when warm enough for the adsorbate to enter the sample cell in the cryostat and the connecting tube evacuated. The appropriate coverage is calculated using a comparison of monolayer capacities of methane and the adsorbate and normalized to units of Torr $\cdot$ cc, which can be interconverted to any GHS system.

The neutron stick the sample is cooled down slowly and returned to the beamline when the calculated amount of adsorbate has been delivered. Care is taken in the cooling of the sample because a rapid cooling of the sample can cause it to condense suddenly because when the adsorbate is delivered a large amount of vapor lies above the sample. Pauses are taken periodically especially during bulk phase transitions like the freezing point and triple points to allow the adsorbate to anneal on the substrate. Most adsorbates have a saturated vapor pressure too low to be detected by any method at the temperatures diffraction measurements are taken. Neutron scans are taken in a $Q$-range where adsorbate peaks are known to occur to ensure that the adsorbate has condensed onto the substrate.

Proper condensation of a thin film on the surface should result in the appearance of Warren-like peak profiles indicative of two-dimensional diffraction after subtraction from the MgO powder signal. These peaks should increase in intensity as the temperature is reduced down to 4.2 K. A second pattern is collected over the entire $Q$-range desired when base temperature has been reached. A series of progressive scans are then taken over the entire $Q$-range desired at temperatures where interesting phase transitions or layering transitions occur as seen from the volumetric isotherm data set.

### 3.7.3 $CH_4$ Isotherms

Methane isotherms are used to characterize the surface quality to substrates before neutron and isotherm experiments. Methane isotherms are used because of the large body of thermodynamic and structural data that exists on the adsorption properties on both magnesium oxide and graphite which is discussed in section 2.4.1. By quickly loading a sample into a quartz tube and heat treating using the procedure outlined in section 3.4.1 a methane isotherm can be performed by submerging the quartz tube in liquid nitrogen. The similarity of the surface structure with the MgO and graphite lattice allows for a distinct layer-by-layer growth of methane on the substrates. The appearance and number of steps and the ratio of step heights relative to each other is a good measure of the quality of the sample. Adsorption isotherms on high quality MgO show up to 7 distinct layering transitions and have nearly equal step height for the first two or three layers. On graphite, methane shows 4 distinct layering transitions including a distinctive incommensurate-commensurate transition just before the monolayer completion point. An illustration of the two isotherms is shown in Figure 3.14. The monolayer capacity of the methane isotherm is also a useful tool when compared to the monolayer capacity of another adsorbate to calculate an approximate molecular area of the adsorbate being interrogated.

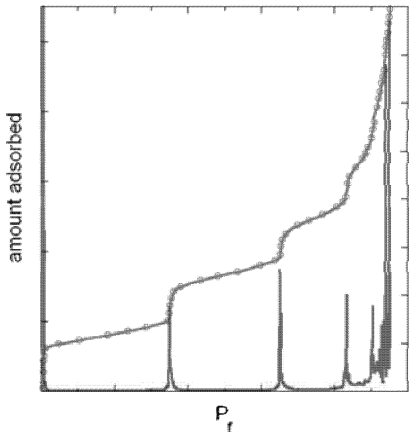


(a)

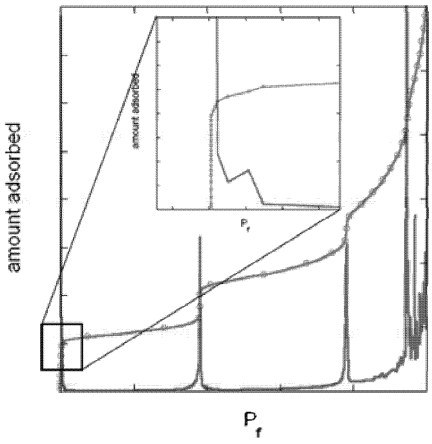


(b)

Figure 3.14: Images of methane adsorption isotherms on MgO and graphite. (a) MgO shows up to 7 distinct layering transitions as can be seen from the associated numerical derivative (red). (b) Graphite shows 4 distinct layering transitions including a incommensurate-commensurate transition (inset) indicating the completion of a monolayer.

Table 3.9: Compilation of methane surface structure parameters formed on MgO and graphite [Larese et al., 1988a] [Larese et al., 1991] [White et al., 1978].

| Substrate | Structure | $a$ (Å) | Configuration | APM (Å$^2$) |
|---|---|---|---|---|
| MgO | $\sqrt{2} \times \sqrt{2}$ $R45°$ | 4.211 | dipod down | 17.74 |
| graphite | $\sqrt{3} \times \sqrt{3}$ $R30°$ | 5.167 | tripod down | 17.8 |

The monolayer capacities of an isotherm can be calculated using a variety of analytical expressions some which are described in chapter 2. The most often used method for calculating monolayer capacities in these studies is the point-$B$ method described in section 2.7.8. The surface structures of $CH_4$ on both substrates have been investigated thoroughly using a variety of methods [Larese, 1998], [Beaume et al., 1984], [Yang et al., 2006], [Kim and Steele, 1992], [Lysek et al., 1983] and have been summarized in Table 3.9.

### 3.7.4 Temperature Programmed Desorption (TPD) Experiments

Temperature Programmed Desorption (TPD) can be used to indentify if an adsorbate dissociatatively chemisorbs or physisorbs to a surface. TPD can give insight to the relative binding energies of adsorbate molecules or chemisorbed species left on the surface. After a series of isotherms is performed, the sample is removed from the GHS sample cell and transferred in a $N_2$ glove bag to a quartz tube. The quartz tube is then attached to a SRS® 200 quadrupole mass spectrometer Residual Gas Analyzer (RGA) which has been integrated into a turbopump based pumping system. A needle valve is placed in-line before the RGA to minimize the exposure of the RGA filament to large amounts of gas. Then the tube is inserted into a programmable Lindberg® Blue furnace. A temperature ramp of your choice can be programmed into the furnace controller. A schematic of the setup is shown in Figure 3.15. The system is pumped on until base pressure of the system is reached. The temperature ramp program can begin once base pressure of the system has been reached. To match the ramping of the furnace, the needle valve is opened at timed increments and desorbed molecules allowed to pass through the RGA where it records the partial pressure

of the gasses in the system and atomic weight. The RGA has a resolution of ± 1 a.m.u..

After series of isotherm experiments the sample was transferred into a quartz tube using the glove box described in section 3.5.2. For samples that isotherm experiments were not performed the following procedure was followed. First, the quartz tube was corrected for dead space within the tube using He expansions into a calibrated volume. The quartz tube was then submerged into a liquid nitrogen dewar and the pyridine was then exposed to the surface by allowing an aliquot of gas to be introduced into a calibrated volume. The valve to the sample was opened the sample was exposed until the pressure equilibrated. Once equilibrated, the pressure is recorded and the liquid nitrogen is removed and the system is allowed to warm up to room temperature. The pressure of the system is recorded again when room temperature is reached and the pressure is equilibrated. The change in pressure of the system can be accounted for by the pyridine molecules which have adsorbed to the surface. This process is then repeated until the final pressure after exposure is constant.

### 3.7.5 Raman Experiments

Raman spectroscopy can provide information about the orientation of an adsorbed molecule relative to the surface. Orientation of the adsorbed molecules can be interrogated by observing changes in the polarizability of the molecule which would be evident by the shifting and splitting of peaks. The experimental setup for a raman measurement is similar to the TPD experiments described in section 3.7.4. After a series of isotherms were performed, the MgO sample is transferred to a quartz tube in a glove bag. In order to gain insight concerning the status of the molecular film the tube was mounted on the 'microstage' of a Dilor XY Raman spectrometer (Instruments S.A., Inc., Edison, NJ). A 514.5-nm line of a Coherent Innova 200 argon ion laser was used for excitation. The monochromator employed a 600 grooves/mm grating with 200 mm slits, giving a band-pass of 0.5 nm. This resulted in an excitation beam diameter of 1 mm at the sample under the focal and alignment conditions used. Raman spectra were acquired in the backscattering mode.

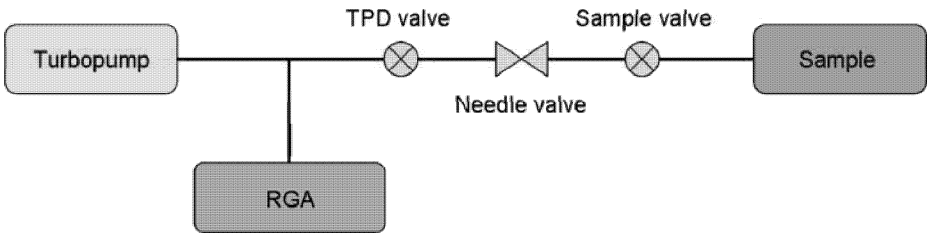


Figure 3.15: A programmable funace is used to heat the quartz tube which is evacuated by a turbomolecular pump with a quadrapole mass spectrometer attached inline.

# Chapter 4

# Thermodynamics

This chapter presents the results of thermodynamic investigations of alkane thin films on magnesium oxide and graphite. Using the experimental techniques described in chapter 3, a series of high-resolution volumetric adsorption isotherms over a large temperature interval were recorded for *n*-hexane, cyclohexane, and pyridine, on MgO and graphite. First the isotherms are corrected and normalized by calculating the dead space volume and determining the actual temperature using published (SVP) data. These corrections were challenging because published (SVP) data for some molecules in the temperature regimes of our measurements does not exist. This made it difficult to cross check the actual temperature of the sample with standard tables. These isotherms were analyzed using the procedure described in chapter 2, for example the number of moles adsorbed and chemical potentials are calculated using information outlined in section 2.7. Similarly, the two-dimensional compressibility, isosteric heat of adsorption can also be calculated and gives information on possible phase transitions and wetting properties can be extracted. From this data. A Clausius-Clapeyron plot can be constructed to obtain the enthalpy, entropy and isosteric heat values for each layer and also an overall picture of the layering properties of the system. Using this data, one can begin to assign a phase diagram.

Finally, in order to learn something about the relative concentrations and types of molecular species adsorbed the substrate as well as their relative binding energies to the surface. Temperature Programmed Desorption, (TPD), experiments were also performed on pyridine adsorbed on MgO.

## 4.1 *n*-Hexane on MgO

To determine the thermodynamic properties of *n*-hexane on MgO, a series of more than 50 isotherms were measured (using different MgO samples) in the temperature range of 196 K to 250 K. Periodically, methane isotherms were run on a sample to check if substrate quality degraded. Isotherm measurements were performed at temperatures above 196 K because at lower temperatures the SVP's were too small to be reliably recorded. resolution of the 16-bit A-to-D converter resulted in a step-wise distribution of data points at the lowest pressures.

*n*-Hexane adsorption on metal oxide surfaces has remained relatively unexplored, its behavior on magnesium oxide has only been examined by Kiselev and Avgul, (KA), who performed volumetric isotherms and by Tait who has studied the desorption kinetics of *n*-hexane on MgO [Tait et al., 2005]. KA found that *n*-hexane forms only one layer [Kiselev and Avgul, 1967] on MgO. Tait et. al. showed that desorption peaks at a temperature of —- K. More studies of *n*-hexane on graphite have been reported. Studies by Taub et. al., Wexler et. al. and Clarke and co-workers have concentrated on the multi-layering properties and melting mechanism of *n*-hexane on graphite both experimentally and theoretically [Hansen et al., 1992], [Roth and Wexler, 2005], [Clarke, 2001].

### 4.1.1 Adsorption Isotherms

*n*-Hexane displays incomplete wetting as defined by [Schick, 1990] over the temperature region scanned. This behavior is consistent with the other studies of linear chain alkanes (i.e. *n*-butane, *n*-pentane, and *n*-heptane on MgO [Arnold et al., 2006], [Cook and Larese,

2006], [Cañoto and Larese, 2007]) published recently. The lattice mismatch and the strength of the interaction between the MgO substrate and $n$-hexane does not promote layer-by-layer growth. A typical isotherm is shown in Figure 4.1, plotted as the number of moles adsorbed versus the difference in chemical potential. Where the difference in chemical potential difference, $(\mu - \mu_0)$, is expressed in units of Kelvin where $\mu - \mu_0 = (T \ln(P/P_0))/k_B$. Figure 4.2 displays an isotherm plotted as a function of reduced pressure versus the number of moles adsorbed and its corresponding numerical derivative. A few general remarks concerning the $n$-hexane isotherms are appropriate. First we find that upon increasing temperature layering transition changes location slightly moving towards higher relative pressures while gradually decreasing in height and broading. A typical isotherm below 248 K displays two distinct layering transitions followed by a slow asymptotic approach to the SVP. This behavior is in contrast to previous adsorption work done by KA which indicacted that $n$-hexane forms only one layer on MgO. This difference is mostly likely due to the difference in substrate quality and the purity of $n$-hexane used.

All isotherms were run above the $T_{triple}$ of $n$-hexane ($T_{triple}$=178 K). The $T_{fusion}$ of $n$-hexane is almost identical to the $T_{triple}$ value. The monolayer melting temperature was determined using neutron diffraction measurements and was found to be between 130-140 K. A comparison of the two-dimensional melting temperature, $T_{2D}$ versus the three-dimensional melting temperature $T_{2D}/\mathrm{T}_{3D}$ gives a value of 0.73 - 0.79 depending on the value used for $T_{2D}$. The proximity of $T_{triple}$ to $T_{fusion}$ suggests that hexane has a strong propensity to form the solid phase upon cooling. Despite this possibility several layering features were observed in the isotherm measurements performed.

Figure 4.3 nicely illustrates the behavior of the the first layer where a gradual decrease in the chemical potential takes place in adsorption as the temperature increased. The first derivative of the isotherms in this region shows a decrease in peak intensity and increase in width.

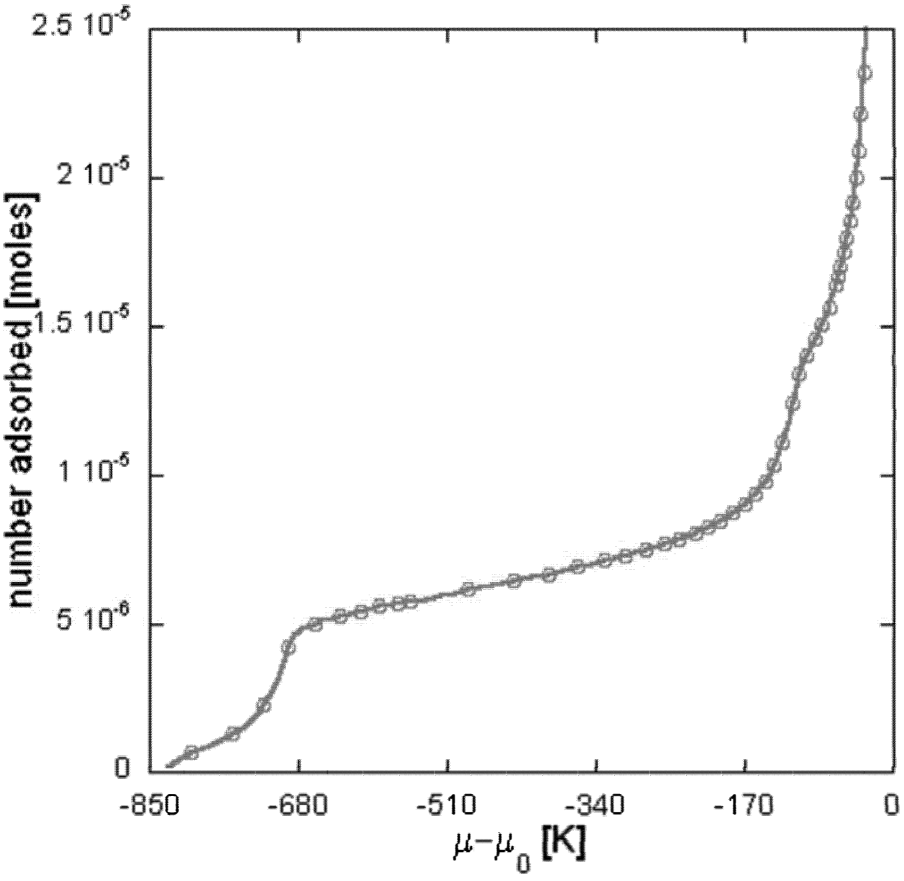


Figure 4.1: An example of a typical $n$-hexane on MgO isotherm plotted in the number of moles adsorbed (y-axis) versus chemical potential (x-axis).

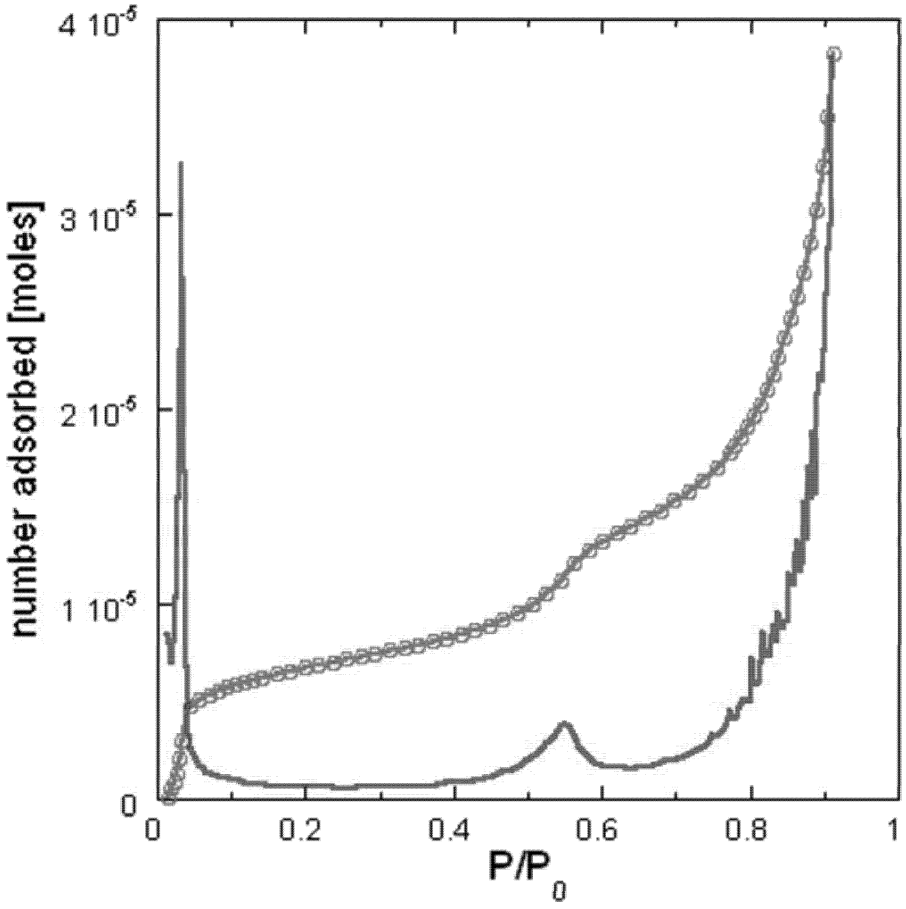


Figure 4.2: An *n*-hexane isotherm and its associated numerical derivative. To identify the layering transitions in the isotherm data (blue), the numerical derivative (red) of each isotherm can be calculated.

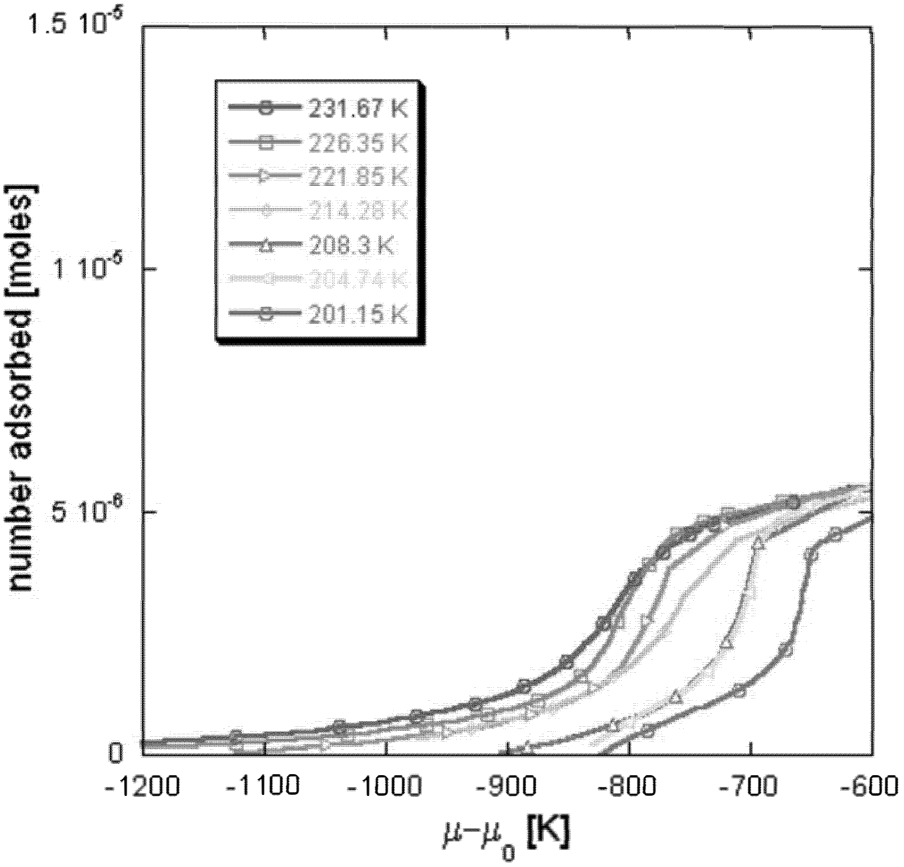


Figure 4.3: A subset of isotherms of *n*-hexane on MgO. This plot illustrates the change of the first layering transition as a function of temperature.

### 4.1.2 Monolayer Capacity

The monolayer capacity of *n*-hexane on MgO is determined by using the procedure outlined in section 3.7.3. By combining a methane and hexane isothermon the same sample the monolayer capacity of *n*-hexane can be calculated using the Area Per Molecule (APM) of methane on MgO (100) (determined from neutron diffraction experiments [Larese et al., 1991]).

Figure 4.4 shows a comparison the relative monolayer capacities of methane and *n*-hexane at 196 K. Using the point-B method, an APM of *n*-hexane on MgO of $\sim 87$ Å$^2$ was found. Naturally, this value is temperature dependent due to thermal motion of the molecules on the surface which could increase or decrease this value. This number lies within the expected APM values of *n*-butane [Arnold et al., 2005] and *n*-pentane [Cook and Larese, 2006] and *n*-heptane [Cañoto and Larese, 2007].

### 4.1.3 Clausius-Clapeyron Thermodynamic Data

Following the procedure in section 2.7.4, a form of the Clausius-Clapeyron equation is used to determine the layering behavior of *n*-hexane. Figure 4.5 shows a plot of the pressure locations of the adsorption steps as a function of inverse temperature in *n*-hexane. The uppermost line in the plot uses the location uses the SVP which can be taken as the bulk coexistence point for the isotherm. The lines below the SVP track the second and first layer behavior is displayed from the top.

This plot can yield some additional insight to the film layering properties. For example, the disappearance of the second layer is not typical. A step usually approaches the SVP asymptotically before reaching the region of bulk behavior before merging with the coexistence line. In the present case this transition stops abruptly at 248 K (never converging to the

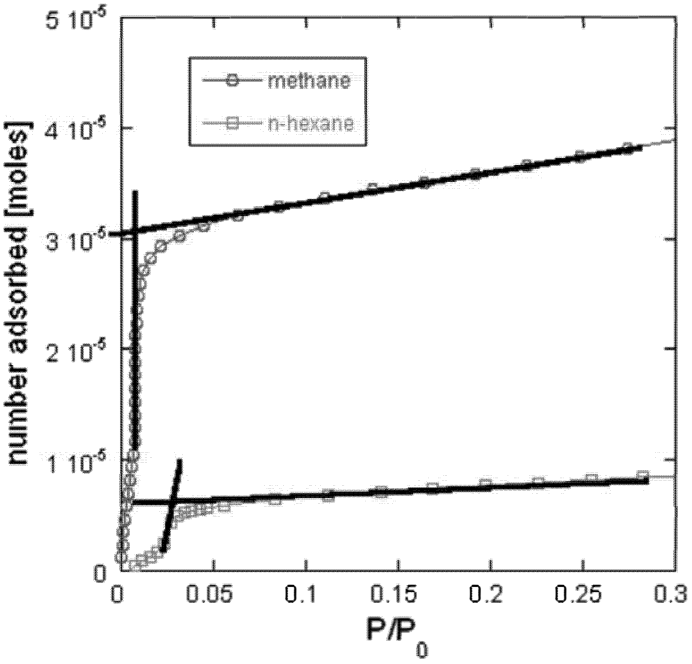


Figure 4.4: Comparison of monolayer methane and $n$-hexane adsorption on MgO at 77 K and 196 K respectively. To calculate the approximate surface area occupied per molecule of $n$-hexane, the methane isotherm on the same sample was used. Previous neutron diffraction data of methane on MgO indicates that the surface area per molecule of methane is 17.74 Å$^2$ [Larese, 1998]. Using this value, a ratio between monolayer capacities can be used to calculate the (APM) which is determined to be $\sim$ 87 Å$^2$.

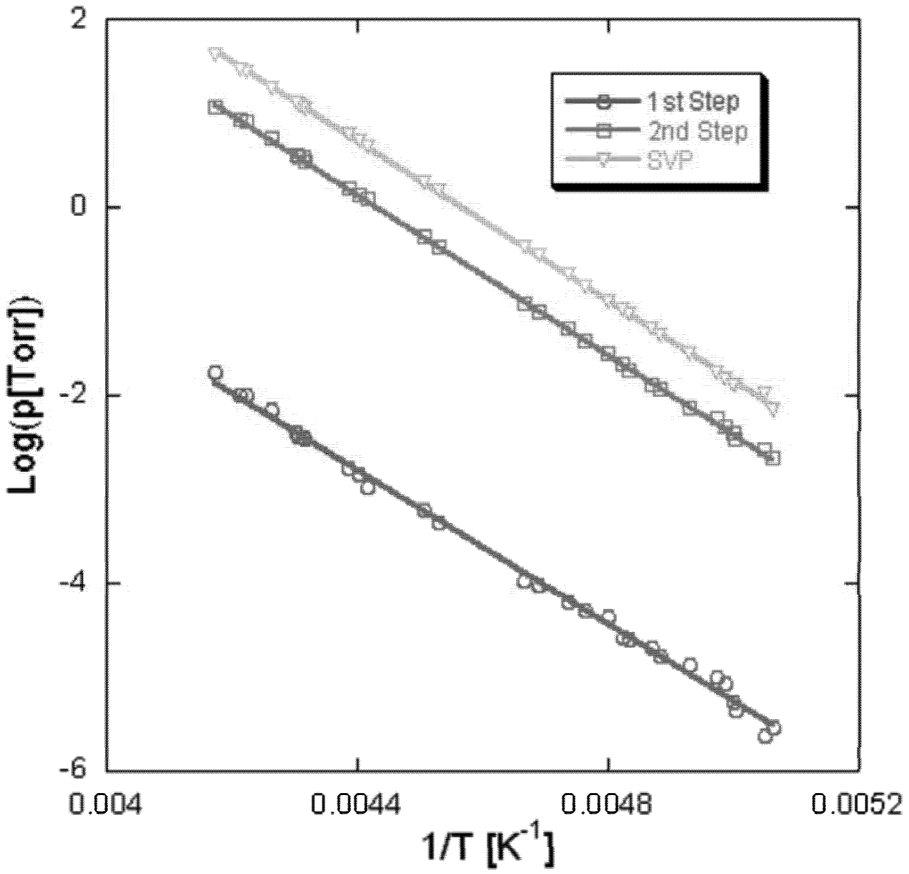


Figure 4.5: Clausius-Clapeyron plot of $n$-hexane on MgO $K_{2D}$ peaks. The locations of the compressibility peaks versus $1/T$, a Clausius-Clapeyron plot can be produced. The figure illustrates how the locations of adsorption steps are plotted useful in constructing a phase diagram for the system.

Table 4.1: Thermodynamic values calculated from Clausius-Clapeyron plot of $n$-hexane on MgO. Using a linear fit to the compressibility peak data, one can calculate the $A^{(n)}$ (slope), and $B^{(n)}$ (y-intercept) values of each layering transition. Using the calculated $A$ and $B$ values, equations 2.106, 2.107, and 2.108 can be calculated for each layer.

| Layer | $A^{(n)}$ | $B^{(n)}$ | Q(kJ/mol) | $\Delta H$ (J/mol) | $\Delta S$ (J/K $\cdot$ mol) |
|---|---|---|---|---|---|
| 1 | 4356.90 | 16.364 | 36.22 | -1.92 | 20.79 |
| 2 | 4192.40 | 18.594 | 34.86 | -0.55 | 2.25 |
| $\infty$ | 4126.50 | 18.865 | 34.31 | – | – |

SVP). Table 4.1 summarizes the calculated thermodynamic quantities from the, $A^{(n)}$(slope), and $B^{(n)}$, (y-intercept) values of the n layers.

### 4.1.4 Two-Dimensional Compressibility, $K_{2D}$

Using equation (2.115) the two-dimensional compressibility can be calculated. This measures the response of the $n$-hexane film to a change in the spreading pressure. Figure 4.6 shows that the compressibility of $n$-hexane exhibits two peaks as a result of its dependence on the derivative of the isotherm which displays similar behavior. The compressibility peak corresponding to the first layer is of higher intensity than the one associated with the second layer throughout the set of isotherms. Hence, the average bilayer compressibility peak is about a factor of 6 smaller than the mean monolayer value. This is most likely due to a decrease in the adsorbate-substrate interaction with increasing film thickness. This suggests that the substrates contribution to film stability decreases as subsequent layers are added. The set of isotherms show an overall trend of decreasing compressibility peak height in both layers as temperature increases.

By plotting the Full-Width-Half-Maximum (FWHM) of the two-dimensional compressibility, ($K_{2D}$), as a function of temperature one can identify regions where a change in the FWHM of the layering transitions take place. If the changes in the FWHM are sudden, it signal the existance of a possible phase transition. Figure 4.7 displays how the temperature dependence of the $K_{2D}$ changes slope near 230 K and 238 K for the first and second layers

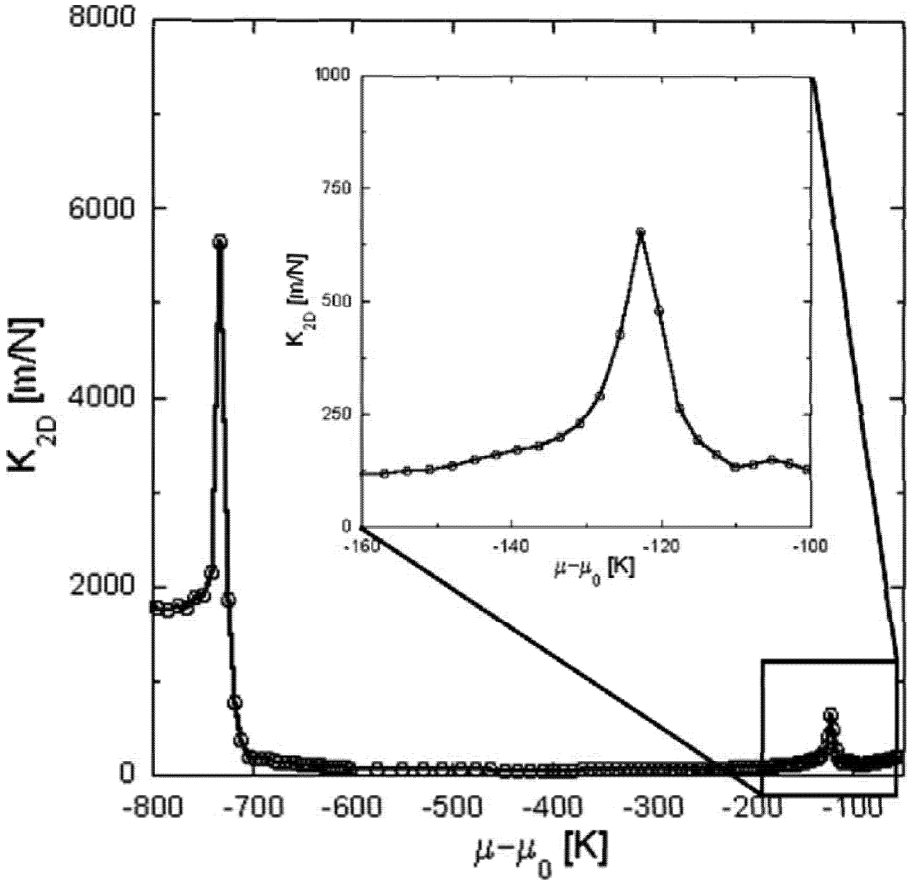


Figure 4.6: A representative two-dimensional compressibility peak of a $n$-hexane on MgO isotherm taken at 201.7 K. Two distinct layering transitions can be seen for all isotherms up to 248 K. The change in the peak shape can give information of possible phases the surface film has adopted.

respectively. The magnitude of FWHM values change by a factor of 7 and 10 for the first and second layers respectively.

While there is a steady increase in the values of the FWHM before the 'transition' temperatures for both layers below the abrupt change in slope, this is behavior that differs from previous studies conducted by our group on smaller members of the linear alkane series. Previous studies show no statistically significant change in their FWHM values until the 'transition' temperature is reached. This may be the result of the difficulty in calculating the FWHM values from the compressibility peaks because the $K_{2D}$ peaks ride on a background which makes them difficult to extract. The procedure used to extract the FWHM of the $K_{2D}$ peaks was to first use a polynomial to subtract off the underlying background and then fitting the remaining peak with a gaussian. Figure 4.8 shows a typical example of this gaussian fitting procedure.

As noted in chapter 2, Larher developed a simple procedure for using the compressibility data to identify the transition temperature the critical exponent $\beta$. Using the data extract we find this analysis yields a value of $\beta = 0.159$ with a rather large error of ($\pm$ 0.050). The large error in the calculation is due to shortage of data in the temperature interval at the intersection of the two linear regimes.

### 4.1.5 Isosteric Heat of Adsorption, $Q_{st}$

Another thermodynamic quantity that can be extracted from adsorption isotherms is the isosteric heat of adsorption (its physical meaning and derivation can be found in section 2.7.7). A typical isosteric heat of $n$-hexane on MgO is shown in Figure 4.9. Large peaks in the heat of adsorption are readily observable for the first and second layers. This observation confirms the fact that as the molecular film condenses at the interface and the number of molecules on the surface increases it becomes increasingly more difficult to bring a molecule into the solid film, especially once the entire surface is covered by the film (i.e., a complete layer forms). In the neighborhood of layer completion, as molecules are added,

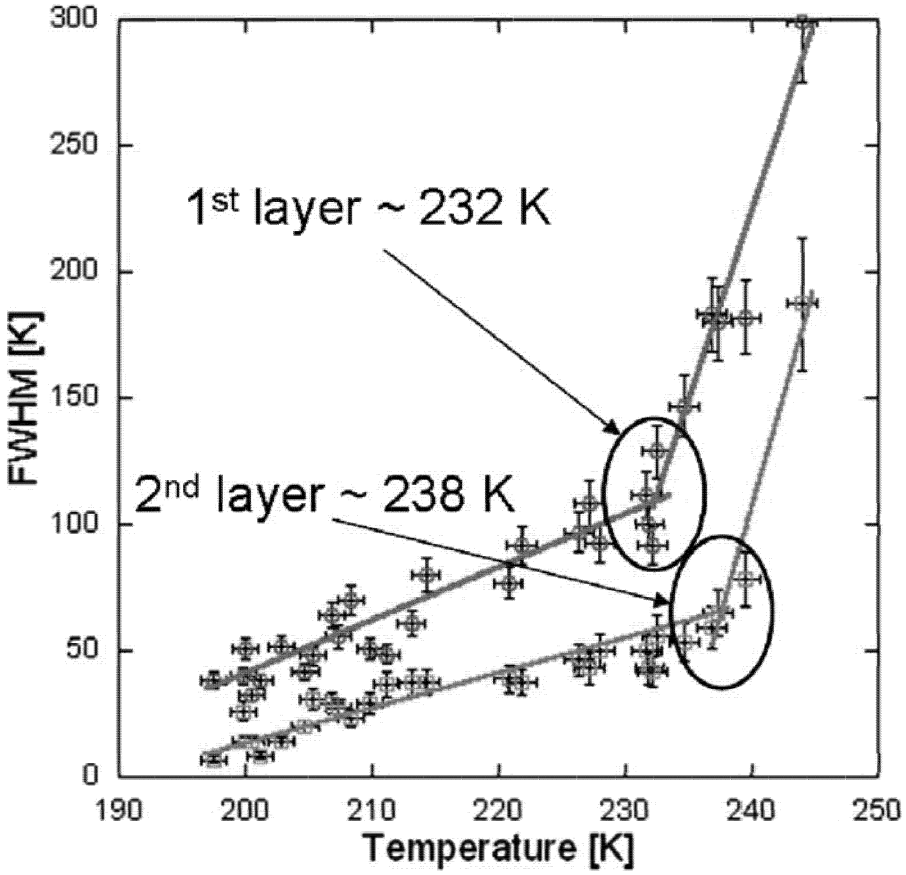


Figure 4.7: A plot of the FWHM values of $n$-hexane on MgO $K_{2D}$ peaks. For each layering transition there is an abrupt change in the FWHM values which could indicate a possible phase transition.

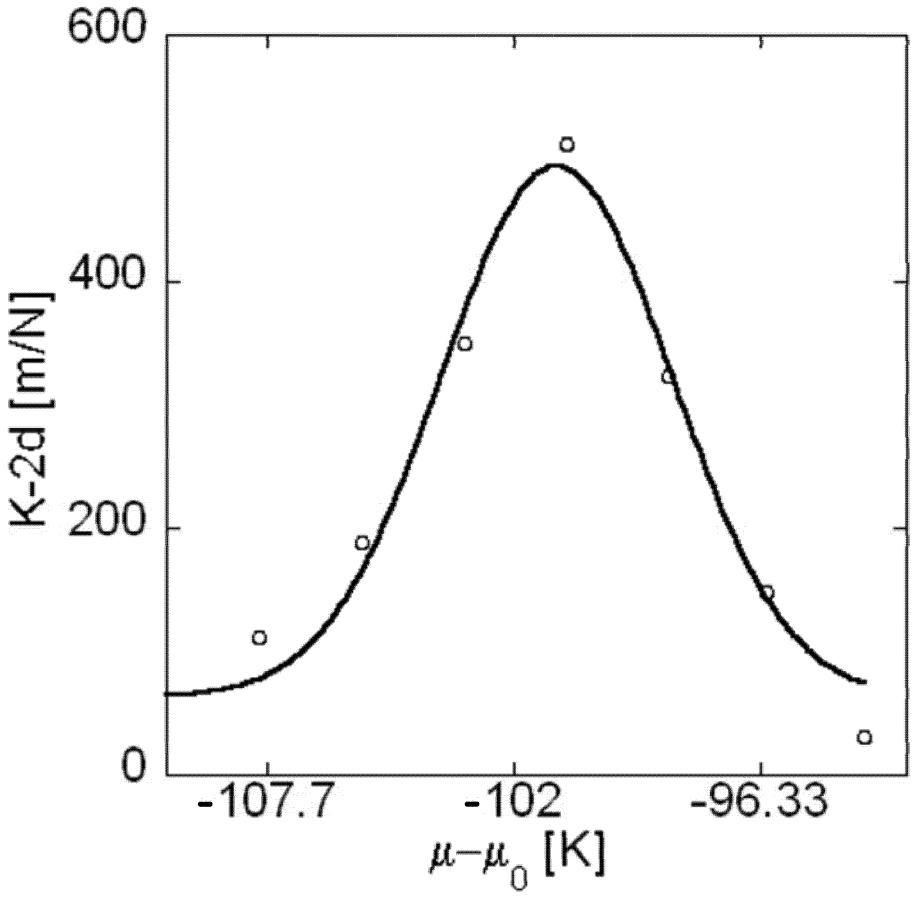


Figure 4.8: Typical gaussian fit to the compressibility peaks. To properly calculate the FWHM of the compressibility peaks the background of each plot was subtracted with a polynomial and the residual peaks were then fit with a gaussian. An example fit to a second layer compressibility peak.

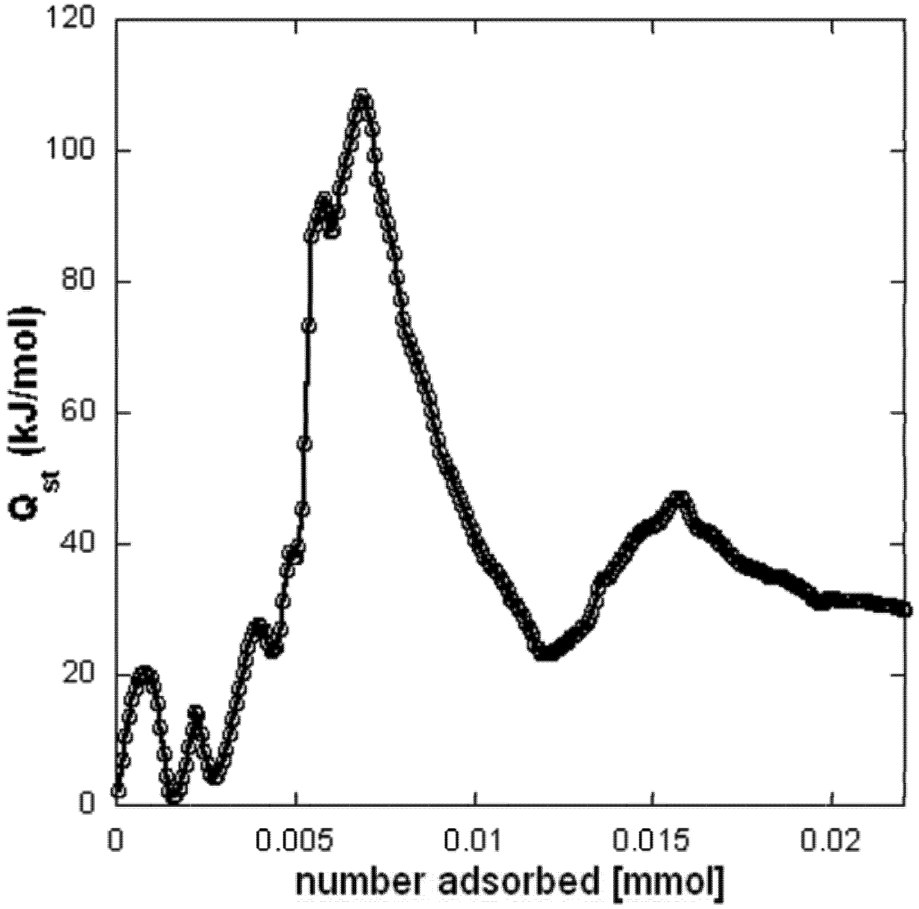


Figure 4.9: $Q_{st}$ of $n$-hexane on MgO. As the number of molecules on the surface increases it becomes increasingly more difficult to bring a molecule into the solid film, especially once the solid covers the entire surface. At increasing coverage, the values of $Q_{st}$ appear to be converging to the enthalpy of adsorption of bulk hexane (31.7 kJ/mol) [http://webbook.nist.gov, 2006].

some compression of the layer(s) closest to the interface can take place. Furthermore, depending on the precise location in the phase diagram, a fraction of the added molecules will begin to occupy the layer(s) further away from the substrate. This behavior of $Q_{st}$ during the layering process can be repeated numerous times; however, the variation of $Q_{st}$ with film thickness will depend on the details of the film growth mechanism. At increasing coverage, the values of $Q_{st}$ appear to converge to the bulk enthalpy of vaporization of *n*-hexane (31.7 kJ/mol) [http://webbook.nist.gov, 2006]. Although all plots of the isosteric heat show the same peaks at the layering transitions, the approximation of the partial derivative with $\Delta \ln P/\Delta T$ still has a dependence on temperature even with an increment of $< 1$ K.

### 4.1.6 Two-Dimensional Phase Diagram

By combining the data from Figures 4.4, 4.5, 4.7, and 4.9, a two dimensional diagram can be constructed as a function of temperature and coverage. Figure 4.10 shows the phase diagram constructed for the two-dimensional film of *n*-hexane. Neutron diffraction and inelastic scattering data has been used to locate the melting of the solid *n*-hexane monolayer. Both measurements suggest a temperature of 130-140 K [Arnold et al., 2006]. The neutron measurements indicate the melting of the solid phase and the onset of the liquid phase signalled by the loss of long-range order (i.e. the broadening of the diffraction peaks and the loss of the elastic line intensity in INS measurements at the onset of the dynamics). Isotherm measurements begin at a temperature of 195 K which is above $T_{triple-3D}$ and $T_{fus-3D}$ of 178 K. *n*-Hexane isotherms pass a low-density dilute gas phase at nominal coverages below $\theta \sim 0.2$ and low temperatures. The more vertical portion of the monolayer region then passes through a liquid-vapor coexistence region. In this region layering is in the form of a 2D liquid. Liquid-like behavior in the volumetric isotherm measurements can be observed by the onset of a more rounded step near monolayer completion. Passage through a liquid-vapor phase is observed until the first layer critical temperature ($T_{c-2D}$) is reached at 232 K. At temperatures above 232 K, the sub-monolayer region passes through a hyper-critical

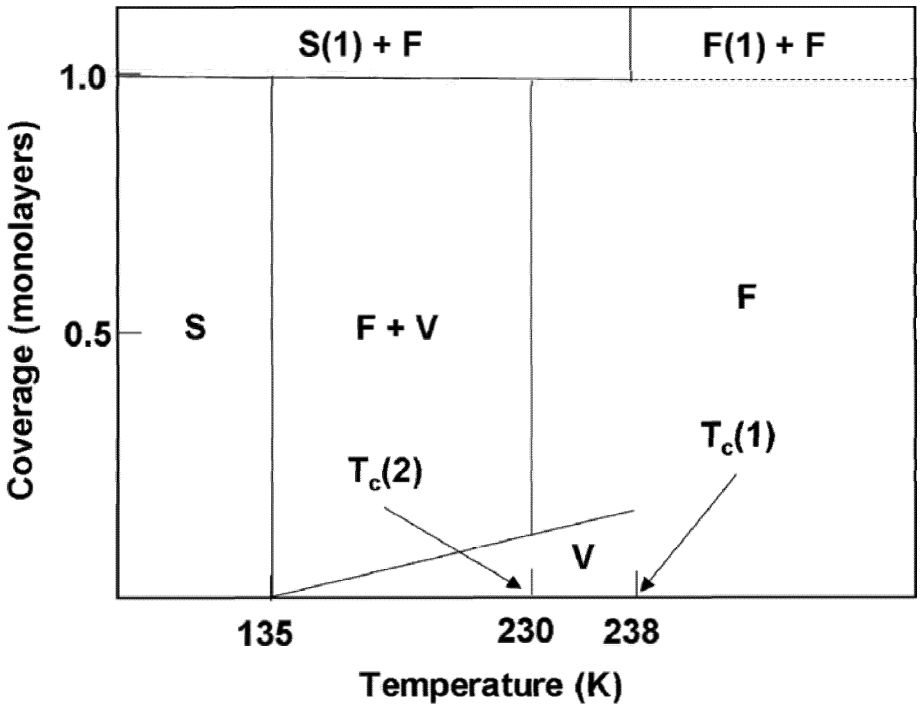


Figure 4.10: Two-dimensional phase diagram of *n*-hexane on MgO. Dotted lines indicate the possible locations of a phase transition.

fluid-vapor phase where layering is no longer discrete, and occurs in a continuous fashion. The onset of this behavior is observed by the drastic increase of the FWHM values of the compressibility peaks and by a ramping feature observed in the isotherm measurements.

Near the second layer, a similar process occurs as in the first layer where at low temperatures near the bulk triple point the isotherm is just slightly above $T_{triple-2D}$ where you pass through a liquid-vapor coexistence region. At temperatures above $T_{c-2D}(2)$, the second layer disappears and is replaced by a steady ramping upwards towards bulk coexistence. This is indicative of the formation of a solid-liquid coexistence or a 2D hypercritical fluid in the second layer.

## 4.2 *n*-Hexane on Graphite

Surprisingly few isotherms are available in the literature that detail the adsorption properties of hexane on graphite. To rectify this shortcoming a series of more than 20 isotherms were conducted on graphite. The lower limit of the isotherms measurements for hexane on graphite were extended to lower temperatures than those conducted on MgO due to the development of an improved program which extends the range of the pressure transducer. The effective resolution of the pressure transducer has been enhanced by a factor of 10. This enhancement allowed for the study of isotherms at SVP values of under 0.01 torr.

### 4.2.1 Isotherms

*n*-Hexane on graphite adsorption measurements showed a change from three layers at low temperatures (see Figure 4.11) to two steps at intermediate temperatures (208 - 280 K), and only one step above 280 K. Contrast this behavior to isotherm data of *n*-hexane on MgO which shows two steps at temperatures up to 248 K.

The following passage describes the general behavior of hexane on graphite adsorption studies. At low temperatures the isotherms display a short linear region followed by an

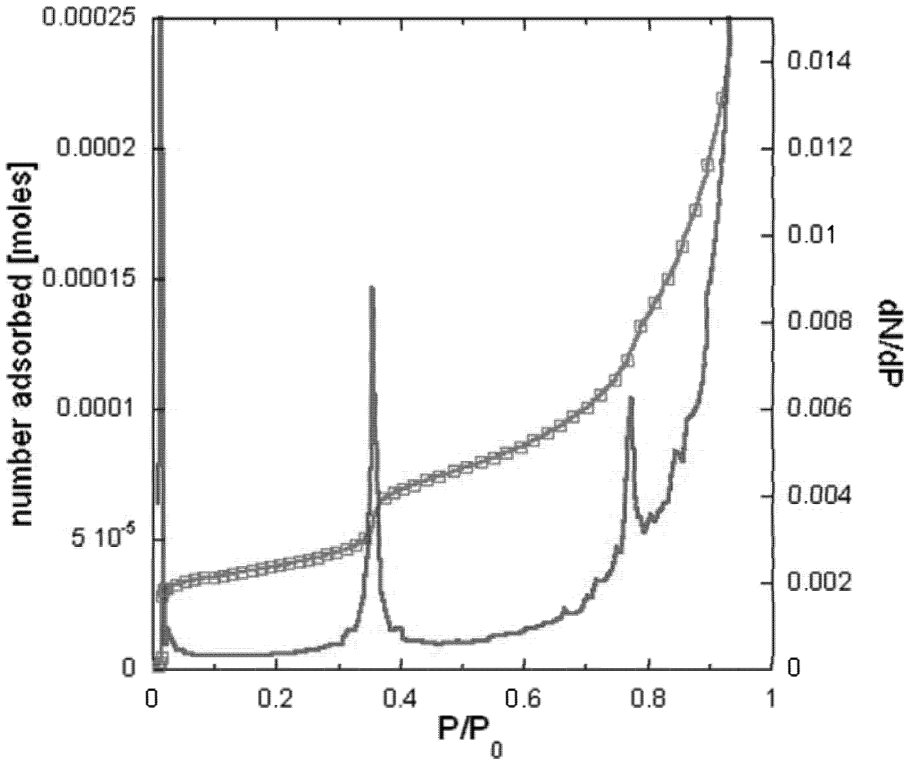


Figure 4.11: A typical isotherm of *n*-hexane on graphite at temperatures below 203 K. The isotherm (blue) shows three distinct layering transitions.

abrupt vertical rise. As the temperature is increased, the low coverage linear portion persists to higher relative pressures. The approach to the vertical portion is more gradual. Near monolayer completion the adsorption curve gradually turns over gradually transforming to a more rounded curve than those at low temperatures. The second layer behavior on graphite behaves in a manner similar to the behavior on MgO where the location of the steps moves towards higher relative pressures as the temperature increases. The third layer behavior moves into the saturated vapor pressure gradually converging with the SVP at 210 K. The location of the third layer adsorption features relative to the second layer one is that they are is much further up in relative pressure when compared to the second and are not evenly spaced. The gradual asymptotic approach to the SVP is similar to what is found with *n*-hexane on MgO. The appearance of three distinct layers and higher temperatures at which the multi-layer adsorption of molecules persists indicates a much stronger interaction with the graphite surface than with MgO. This probably reflects the better match of the *n*-hexane molecule with the potential energy surface of the graphite basal plane.

Previous studies by Taub et. al. have shown the $T_{2D}$ to be around 170 K using quasi-elastic neutron scattering experiments and 151 K using LEED measurements. Simulations by Clarke et. al. and Taub et. al. have calculated the $T_{2D}$ to be 195 K and 221 K respectively [Krishnan et al., 2003], [Herwig et al., 1997], [Hansen et al., 1992]. Using these values give $T_{2D}/T_{3D}$ values of 0.95 and 0.86 for the quasi-elastic neutron scattering measurements and LEED measurements respectively and 1.1 and 1.24 for the simulation values respectively.

### 4.2.2 Monolayer Capacity

A comparison of a *n*-hexane on graphite isotherm can be made with a methane on graphite isotherm. The surface structure of a methane on graphite is also well known (see section 3.7.3). Using a methane and *n*-hexane isotherm on the same graphite sample the monolayer capacity and relative APM of *n*-hexane can be determined. Figure 4.12 shows a comparison

Table 4.2: Thermodynamic values calculated from Clausius-Clapeyron plot of $n$-hexane on graphite. Using a linear fit to the compressibility peak data, one can calculate $A^{(n)}$ (slope) and $B^{(n)}$ (y-intercept) values of each layering transition. Using the calculated $A$ and $B$ values, equations 2.106, 2.107, and 2.108 can be calculated for each layer.

| Layer | $A^{(n)}$ | $B^{(n)}$ | Q (kJ/mol) | $\Delta H$ (J/mol) | $\Delta S$ (J/K $\cdot$ mol) |
|---|---|---|---|---|---|
| 1 | – | – | – | – | – |
| 2 | 4340.4 | 18.725 | 36.09 | -0.88 | 4.41 |
| 3 | 4192.40 | 21.841 | 39.74 | -4.53 | -21.50 |
| $\infty$ | 4234.9 | 19.255 | 35.21 | – | – |

of a methane and $n$-hexane isotherms at 77 and 196 K respectively. The ratio of monolayer capacities gives an APM value of 70 Å$^2$. This APM value is less than the value found on MgO (100). This may be attributed to either a dependence on temperature of the APM or that the surface structure allows for packing of molecules on the surface. Previous work by Arnold et. al. calculated a value of 83 Å$^2$.

### 4.2.3 Clausius-Clapeyron Thermodynamic Data

Following the same procedure described previously, the location of the compressibility peaks were used for a Clausius-Clapeyron analysis can be constructed. Figure 4.13 shows the hexane on graphite C-C plot. The points at which the lines intersect indicate the temperatures at which a layering transition 'merge' into another layer. The plot shows that the third layer gradually disappears merging with the SVP line as the temperature increases. The second layer shows no such tendency to merge with the SVP and disappears at 280 K where the layer disappears and hence the liquid interface is rather diffuse and adsorption takes place in multiple layers simultaneously. Table 4.2 shows the thermodynamic values extracted from the Clausius-Clapeyron plot.

The values obtained from the Clausius-Clapeyron data are difficult to interpret because of the low pressures that are present for the first layer. The second and third layers show an overall reduction in entropy, enthalpy, and isosteric heats towards the published bulk

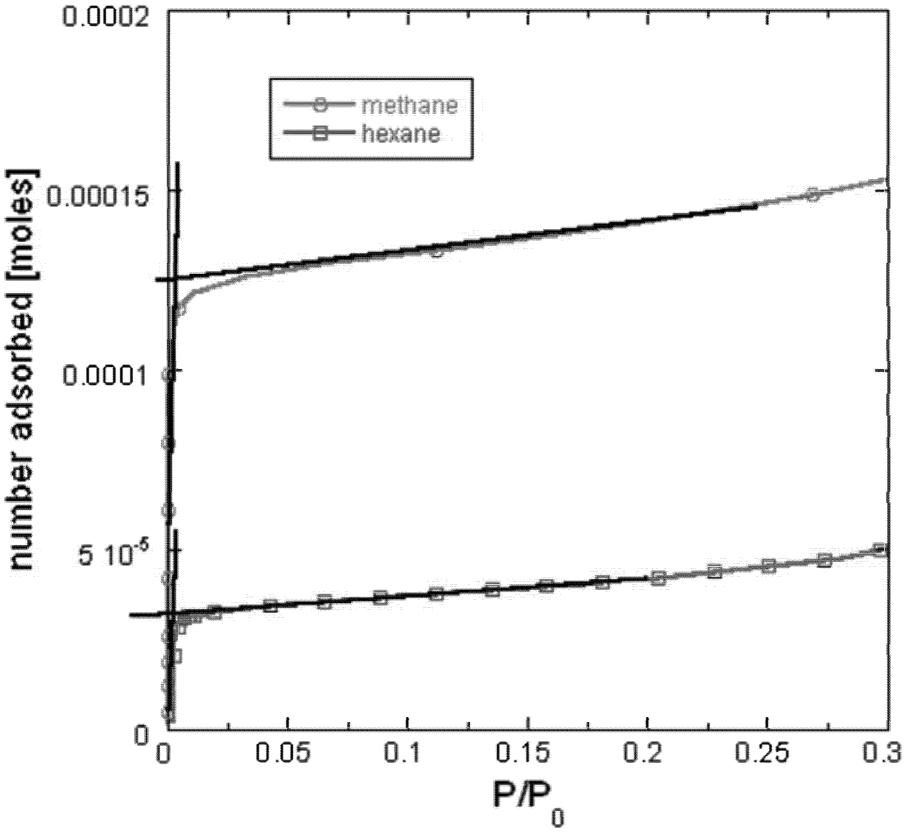


Figure 4.12: A comparison of a methane and $n$-hexane isotherms run successively on the same sample. An APM of $\sim$ 70 Å$^2$ was calculated using the ratio of monolayer capacities.

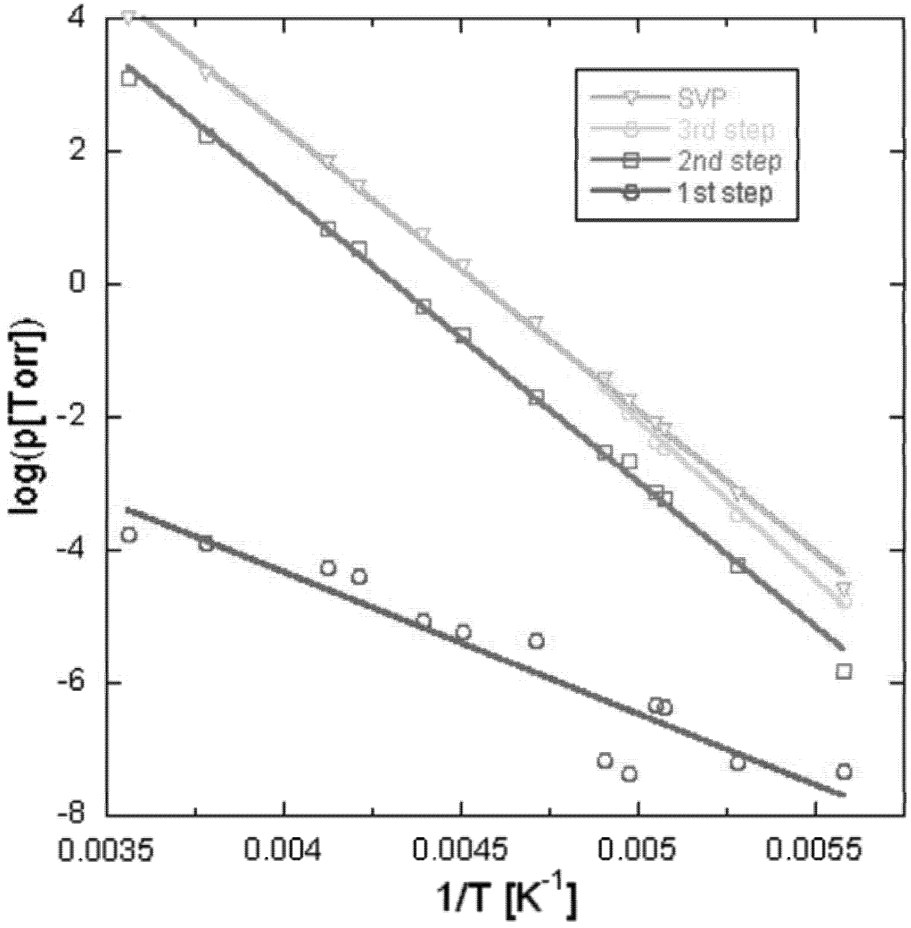


Figure 4.13: Plotting the locations of the $n$-hexane on graphite compressibility peaks versus $1/T$ a Clausius-Clapeyron plot can be produced. The Clausius-Clapeyron plot illustrates locations of layering transitions and is useful in constructing phase diagrams for the system.

values even though the data is not of exceptional quality. The progression of peak locations exhibit a prograssion that is similar to those recorded for methyl chloride films adsorbed on MgO and present significant difficulties extracting differential thermodynamic data from the plot [Sprung and Larese, 2000].

### 4.2.4 Two-Dimensional Compressibility, $K_{2D}$

In examining the series of isotherms on graphite, one can see a gradual reduction in intensity in the corresponding compressibilities as temperature is raised for all layers (see Figure 4.14). The relative intensities of the successive layers are weaker as the number of layers is increased. This reduction of intensity as layering is increased is due to the reduced amount of work needed to place another molecule on the surface as the isotherm reaches the bulk coexistence. It becomes far more favorable at $T < T_{melt}$ to form bulk crystals than an adsorbed phase. At these chemical potentials, the lattice mismatch of the surface lattice becomes too strained to allow for more adsorbate molecules to adopt that surface structure. This is caused by the weak A-S interaction and dominant A-A interaction energy which favors the formation of bulk crystals.

Once again plots of the FWHM of the compressibility peaks identifies temperature regimes of possible phase transitions. Broadening of the compressibility peaks is caused by the transition to a liquid-like structure as noted in section 2.7.6. Figure 4.15 shows the plot of the FWHM values of the compressibility peaks and inflection points for each layer. Values of the FWHM for the first layer were not included because of the the vertical nature of the first layer. The numerical derivatives were not able to be determined because many of the pressure readings are close to the resolution limit of the pressure transducer. This situation exists even with the use of the improved pressure resolving program. Transitions for the second and third layers both occur at $\sim 198$ K.

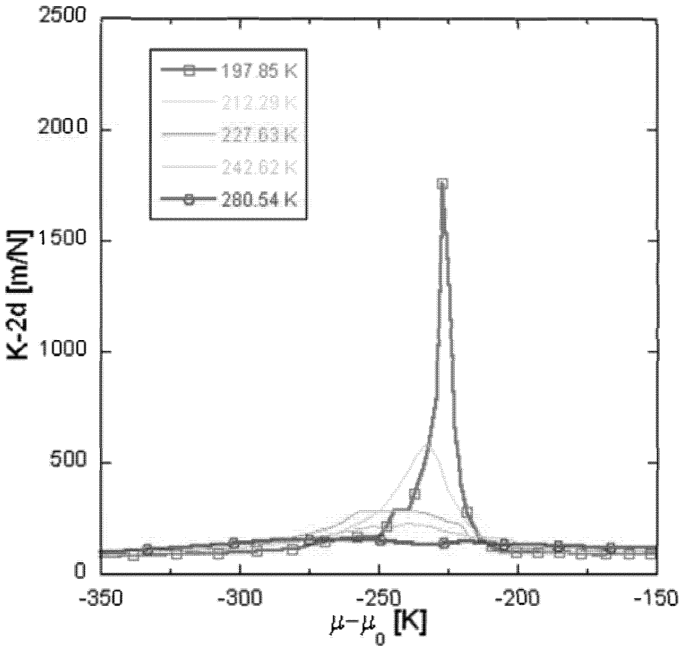


(a)

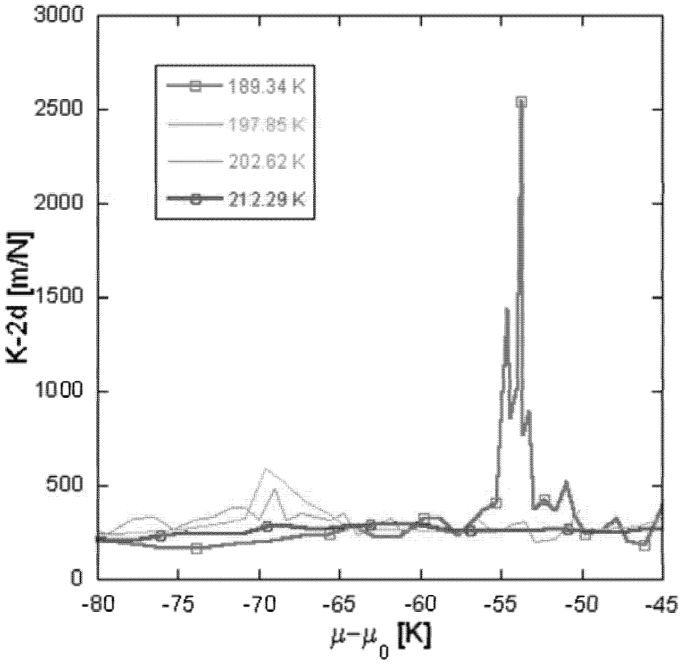


(b)

Figure 4.14: $K_{2D}$ peaks of the second and third layering transitions of $n$-hexane on graphite. Both layering transitions show a simultaneous decrease in intensity and broadening. (a) second layer (b) third layer.

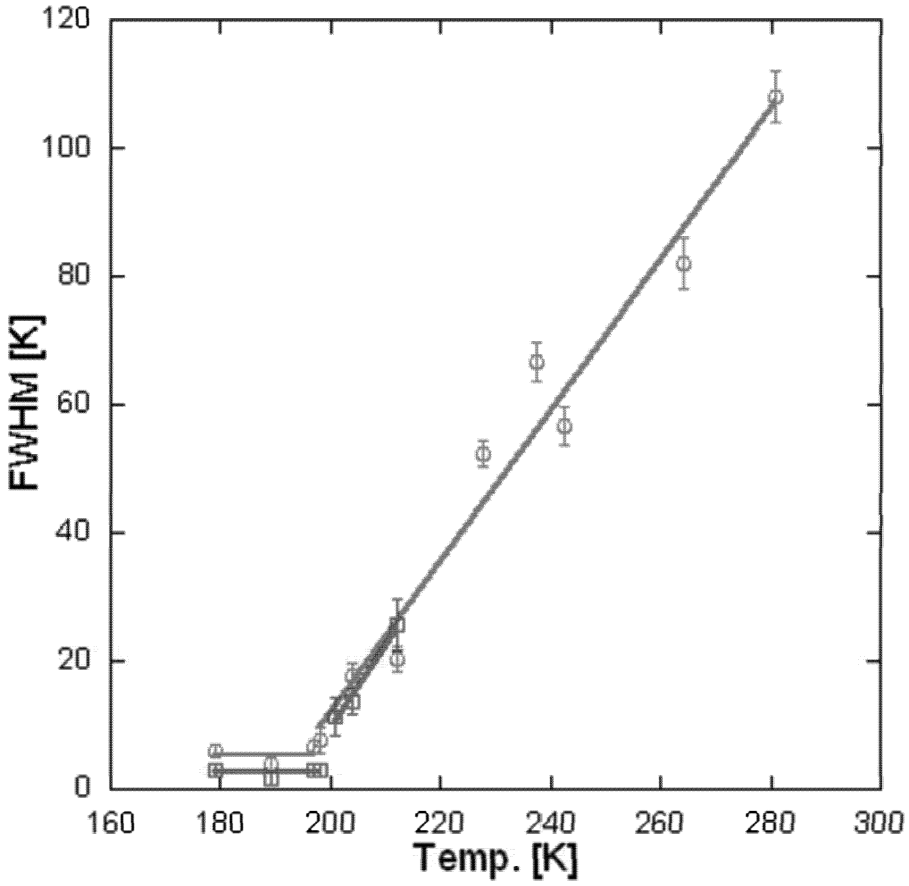


Figure 4.15: A plot of the FWHM values of $n$-hexane on graphite $K_{2D}$ peaks. The intersections where FWHM values change abruptly are locations of possible layer phase transitions due to the crossing over critical points of each respective layer, $T_c(n)$. Critical points are located at $\sim$ 198 K for the second layer (blue), and third layer (red).

### 4.2.5 Isosteric Heat of Adsorption, $Q_{st}$

Figure 4.16 displays a typical isosteric heat for hexane on graphite and illustrates the characteristic behavior increasing in value near the completion of a layer, the gradual reduction in value with increased film thickness, and convergence towards the bulk enthalpy of vaporization. The profile of the first isosteric heat peak of *n*-hexane on graphite is remarkably symmetric which most likely signals a greater A-S interaction between the hexane film and graphite. Thus the amount of work need to place a molecule on the surface increases dramatically as the surface coverage heads towards monolayer completion because there is likely less mobility of the adsorbed molecules because of the increased surface density and the preference to stay closer to the surface. After the completed monolayer, the isosteric heat drops dramatically because of the second layer adsorption sites becoming available. As coverage is increased towards second layer completion, an increase in the isosteric heat is observed that is significantly lower because the layer that forms on top of the first layer has weaker interaction with the substrate and thus greater rotational and translational freedom. Molecules in the second layer are further from the surface whuch can adsorb with less work.

### 4.2.6 Two-Dimensional Phase Diagram

Figure 4.17 illustrates the proposed phase diagram derived from volumetric isotherm measurements. The behavior up to monolayer coverage of *n*-hexane on graphite is much different than that on MgO. At sub-monolayer coverage near the bulk triple point temperature ($T_{triple}$), the isotherm has only a very short linear region which abruptly stops then begins a vertical step region where the relative pressure only changes negligibly. This corresponds to an adsorption path that passes through the liquid-vapor coexistence region at low coverage. This should be due to the interaction energy between the graphite basal plane adsorption sites and the adsorbate molecule. As temperature is raised, there is an increase in the linear region at low-coverage and concomitant decrease in the slope of the vertical region which indicates a path that traverses a greater region in the vapor phase and a growing liquid phase. The second layer behaves similar to the second layer on MgO. The second layer

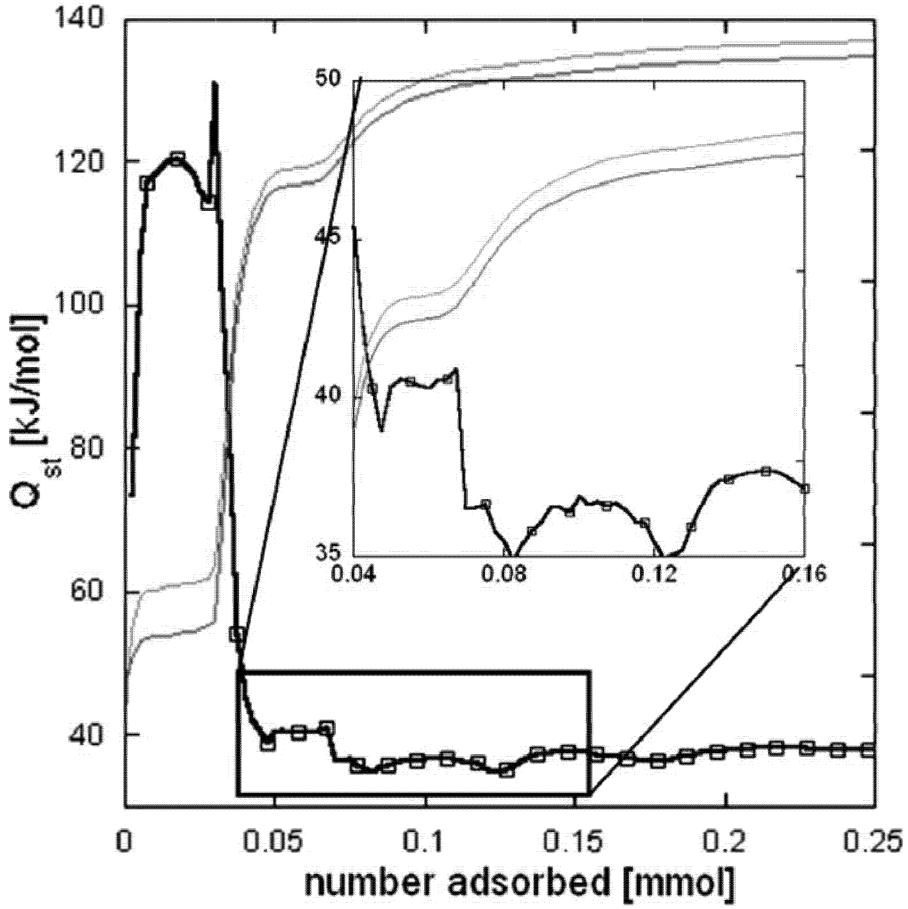


Figure 4.16: $Q_{st}$ of $n$-hexane on graphite at 232 K. The corresponding isotherms used to make the isosteric heat measurement are shown in red and blue.

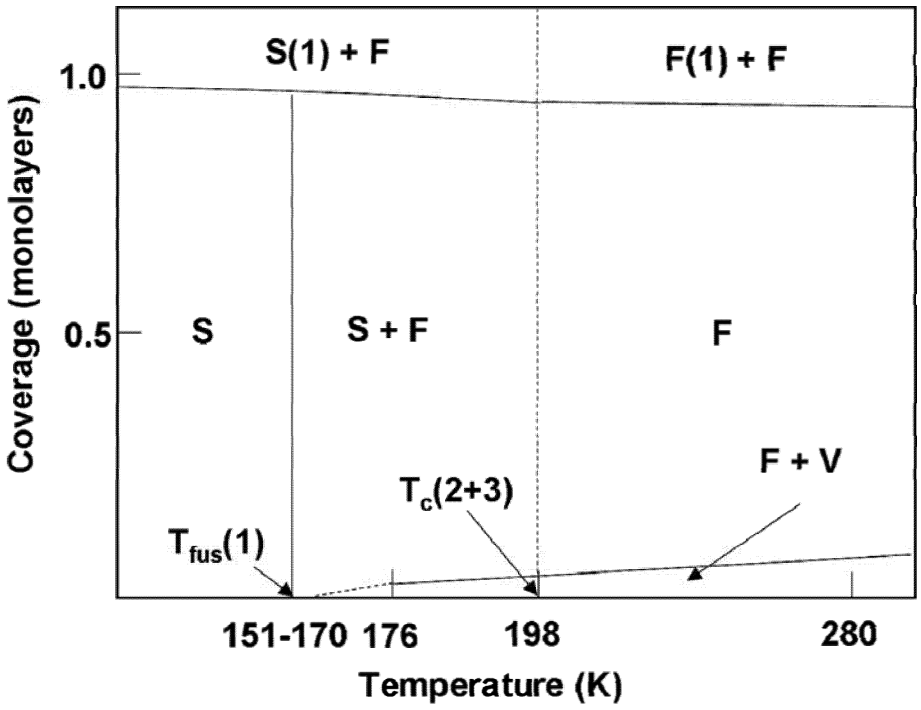


Figure 4.17: Two-dimensional phase diagram of *n*-hexane on graphite. Dotted lines indicate the possible location of a phase transition.

forms a liquid-vapor at low temperatures and as temperature is increased this high density fluid gradually transforms to a 2D hypercritical fluid which exhibits continuous layering up to the SVP.The presence of more rounded transitions is indicative of a transition through a liquid-vapor region of the phase diagram [Phillips and Larese, 1997]. This behavior of the second layering transition is similar to hexane on MgO where the formation of a 2D hypercritical fluid disallows condensation at the growth front and only a ramping of the isotherm can be seen.

## 4.3 Cyclohexane on MgO

A series of more than 25 isotherms were performed in the temperature range of 186 K to 279 K. As usual, the lower temperature limit of this set of isotherms was set by the pressure resolution of the pressure gauge.

Previous studies on cyclohexane adsorption have concentrated on its adsorption properties on graphite, metal surfaces and porous media such as MCM-48 [Hartmann and Biscof, ] and zeolites [Vitale et al., 1997]. These studies concentrated more on the chemisorption properties of cyclohexane on the more chemically active surfaces and the catalytic properties exhibited by the materials in the dehydrogenation of cyclohexane to benzene and hydrogen [MacPherson and Leung, 1996]. None of these studies reported any information on multi-layered adsorption phenomena in their publications.

### 4.3.1 Isotherms

A subset of cyclohexane on MgO isotherms are shown in Figure 4.18. Cyclohexane on MgO exhibits a transition from incomplete wetting behavior at higher temperatures (similar to linear alkanes) and a gradual transition to non-wetting behavior at lower temperatures. This is clearly observed as the isotherms change from an asymptotic approach to the SVP at high temperatures where the pressure at lower temperatures abruptly saturates at SVP.

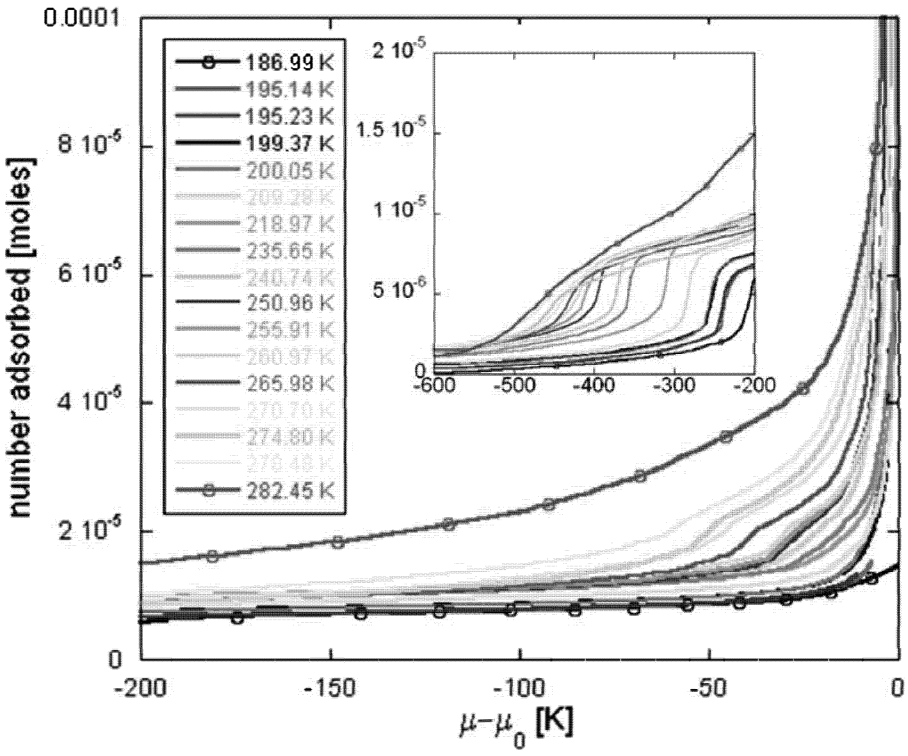


Figure 4.18: A subset of cyclohexane on MgO isotherms illustrating the evolution from one step at high temperatures to two at intermediate temperatures and one step at low temperatures.

Several adsorption steps and wetting behaviors can be observed in the set of isotherms. At low temperatures the isotherms show one step (see in Figure 4.19). As the temperature is increased, a second step gradually appears beginning at 232 K. Figure 4.20 shows this second layering transition appears as temperature is increased above 232 K. A nearly linear increase in the height of the numerical derivative associated with the second step continues until $\sim$ 245 K, where the peak begins to broaden with increasing temperature. The second layer disappears again at $\sim$ 281 K just like the second layer transition of *n*-hexane on MgO and graphite.

There is a remarkable change in the shape of the first adsorption step as a function of temperature. At low temperatures and surface coverage there is a substantial linear adsorption region extending out to a reduced pressure, $(P/P_0)$, of 0.3 which can be seen in Figure 4.21. As cyclohexane coverage increases beyond $P/P_0 \sim 0.3$, the isotherms follow a more vertical path that gradually become more rounded as temperature is increased. This behavior can be seen in a series of numerical derivatives of the first layer region. As temperature is increased further, the region of $P/P_0$ occupied by the low-coverage linear portion decreases. As the low coverage linear portion increases to higher relative pressures and coverage, the corresponding vertical portion of the first layering transition decreases in size. This gradual decrease in the slope of the vertical portion of the first layering transition begins to match that of the low coverage linear portion until one linear portion from zero coverage to the monolayer completion point is formed and no layering transition is visible.

### 4.3.2 Monolayer Capacity

Because of the various behaviors that cyclohexane on MgO exhibits we must be careful in assigning an APM. Choosing the appropriate isotherm to use the point-$B$ calculation is important because of the sensitivity of the monolayer capacity to the shape of the profile as discussed by [Gregg and Sing, 1982]. It is preferable to select an isotherm of a 'well-defined

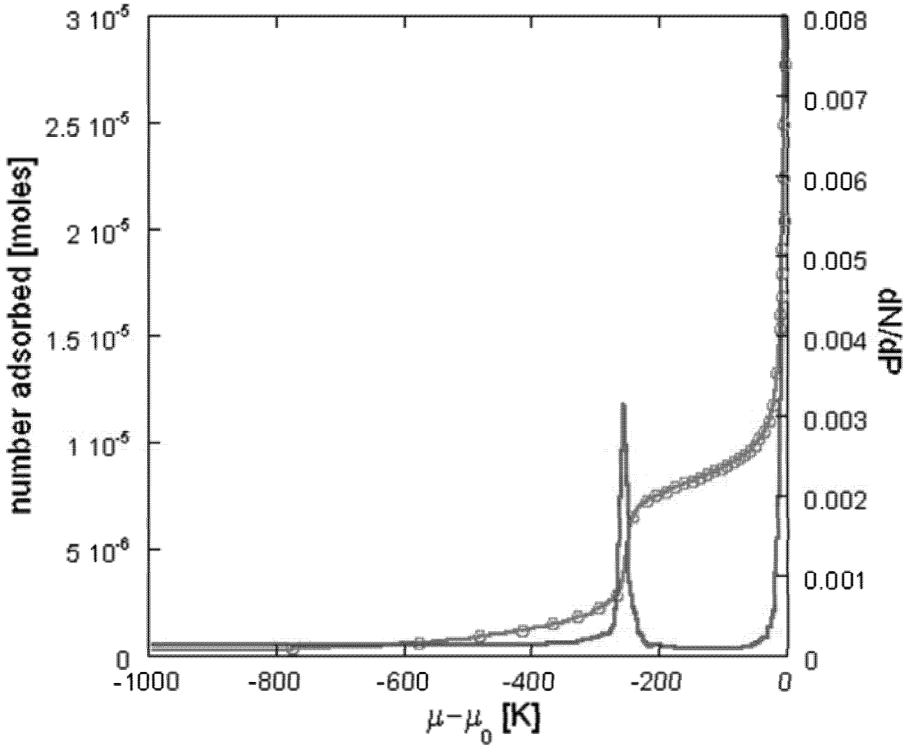


Figure 4.19: An example of a low temperature cyclohexane on MgO isotherm below 232 K where only one layering transition is present.

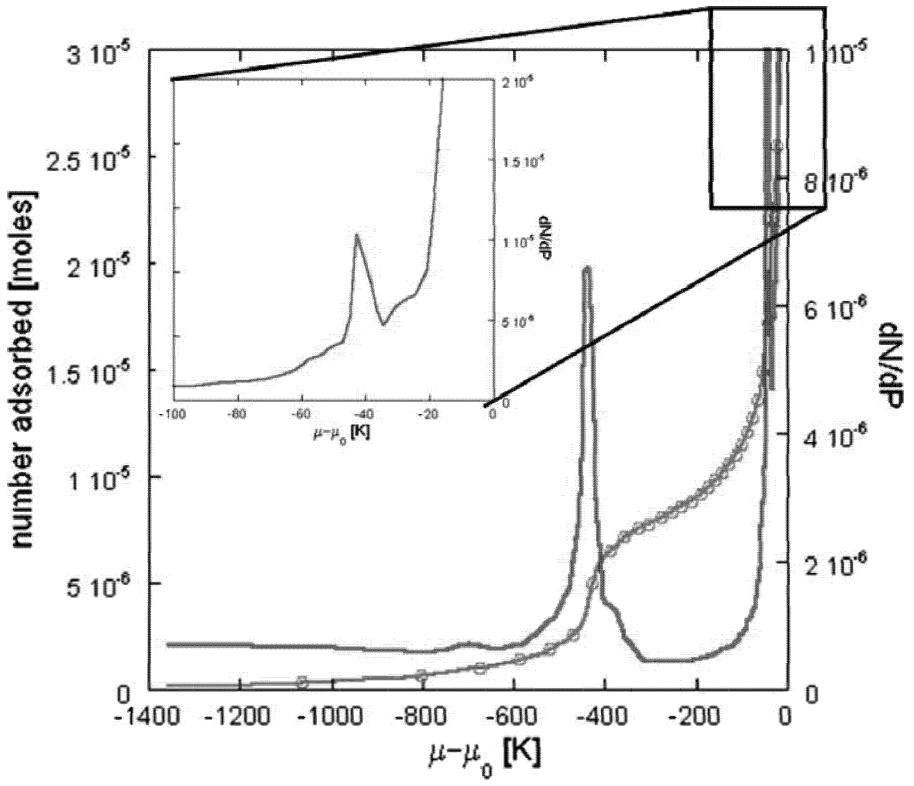


Figure 4.20: An example of a cyclohexane on MgO isotherm at above the 232 K where the onset of a second layering transition develops.

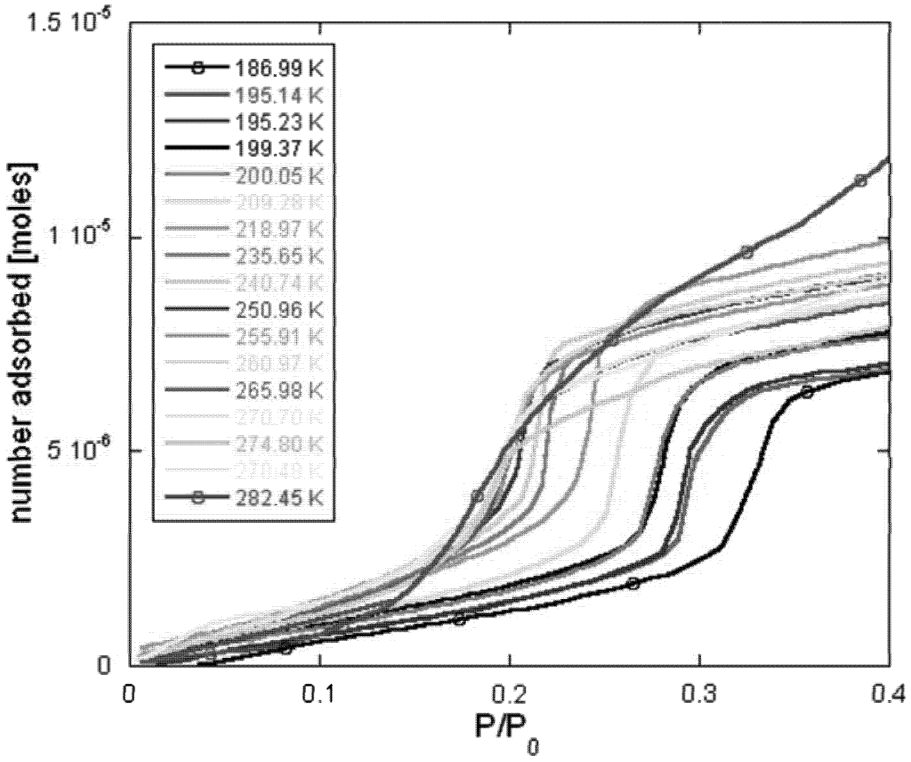


Figure 4.21: A subset of cyclohexane on MgO isotherms shown in number adsorbed (y-axis) and $P/P_0$ (x-axis). As temperature is increased the low-coverage linear portion of the first layer is visible at lower $P/P_0$ values until at $\sim$ 282 K the slope of the vertical riser begins to match that of the low-coverage linear portion.

Table 4.3: Thermodynamic values calculated from Clausius-Clapeyron plot of cyclohexane on MgO. Using a linear fit to the compressibility peak data, one can calculate $A^{(n)}$ (slope) and $B^{(n)}$ (y-intercept) values of each layering transition. Using the calculated $A$ and $B$ values, equations 2.106, 2.107, and 2.108 can be calculated for each layer.

| Layer | $A^{(n)}$ | $B^{(n)}$ | Q (kJ/mol) | $\Delta H$ (J/mol) | $\Delta S$ (J/K $\cdot$ mol) |
|---|---|---|---|---|---|
| 1 | 4256.90 | 17.27 | 35.39 | 2.20 | 13.26 |
| 2 | 4059.10 | 17.98 | 33.75 | 3.84 | 7.36 |
| $\infty$ | 4521.50 | 19.90 | 37.59 | – | – |

Type II' using the BET classification of isotherms [Brunauer, 1945]. This corresponds to a $c$-value in the BET equation of below 20. As seen in Figure 4.22 the isotherms that most closely match this value of $c$ are at low temperatures. Using an isotherm taken at 185 K the APM was determined to be 64.9 Å$^2$. A temperature increase of 5 K above 185 K results in an APM of 68 Å$^2$.

### 4.3.3 Clausius-Clapeyron Thermodynamic Data

Figure 4.23 displays the Clausius-Clapeyron analysis for cyclohexane on MgO. The uppermost line in the plot is the saturated vapor pressure (i.e. the bulk coexistence point for the isotherm). The other lines are the second and first steps in order from the top.

The isotherms in the neighborhood of second layer asymptotically approach the SVP as the temperature decreased. The second layer line merges with the SVP line and corresponds to the disappearance of discrete second layer formation at high temperatures. Table 4.3 shows the calculated thermodynamic quantities from the, $A^{(n)}$ (intercept), and $B^{(n)}$ (slope), values of each respective layer.

### 4.3.4 Two-Dimensional Compressibility, $K_{2D}$

Because there is only one discrete adsorption step at 232 K, the compressibility profiles only exhibit one peak in response to a single layering transition. The first derivative shows a slight increase in height up to 194.5 K. At this temperature peaks begin a downward trend

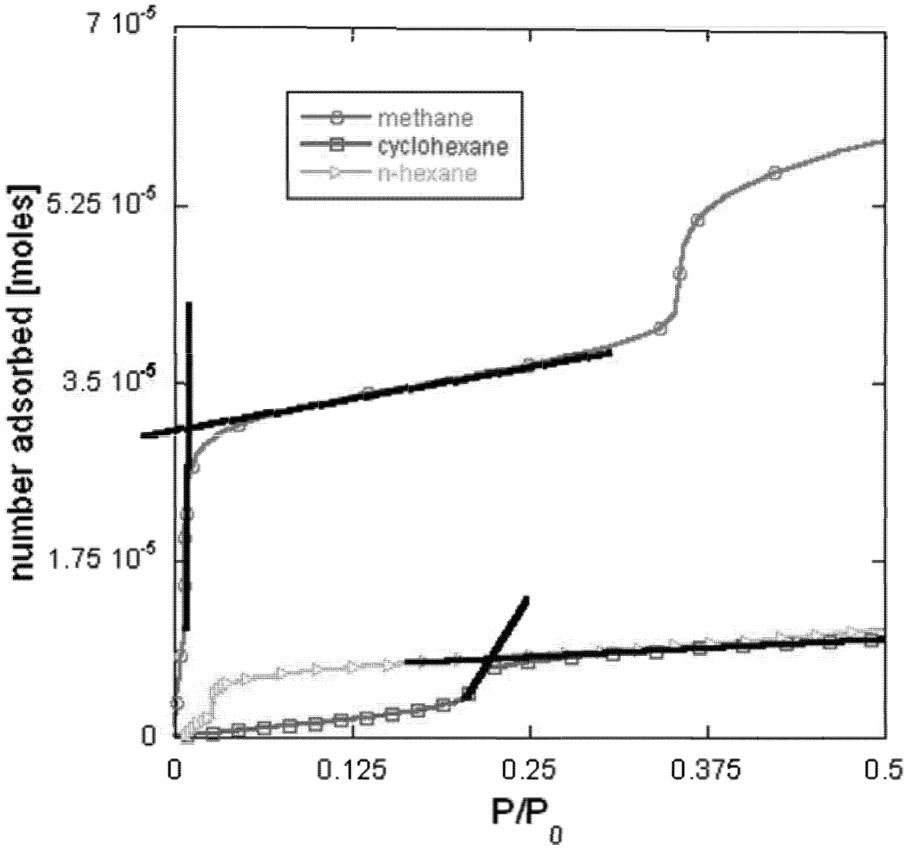


Figure 4.22: Monolayer comparison of methane and cyclohexane on MgO. Using a methane isotherm on the same sample and a low temperature cyclohexane isotherm, one can calculate the approximate APM a cyclohexane molecule occupies on an MgO surface which is determined to be 64.9 $Å^2$.

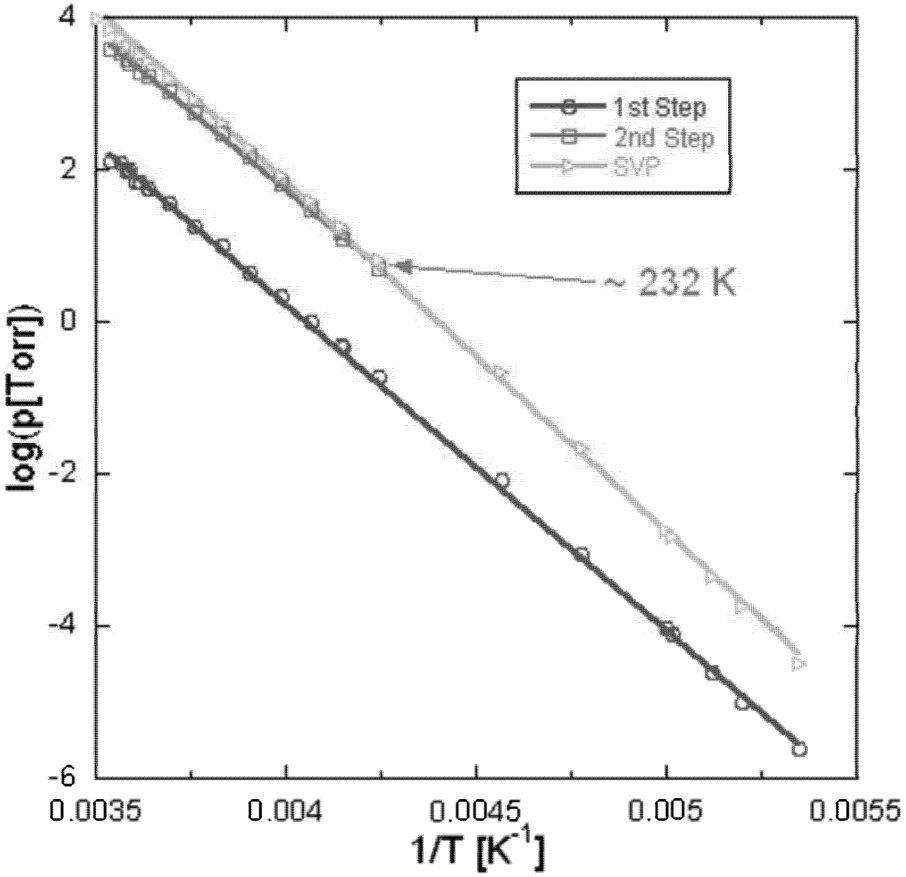


Figure 4.23: Clausius-Clapeyron plot of cyclohexane on MgO $K_{2D}$ peaks. Plotting the locations of the compressibility peaks versus $1/T$ a Clausius-Clapeyron can be produced. The intersection of lines at 232 K indicates the onset of a layering transition.

in intensity (see Figure 4.24). At temperatures above 232 K, two compressibility peaks are present. The first peak continues to diminish in height while the second layer displays a gradual increase in height with a temperature increase. This second layer increase reaches a maximum value at 260 K then begins to decline in intensity (see Figure 4.25).

The FWHM values for the first compressibility peaks shows no appreciable change in value and remain constant until a temperature of 271 K where an abrupt change in the FWHM is observed for the first layer (see Figure 4.26). The second layer shows a similar constant value of FWHM until a temperature of 278 K. At 278 K, an abrupt change in slope of the FWHM values is seen up to the temperature which the first layering transition disappears at $\sim$ 282 K.

A somewhat unusual result from the FWHM data is that the transition temperature of the first layer takes place at a lower temperature than the second. A possible reason for this could be the the liquid-like behavior could still be able to support a second layering transition but essentially destabilized the multi-layer film as temperature is increased slightly to 278 K where the second layer changes phase. Structural work is needed to further interrogate the behavior near the layering critical points.

### 4.3.5 Isosteric Heat of Adsorption, $Q_{st}$

A series of isosteric heats of adsorption calculations were performed using isotherms in close proximity ($\sim$ 1 K) to one another. Figure 4.27 shows a couple of isosteric heat calculations taken from two pairs of isotherms. At higher temperatures where two layering transitions are present, the isosteric heat exhibits two peaks corresponding to layer formation. The intensity of the second peak is much weaker than the first layering peak (factor of 30). This large variation in peak intensity suggests that a substantial amount of work needed to adsorb a molecule near monolayer completion. This is most likely due to the solid-like state of the surface film and a slight compression of the layer closest to the interface. At 190 K, the isosteric heat of adsorption converges to a value of 38 kJ/mol. At 240 K

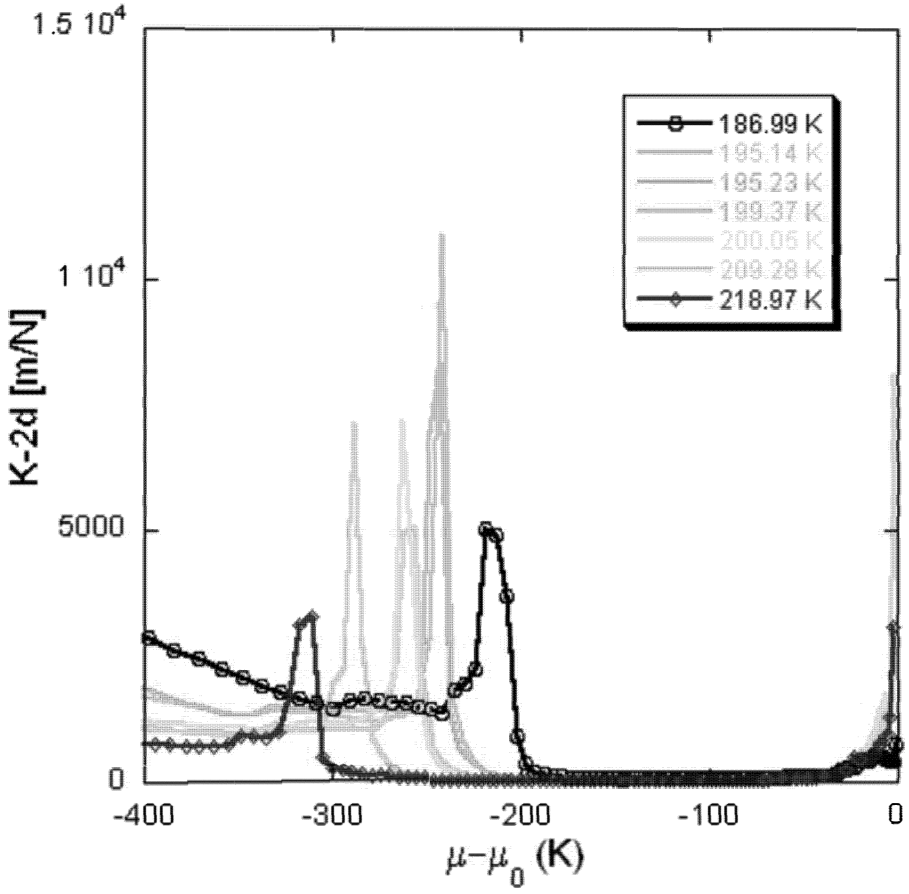


Figure 4.24: $K_{2D}$ peaks of cyclohexane on MgO at low temperatures. The first layering transition shows a maximum of the peaks occurring at $\sim$ 195 K then begins to decline as temperature is increased or decreased.

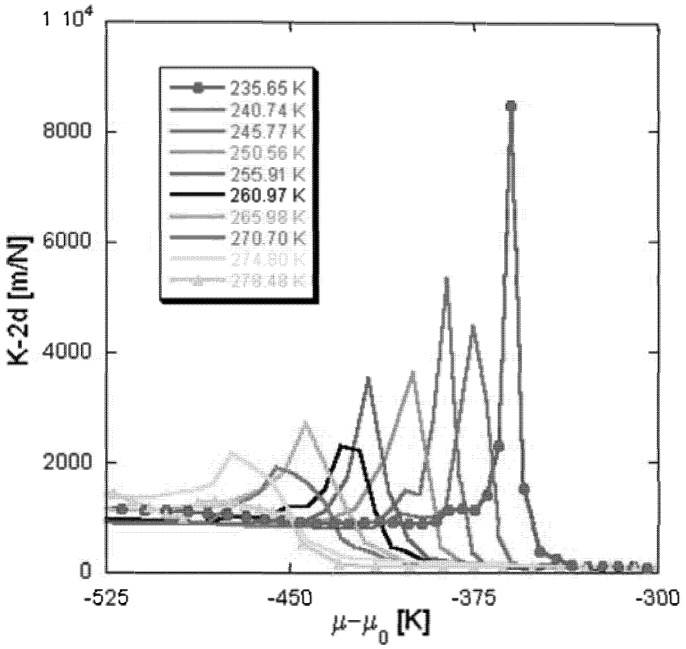


(a)

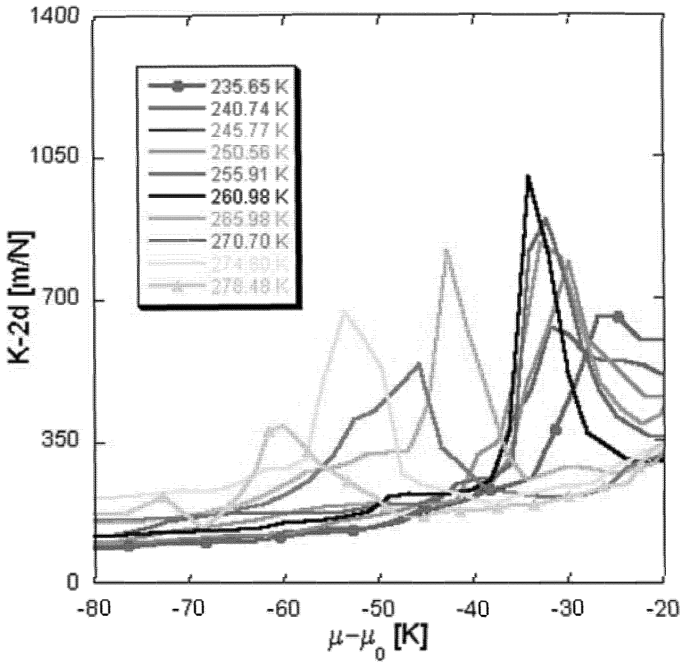


(b)

Figure 4.25: $K_{2D}$ peaks of cyclohexane on MgO at low temperatures. At higher temperatures two layering transitions exist both which have a downward trend in intensity as temperature is increased. (a) first layer. (b) second layer.

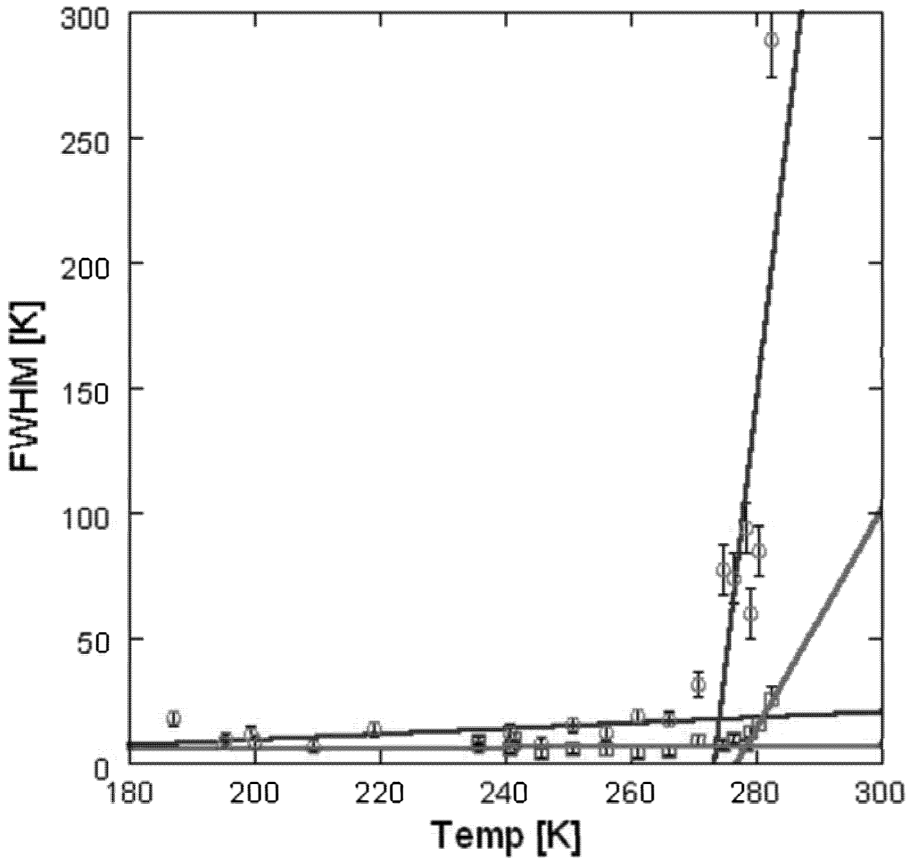


Figure 4.26: FWHM of the compressibility peaks of the first layer (red) and second layer (blue) of cyclohexane on MgO. The first and second layers show an abrupt change in FWHM at 271 K and 278 K respectively indicating a temperature where a possible phase transition occurs.

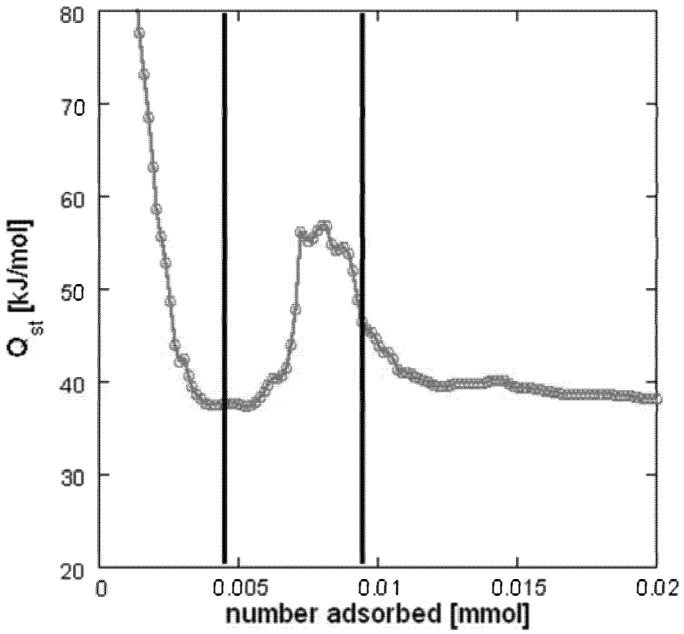


(a)

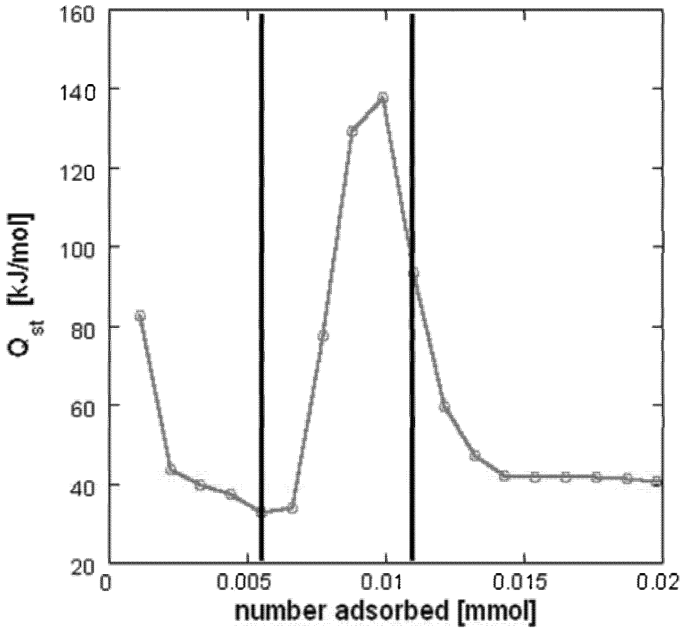


(b)

Figure 4.27: $Q_{st}$ of cyclohexane on MgO at two different temperatures. The monolayer capacities for each calculations were calculated using the average of the first compressibility peaks (black lines). The second layer is calculated by multiplying the monolayer capacity by 2. (a) at 199.7 K. (b) 278.8 K. The scales of the peaks vary with the $\Delta T$ between the two isotherms used.

the isosteric heat calculation at the saturated vapor pressure converged to a value of 40.8 kJ/mol. These values correspond very well with the bulk enthalpy of sublimation of 37.7 kJ/mol. At a temperature of 279 K the isosteric heat converged to a value of 32.8 kJ/mol which corresponds very well with the bulk enthalpy of vaporization of 32 kJ/mol. This temperature is right along the $T_{fusion}$ of bulk cyclohexane.

Figure 4.27 shows that both isosteric heats have large distinct peaks after monolayer completion using the location of the $K_{2D}$ peaks as an indication of monolayer completion. This is indicative of incomplete wetting where islands of multiple layers are formed on the surface before monolayer completion. The peak in the isosteric heat is indicative of when the first layer has been completed which occurs after layer completion as seen from the compressibility peaks.

### 4.3.6 Two-Dimensional Phase Diagram

A phase diagram of cyclohexane shown in Figure 4.28 can be constructed from the data presented above. The linear portion at low coverage is indicative of a dilute two-dimensional gas being formed on the surface. At low temperatures, the vertical portion of the isotherm has a steep slope which corresponds to a thermodynamic phase that proceeds through a solid-vapor coexistence region as coverage is increased. As the film thickness approaches monolayer coverage, a solid-like first layer forms. This suggests that the thin film passes through a solid-vapor coexistence phase where regions of solid are formed with the boundaries between the solid regions comprised of a less dense 2D vapor. As coverage approaches monolayer completion, the density of the film on the surface is such that the molecules begin to lock into adsorption sites and a 2D solid begins to take shape. As the temperature of the system is raised, the slow decrease in the slope of the vertical portion and rounding the step of the first layering transition is due to the movement of the isotherms through a phase boundary between a solid-vapor and liquid-vapor coexistence phases. As temperature is increased beyond the $T_{c-2D}(1)$ temp of 271 K, layering begins to appear in a continuous fashion where there are no defined layering transitions. This transition is termed a 2D

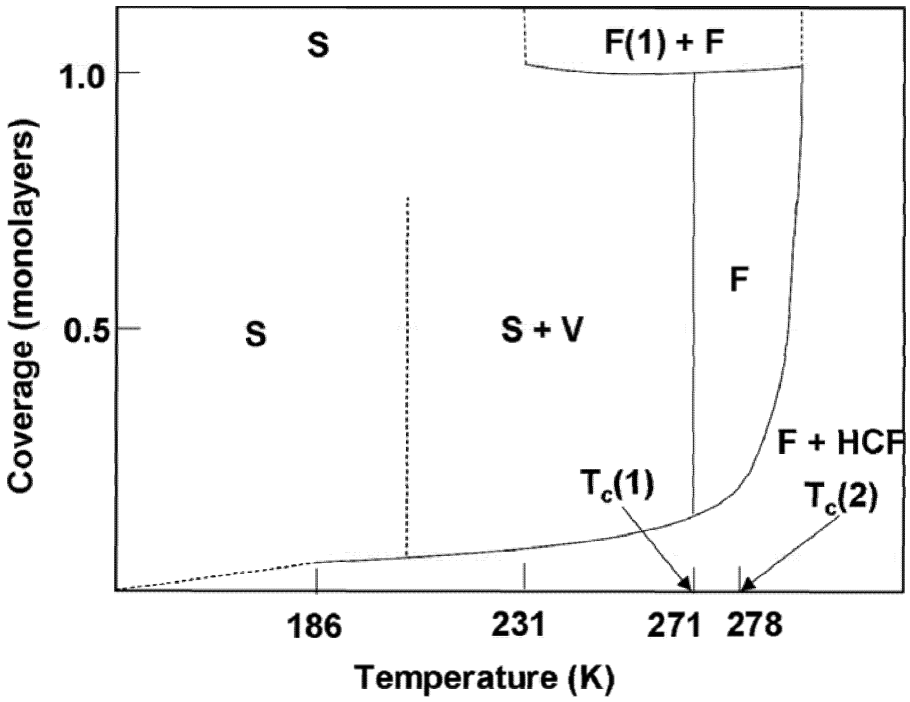


Figure 4.28: Two-dimensional phase diagram of cyclohexane on MgO. Dotted lines indicate the possible location of a phase transition.

hypercritical fluid and begins to take place.

The appearance and disappearance of the second layering transition can be described using the phase diagram as follows. At low temperatures there is only one layering transition because after completion of a solid monolayer the A-S interaction is much weaker than the A-A interaction. As the amount of molecules is increased past a monolayer, molecules stay in a vapor phase above the substrate until SVP pressure has been reached. At temperatures above 232 K, the onset of the second layering transition signifies the temperature region where the monolayer is sufficiently relaxed as to allow for interaction between the second adsorbed layer and the the substrate. This enhanced interaction energy with the surface allows for the formation of a discrete second layering transition. The second layer formed is a in a solid-liquid coexistence due to the solid regions present and the regions between the solid regions which is comprised of a 2D liquid. The boundaries between the solid regions are liquid-like in nature because of the variable density of these regions due to its interaction with the vapor above the film. At a temperature of 278 K, the second layer is predominantly in a liquid-like state. At temperatures above 282 K, no layering transitions are present only a slow monotonic rise to the SVP value due to the continues growth of the film front. This region signifies entrance into the 2D hypercritical fluid phase of the film. This behavior is similar to high temperature work of $NH_3$ on graphite where it is thought to be indicative of complete wetting [Larese and Lee, 1997].

## 4.4 Cyclohexane on Graphite

A series of more than 25 isotherms were recorded between 208 K and 292 K. Once again these measurements were restricted to these temperatures due to the resolution limit of the 1 torr MKS baratron pressure transducer at low temperatures and the upper limit being set by the difficulties associated with accurate temperature control ($\pm$ 2 mK) becomes difficult in a displex above room temperature. Cyclohexane on graphite isotherms show drastically

different wetting properties compared to its adsorption on MgO.

Previous adsorption studies of cyclohexane on graphite were done by Cordes et. al. where only one adsorption step was located [Smith et al., 1950]. Theoretical adsorption studies were performed by Ricca et. al., where the minimum energy equilibrium configuration on graphite was calculated using Steele's 10-4 potential treatment and interatomic potential values calculated by Kiselev [Battezzati et al., 1975], [Steele, 1974], [Kiselev and Avgul, 1967]. Most studies have concentrated on the effects catalysts have on cyclohexane conversion on metal surfaces and zeolites [Vitale et al., 1997], [Tsai and Muetterties, 1982], [Land et al., 1989], [Sivasankar and Vasudevan, 2004], [Firment and Samorjai, 1978].

### 4.4.1 Isotherms

Cyclohexane on graphite shows 3 distinct steps identified using numerical derivatives. The second and third steps appear throughout all isotherm measurements but significantly decrease in amplitude as the temperature increases (see Figure 4.29). The location of the third and second layering features move slightly towards SVP as temperature is increased and change linearly in the height as measured by the numerical derivative. The profile of the first step changes as a function of temperature. At low temperatures, the isotherms show a sharp, nearly vertical step in the amount adsorbed versus pressure. This behavior changes gradually to a shape that has a linear low-pressure, low-coverage region and a more gradual sloping riser to the monolayer completion point as shown by the numerical derivative. All adsorption isotherms exhibit measurements follow an asymptotic approach to the SVP suggesting that the layering on graphite appears to be somewhat between incomplete and complete.

### 4.4.2 Monolayer Capacity

The monolayer capacity calculated using the point-$B$ method (see Figure 4.30) from isotherms of methane and cyclohexane on the same sample yields an average value $\sim 40.40\ \mathring{A}^2$. The

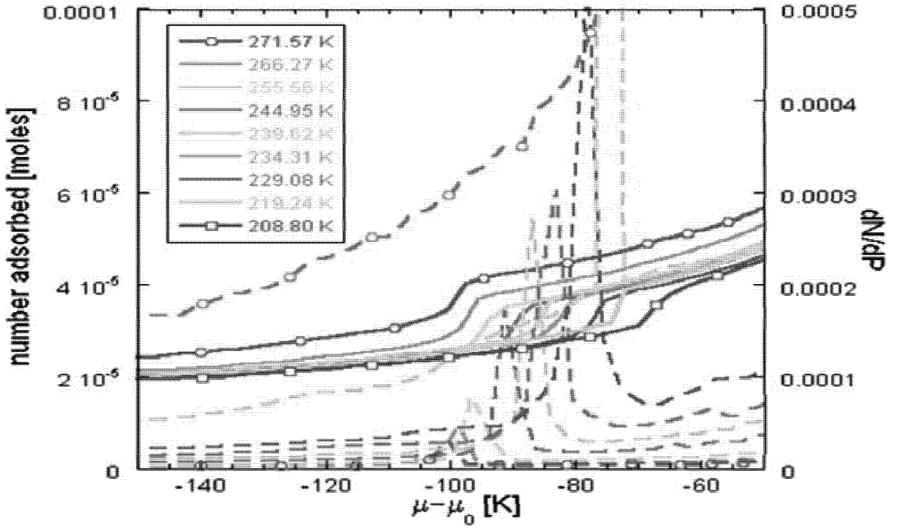


(a)

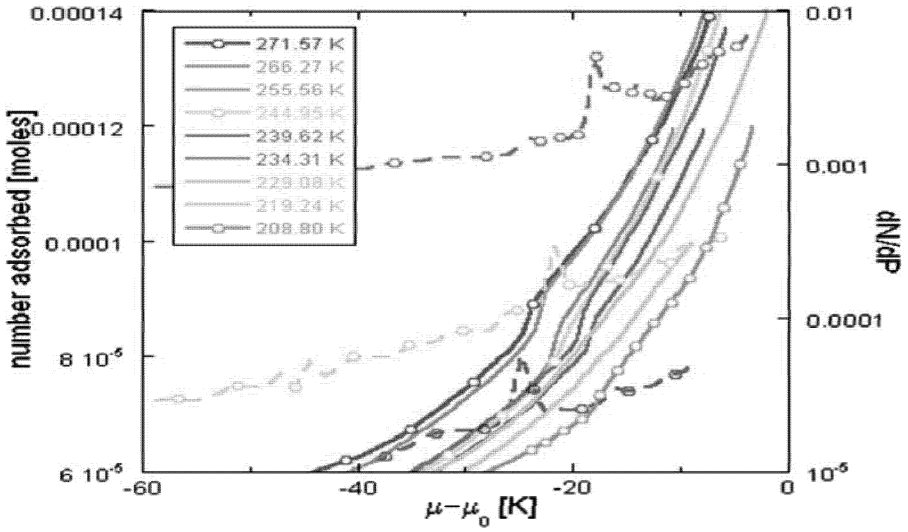


(b)

Figure 4.29: Subset of cyclohexane on graphite isotherms (solid), and their associated derivatives (dashed). (a) second layering transition. (b) third layering transition of the same subset of isotherms showing a strong dependence on temperature (note difference in scale between figures a and b).

Table 4.4: Thermodynamic values calculated from Clausius-Clapeyron plot of cyclohexane on graphite. Using a linear fit to the compressibility peak data, one can calculate $A^{(n)}$ (slope) and $B^{(n)}$ (y-intercept) values of each layering transition. Using the calculated $A$ and $B$ values, equations 2.106, 2.107, and 2.108 can be calculated for each layer.

| Layer | $A^{(n)}$ | $B^{(n)}$ | Q (kJ/mol) | $\Delta H$ (J/mol) | $\Delta S$ (J/K $\cdot$ mol) |
|---|---|---|---|---|---|
| 1 | 4972.6 | 16.754 | 41.34 | -4.93 | 21.63 |
| 2 | 4339.6 | 18.817 | 36.07 | 0.34 | 4.48 |
| 3 | 4394.0 | 19.327 | 36.53 | -0.12 | 0.24 |
| $\infty$ | 4379.0 | 19.356 | 36.41 | – | – |

isotherms chosen all displayed a well-defined layering transition and monolayer completion point which coincides well with the criteria of the point-B method (see section 2.7.8).

### 4.4.3 Clausius-Clapeyron Thermodynamic Data

Once again Figure 4.31, shows the Clausius-Clapeyron plot derived from the $K_{2D}$ peaks as a function of inverse temperature. The uppermost line is the saturated vapor pressure curve and the lines beneath it are the $3^{rd}$, $2^{nd}$, and $1^{st}$ layering transitions respectively. The lines display a linear behavior with the exception of the first layer which does not have the same quality statistics as the other layering transitions, due to both the resolution limit of the pressure transducer and the sharp vertical risers at low temperatures.

Figure 4.31, the $3^{rd}$ layer does not move relative to the SVP or the $2^{nd}$ layer. The same is true for the second layer as well. Table 4.4, summarizes the thermodynamic information calculated using the slope and intercept values of the Clausius-Clapeyron plot. The values of the isosteric heat $Q^{(n)}$ for each layer show a decrease and convergence to the bulk enthalpy of vaporization ($\Delta H$) of 32.2 kJ/mol [http://webbook.nist.gov, 2006]. This corresponds to a decrease in $\Delta H^{(n)}$ and $\Delta S^{(n)}$ as you approach bulk. The $\Delta H$ values for the third layer is slightly unusual since one is a negative value. This most likely is a positive value very near zero indicating its resemblance to the bulk enthalpy of sublimation. The values of $\Delta S^{(n)}$

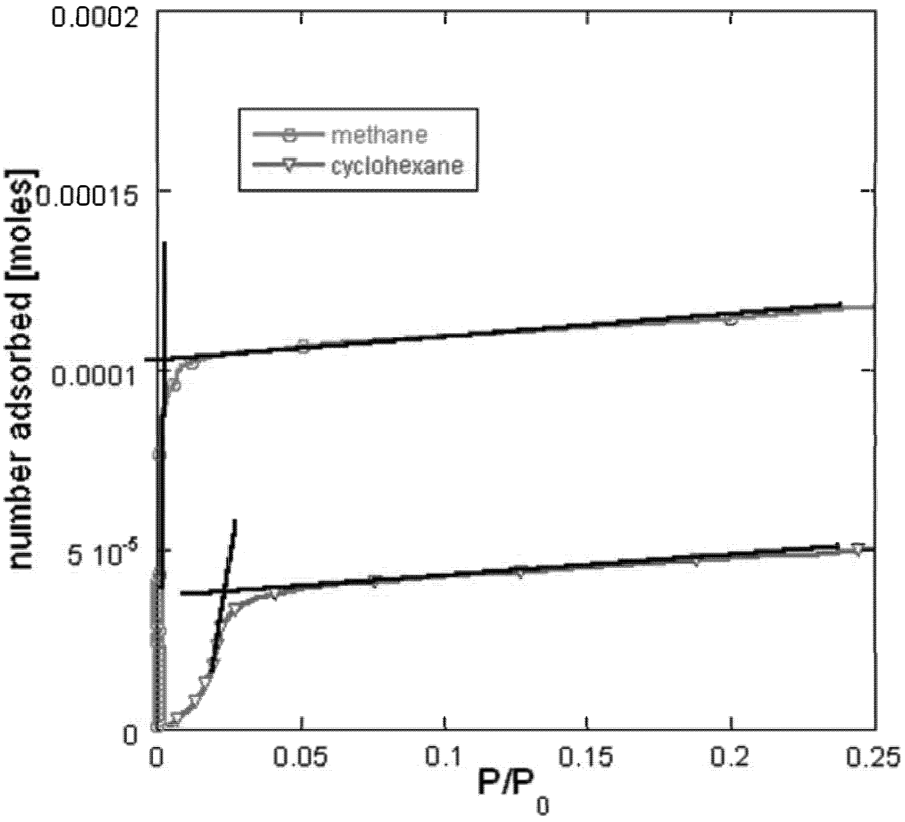


Figure 4.30: A comparison of cyclohexane with a methane isotherm (with a known APM) on graphite. One can calculate the APM of cyclohexane to be 40.4 $Å^2$.

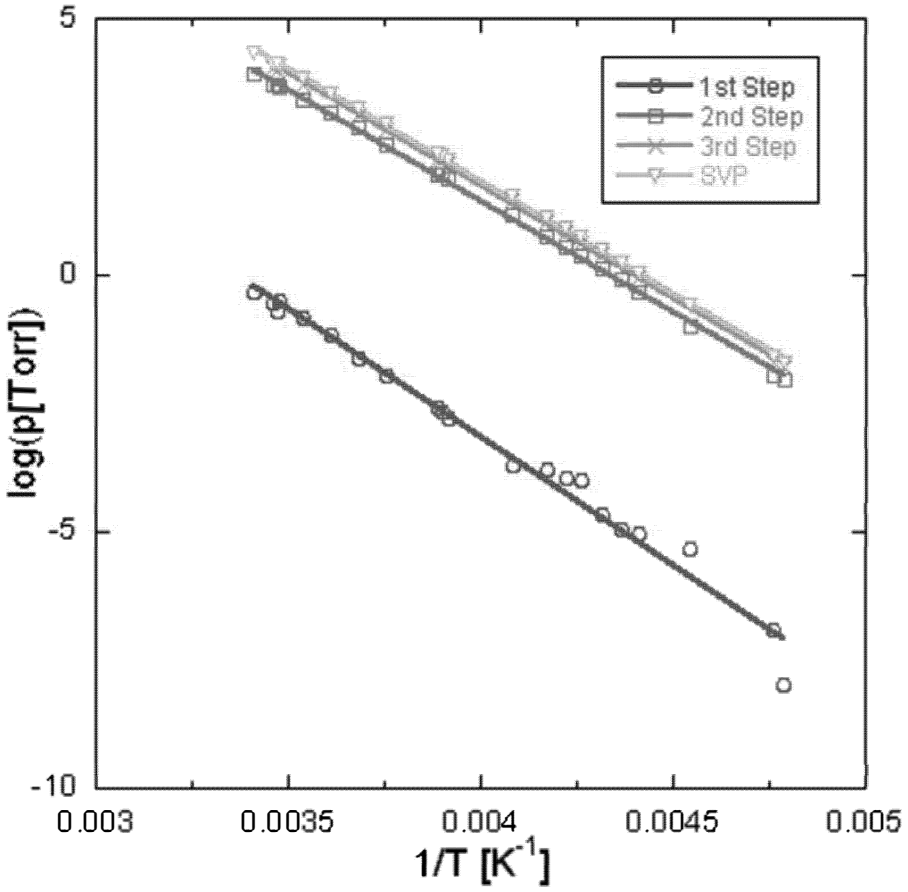


Figure 4.31: Clausius-Clapeyron plot of cyclohexane on graphite $K_{2D}$ peaks. Plotting the locations of the compressibility peaks versus $1/T$ a Clausius-Clapeyron can be produced.

are all positive indicating that the formation of the surface film is entropically favored to forming bulk crystallites [Arnold et al., 2005].

### 4.4.4 Two-Dimensional Compressibility, $K_{2D}$

As temperature is increased, the first layer exhibits changes that can be associated with changes in the layering behavior. The compressibility features show a gradual increase in peak intensity in the second and third layers as a function of temperature reaching a maximum value at 240 K for both layers (see Figure 4.32). The increase in the peak height of the second and third layers seem to be correlated. Figure 4.33 shows a plot of the half-maximum (HM) values of the peaks versus temperature. The figure seems to suggest that the increase and decrease in intensity is approximately linear. The coincidence of the locations of the peak heights might indicate that as the second layer becomes more solid-like, that the third layer can also become more solid-like. At temperatures above 240 K, the ratio between the second and third peaks begins to linearly decrease until the peak widths are near even.

The behavior of the $K_{2D}$ associated with the first layer is difficult to interpret for most isotherms due to the shape of the first laying transition. This makes an accurate calculation of the FWHM difficult and after the large variations in values were recorded the data was judged undependable. The FWHM of the peaks associated with the second and third layers both show FWHM values that increase drastically (see Figure 4.34). Transitions occur at around 279 K for the third layer and 286 K for the second layer. The error bars represent error in the gaussian fits to the compressibility peaks. The errors bars become larger as the FWHM values get larger because the broader peaks are typically asymmetric which makes fitting a symmetric function like a gaussian difficult.

### 4.4.5 Isosteric Heat of Adsorption, $Q_{st}$

Isosteric heats of adsorption were calculated using isotherms which are in close proximity ($\leq$ 1 K ), of each other. As can be seen from Figure 4.35, the intensity of the isosteric heat

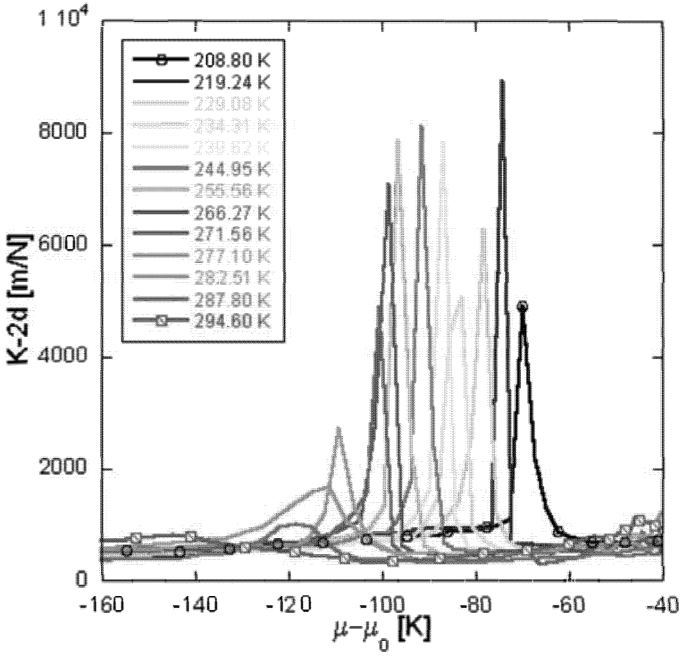


(a)

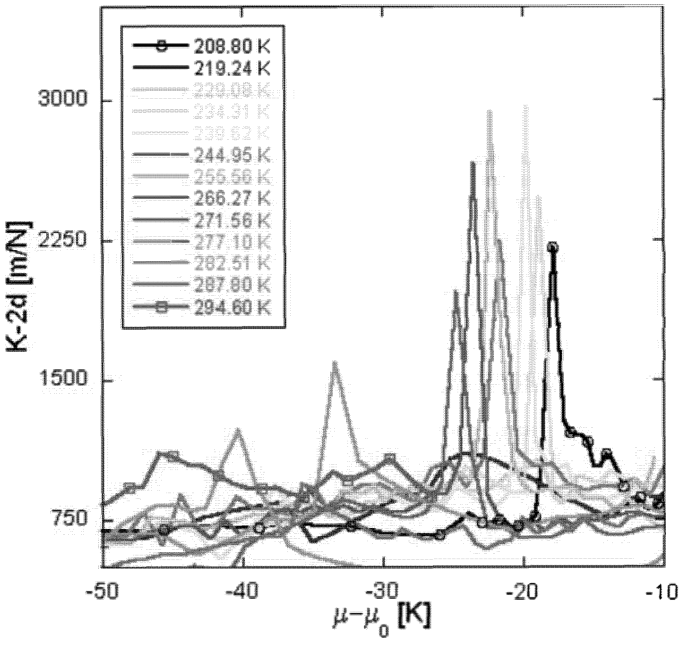


(b)

Figure 4.32: Subset of $K_{2D}$ plots of cyclohexane on graphite isotherms for the second and third layering transitions. (a) second layer. (b) third layer.

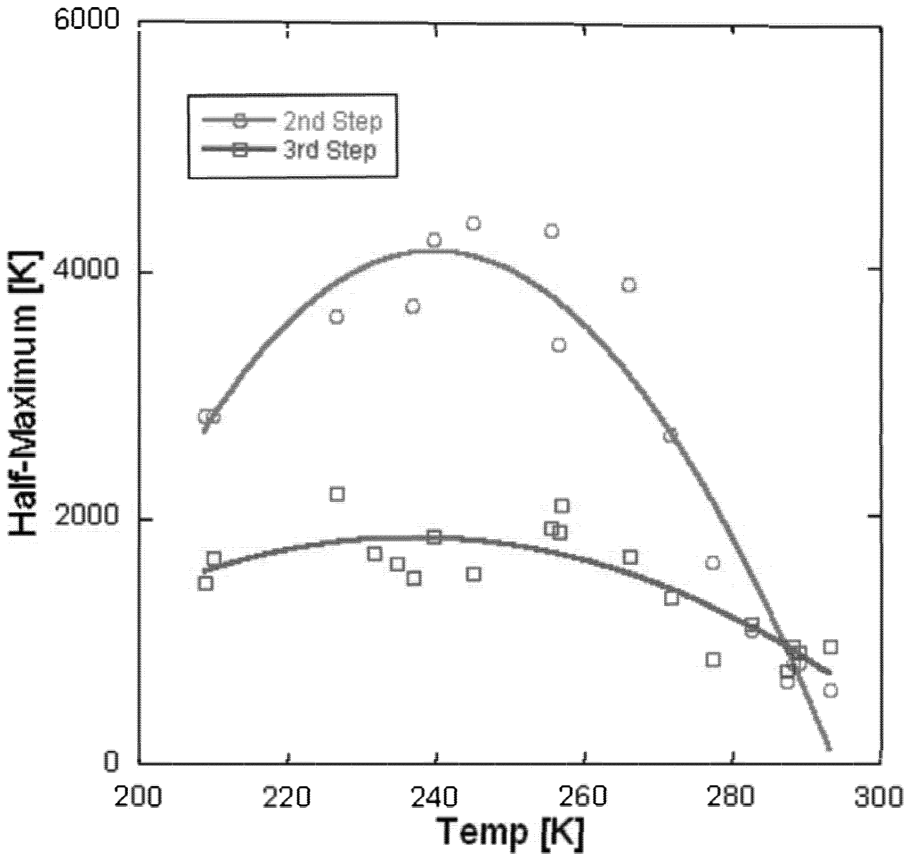


Figure 4.33: The maximum HM values of the cyclohexane on graphite $K_{2D}$ peaks for the second and third layers coincide at a temperature around 240 K.

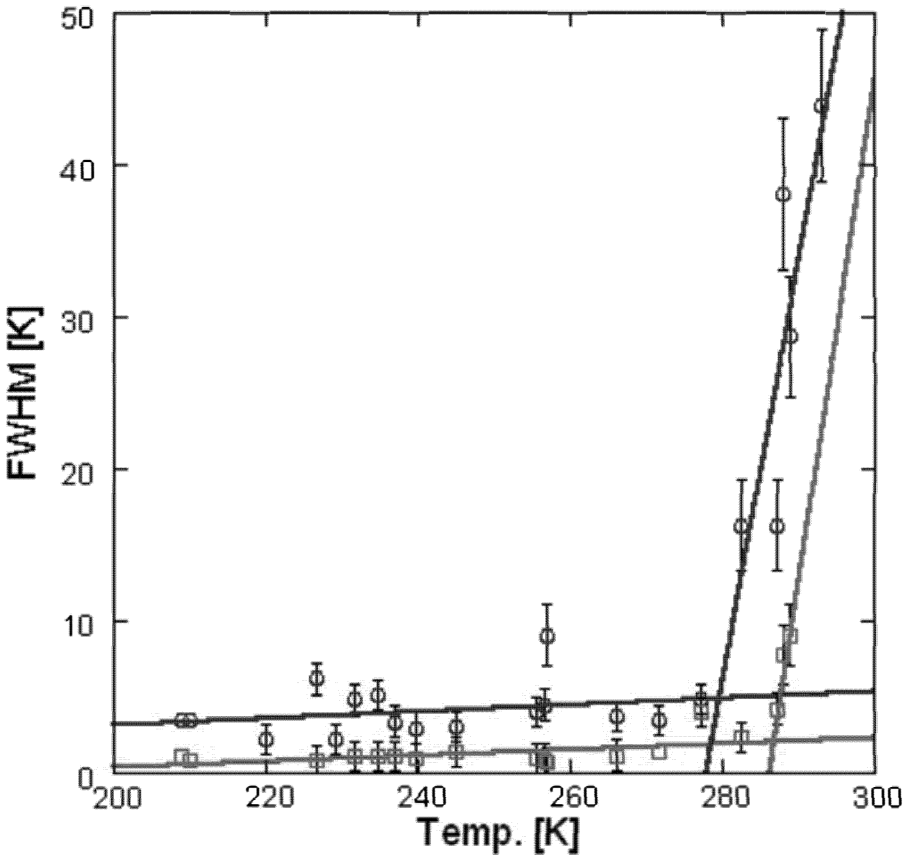


Figure 4.34: The $K_{2D}$ peaks from cyclohexane on graphite each show a change in FHWM values at 278 K and 286 K for the second (blue) and third (red) steps respectively.

near the first layering transition increases as temperature is decreased. As temperature is increased layering becomes more continuous which makes increases the types of adsorption sites available due to the presence of multi-layer islands before monolayer completion. This creates adsorption sites which less work is needed to bring a molecule from the bulk vapor phase which reduces the peak height.

After the first layering feature it becomes more difficult to identify layering transition peaks associated with layers further from the surface since they merge with the background behavior. The second layer peak is significantly broader and less intense than the first peak. At higher coverage, the isosteric heats converge towards the bulk enthalpy of vaporization of 32.2 kJ/mol [http://webbook.nist.gov, 2006]. The lack of a discernable third peak could be indicative of the third layer coexisting very near the SVP line where bulk crystallites are present.

### 4.4.6 Two-Dimensional Phase Diagram

In a fashion to the previous systems, a phase diagram produced using the thermodynamic data collected (see Figure 4.36). Cyclohexane on graphite displays a similar set of transitions as other systems up to monolayer coverage. The isotherms thermodynamic path the isotherms follow passes through a low-coverage, low-pressure dilute gas phase while at higher coverage, the vertical rise signals a passage through a solid-vapor coexistence region. Near monolayer completion, the isotherm path enter a solid phase region as the monolayer is completed. The thermodynamic paths followed by the isotherms in the region of the second and third layers involve passages through liquid-vapor coexistence regions at low temperatures and a solid underlayer with a fluid outermost layer at higher temperatures.

## 4.5 Pyridine on MgO

Twenty five isotherms were recorded with three different samples of MgO between 223 K and 287 K. Isotherms above room temperature were not performed because we were unable

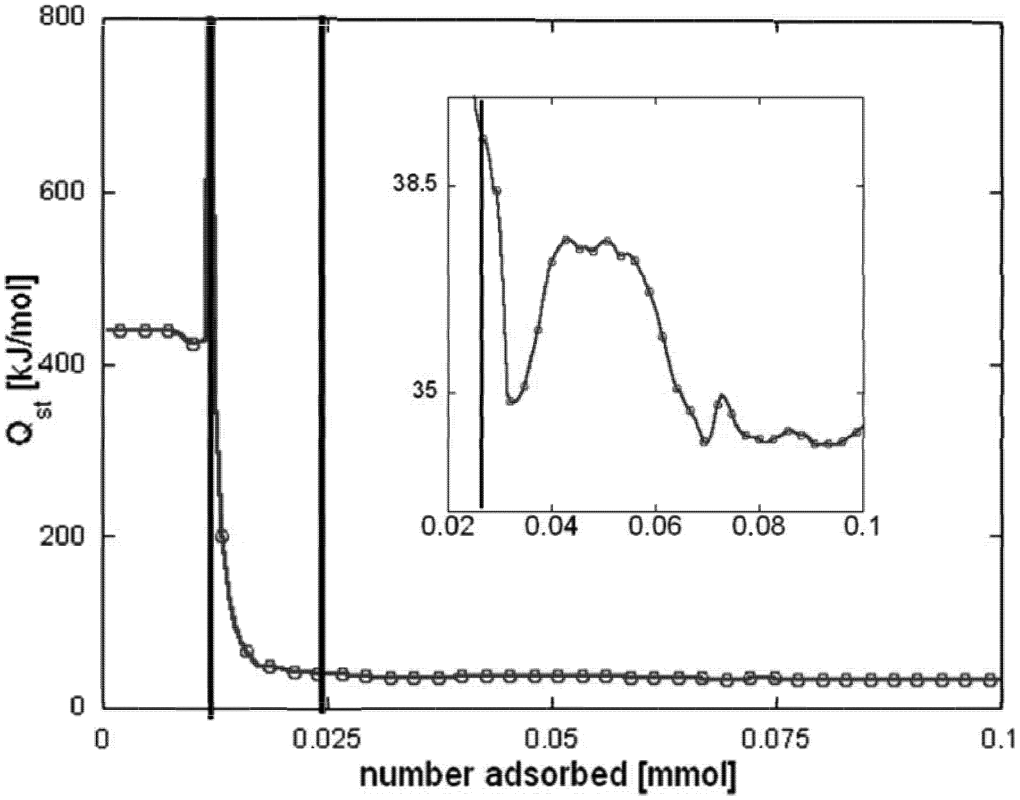


Figure 4.35: $Q_{st}$ of cyclohexane on graphite at 208.7 K. The black lines indicate monolayer and bi-layer completion points.

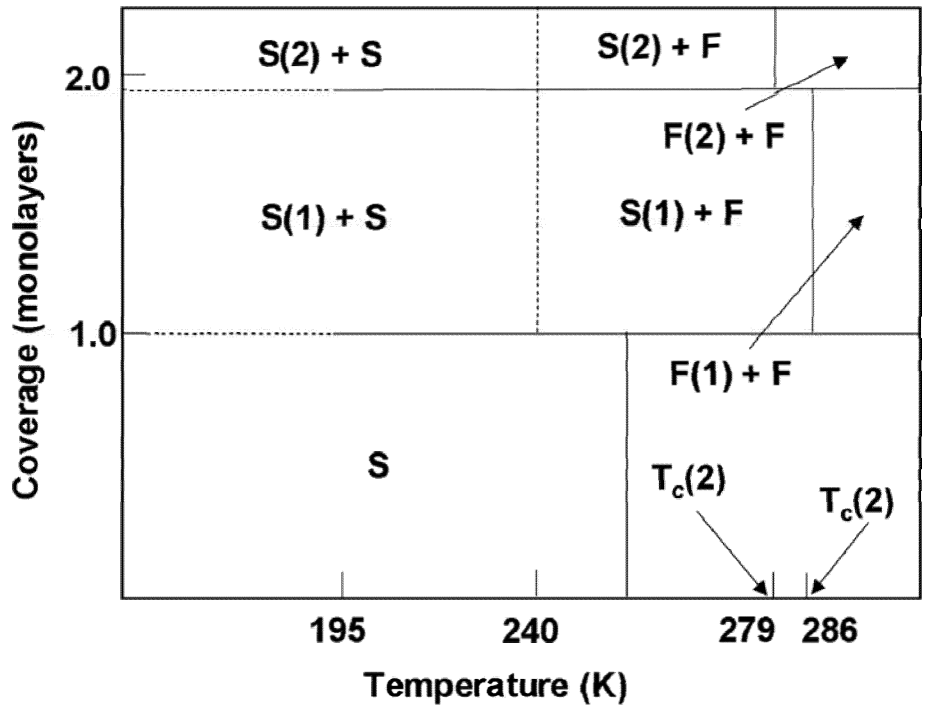


Figure 4.36: Two-dimensional phase diagram of cyclohexane on graphite. Dotted lines indicate the possible location of a phase transition.

to regulate the sample temperature. Isotherms below 223 K were not performed due to the resolution limit of the 1 Torr pressure transducer.

In the past, a variety of studies have been performed on the adsorption characteristics of pyridine on MgO. Most studies of pyridine adsorption on MgO have focussed on the surface acidity (see section 2.3.6) of the MgO surface to characterize its use as a potential catalyst. MgO when mixed with another oxide is typically used in the catalytic oxidative dehydrogenation of hydrocarbons [Dollimore et al., 1971a], [Dollimore et al., 1971b]. Pyridine was chosen in particular because the nitrogen lone pair can hydrogen bonded to the surface weakly to acidic $OH^-$ groups, yielding a very weak perturbation of the adsorbed molecule. If the Brönsted acidity of a surface $OH^-$ group is sufficiently high, a proton can be extracted to yield a pyridinium ion species. The nitrogen lone pair can interact by $O^{2-}$ charge donation to surface cationic centers, acting as Lewis acid sites on the MgO surface.

### 4.5.1 Isotherms

Isotherms of pyridine on MgO (100) show two distinct layering transitions up to a temperature of 287 K. The first layering transition consists of a sharp vertical riser region until the first layer is reached. These isotherms do not exhibit any low-coverage linear portion after the first few isotherms. *This low coverage behavior is indicative of a strongly physisorbed system or chemisorbed system.* In some cases at significantly low temperatures (i.e. under 240 K), the initial vertical rise was so steep that the pressure transducer recorded the pressure as not changing, a situation that produces an infinite $dN/dP$ value. This behavior has not been observed in any other MgO system studied so far. After the first isotherm the shape of the first layering transition is largely independent of temperatures and only slight changes in slope appear as temperature is increased. The equilibration times of the points on the first layering transition during the experiments were very long ($\sim$ 2 hours per point).

### 4.5.2 Monolayer Capacity

One of the most striking features of the pyridine series of isotherms performed was the reduction in the monolayer capacity as successive isotherms were performed. A representation of this effect can be seen in Figure 4.37. This figure shows successive isotherms performed at the same temperature on the same sample. It can be readily seen that the monolayer capacity of the MgO substrate was reduced by a factor 4 over this particular series of isotherms. The reduction in monolayer capacity of the substrate also affects the layering properties of the pyridine. This effect is especially pronounced when isotherms at higher temperatures are performed. To further illustrate the chemisorption or strong physisorption to the MgO, a methane isotherm was run subsequent to a series of pyridine isotherms. Figure 4.38 shows a methane before and after a series of pyridine isotherms. The methane isotherm performed after the pyridine adsorption shows only one layering transition and a slow ramp to a sudden rise at SVP. The methane isotherm run prior to exposure normal shows 5 visible layering transitions without the use of a numerical derivative, indicative of a clean MgO surface. The purpose of these studies was to illustrate how chemical activity may override molecular symmetry.

The reduction in monolayer capacity as the number of isotherms performed increases makes calculating of the monolayer capacity of pyridine on MgO difficult. In order to insure as little surface degradation as possible, only the first isotherm performed after a methane isotherm was used to calculate the APM. The average value of 64.9 $\mathring{A}^2$ (see Figure 4.39) is found. Values in literature have quoted values of 20 - 35 $Å^2$ [Hendra et al., 1971], [Rahman and Ghosh, 1980]. This compares to a flat adsorption steric model of 24.4 $Å^2$.

### 4.5.3 Clausius-Clapeyron Thermodynamic Data

The Clausius-Clapeyron plot shown in Figure 4.40, displays the dependence of temperature on the location of the layering transitions relative to each other. Because we suspect some species reside on the surface between isotherms the locations of the first layering transitions

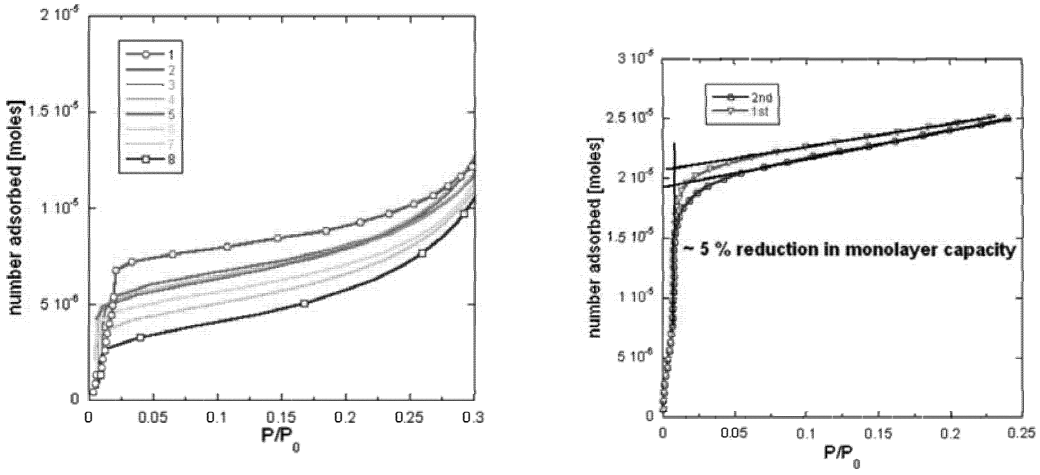


(a) (b)

Figure 4.37: A comparison illustrating the reduction in monolayer capacity caused by pyridine adsorption. (a) The capacity of the MgO surface decreases by up to a factor of $\sim 4$ due to pyridine adsorption. (b) a comparison to two successive methane isotherms run on the same sample.

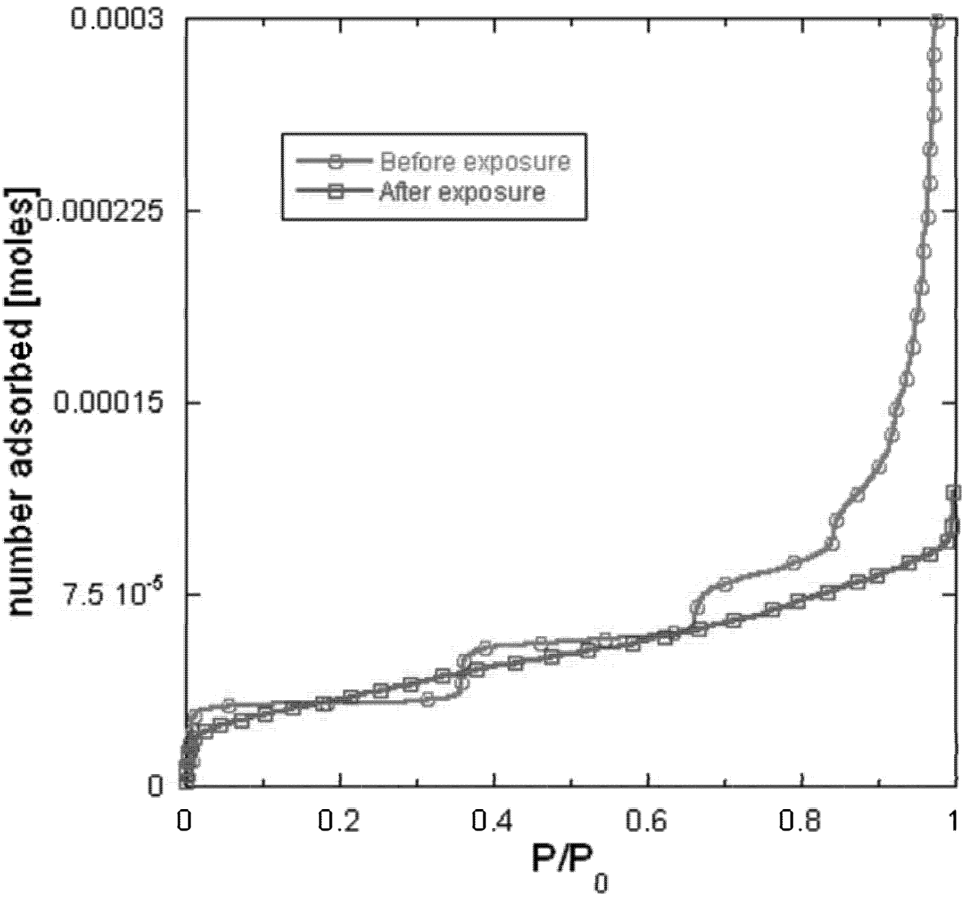


Figure 4.38: Comparison of methane isotherms run before and after pyridine exposure.

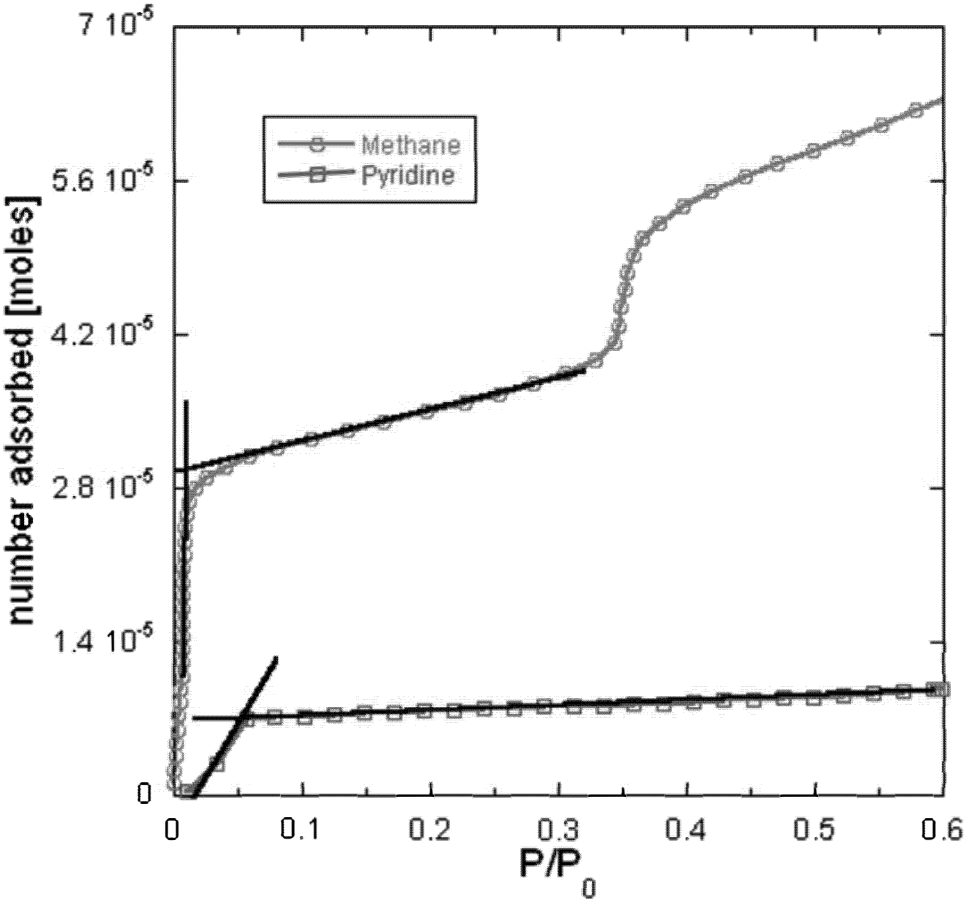


Figure 4.39: Monolayer comparison of pyridine on MgO. The area per molecule (APM) of pyridine calculated from a comparison to a methane isotherm run on the same sample. The first pyridine isotherm was used after the methane isotherm test due to the decrease in monolayer capacity of the MgO after successive isotherms are run on the sample. An APM of 64.9 $Å^2$ was determined.

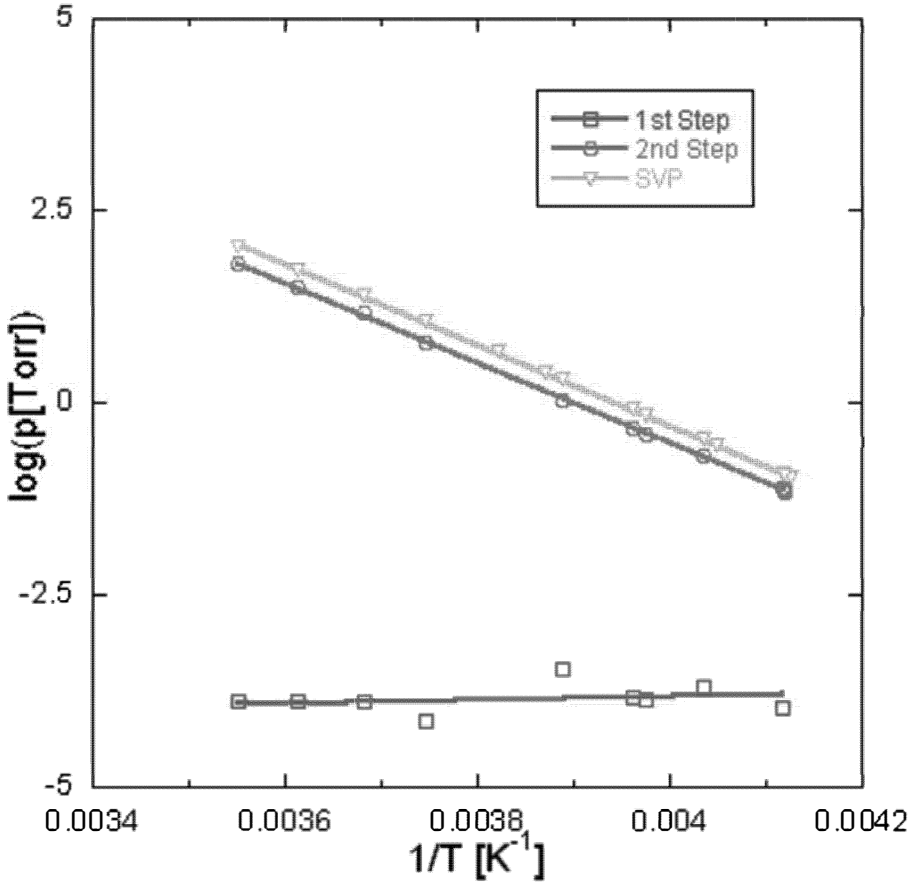


Figure 4.40: Clausius-Clapeyron plot of pyridine on MgO $K_{2D}$ peaks. Plotting the locations of the compressibility peaks versus $1/T$ a Clausius-Clapeyron can be produced.

Table 4.5: Thermodynamic values calculated from Clausius-Clapeyron plot pyridine on MgO. Using a linear fit to the compressibility peak data, one can calculate $A^{(n)}$ (slope) and $B^{(n)}$ (y-intercept) values of each layering transition. Using the calculated $A$ and $B$ values, equations 2.106, 2.107, and 2.108 can be calculated for each layer.

| Layer | $A^{(n)}$ | $B^{(n)}$ | Q (kJ/mol) | $\Delta H$ (J/mol) | $\Delta S$ (J/K $\cdot$ mol) |
|---|---|---|---|---|---|
| 1 | – | – | – | – | – |
| 2 | 5285.10 | 20.84 | 43.94 | -0.65 | -4.43 |
| $\infty$ | 5206.60 | 20.31 | 43.29 | – | – |

suffered from similar pressure transducer resolution problems described in some of the low temperature cyclohexane on graphite isotherms. This problem could also be attributed to the very long equilibration times of the points in the first layering transition. The lack of reliable compressibility location data hinders the ability to calculate any quality thermodynamic data for the first layer. Table 4.5, the thermodynamic quantities extracted from the slope and intercept values as calculated from the linear fits to layering transition locations as determined by the peaks of the two-dimensional compressibility peaks.

### 4.5.4 Two-Dimensional Compressibility, $K_{2D}$

The compressibility peaks of pyridine experience the same temperature dependent affects as seen with other adsorbates on MgO. The compressibility of the first peak is difficult to interpret due to similar problems described in section 4.3.4. The strong adsorption and subsequent decrease in monolayer capacity made comparisons of a two-dimensional compressibility values difficult. Therefore the analysis of this data was omitted. A comparison of the two-dimensional compressibilities from the first and subsequent isotherms run at the same temperature show a broadening and reduction in intensity of the second layering transition while the first layer shows an increase in compressibility values as isotherms are run due to the change of the first.

### 4.5.5 Isosteric Heat of Adsorption, $Q_{st}$

Isosteric heats of adsorption were calculated for isotherms which were performed within a 1 K proximity from each other. The isosteric heats shown in Figure 4.41, show a similar profile as other adsorbate-substrate systems which exhibit two layering transitions where the first layering transition can be identified by a large increase in the isosteric heat of adsorption as it approaches the monolayer capacity. After monolayer completion, this increase is followed by a more gradual decrease in the isosteric heat. A small increase can be seen near the second layering transition but this peak is at a larger value than doubling the monolayer capacity. At higher coverage the values converge towards the bulk enthalpy of vaporization value of 40.21 kJ/mol [http://webbook.nist.gov, 2006].

### 4.5.6 Temperature Programmed Desorption (TPD) experiments

After the noticeable reduction in the adsorption capacity it was decided to perform a series of temperature programmed desorption (TPD) experiments on samples after exposure to pyridine or after a series of isotherms have been run on the same sample. Desorption experiments were performed using a setup described in section 3.7.4. Different ramping rates were attempted from 1 C° per minute to 10 C° per minute. After a series of pyridine adsorption isotherms, the MgO powder has a pink-purple color to it. In the past literature this color change is attributed to the filling of $F^-$ centers (Lewis acid sites) which are the primary types of defects on an MgO surface [Hendra et al., 1971], [Iizuka and Tanabe, 1975], [Che et al., 1977], and [Zecchina and Stone, 1986].

Figure 4.42 shows the results of a TPD experiment with a ramping rate of 5 C°/min compared to the mass spectra from a bulk liquid pyridine sample. At 60 C°, a large increase in the intensity of the mass spectrometer peaks occurs centered at 28, 52, and 79 a.m.u. takes place. The peaks at 28 a.m.u. and 52 a.m.u. in bulk pyridine spectrum result from fragments of pyridine by the ionizer on the quadrupole mass spectrometer. Furthermore at 28 a.m.u. it could also be $N_2$ or CO which is desorbing from the surface. The relative

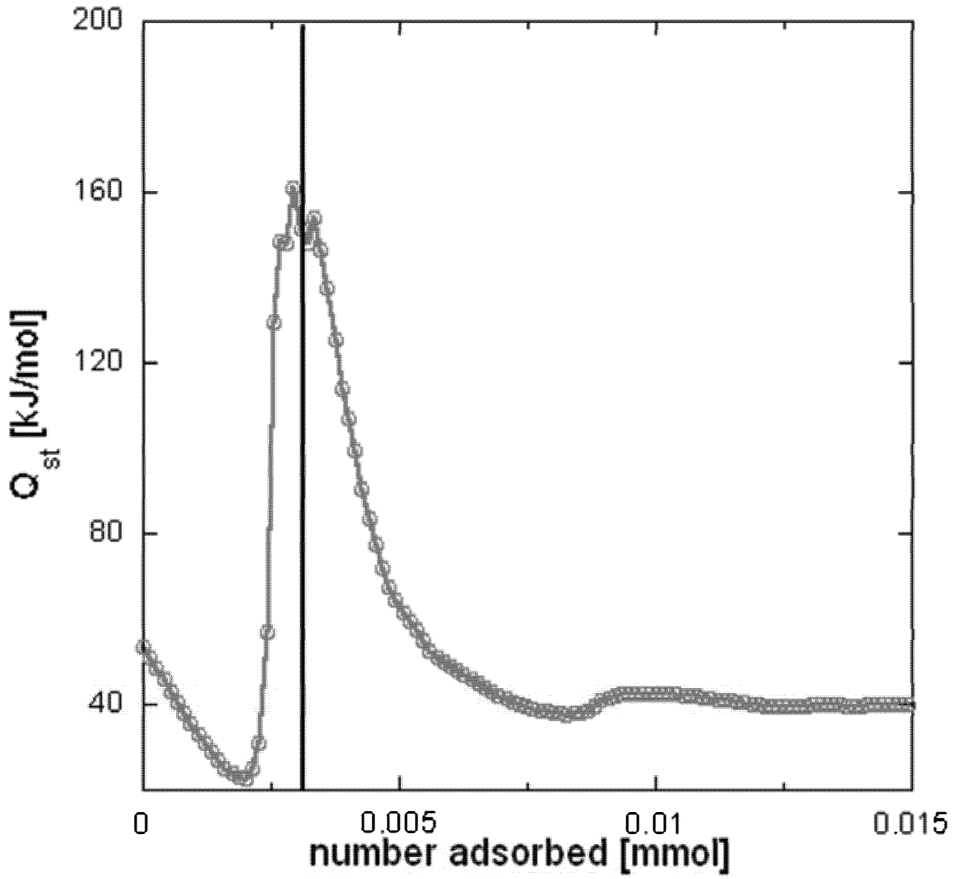


Figure 4.41: $Q_{st}$ of pyridine on MgO at 240 K. The black line indicates the monolayer completion point.

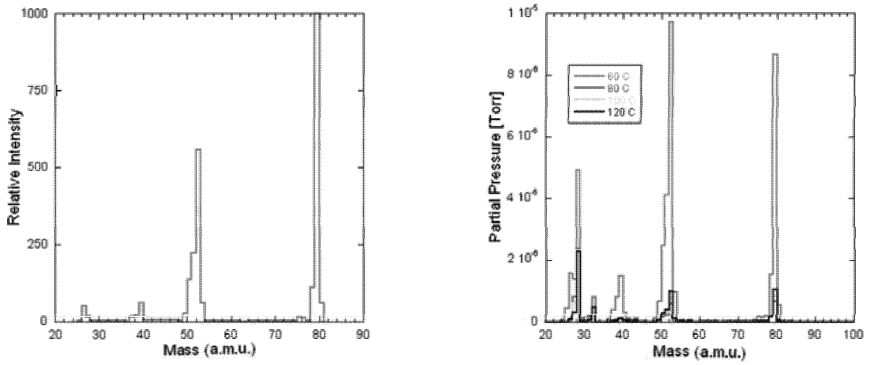


(a) (b)

Figure 4.42: Temperature programmed desorption (TPD) of pyridine adsorbed on MgO. A comparison of the bulk mass spectrometer signal compared to the desorption off the surface yields an increase in relative intensity of peaks centered at 28 and 52 a.m.u.. which indicates a higher concentration of dissociated ionized pyridine fragments desorbing off the surface indicative of dissociative chemisorbed species.

intensity of the peaks is different than that of bulk pyridine particularly the intensities of the peaks centered at 28 and 52 a.m.u.. Mass peaks at 28 and 52 a.m.u can also be indicative that $HCN^-$ and $C_4H_4{}^+$ species from the dissociation of pyridine are present. If the species desorbed from the MgO were only molecular pyridine the relative intensities of the peaks would be nominally as those of bulk pyridine. The change in relative intensities suggests that either of the molecular species are present besides pyridine and that desorb (perhaps dissociately) off the surface beginning around 60 C°. As temperature is increased further, the intensity of the peaks decrease but their intensities relative to each other did still indicated an elevated concentration of species not strictly entact pyridine were still present on the surface. At 80 C°, the peak centered at 28 a.m.u. was the highest in relative intensity. As the temperature was increased further the intensities of all three peaks were equivalent.

The TPD was performed until the temperature reached 300 C°. A methane isotherm was run on the sample after the heating. Figure 4.43, shows a comparison of a methane isotherm after the TPD experiment and after further heating at 950 C°. The results show the reappearance of five visible steps characteristic methane adsorption on a clean surface MgO surface which indicates that molecules and fragments on the surface can be desorbed with minimal degradation to the surface. The TPD result is somewhat unusual considering breakdown of pyridine in other catalytic reactions usually takes place at very high temperatures due to the stability provided by the conjugated $\pi$-bonding system. MgO has previously been classified as a weak catalyst, which makes dissociative chemisorption take place with little to no alteration or degradation of the surface an unusual result.

A redhead analysis of the TPD data yields the approximate binding energy of the desorbed species. The coverage dependent desorption energy can be calculated from the redhead equation yielding a peak value of 34 kJ/mol at 60 C°or 333 K. This value is close to the pyridine bulk enthalpy of vaporization value of 32.2 kJ/mol and suggests that the

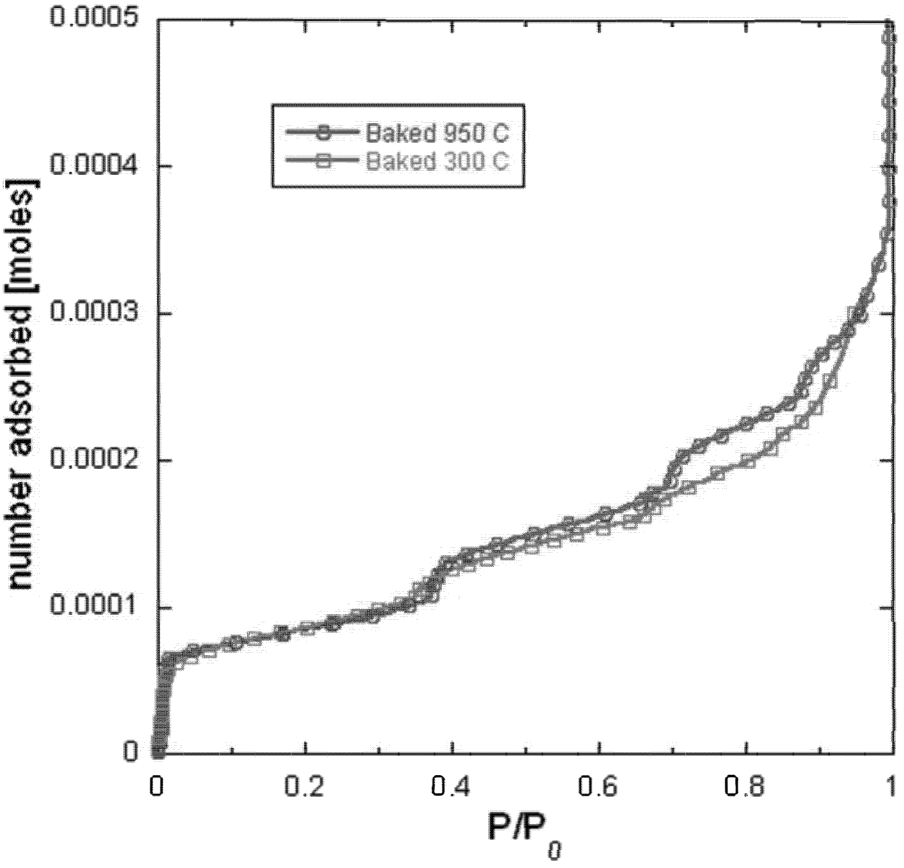


Figure 4.43: Subsequent to a TPD experiment, a set of methane isotherms were run to determine the quality of the MgO. After baking the sample at 300 C°, the MgO shows partial recovery of surface quality. The sample baked out at 950 C° shows five layering transitions on MgO indicating a clean surface.

assumptions made in performing the calculations may not be valid. Considering the TPD and the methane isotherms before and after pyridine exposure it is clear that the bonding of the molecule to the MgO surface is representative of a strongly physisorbed system.

### 4.5.7 Raman Experiments

Raman experiments were also performed with pyridine adsorbed on MgO. A quartz sample tube was also used in these experiments and the samples were prepared in a similar method as described in section 3.7.4. Raman spectra were recorded first from an empty, evacuated quartz tube and another quartz tube filled with pristine MgO so that a background could later be subtracted from a sample dosed with the molecular film. The raman spectrum was measured on a sample exposed with pyridine. The only signal detected was a broad peak presumably is a resultant of the significant fluorescence from the small MgO particles first identified by Loader et. al. [Hendra et al., 1971], or by the refraction of the laser beam by the quartz tube. To eliminate the refraction off the curved quartz tube the sample was removed and the spectra quickly taken. The vapor pressure of pyridine at room temperature is only $\sim 20$ torr so desorption should be negligible. Figure 4.44 shows the resulting raman spectra from the sample removed from the quartz tube.

Two peaks at 991 and 1030 $cm^{-1}$, are indicative of the $\nu_1$ and $\nu_{12}$ vibrational modes, respectively [Partal et al., 2000]. The $\nu_1$ corresponds to the symmetric ring puckering mode and the $\nu_{12}$ mode corresponds to the symmetric breathing mode where the three members of the six-member ring move outwards away from the ring center and the remaining three move inwards [Kline Jr. and Turkevich, 1944]. The result shows little to no shifting in peaks indicating the presence of bulk pyridine or a weak interaction with the surface as observed in pyridine adsorption on activated carbon by Lennon et. al. [Lennon et al., 2002]. Previous IR and raman studies of pyridine adsorption on MgO have shown upon adsorption a variety of peak splitting occur within this region of the spectra [Partal et al., 2000], [Lennon et al., 2002], [Kline Jr. and Turkevich, 1944], and [Corrsin et al., 1953]. One would expect that if

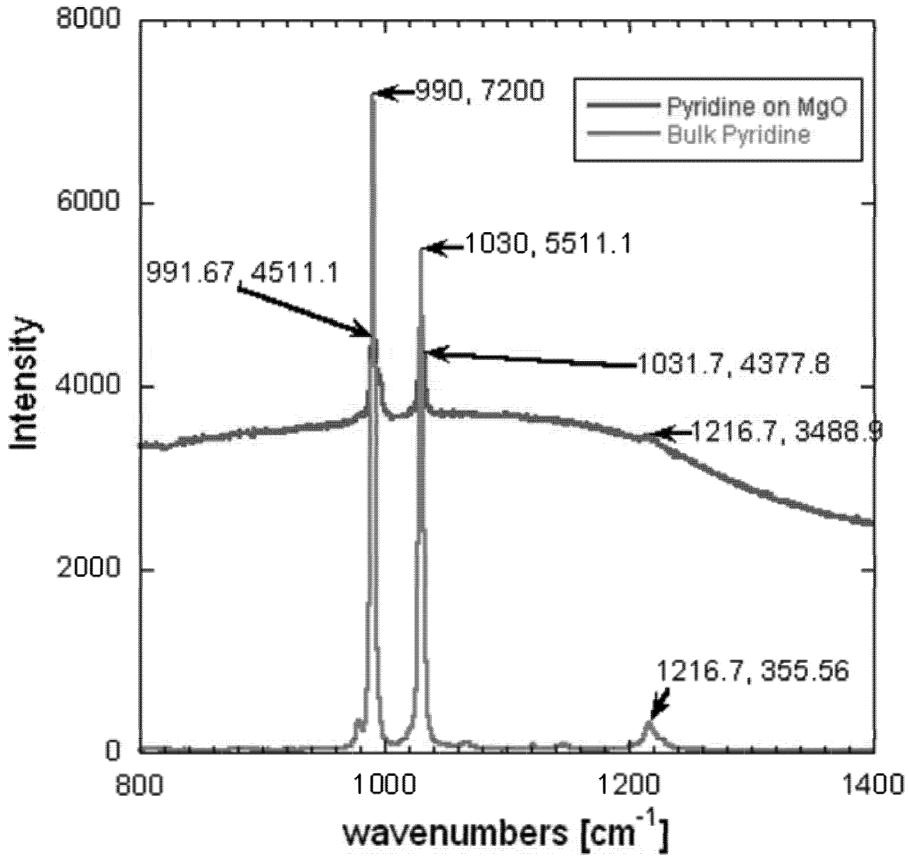


Figure 4.44: Raman spectra of pyridine adsorbed on MgO. Experiment shows little to no change in the positions or intensities of the bulk peaks which indicates the presence of bulk pyridine or that the the interaction of pyridine with the MgO surface is weak.

adsorption of pyridine to the surface took place via the nitrogen atom it would dampen the symmetric puckering and dilation of the ring causing either a shift, broadening, or splitting of bulk peak. Admittedly this result is a little surprising but future INS measurements with neutrons *in-situ* could alleviate the need to remove the pyridine dosed sample from the cell.

## 4.6 Pyridine on Graphite

Isotherms were performed within the same temperature range as described in the previous section detailing pyridine adsorption on MgO. Previous studies of pyridine adsorption on graphite have focussed on the surface characterization of various types of carbon polymorphs such as activated carbon and graphite. Pyridine is often used to detect surface acidity because of the lone pair of electrons on the nitrogen atom can readily be donated [Lennon et al., 2002], [Che et al., 1977], and [Zecchina and Stone, 1986].

### 4.6.1 Isotherms

With the exception of the behavior in the monolayer regime adsorption of pyridine on graphite appears to be similar to adsorption on MgO (see Figure 4.45). It is characterized by the nearly vertical rise with no inflection point up to monolayer completion, a behavior that mainly persists throughout most of the temperature range studied. Furthermore, the equilibration times in the first layer were very long ($\sim$ 2 hours), requireing nearly 72 hours per isotherm and thus made data collection difficult.

### 4.6.2 Monolayer Capacity

A comparison of isotherms performed on MgO and graphite show the same differences found in other systems where the graphite shows a more vertical step than MgO. Using a comparison with methane (see Figure 4.46), the APM of pyridine on graphite is calculated to be $\sim$ 75 Å$^2$. The series of isotherms indicates that the monolayer capacity of graphite does not suffer from the same surface degradation as MgO.

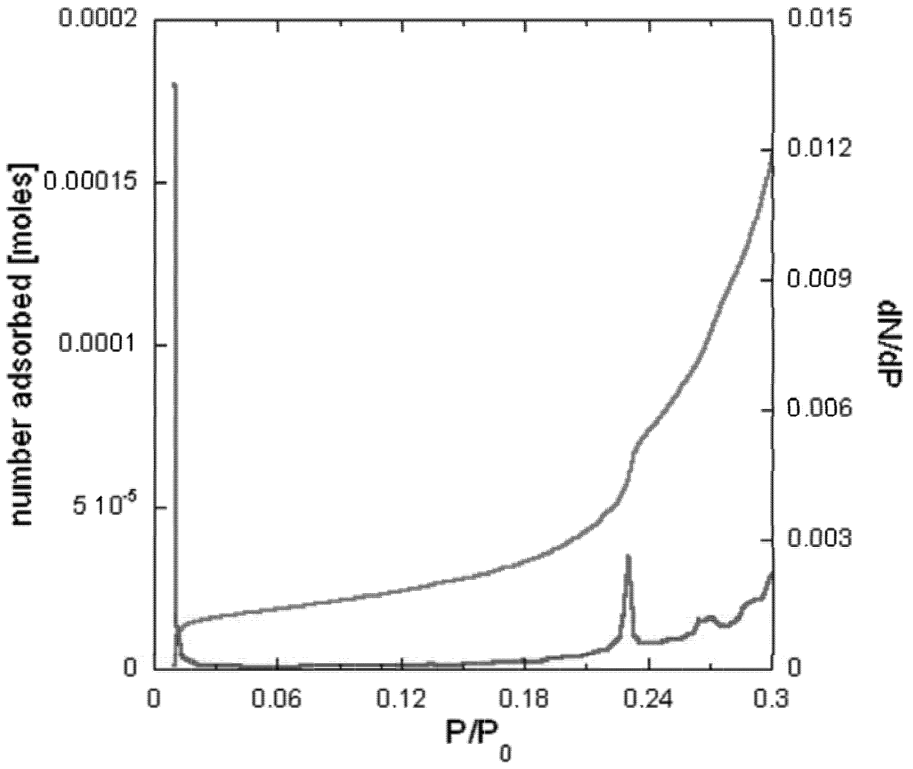


Figure 4.45: An isotherm (blue) of pyridine on graphite at 242 K and its associated numerical derivative (red).

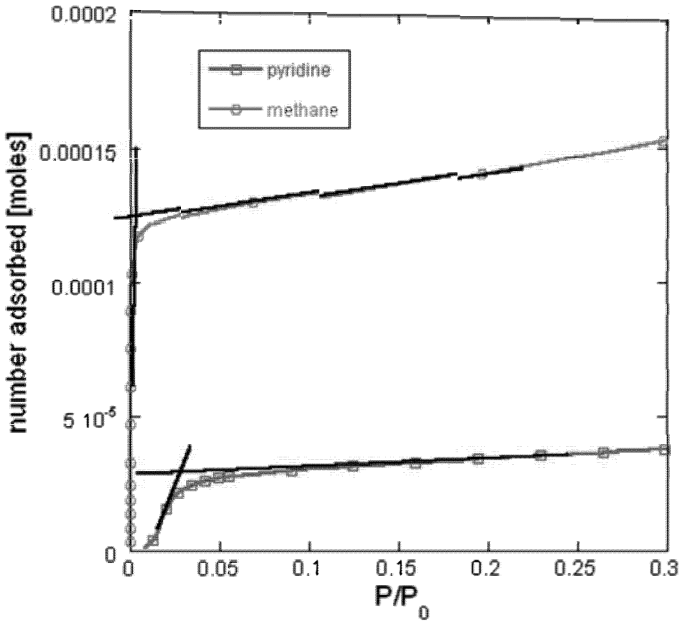


Figure 4.46: Monolayer comparison of methane and pyridine on graphite. From this comparison, an approximate area per molecule (APM) which pyridine occupies on graphite can be determined of $\sim 75$ Å$^2$.

Table 4.6: Thermodynamic values calculated from Clausius-Clapeyron plot of pyridine on graphite. Using a linear fit to the compressibility peak data, one can calculate $A^{(n)}$ (slope) and $B^{(n)}$ (y-intercept) values of each layering transition. Using the calculated $A$ and $B$ values, equations 2.106, 2.107, and 2.108 can be calculated for each layer.

| Layer | $A^{(n)}$ | $B^{(n)}$ | Q (kJ/mol) | $\Delta H$ (J/mol) | $\Delta S$ (J/K $\cdot$ mol) |
|---|---|---|---|---|---|
| 1 | – | – | – | – | – |
| 2 | 5090.10 | 19.75 | 42.32 | 1.32 | 7.87 |
| $\infty$ | 5248.30 | 20.70 | 43.63 | – | – |

### 4.6.3 Clausius-Clapeyron Thermodynamic Data

Figure 4.47 displays a Clausius-Clapeyron analysis for each layering transition. This system is different from pyridine adsorption on MgO notably in that the second step on graphite persists to higher temperatures than on MgO. Characterizing the first layer behavior id difficult at low temperaturesdue to the low pressures and almost vertical rise of the isotherm which is close to the resolution limit of the pressure transducer making determination of the location of the step difficult using the numerical derivative. Table 4.6 summarizes the values derived from the Clausius-Clapeyron analysis for ecah of the steps. There are some unusual values such as a positive $\Delta H$ for the second layer. A $\Delta H$ value near zero is indicative of bulk-like behavior at the second step.

### 4.6.4 Two-Dimensional Compressibility, $K_{2D}$

As noted above measuring the vapor pressure accurately in the monolayer regime is difficult. Hence the $K_{2D}$ was not used in the FWHM calculations for the first layer. The second layer $K_{2D}$ peaks are shown in Figure 4.48. A systematic decrease in intensity as temperature is increased is observed. This decrease in intensity and concomitant increase in peak width indicate the onset of a more liquid-like second layer.

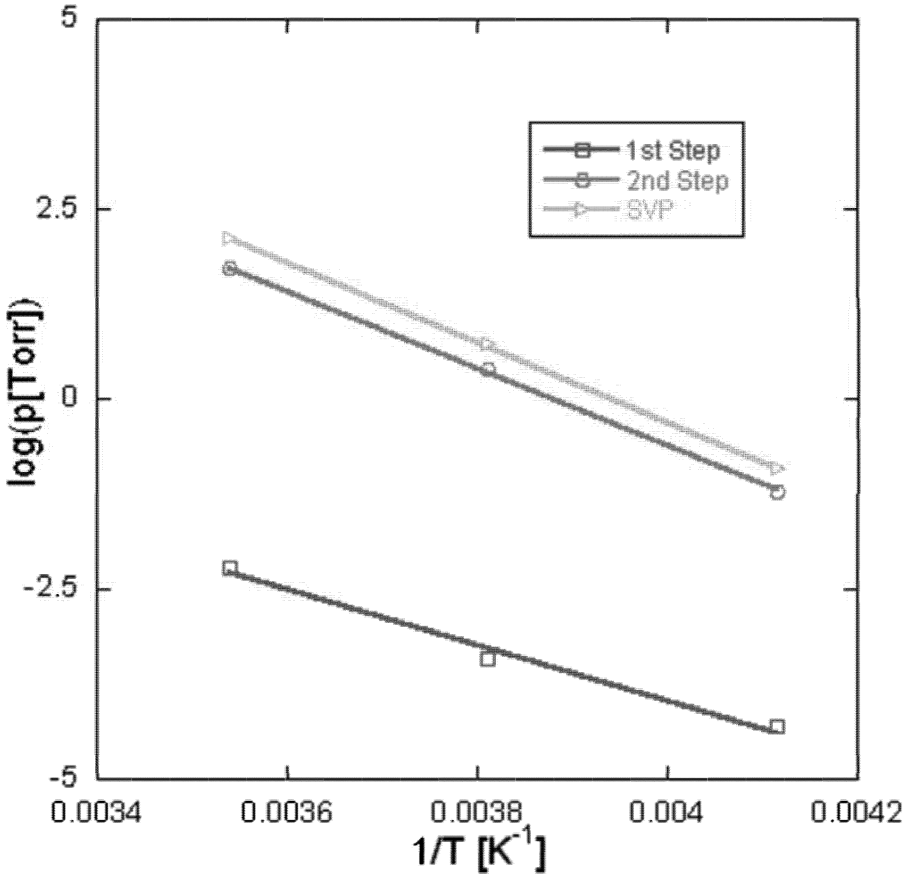


Figure 4.47: Clausius-Clapeyron plot of pyridine on graphite $K_{2D}$ peaks.

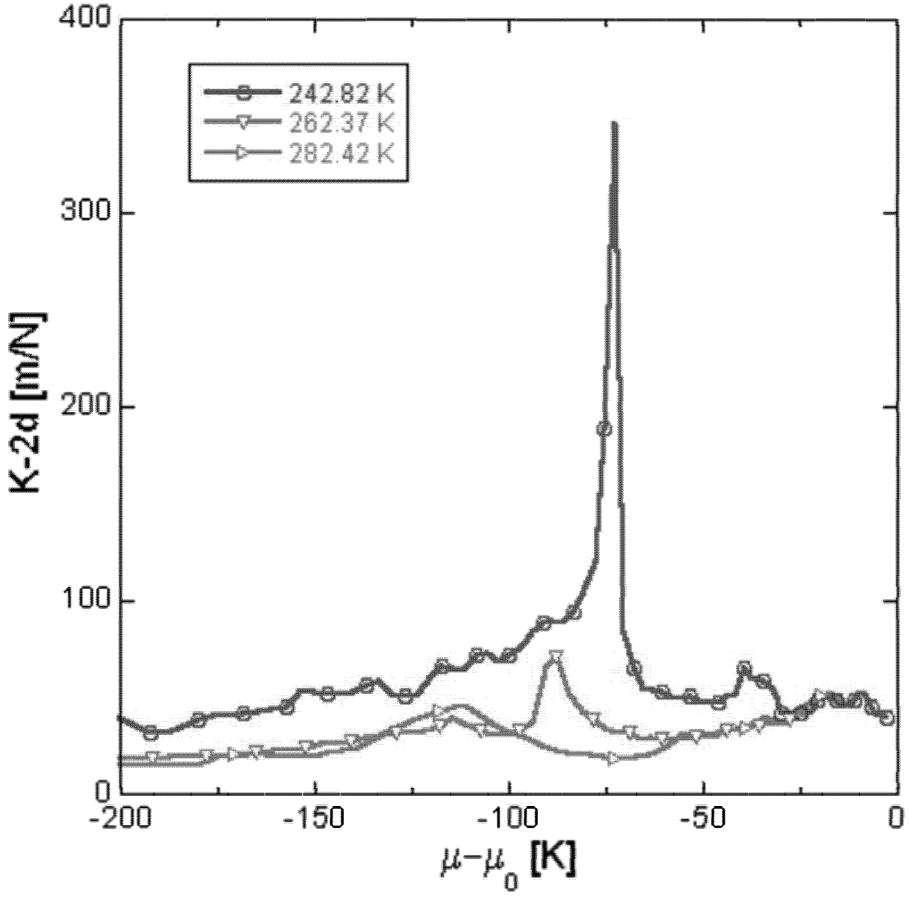


Figure 4.48: $K_{2D}$ plot of the second layering transition of pyridine on graphite. The compressibility peaks show a decrease in intensity and simultaneous broadening as temperature is increased.

### 4.6.5 Isosteric Heat of Adsorption, $Q_{st}$

The isosteric heat of adsorption was determined using isotherms more than 1 K apart. The assumption that the partial derivative can be approximated (see equation 2.118) using the difference between two isotherms seperated by a small temperature ($\sim$ 1 K) difference is less reliable when a large temperature difference is used. Figure 4.49 shows the result of such a calculation using two isotherms 20 K apart. A peak in the isosteric heat value near monolayer completion is observed as is the convergence to the bulk enthalpy of vaporization indicating that a large coverage the film converges to bulk liquid behavior.

## 4.7 Benzene on MgO

Studies that probed the nature of benzene adsorbed on MgO indicates little or no discrete layering takes place at any temperature. However it is interesting that there is a clear sign that a gradual transition from a non-wetting to complete wetting behavior is observed. Figure 4.50 shows a few benzene isotherms which illustrates the change in the wetting of the system. The absence of a discrete layering transitions is most likely a result of the large quadrupole moment of a benzene molecule. This quadrupole moment is generated by the conjugated $\pi$-bonding system of the aromatic ring which creates a positive and negative lobe. This potential difference generates an electric field. It seems that the adsorbate-adsorbate interaction overwhelms any adsorbate-substrate interaction resulting in an isotherm that forms the bulk phase on the surface creating droplets on the surface at droplets on the surface at $T > T_{triple}$. As a comparison with pyridine which is also an aromatic ring molecule, a methane isotherm was run prior to exposure to benzene and after a series of isotherms were performed. The difference in the layering transitions and monolayer capacity enables one to see how benzene affects the the MgO surface. Figure 4.51 shows the results of a methane isotherm run before and after exposure to benzene. The figure shows no surface degradation as is evident in the presence the same layering transitions found in the initial isotherm with little to no reduction in step height. The monolayer capacity of the isotherms are identical

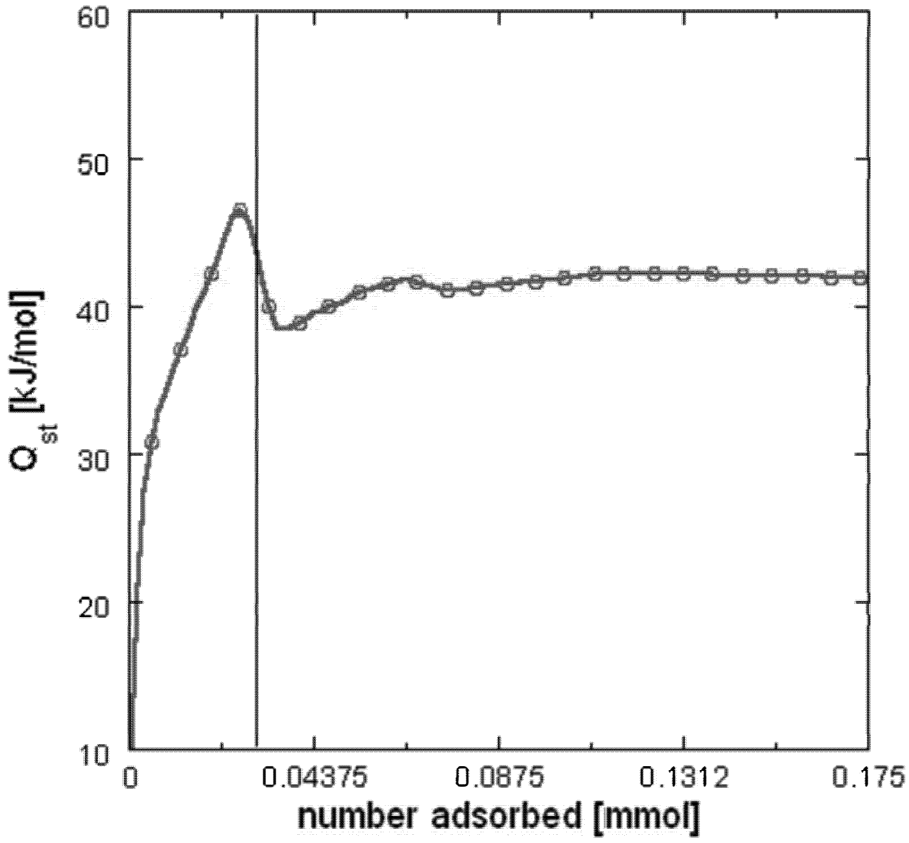


Figure 4.49: $Q_{st}$ of pyridine on graphite. Although this calculation is not of the quality of previous systems, one can still see an increase peak near monolayer completion and a convergence to the bulk enthalpy of vaporization.

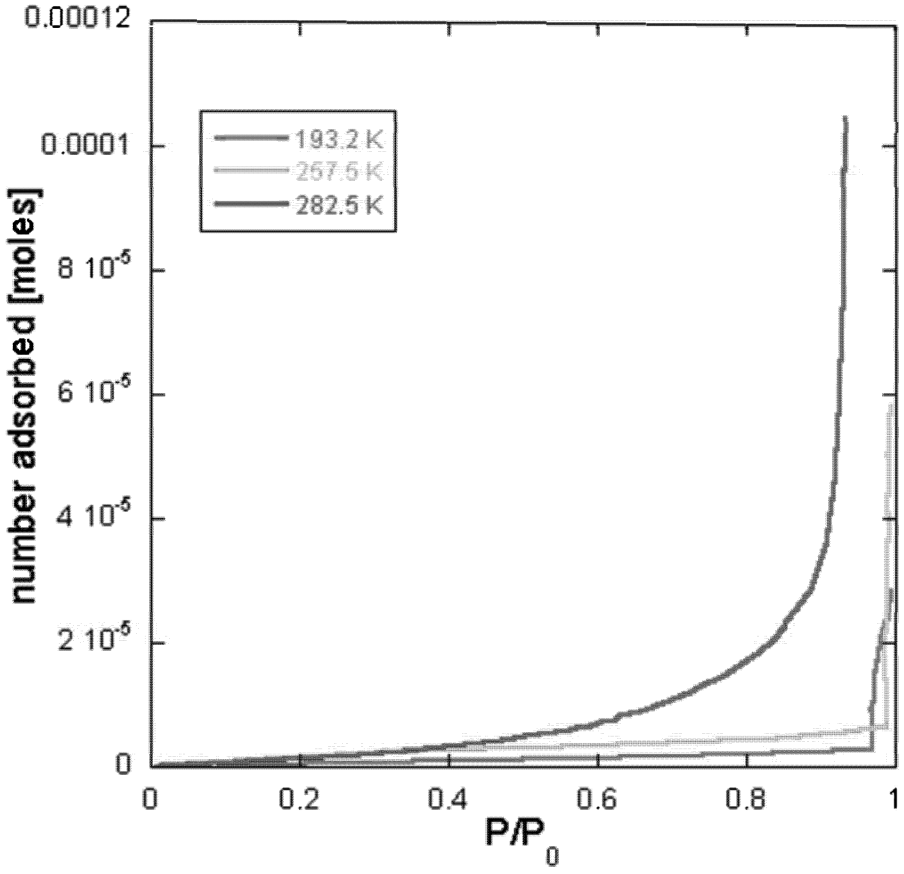


Figure 4.50: A set of Benzene on MgO isotherms. As temperature is increased, there is a continuous change from a non-wetting to a completely wetting system. Benzene also displays no discrete layer monolayer formation at any temperature which is indicative of a weak interaction with the MgO surface.

indicating little to no dissociate adsorption or strong physisorption of benzene to the MgO surface.

## 4.8 Benzene on Graphite

Adsorption of benzene on graphite studies were performed to characterize the adsorption properties and to provide a comparison with other adsorbates on graphite. One layering transition and a distinct change in its wetting properties as function of temperature was observed. At low temperatures benzene exhibits a nearly horizontal adsorption curve and an abrupt rise at the SVP indicating non-wetting behavior. An increase in temperature results in the wetting behavior changing to an incompletely wetting system while at higher temperatures, complete wetting takes place. A series of isotherms illustrating this behavior is shown in Figure 4.52.

Previous experimental and theoretical investigations have been performed. Delachaume et. al. found that benzene's wetting behavior changes from a non-wetting to incomplete wetting system using adsorption isotherms [Delachaume et al., 1983]. Neutron diffraction has also been conducted which that $T_{2D}$ occured at 130 K. This results in a $T_{2D}/T_{3D}$ ratio of 0.47, which is much lower than values of other adsorbed systems studied.

### 4.8.1 Monolayer Capacity

The monolayer capacity of benzene can be used to obtain an approximate area per molecule (APM) for benzene adsorption on graphite. In Figure **??** we compare a methane to benzene adsorption on graphite. This comparison yields an APM of 146.7 Å$^2$. The APM calculated is a very large in comparison to other adsorbate molecules and from previous experimental and theoretical work carried out by [Kiselev and Avgul, 1967], [Matties and Hentschke, 1996], and [Delachaume et al., 1983]. The APM calculated from previous work gives values ranging from 39.5 to 42.4 Å$^2$ [Delachaume et al., 1983], [Kiselev and Avgul, 1967]. The thermodynamically determined result obtained is unusual considering the the APM values from other adsorption experiments. The values from Kiselev et. al. and Bonnetain et. al.

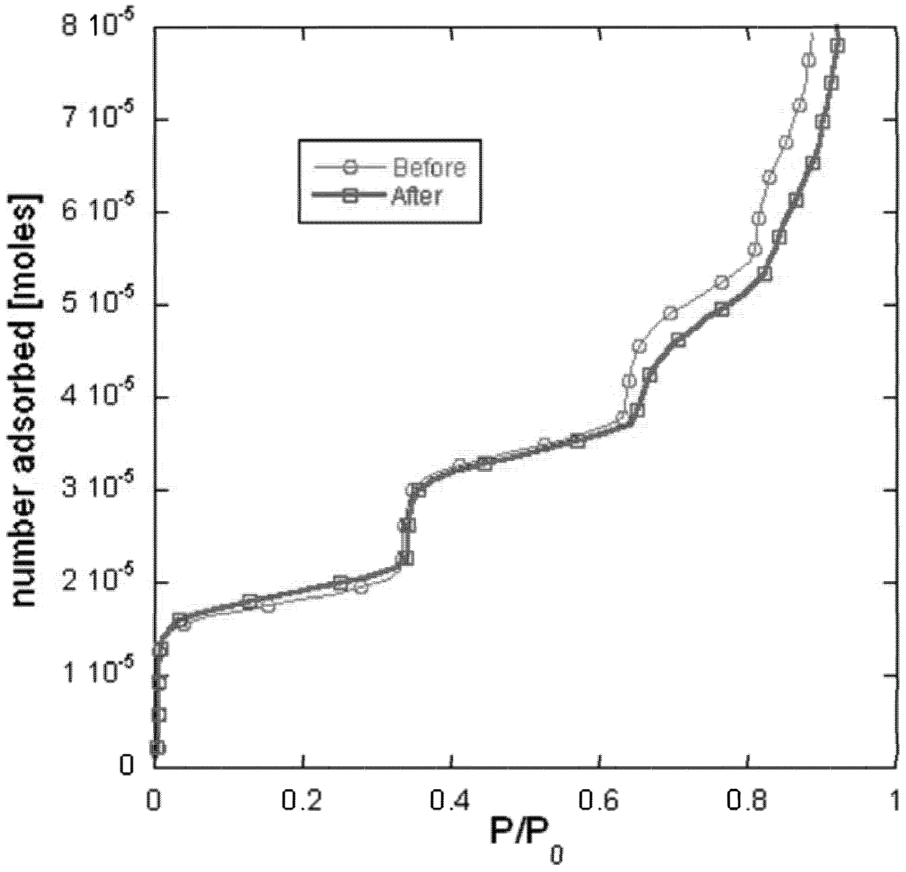


Figure 4.51: Methane isotherms before and after exposure to benzene show little no reduction in monolayer capacity and little change in step heights.

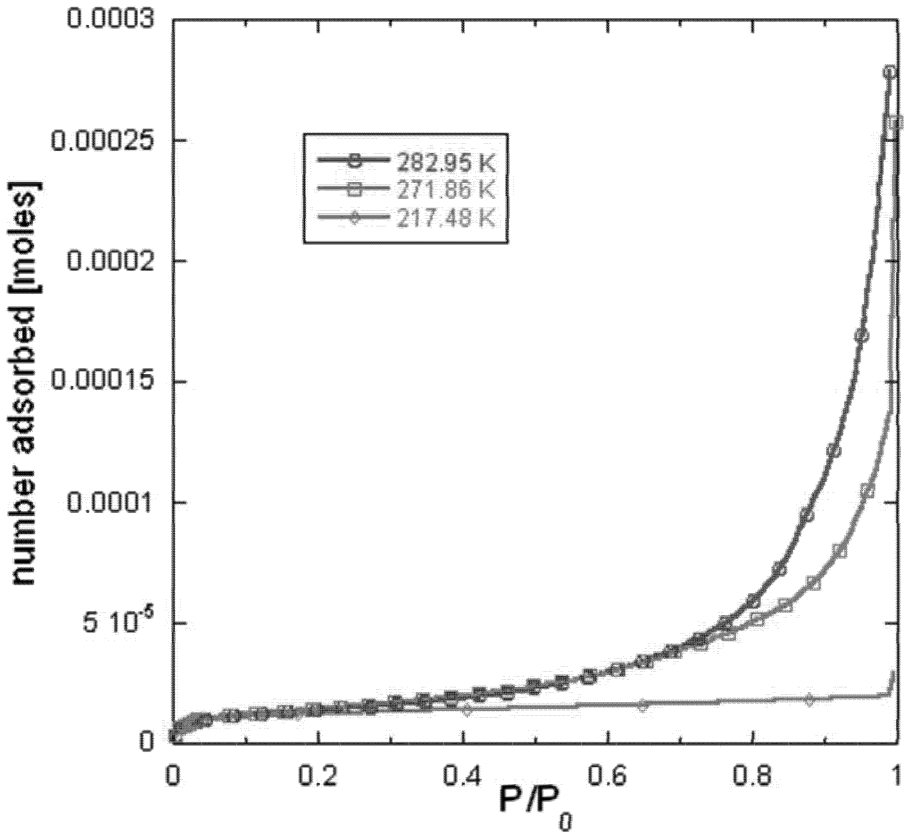


Figure 4.52: A subset of isotherms of benzene adsorbed on graphite. There is a distinct change from non-wetting to wetting behavior as temperature is increased.

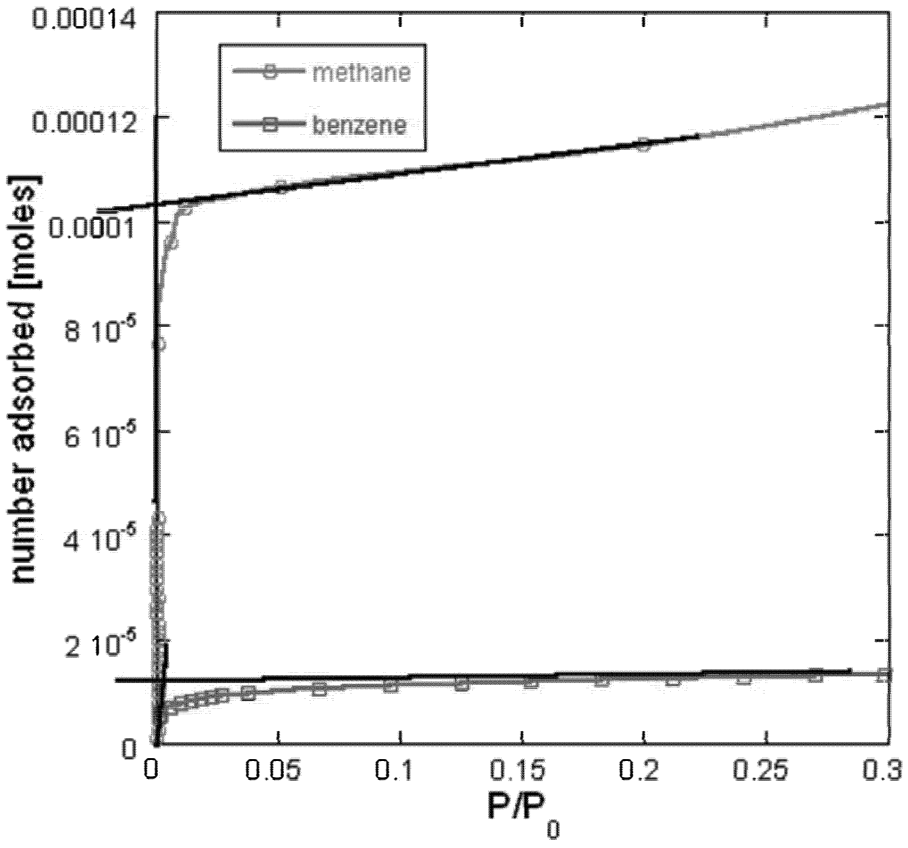


Figure 4.53: Area per molecule (APM) of benzene on graphite calculated from a comparison with a methane isotherm. The calculated values give a large value of 146.7 $Å^2$.

more closely resemble single molecule gas-phase calculations and range in value from 30 – 40 Å2. The unusual results could be a result of capillary condensation. The temperature of the isotherm used in relation to the bulk triple point can affect the thermodynamically perceived APM. The isotherm used for this comparison was taken at a temperature of 217.48 K. This temperature is far below the bulk triple point of benzene of 278.5 K which affects the APM calculation.

### 4.8.2 Isosteric Heat of Adsorption, $Q_{st}$

A representative isosteric heat of adsorption trace is shown in Figure 4.54. A comparison of the isosteric heat curves above and below the wetting transition reveals a difference in the peak profiles around the monolayer completion coverage. The isosteric heat calculated at 283.3 K shows a broad, asymmetric peak while sample calculation at low temperature shows a sharper, more asymmetric peak. The low temperature $Q_{st}$ peak rises rapidly, then after reaching its peak slightly before monolayer coverage, slowly declines in intensity. The high temperature $Q_{st}$ curve in the incomplete wetting portion of the phase diagram is broader suggesting that as coverage is increased, the amount of work needed to place a molecule on the surface slowly increases due to highly-liquid like state of the first layer being formed. This can be attributed to the relatively weak A-S interaction allowing benzene molecules on the surface to translationally move. As surface coverage approaches values near the peak $Q_{st}$ values the amount of space left for a molecule to diffuse on the surface decreases resulting in a greater barrier to diffusion creating solid-like regions on the surface. As coverage moves away from the peak the amount of work needed to place a molecule on the surface is reduced slowly because adsorption into the second layer becomes favorable before all adsorption sites near the substrate have been filled. Both isosteric heat plots when extended beyond the scope of the plot shown, converge to the heat of sublimation value of 44.4 kJ/mol.

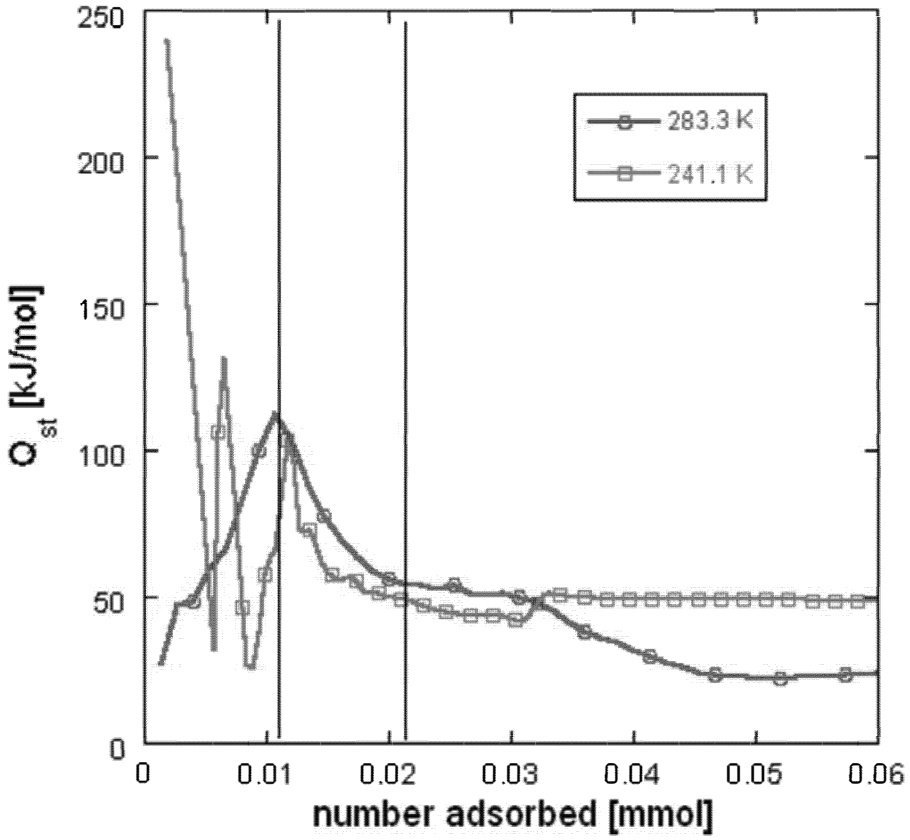


Figure 4.54: $Q_{st}$ of benzene adsorbed on graphite. Shows isosteric heats calculated at two different temperatures one in the incomplete wetting region and one below. The black lines indicate monolayer and theoretical bi-layer capacity.

The interaction energy between benzene molecules is primarily due to the large electric field created by the conjugated $\pi$-bonding scheme of the aromatic ring. This creates the favorable 'T'-configuration which benzene molecules preferably orient to lower their interaction energy. Dunitz et. al. used theoretical methods to calculate the dimer energies of molecules in this configuration and found that the T-configuration interaction energy is on the order of 2.7 kcal/mol [Schweizer and Dunitz, 2006]. This dimer energy is most likely more favorable than the interaction of the benzene with the surface structure. This is primarily due to the large quadrupole moment the molecule possesses of -23.9 $\times$ $10^{-40}$ C $m^{-2}$ [Do and Do, 2005].

# Chapter 5

# Structure and Simulation Results

To properly ascertain the structure of adsorbed thin films an experimental technique is needed which is sensitive enough to detect a atomically thin layer adsorbed on a powder sample. Neutron diffraction provides the ideal probe to study thin films of small hydrocarbon structures due to the properties described in section 2.8. To interpret the results from a neutron diffraction experiment, an analysis peak fitting program is needed to fit the diffraction peaks with an appropriate unit cell. Verification of neutron scattering studies requires theory to match results. Computer simulations can also be used as a bridge between experiment and theory by either either providing an initial prediction to the unit cell or to provide corroborative theoretical evidence of an experimental structure. This chapter describes the neutron diffraction and simulation results of the system studied.

## 5.1 Neutron Diffraction of *n*-Hexane on MgO

Neutron diffraction experiments were conducted at the ISIS pulsed spallation neutron source at the Rutherford Appelton Laboratory (Chilton, UK), using OSIRIS, a time-of-flight (TOF) instrument operating in a backscattering diffraction mode. The wavelength defining choppers are typically run at a frequency of 25 Hz producing a selectable 4 Å wide wavelength band at the sample position. The high flux and resolution available in the diffraction mode makes OSIRIS well suited for studies of adsorbed alkane thin films. The

diffraction studies were performed and analyzed using a difference technique described in section 2.12.

## 5.2 Two-Dimensional Peak Fitting

To index the diffraction peaks, a FORTRAN program is used which generates a 2D diffraction pattern given a lattice and basis. This program was adapted from one written initially by J.C. Newton at the University of Missouri-Columbia [Newton, 1989]. The code has since been and adapted for use with both x-rays and neutrons including x-ray image plates [Sprung, 2001]. Solving structures of monolayer adsorbed films is challenging because of the small number of bragg peaks and the signals are often weak.

To generate an initial guess several methods can be used. One method which may be characterized as the 'brute force' used a program which generates all possible unit cell configurations consistent with the observed diffraction trace. The program requires the input of an $a$ and $b$ unit cell parameter and an angle, $\phi$, which defines the angle of the parallelogram. Tolerances are then set for each parameter to narrow down the number of possible solutions. To reduce the number of possible solutions further, another program is used to test if any commensurate structures exist that could reproduce the observed reflections. This assumes the surface structure is commensurate with the surface similar to previous work done on smaller alkanes on MgO. This is accomplished by searching for unit cell which are multiples of the substrate unit cell. The maximum $Q$-range, size of the unit cell and $h$, $k$ values can also be set. The solutions are then sorted further to eliminate any unrealistic solutions. Angles at 90° are considered to be of higher probability than other angles because unit cells of smaller alkanes on MgO which have followed a similar structural motif all adopt a rectangular unit cell.

## 5.3 Computational Modeling

Matching theory to experimental results one can determine the forces which control the interactions with surfaces. Geometry optimizations were conducted using *Forcite* which is a molecular-mechanics based program which is part of *Materials Studio 4.1*® from Accelrys. The calculations in Forcite are based on the *ab-initio* parameterized *COMPASS* forcefield which is based on experimental results of the liquid and crystal structures of alkanes, and aromatic alkanes [Sun, 1998]. COMPASS is a forcefield method which uses a set of empirical formulas to mimic interatomic interactions. COMPASS ignores details of electron-electron and electron-nucleus interactions but rather concentrates on properties of interest in larger systems such as atomic and molecular dynamics. Forcite geometry optimization is based on reducing the magnitude of calculated forces until they become smaller than defined convergence tolerances. The forces on an atom are calculated from the potential energy expression and will therefore, depend on the forcefield that is selected.

The simulations are setup as a periodic system where one molecule is placed on the smallest possible lattice. The unique adsorption points on a lattice were then chosen as starting locations for the optimizations. The center of mass of the molecule is then placed above these points at a distance which avoids a large repulsive van der Waals interaction with the surface due to the overlap of orbital wavefunctions. The molecule is then rotated by increments until all unique angles are produced. The substrate lattice is then constrained, leaving only the adsorbate molecule to move. Geometry optimizations were also run with rigid body constraints applied to the adsorbate molecule. This disallows the molecule to change conformation during optimization. Rigid body constraints are useful in preventing the geometry optimizer from exploring unrealistic regions of configuration space. Comparison of the calculations can determine what effect the molecular conformation has on the surface structure and can give information on the strength of the interaction with the surface.

A theoretical binding energy can be extracted from the geometry optimization calculations using the formula,

$$E_{binding} = E_{surface} + E_{molecule}, \tag{5.1}$$

where $E_{surface}$ can be derived from the geometry optimization calculations by running the final configuration found by the optimization as two separate calculations. Running optimizations on the surface and single molecule in its final configuration one obtains the separated energies. The procedure is somewhat simplified due to the surface being constrained. The constrained surface contributes no energy to the total energy of the system so the final energy of the optimization should equal $E_{binding}$. Energies from optimizations provide an adequate comparison between other optimizations but not to experimentally determined values. A scaling factor is needed for the periodicity of the surface in the simulations to calculate $E_{surface}$. This problem with scaling also affects comparisons with different types of surfaces.

The Forcite program was also used to generate initial guesses at the unit cell by taking the lowest energy geometry optimized structure and placing molecules on a surface at different densities. Quenching, annealing, and dynamics simulations can then be run to find the minimum energy structure and unit cell of the minimized structure. The results from these simulations can then be input into 2Dim to generate a diffraction pattern. To test the validity of the modeling results, simulations were first run using *n*-butane on MgO and hexane on graphite. These systems were chosen because these surface structures have already been determined and can be used as a test to validate the simulation methods.

### 5.3.1 *n*-Butane on MgO

The butane on MgO surface structure calculated from previous 2Dim calculations was first input on top an MgO surface to form its unit cell. The system was then optimized and the final surface structure obtained (see Figure 5.1). Comparison of the Forcite unit cell to the neutron diffraction data shows a slight difference in the axial angles and herringbone angles

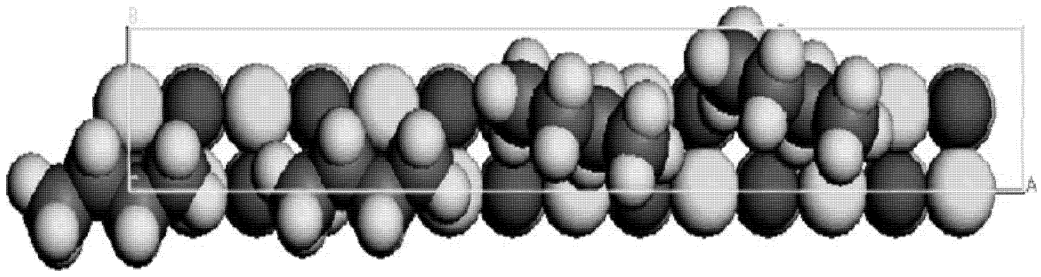


(a)

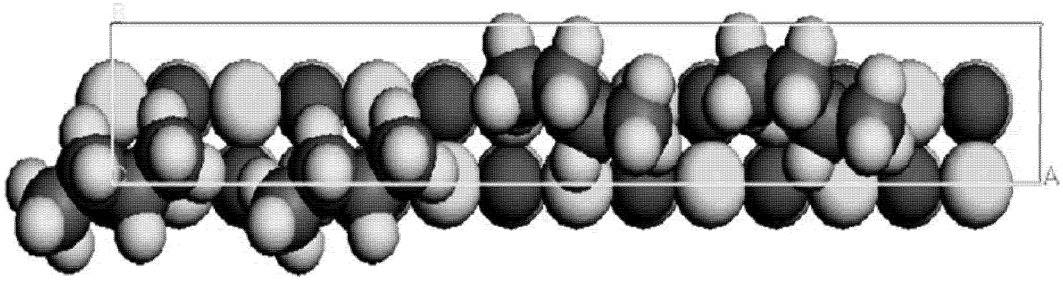


(b)

Figure 5.1: Unit cell of *n*-butane on MgO determined using Forcite, (a) and from a best-fit to neutron diffraction, (b). Both structures gives $7\sqrt{2} \times \sqrt{2}$ unit cell but differ in their respective herringbone and axial angles.

from the fit to experimental data. The Forcite simulations were allowed for axial rotations and conformation of the molecule whereas the fit to experimental data did not.

One can see in Figure 5.2 the dependence of herringbone angle and axial angles on the fit to experimental data. Slight changes in the herringbone angles can drastically change not only the number of peaks but their intensities drastically. By adjusting the herringbone angle an optimal fit was found using a herringbone angle of 18 degrees. In contrast, a change in the axial angles of the molecules within the unit cell only slightly changes the intensities of the peaks. Figure 5.2 shows a change in the axial angles of the two pairs of molecules within the unit cell. A supercell was constructed using the coordinates of geometry optimized single molecule on the surface repeated over the supercell (see Figure 5.3). A supercell of randomly oriented $n$-butane molecules on MgO was also constructed and optimized. These equilibrium structures were then compared and the coordinates input into 2Dim to determine the resulting diffraction pattern. Neutron diffraction shows butane adopts a commensurate $7\sqrt{2} \times \sqrt{2}$ R45 structure with lattice constants of $a = 29.47$ Å and $b = 4.21$ Å, $P_{2gg}$ symmetry and 4 molecules per unit cell. Results indicate that the COMPASS forcefield is a capable method of calculating two-dimensional surface structures and can provide some useful insight for determining surface structures of alkanes adsorbed on MgO.

## 5.4 *n*-Hexane on MgO

### 5.4.1 Initial Guess to *n*-Hexane on MgO Unit Cell

The solved structure of $n$-butane was used as a guide to generate an initial guess to the surface structure adopted by $n$-hexane on MgO. Previous diffraction work on smaller alkanes of the homologous alkane series display a structural a $x\sqrt{2} \times \sqrt{2}$ R45 motif. This $x\sqrt{2} \times \sqrt{2}$ structure is a motif found in smaller alkane surface structures adopted on MgO. If this motif is assumed to continue in $n$-hexane, then the first initial guess would be a $9\sqrt{2} \times \sqrt{2}$ structure, with four molecules per unit cell. Other initial guesses would include other values

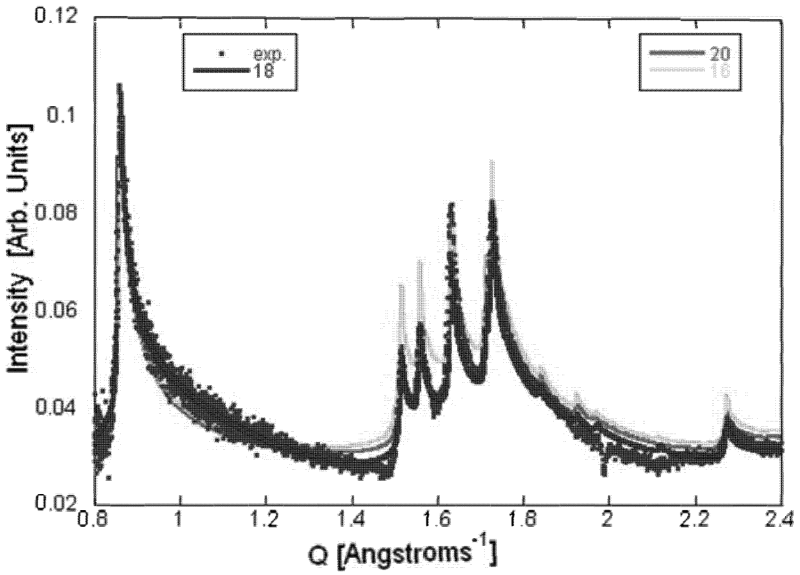


(a)

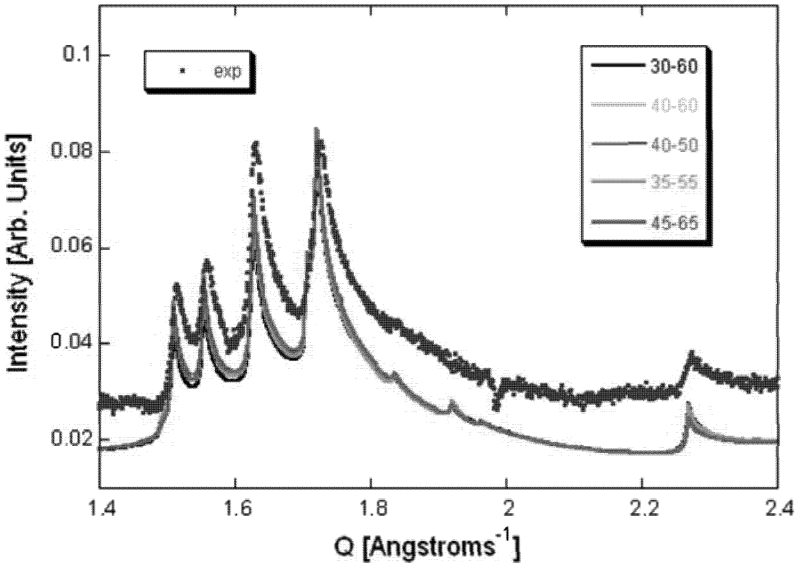


(b)

Figure 5.2: Adjusting the herringbone angles (a) slightly can alter the peak fit intensities more than by changing the axial angles (b). The best fit to the experimental data used a herringbone angle of 18 degrees.

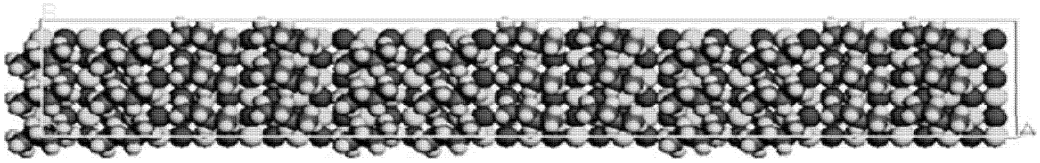

Figure 5.3: Geometry Optimized final structure of a supercell of *n*-butane on MgO. From this structure a repeat unit like the unitcell shown in Figure 5.1 can be seen.

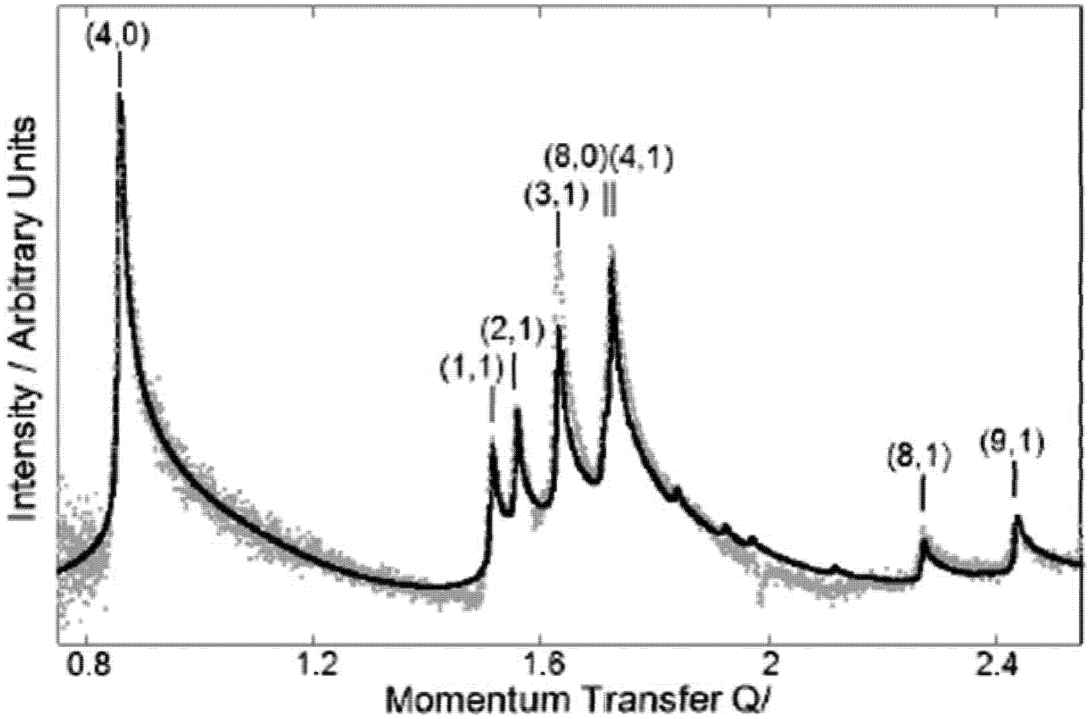


Figure 5.4: Experimental diffraction pattern and 'best-fit' calculated pattern by for *n*-butane adsorbed on MgO determined by 2Dim and quenching simulations. The peaks are indexed for the rectangular unit cell $a$=29.47 Å $b$=4.21 Å.

of $x$ in the $a$ lattice parameter direction and adjusting the number of unique molecules per unit cell. $n$-Hexane is assumed to be commensurate with the surface like smaller linear alkanes.

Previous studies conducted on smaller alkanes adsorbed on MgO have adopted $P_{2gg}$ symmetry. Figure 5.5 illustrates the $P_{2gg}$ symmetry group, the unique symmetry locations within the cell, and the allowed and disallowed reflections. The $P_{2gg}$ symmetry group only allows for ($h$,0) and (0,$k$) reflections where $h = 2n$ and $k = 2n$ [IUC, 1952]. Higher symmetry space groups such as $c2mm$ and $cm$ (see Figure 5.5) have also been found in other small alkane and substituted alkane systems studied and warrant exploration. Altering the number of molecules in the unit cell results in dramatically altered diffraction patterns. Figure 5.6 shows the resulting diffraction patterns from these initial guesses. The figure shows that none of the initial guesses match well with the experimental diffraction pattern (grey) collected. This could be attributed to a breaking of the structural motif on MgO due to a different symmetry group or larger unit cell.Another initial guess can be inferred by finding crystallographic faces of the bulk crystal which might match well with the underlying surface. Bulk $n$-hexane forms a $P\bar{1}$ symmetry unit cell with only 1 molecule per unit cell. $P\bar{1}$ is low symmetry space group and makes a comparison to the unit cell structure difficult.

To generate an intuitive initial guess another program can be used which generates all possible unit cell configurations from experimental peak positions. The results from this program gives 18 possible solutions for the unit cell parameters. Although the diffraction patterns match the peak locations of the experimental data, the intensities of the peaks do not match. One problem with the experimental data is the lack of a proper scan at $Q$-ranges $\leq 0.8$ Å$^{-1}$. Previous studies of alkane structures on MgO have shown a large predominant peak at $Q$-values $\leq 1$ Å$^{-1}$. This peak was not captured due to the large amounts of time needed to accumulate an appropriate number of counts at these $1.0 < Q < 0.5$ Å$^{-1}$ i.e. large $d$-spacings low-$Q$ values. This is due to the small number of backscattering events

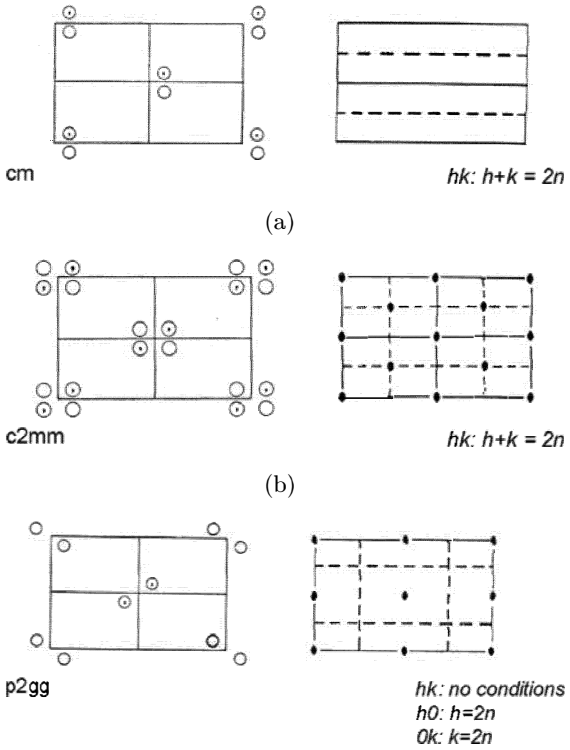


Figure 5.5: Illustration of the $cm$, $c2mm$, and $p2gg$ two-dimensional space group symmetries. To the bottom right of each figure are the allowed reflections for each space group. The right figure illustrates the location of rotation points where the circles indicate a points of symmetry. The figure on the left indicates symmetry elements where solid lines indicate mirror planes and dashed lines indicate glide planes.

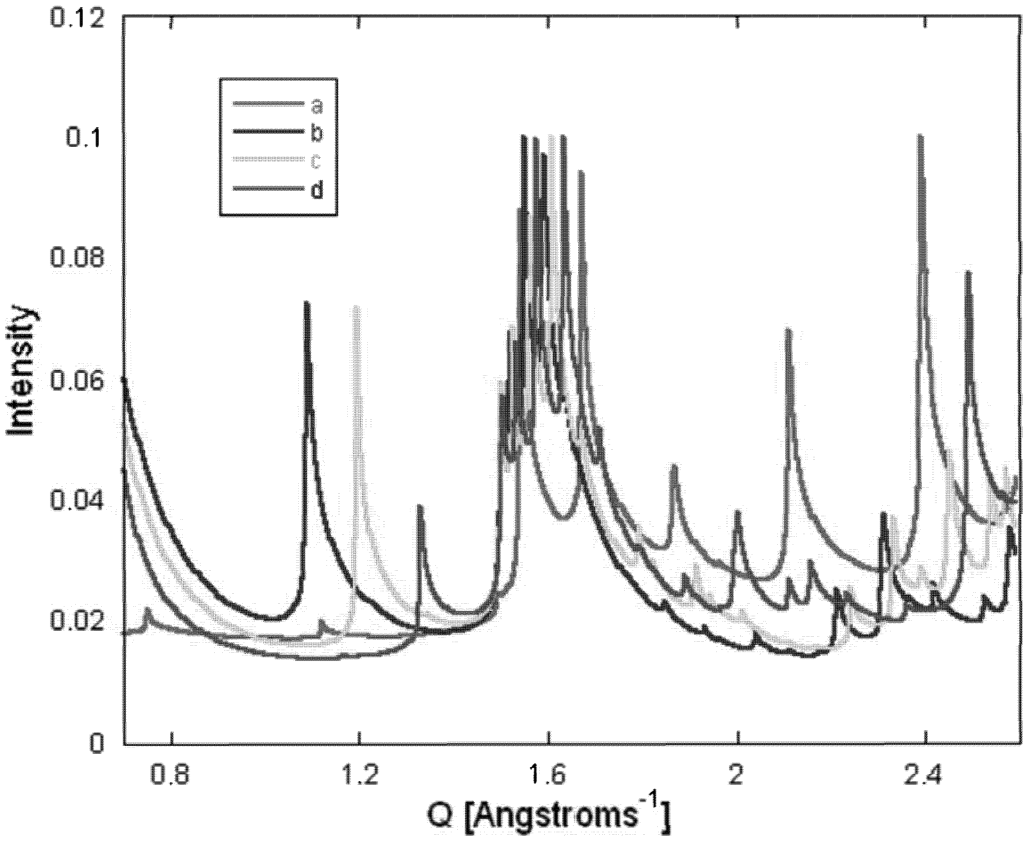


Figure 5.6: Diffraction patterns of initial guesses of the *n*-hexane on MgO unit cell. The grey trace represents the experimental data. The (a) line corresponds to a $4\sqrt{2} \times \sqrt{2}$ cell with 2 molecules per unit cell similar to *n*-pentane on MgO. (b) is an $11\sqrt{2} \times \sqrt{2}$ with 4 molecules per unit cell. (c) is a $10\sqrt{2} \times \sqrt{2}$ with 4 molecules per unit cell. (d) is a $9\sqrt{2} \times \sqrt{2}$ with 4 molecules per unit cell. All cell used a herringbone angle of 12° as a starting angle.

which occur at this angle. The lack of this dominant feature makes proper fitting of the diffraction pattern difficult. Another potential problem could relate to possible instrument problems in the low-$Q$ detector banks which may have artificially moved the diffraction peaks due to an error in the calculated TOF due to a binning error, however this cannot be determined yet for certain.

### 5.4.2 Simulations of *n*-Hexane on MgO

Geometry optimizations of single molecules on an MgO surface were first run using the procedure described in section 5.3. The MgO lattice was constructed so to properly capture a unit cell of the surface structure. Hexane was found to adopt two different minimum energy configurations on the MgO surface shown in Figure 5.7. The hexane molecule orients itself so that the carbon backbone follows a corrugation which maximizes the carbon interaction with the bridge adsorption sites of the lattice. The two different structures at very close final energies suggests a complex potential energy surface of MgO and a non-ideal interaction between the hexane and MgO PES which causes slight changes in conformation and orientation. Optimizations carried out with the hexane held rigid show adsorption in similar locations and orientation as the flexible optimizations (see Figure 5.12). This indicates torsion of the molecule or change in conformation plays little part in the adsorption of the molecule. This coupled with the presence of multiple final energy structures suggest a moderate A-S interaction.

Multiple molecules were placed on a larger surface supercell with the centroid and orientation of each molecule placed at the minimum energy location and orientation found from the geometry optimization. This larger supercell system provides the basis of the dynamics simulations. Simulations were attempted at different surface coverage densities to determine the lowest final energy configuration as described in section 5.3.

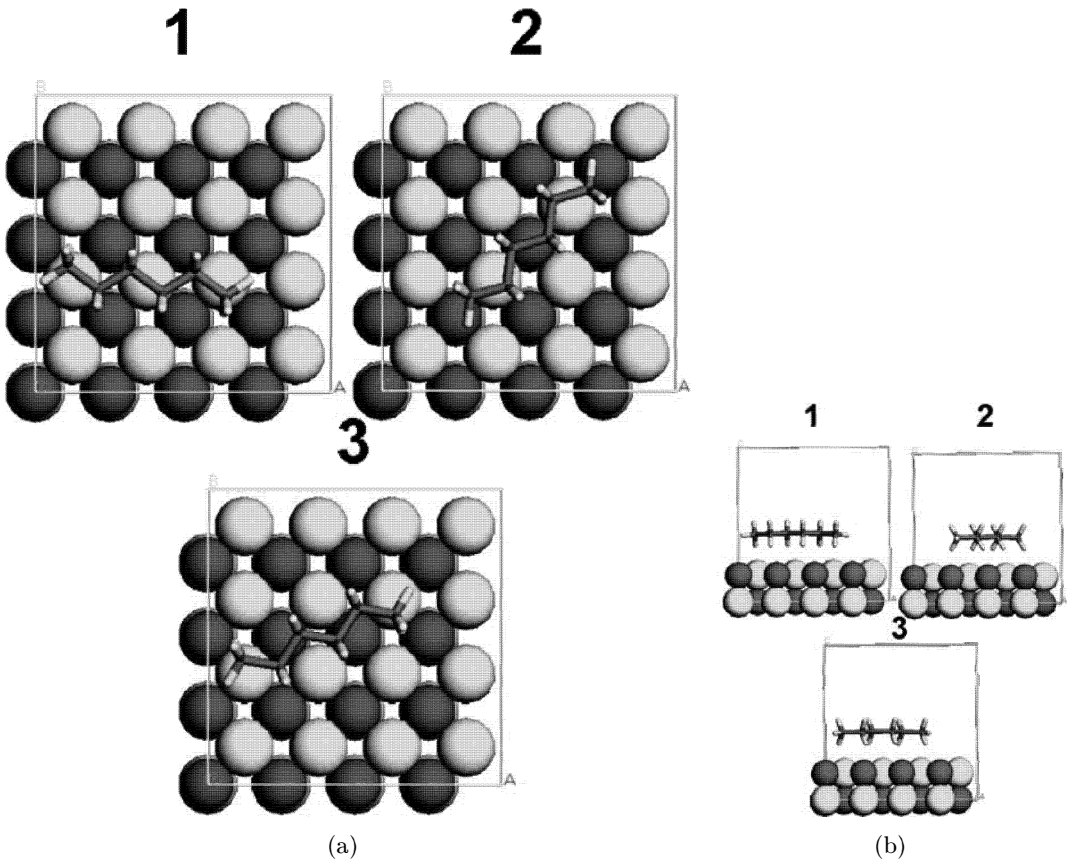


(a) (b)

Figure 5.7: Geometry optimized structures of *n*-hexane on MgO. (a) top, (b) side.

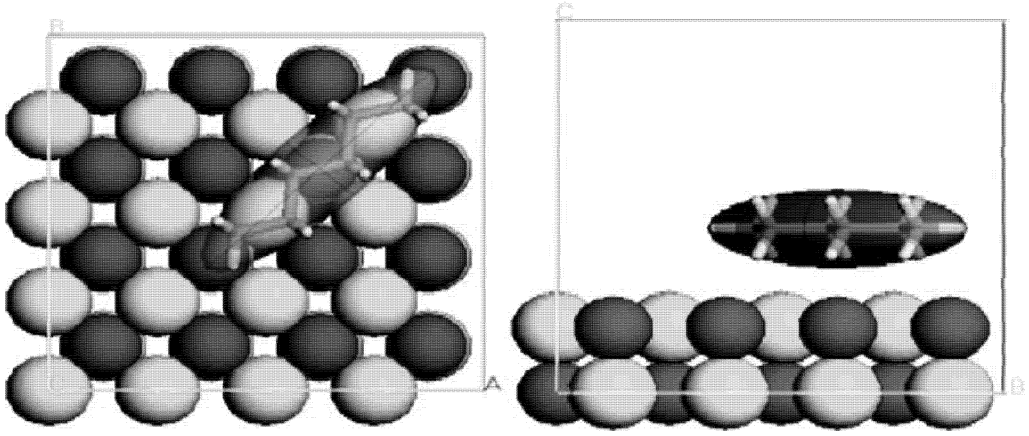

Figure 5.8: Minimum energy geometry optimized configuration of *n*-hexane on MgO with rigid molecule constraints. (a) top, (b) side.

### 5.4.3 Melting of *n*-Hexane on MgO

Running successive diffraction scans while gradually raising temperature one can observe the melting of the *n*-hexane on MgO. Figure 5.9 illustrates a set of diffraction data at different temperatures. As the temperature of the cryostat is raised there is a loss of long-range order which is indicated by the broadening of the diffraction peaks. This transition occurs in the temperature range of 130–140 K. This melting transition can be observed in both the heating up of a sample and the cooling of a samples illustrating that the diffraction peaks are not due to freezing out of a sample due to improper annealing of the sample during cooling.

### 5.4.4 APM of *n*-Hexane on MgO

Using the thermodynamic data as an upper-bound guide and a van der Waal calculation of a free molecule as a lower-bound, the molecular area hexane occupies on an MgO surface can be determined from computationally determined equilibrium structures and the match to the experimental diffraction pattern. Thermodynamic data calculates a thermodynamically averaged molecular area of 87 $Å^2$. Van der Waal calculations give a lower-limit molecular footprint of 24.2 $Å^2$. The molecular area calculated from unit cell parameters derived from simulations yield a value of 66.7 $Å^2$ which is smaller than the thermodynamically derived value but much larger than comparisons with simulation results from other systems. The deviation in these values can be attributed to the liquid-like nature of the first monolayer at the temperatures which isotherms were run at.

## 5.5 *n*-Hexane on Graphite

The structure of *n*-hexane on graphite has been determined previously by Taub et. al. Clarke et. al. and Wexler et. al. [Wu et al., 2001], [Herwig et al., 1997], [Roth and Wexler,

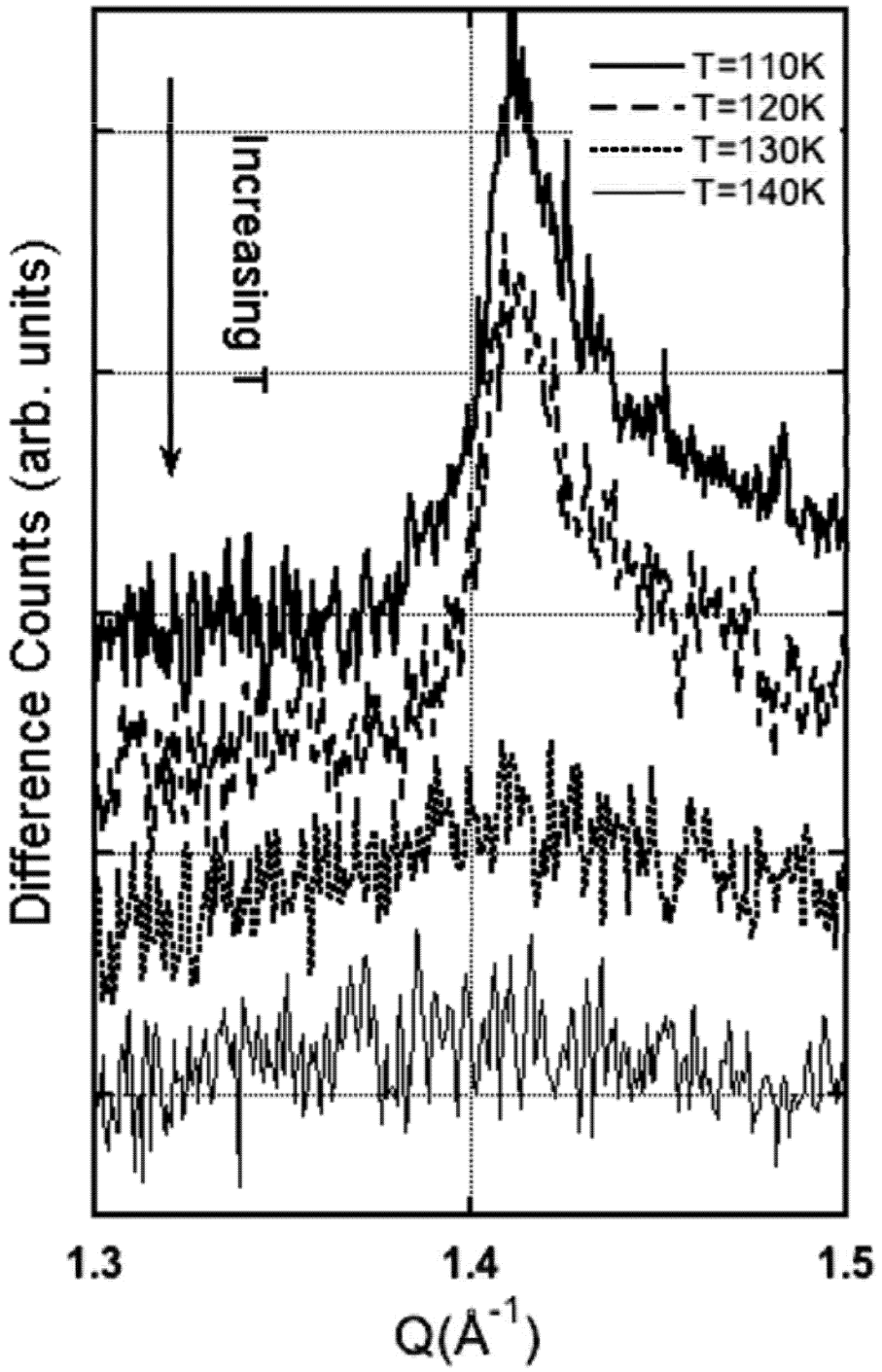


Figure 5.9: Melting of $n$-hexane on MgO. As temperature is increased, peak broadening of the peaks occur indicating a loss of long-range order.

2005]. The diffraction and simulation results yield a $4\sqrt{3} \times 2$ unit cell with $P_{2gg}$ symmetry and dimensions of $a$=17.04 and $b$=4.92 Å. Taub et. al. have found that $n$-hexane undergoes a uniaxial incommensurate to commensurate transition prior to monolayer completion along the $b$-axis.

Geometry optimizations find that hexane preferentially adsorbs with its carbon backbone along the graphite corrugation as shown in Figure 5.10. This configuration maximizes the interaction each carbon atom has with the three-fold hollow adsorption site and the hydrogen interaction with the center sites. Thermodynamic data suggests that the interaction of hexane with the graphite surface is stronger due to the profile of the first layering transition and the presence of three layering transitions on graphite as opposed to two on MgO.

Quenching, annealing, and dynamics calculations run with molecules started at the previously determined unit cell structure and at random locations to determine whether the simulations could yield a unit cell similar to the experimentally determined results. Previous simulations which have matched experimental results have required large amounts of computing time and higher order theory than that provided by the COMPASS forcefield method. The forcefield calculations have yielded unit cells similar to the higher level simulation data but simulations on larger surfaces still need to be carried out.

### 5.5.1 Melting of *n*-Hexane on Graphite

Previous melting simulations of monolayer $n$-hexane on graphite have been conducted primarily by Taub et. al., Clarke et. al. and Wexler et. al. [Hansen et al., 1992], [Clarke, 2001], [Roth and Wexler, 2005]. Simulations by Taub and Clarke predict monolayer melting temperatures well over the three-dimensional melting temperature of 178 K which is an unrealistic solution. General theory dictates that $T_{2D}$ should be around 0.6 of $T_{3D}$. The only simulation results which have yielded somewhat accurate monolayer melting temperatures have been by Wexler which calculates the onset of melting to occur at 138 K. This

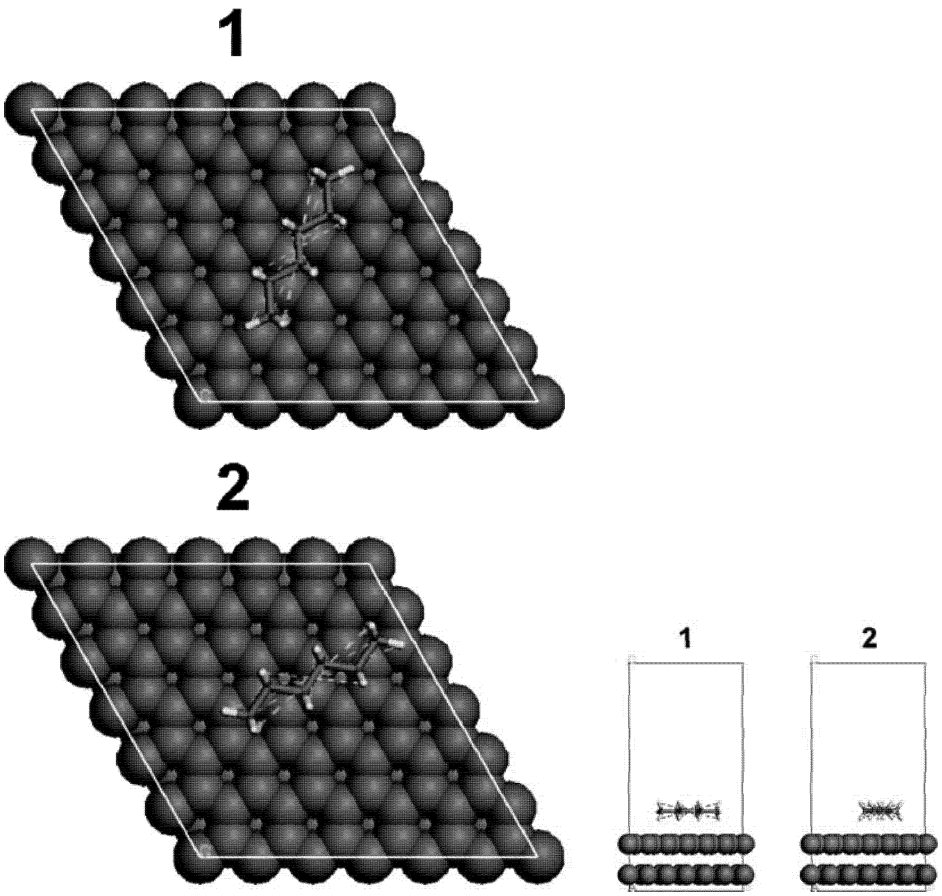


(a) (b)

Figure 5.10: Minimum energy geometry optimized configuration of *n*-hexane on graphite. (a) top, (b) side.

value approaches the experimental temperatures determined by LEED and QENS results. Experimental results have also shown a variety of monolayer melting temperatures. LEED experiments by Krim et. al. found melting of a hexane monolayer to occur at 151 K. Quasi-elastic neutron experiments performed by Hansen et. al. found monolayer melting temperatures at 170 K. Overall the monolayer melting temperature of hexane on graphite is shown to occur at higher temperatures than on MgO which is another indication of a stronger binding energy to graphite than MgO. The higher binding energy on graphite also contributes stability as seen by the three layering transitions found on graphite as opposed to the two found on MgO.

## 5.6 Cyclohexane on MgO

Geometry optimizations of cyclohexane on MgO gives two well defined minimum energy configurations (see Figure 5.13). The lowest energy structures place the center of mass of the cyclohexane above the center site and magnesium a-top sites. Adsorption over the center site maximizes the interaction of the downward facing equatorial hydrogens with the neighboring bridge adsorption sites. This configuration also maximizes the interaction of the downward axial hydrogens with the center adsorption sites. The adsorption site above the a-top oxygen site also maximizes these interactions although one axial hydrogen aligns itself with a bridge site and therefore causes a slight upward tilt in the molecule indicating a shallower potential well at the bridge site. This indicates that minimizing the interaction of the downward axial and equatorial hydrogens is of more importance in finding the lowest energy configuration than the interactions of carbon with the magnesium or oxygen. The cyclohexane seems to be able to utilize its three-fold axial hydrogen symmetry despite MgO's four-fold symmetric PES. Rigid-body geometry optimizations yield two minimum energy configurations with similar adsorption sites and orientations indicating there is no additional molecular torsion of the methyl groups beyond its equilibrium chair conformation. Leventis et. al. calculated the three-dimensional PES of cyclohexane and calculated a barrier height of 10.8 kcal/mol needed to change from chair to boat conformation [Leventis

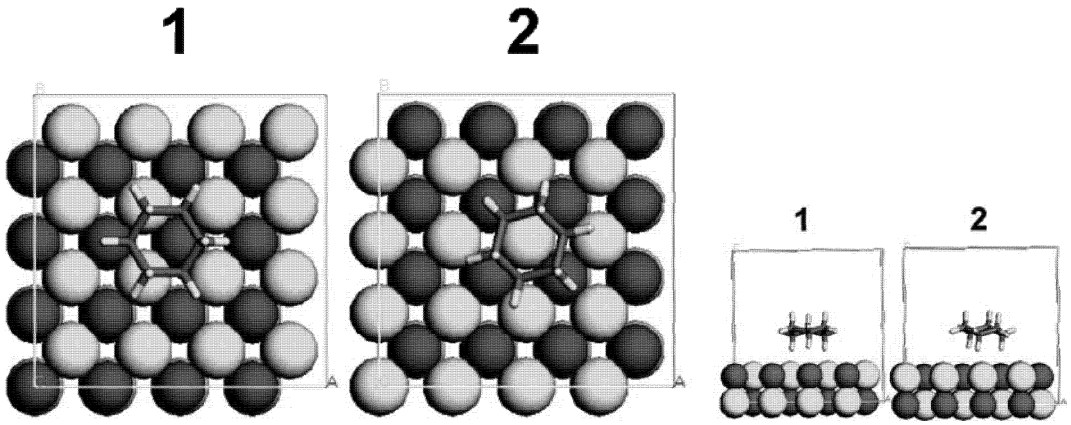


(a) (b)

Figure 5.11: Minimum energy geometry optimized configuration of cyclohexane on MgO. (a) top, (b) side.

et al., 1997].

Quenching simulations of cyclohexane on MgO at low coverage densities give a surface structure similar to the initial configuration of atoms. The one difference is the change in the orientation of the molecule about the surface. The molecule no longer lies oriented parallel to the surface but tilted by a slight angle. The tilted orientation affects all molecules and seems to be a result of A-A interactions pushing the molecules slightly out-of-plane from the surface. Figure 5.12 shows the final structure obtained from a quenching simulation run at 40.0 K. Quenching simulations at other temperatures were also performed at yielded similar final structures. Simulations run at a higher surface coverage density yielded an abundance of molecules promoted above the first layer and were not used for further studies.

### 5.6.1 APM of Cyclohexane on MgO

A comparison of the proposed surface structure of cyclohexane on MgO can be made with the bulk structure of cyclohexane. Two equilibrium bulk structures exist which are temperature dependent. Section 3.1.2 illustrates the two different structures which undergo a transition at a temperature of 186 K. The monoclinic Phase II exists at temperatures below 186 K with dimensions of 11.23, 6.44, 8.20 Åfor $a$, $b$, and $c$ respectively. The $a$,$b$ plane provides room for two molecules to fit end to end and shows a similar tilting motif of the molecules within the cell (shown by the line in Figure 5.13). The area occupied by the molecules in this plane is equal to 75.3 $Å^2$ which gives an APM of 37.7 $Å^2$. This values lies in between the lower-limit cutoff of the van der Waal area of 24.9 $Å^2$ and the upper limit set by thermodynamic data at 196 K of 70.70 $Å^2$. The orientation of cyclohexane molecules on this bulk crystallographic face also coincide with results in quenching simulations. Accelrys simulations give an APM of 29.1 $Å^2$ which is closer to the lower-limit van der Waal area per molecule. Isotherm measurements were taken at temperatures above 196 K which is above the transition temperature of the bulk crystal from the Phase II to Phase I structure. The

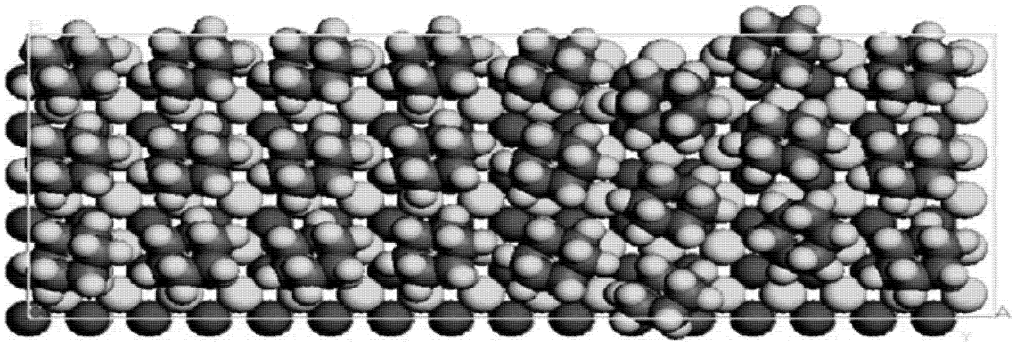

Figure 5.12: Minimum energy geometry optimized configuration of cyclohexane on MgO . The adsorbed molecules all have tilted off parallel from the surface which indicates a A-A interaction affecting the orientation of the molecule on the surface.

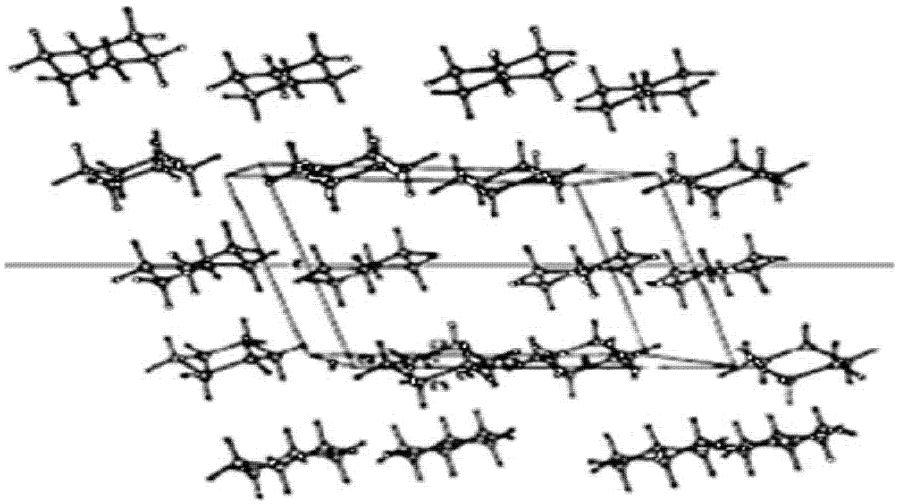

Figure 5.13: Bulk crystallographic structure of cyclohexane with proposed crystallographic face of surface growth of the Phase II crystal. The Phase II crystal exhibits rhombohedral symmetry with the unit cell dimensions of $a$=11.23, $b$=6.44, and $c$=8.20 Å. The lines indicate the proposed bulk crystallographic face surface growth could mimic on MgO or graphite.

Phase I structure is a cubic structure with 4 molecules per unit cell and an $a$ lattice parameter of 8.61 Å. However the Phase I crystal is a plastic crystal and molecular coordinates have only been obtained via monte carlo annealing simulations using the Phase II crystal as a starting point [Kahn et al., 1972].

## 5.7 Cyclohexane on Graphite

The procedure described in section 5.3 was used to attempt to extract a diffraction pattern using only simulation data. Geometry optimzations of cyclohexane on graphite yields only one minimum energy structure seen in Figure 5.14. Cyclohexane preferentially adsorbs with its center of mass above the three-fold adsorption site with its three downward axial hydrogens located in the center adsorption site of each graphene ring on the surface. The equatorial hydrogen interactions are also minimized by orientation with three-fold and center adsorption sites on the surface. Isotherm and thermodynamic calculations show cyclohexane on graphite displays the most stable thin films due to the presence of three distinct layering transitions all which are visible up to temperatures of 280 K.

Previous calculations of cyclohexane adsorption on graphite by Ricca et. al. show a similar minimum energy configuration on graphite with the center of mass occupying the three-fold adsorption site [Battezzati et al., 1975]. Ricca used a Steele's 10–4 potential with additional terms from Kiselev to analytically model the lowest energy adsorption site.

A series of dynamics and quenching calculations were performed on a larger supercell. Results show a similar tilting of the cyclohexane molecule on the surface indicating A-A interactions of sufficient strength to affect the molecular orientation on the surface. More quenching and annealing simulations need to be performed before any conclusions can be drawn from the simulations.

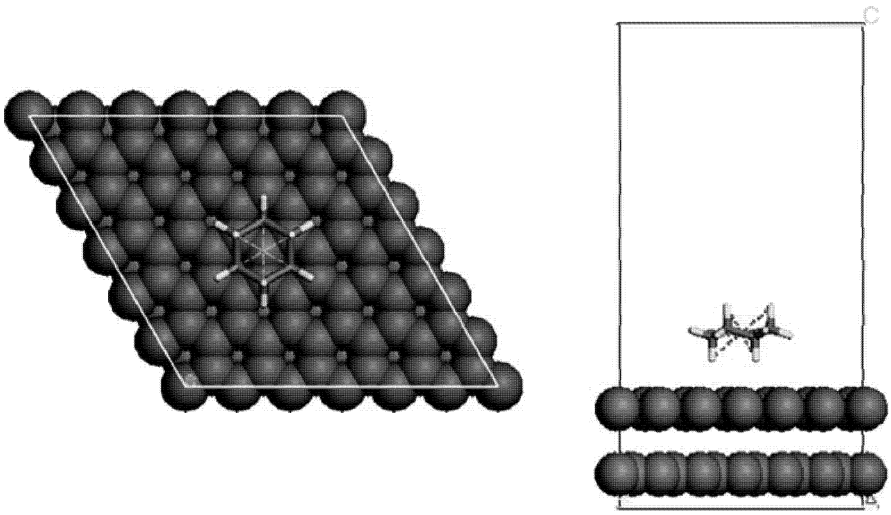

Figure 5.14: Minimum energy geometry optimized configuration of cyclohexane on graphite.

## 5.8 Pyridine on MgO

Pyridine on MgO shows only one optimized minimum energy structure which places the nitrogen atom a-top above the oxygen atom on the lattice (see Figure 5.15). To optimize this interaction between the nitrogen and the a-top oxygen site the molecule is canted slightly with the nitrogen closer to the surface than the rest of the molecule. This orientation maximizes the interaction between the neighboring planar hydrogens and the a-top magnesium adsorption sites. Taking the final coordinates the molecule lies 18° degrees from parallel with respect to the surface. The results show one minimum energy configuration which suggests that a more solid-like structure could be formed on the surface due to the strong propensity to adsorb at the same adsorption site with a high binding energy. Thermodynamic data supports the filling of the lowest energy potential sites on the surface with a tightly bound pyridine molecule which reduces the effective monolayer capacity of the surface due to much stronger binding energy. Isotherms display two distinct layering transitions before monolayer capacity is reduced significantly and only one layer is displayed.

Quenching simulations were performed and gave a periodic lattice of pyridine adsorbed with the same configuration as the single molecule geometry optimization. The initial and final structures show no change in orientation and configuration on the surface. Annealing simulations were also run on the system to determine if the quenching temperature of the simulation at 4.2 K is too cold to allow for any translational motion of the pyridine molecule. Annealing up to temperatures of 300 K showed a change in the orientation of the molecule about the nitrogen atom but no translational motion which indicates a strong interaction between the nitrogen and oxygen a-top adsorption site.

## 5.9 APM of Pyridine on MgO

APM calculations of pyridine on MgO can be inferred from quenching simulations performed and compared to thermodynamic and van der Waal calculations. The value from quenching

simulations gives a value of 27.30 Å$^2$. The value obtained from quenching simulations is very close to the van der Waal calculation of a pyridine molecule of 29.2 Å$^2$ and indicates tight packing of the pyridine molecules on the MgO surface. The packing of the molecules in the quenching simulations was also aided due to the tilt of the molecules which likely facilitated the closer packing of molecules on the surface. The simulation values were closer to the lower-limit van der Waal area due to the lack of motion by the molecules on the surface due to the tight binding potential of the molecule and the density of the molecules on the surface allowed for close packing of the molecules. Thermodynamic data yields a value of 64.9 Å$^2$. The thermodynamic APM calculation was performed using the lowest temperature isotherm available at 202 K. This temperature is below $T_{fus}$ for pyridine and thus should have solid-like properties on the surface. Previous studies in literature have quoted values between 20–35 Å$^2$.

## 5.10 Pyridine on Graphite

Thermodynamic results of pyridine on graphite shows no reduction in monolayer capacity over a series of isotherms which would indicate that pyridine has a weaker interaction with the graphite surface than MgO. Optimization results show that pyridine optimizes into two minimum energy configurations (see Figure 5.16). The lowest energy configuration places the nitrogen above a center adsorption site which places all planar hydrogens above a center or three-fold adsorption site. The second lowest energy configuration places the nitrogen above the three-fold adsorption site which also allows for the planar hydrogens to orient well with the three-fold and center adsorption sites on the surface. The final configurations show no canting of the molecules relative to the surface to maximize any interactions with the PES of the graphite surfaces seen in Figure 5.16. The presence of multiple geometry optimized structures indicates a possible weaker interaction with the surface and a more liquid-like state of the thin film formed.

Isotherm data shows two distinct layering transitions both which persist to higher temperatures than on MgO. The first layering transitions shows no features and an almost infinite rise until monolayer completion this is indicative of a higher binding energy of pyridine on graphite than MgO. However the reduction in monolayer capacity on MgO would indicate an even higher binding energy on MgO at selected sites on the surface, however proper identification of these sites cannot be assigned for certain.

## 5.11 Benzene on MgO

Optimizations of Benzene on MgO shows a variety of minimum energy structures which indicates a relatively weak interaction with the MgO surface. This is supported by thermodynamic data which shows no discrete layering transitions and only a change from a non-wetting surface to a complete, continuous wetting surface as temperature is increased. Figure 5.17 illustrates the an example of three lowest energy configurations. Simulations revealed many more configurations with slight variations of these structures. The optimized structures show no preference for a particular adsorption site on the surface or orientation which optimizes the interaction of its planar hydrogens with the MgO PES which indicates a highly liquid-like behavior and weak surface wetting behavior. Quenching simulations run using the lowest energy configuration yielded final structures with no periodic surface structure also indicating a weak interaction with the surface.

The bulk structure of benzene forms an orthorhombic unit cell with *Pbca* symmetry, 4 molecules per unit cell and unit cell dimensions of 7.39, 9.42, 6.81.(see section 3.1.4). The bulk unit cell illustrates the propensity of benzene to form perpendicular dimers. No crystallographic face of the bulk structure shows an absence of perpendicular dimers and is therefore very difficult to construct a surface structure using the parameters provided by the cell without the inclusion of perpendicular dimers.

### 5.11.1 APM of Benzene on MgO

APM comparisons could not be made with benzene on MgO simulations due to the lack of structure of the system which made it difficult to calculate a proper APM.

## 5.12 Benzene on Graphite

Optimizations of benzene on graphite show a different behavior than on MgO. Benzene is found to adopt only one orientation on the graphite surface with the center of mass of the molecule placed over the three-fold adsorption site. The orientation of the benzene molecule is such that it minimizes the interactions of the hydrogens with the surface by placing them over neighboring center or three-fold adsorption sites. The optimized structure showed no tilting and stayed parallel to the surface. Figure 5.18 shows the minimum energy geometry optimized structure and the initial and final energies of each optimization performed. The optimizations yielded a much higher energy than with other alkanes indicating a weak interaction with the surface. Quenching simulations run using optimized structures yielded a final structure with no periodic structure and molecules oriented perpendicular to the surface. This configuration was most likely preferred due to the large quadrapole moment of benzene and its strong propensity to form these perpendicular dimer interactions both with the surface and each other. Thermodynamic data suggests a stronger binding energy of benzene to graphite than to MgO. This is evident in the presence of a distinct layering transition on graphite as opposed to none on MgO.

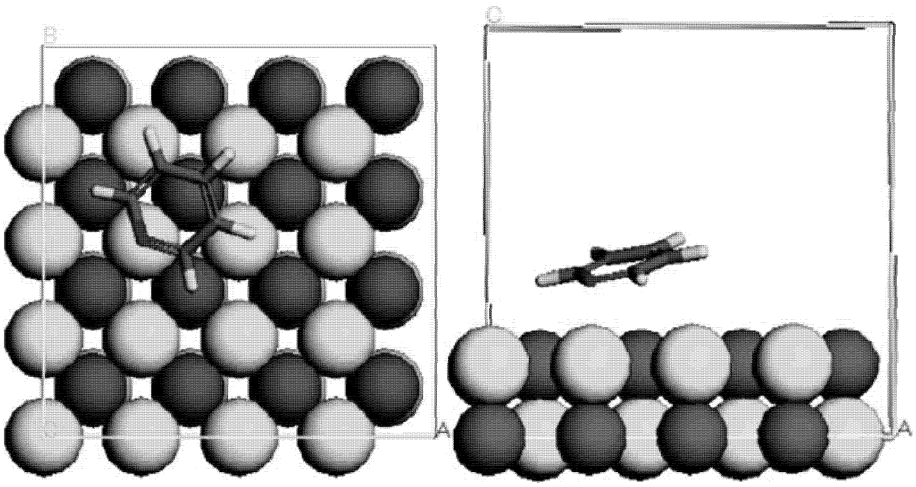


Figure 5.15: Minimum energy geometry optimized configuration of pyridine on MgO.

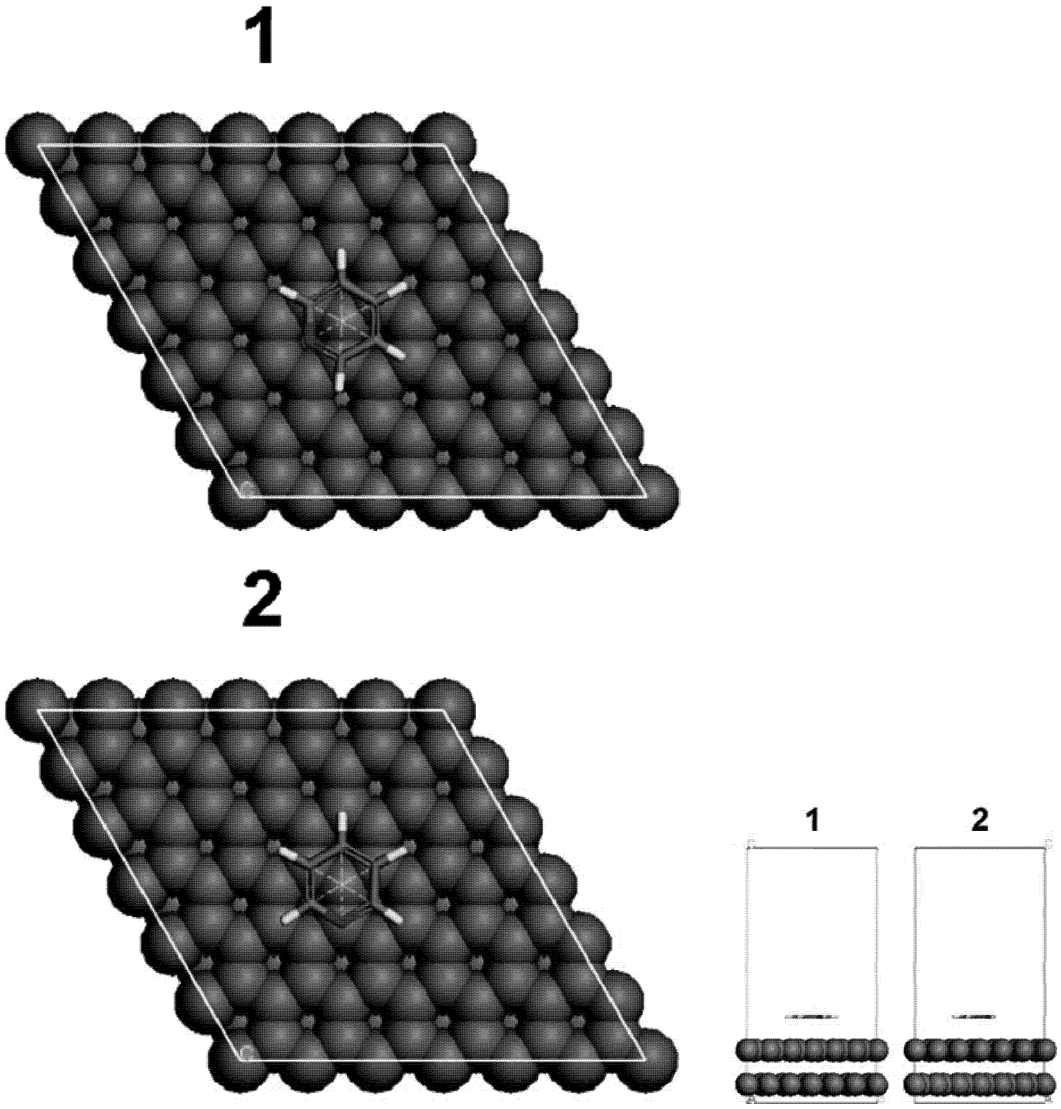


(a) (b)

Figure 5.16: Minimum energy geometry optimized configuration of pyridine on graphite. (a) top, (b) side.

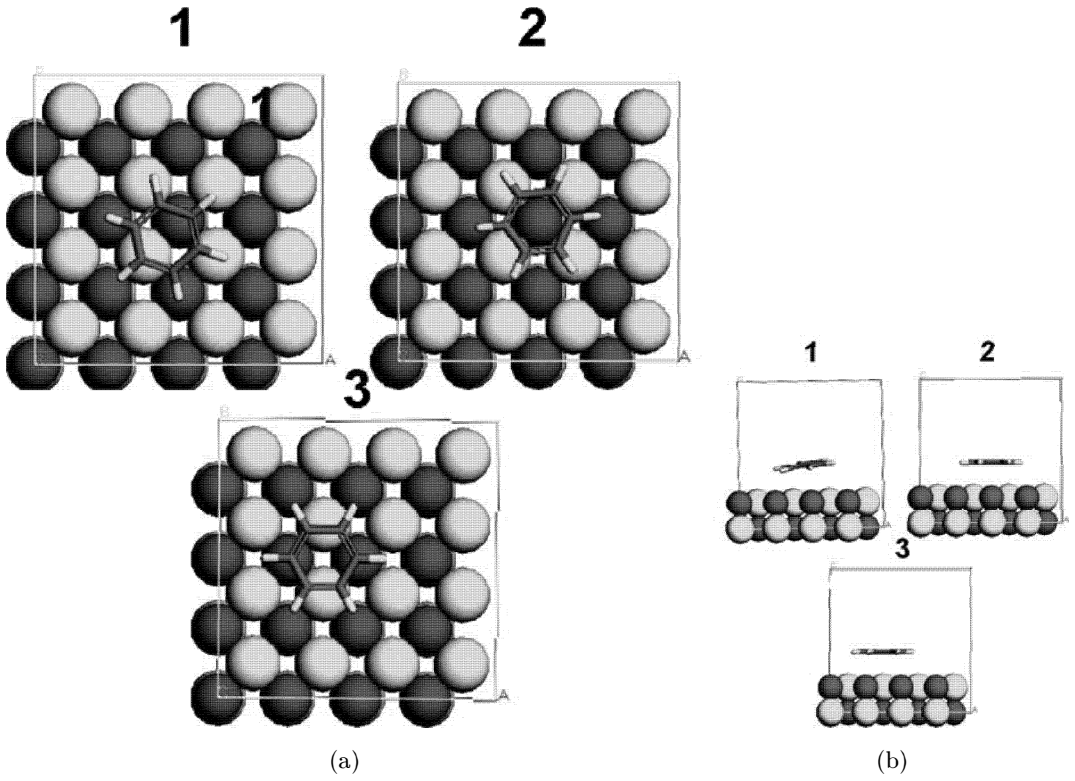


(a) (b)

Figure 5.17: Minimum energy geometry optimized configurations of benzene on MgO. (a) top, (b) side.

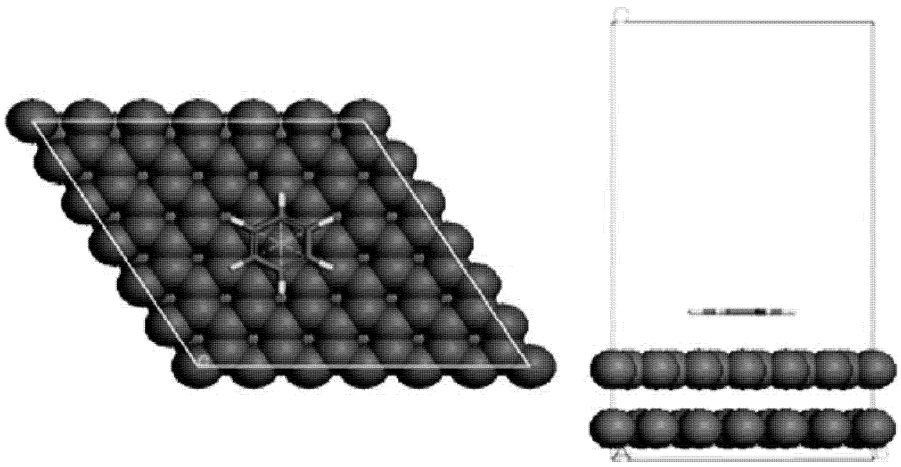

Figure 5.18: Minimum energy geometry optimized configuration of benzene on graphite.

# Chapter 6

# Conclusions

## 6.1 Thermodynamics

The use of volumetric isotherms has proven to be an effective method to extract a variety of thermodynamic parameters describing the physisorption of thin films of MgO and graphite. The use of other techniques like differential scanning calorimetry (DSC) or temperature programmed desorption (TPD) could provide additional thermodynamic information on these systems by supplying information about the heat capacities and binding energies of adsorbed thin films.

## 6.2 Neutron Diffraction

Despite the large background spectra and relatively weak signal, neutron diffraction has proven to be an invaluable to ascertain the surface structures the molecules form on MgO and graphite. Using a simple background subtraction, two-dimensional diffraction patterns can be extracted from the spectra giving the thin-film structures formed by the molecules interrogated.

## 6.3 Simulations

The use of the COMPASS forcefield has proven to be effective as a preliminary technique to predict minimum energy orientations of molecules on surfaces. The final configurations from the single molecule minimizations have yielded good starting points for further computational studies. Multiple molecule calculations on larger surfaces however do not seem to give as accurate results and their results cannot be relied on. The use of higher level calculations are needed to calculate more realistic minimum energy configurations. These calculations need to include a more sophisticated theory to more accurately model the electron-electron interactions between atoms and molecules. These interactions can more accurately model the A-A interactions in conjunction with the A-S interactions to give a more accurate picture of the interactions between these forces. Overall the use of this forcefield has proven to be an effective and very quick method to determine minimum energy structures on surfaces.

## 6.4 *n*-Hexane

A comparison of hexane adsorbed on MgO and graphite shows a greater binding energy with graphite than MgO. Evidence of this can be found in the thermodynamic data extracted from isotherm measurements, neutron scattering measurements, and simulations. A comparison of the entire set of isotherms shows the appearance of three layers on graphite and only two layers on MgO. The second layering transition disappears at 248 K and 280 K for MgO and graphite respectively. The $T_c(2)$ values are 230 K and 198 K for MgO and graphite respectively. This result is contradictory to the temperatures where the layering transitions occur. One would expect that for hexane on graphite that the $T_c(2)$ would be larger than on MgO because of the need to support a third layer would necessitate a solid-like support as the underlying structure. $T_c(3)$ of graphite also occurs at a temperature of 198 K which indicates an onset of liquid-like behavior in both the second and third layers of graphite. The onset of $T_c(2)$ and $T_c(3)$ would indicate a large amount of layer promotion and demotion between the two layers and the presence of a two-dimensional fluid in the

second layer. Thermodynamic data derived from Clausius-Clapeyron data shows comparable values of $Q^n$, $\Delta H$, and $\Delta S$ indicating binding energies of the same magnitude.

A comparison of the two-dimensional melting temperature versus the three-dimensional melting temperature $T_{2D}/T_{3D}$ can provide a comparison of the dimensionality of the system. Hexane on MgO gives a $T_{2D}/T_{3D}$ value of 0.73–0.79 depending on the value used for $T_{2D}$. Using results from LEED and QENS measurements the $T_{2D}/T_{3D}$ value ranges from 0.86–0.96 for $n$-hexane on graphite in [Herwig et al., 1997] [Krim et al., 1985]. This indicates more three-dimensional behavior on graphite than MgO and this is supported in the locations of the $T_c$ temperatures. The proximity of $T_c(2)$ and $T_c(3)$ of $n$-hexane on graphite suggests that there is significant interlayer promotion and demotion.

A comparison of the thermodynamically derived APM by comparison to methane shows a smaller APM on graphite than MgO. This result could suggest a more liquid-like behavior on MgO and hence a weaker A-S interaction than with graphite.

Geometry optimizations of both systems show several minimum energy structures which indicates that the binding energies of hexane on MgO and graphite are comparable in energy. A one-dimensional potential energy surface can be created using the geometry optimizations calculated at different adsorption sites on the MgO and graphite surfaces. Figure 6.1 shows the potential energy surfaces derived from initial energy calculations of a hexane molecule on MgO and graphite rotated about its center of mass at the four unique adsorption sites. Both PES show a large number of minima which correspond the possible configurations hexane favors on the MgO and graphite surface. It is difficult to determine whether melting is first order or second order on MgO or graphite. Taub and Wexler describe a temperature dependent phase change based on the creation of dislocations in the thin film due to conformational changes in the hexane molecule similar to KTHNY theory of the melting of two-dimensional crystals. However this is only supported by simulation

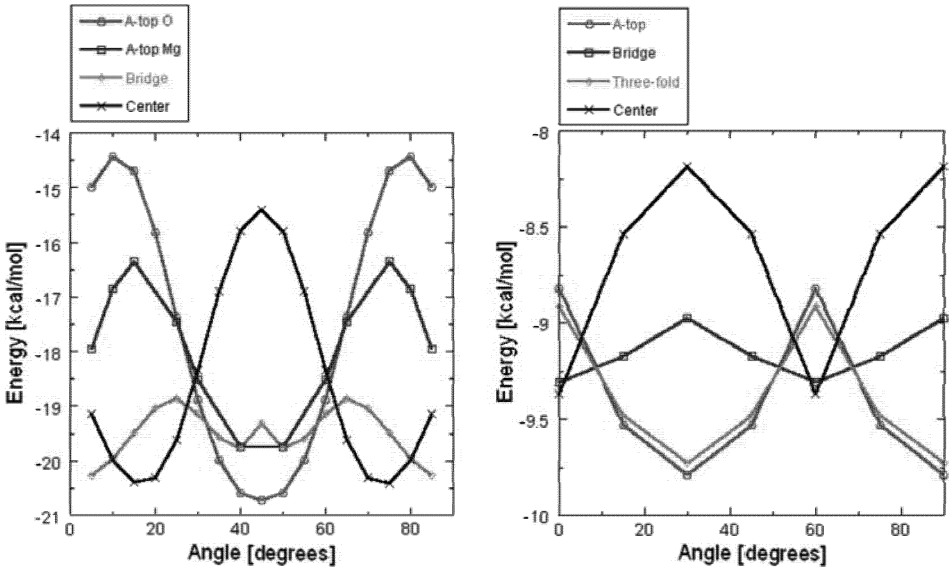


(a) (b)

Figure 6.1: Potential energy surfaces of *n*-hexane on MgO and graphite generated from single molecule geometry optimizations. (a) MgO, (b) graphite.

data. KTHNY theory is not applicable to these systems because these are not truly two-dimensional systems due to the significant layer promotion and demotion creating a flux of molecules in and out of the surface structure. Neutron diffraction, INS, and QENS are needed to properly determine the order of phase change.

## 6.5 Cyclohexane

Thermodynamic data of cyclohexane shows two layering transitions on MgO and three layering transitions on graphite. The second layer on MgO is only visible over temperatures of 232 K up to a temperature of 281 K. Cyclohexane on MgO undergoes a transition from a non-wetting system at low temperatures to an incomplete wetting at moderate temperatures to a complete wetting system at high temperatures. Within the same temperature range cyclohexane on graphite maintains three layering transitions throughout almost the entire temperature range. FWHM data of isotherm compressibility peaks show a $T_c(2)$ of 278 K on MgO 286 K on graphite. FWHM data of of cyclohexane on graphite gives a $T_c(3)$ of 279 K. The $T_c(2)$ values coincide with isotherm layering trends which show three distinct layers on graphite throughout a large temperature range as opposed to two on MgO which indicates a much tighter binding to the graphite surface. The value of $T_c(3)$ from FWHM data is close to the value of $T_{fus}$ and $T_{triple}$ of 279.7 K and 279.6 K respectively. The proximity of $T_c(3)$ to the fusion point and triple point is indicative of the formation of bulk-like fluid layers and the onset of a hypercritical fluid phase with continuous layering process.

Comparisons of isosteric heat calculations on MgO and graphite show a sharp defined peak near monolayer completion on graphite. This indicates a sharp rise in the amount of work needed to adsorb a molecule near monolayer completion due to the inability of the thin film to compress any further which is indicative of a more solid-like surface with higher binding energy. Isosteric heats of adsorption near monolayer completion on MgO shows a broader peak and slow rise up to the maximum before and after monolayer completion

which indicates a compressible liquid-like surface.

A comparison of the thermodynamically derived APM calculations shows a significant differences between MgO and graphite. The 40.4 $Å^2$ value obtained on graphite is much smaller than the 64.9 $Å^2$ value calculated on MgO. The values calculated were both derived from isotherms conducted at similar temperatures which would eliminate any difference attributed to thermal motion of the adsorbed molecules.

A PES surface of cyclohexane on MgO and graphite can be constructed using geometry optimizations over each adsorption site and all unique angles. The large changes in potential energy between the minima and maxima indicate preferred orientation on the surface and distinctive adsorption sites for the molecules.

## 6.6 Pyridine

Thermodynamic data of pyridine shows a stronger interaction with MgO than graphite. The reduction of monolayer capacity on MgO coupled with thermodynamic and TPD data indicates a strongly physisorbed or chemisorbed species. Pyridine on graphite shows two layering transitions like MgO, but no decrease in monolayer capacity as a function of exposure indicating only a weakly physisorbed interaction. Simulations also support a stronger interaction with MgO. Optimizations show one final energy configuration where the nitrogen is located a-top above an oxygen atom. This configuration is most likely chosen to maximize the interaction between the neighboring hydrogen atoms and the oxygen atom of MgO. This scenario can be due to that both the nitrogen and oxygen are Lewis bases. The nitrogen being a slightly stronger Lewis base than carbon would draw electrons towards it and away from the neighboring hydrogens and carbons. This would allow for the Lewis base oxygen to interact with the electron deficient hydrogens on the pyridine molecule. This interaction is most likely a strongly physisorbed interaction because a more likely location for chemisorption to occur on MgO would be at the a-top magnesium adsorption site. In order for electron transfer to occur at the nitrogen site on pyridine a electron withdrawing

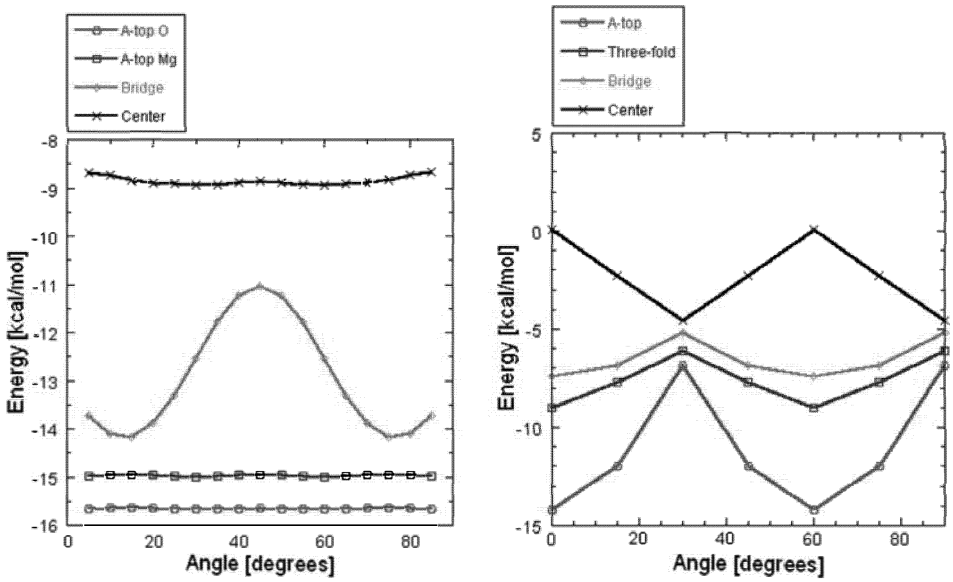


(a) (b)

Figure 6.2: Potential energy surfaces of cyclohexane on MgO and graphite generated from single molecule geometry optimizations. (a) MgO, (b) graphite.

Lewis acid site is needed. The slightly ionic nature of MgO could create an electron deficient magnesium site. This would allow for the creation of a metal ligand complex of magnesium nitride to form. This scenario is most likely not possible though. Previous work has shown that MgO is a weak Lewis base which supports the case for a strongly physisorbed molecule.

The weaker interaction with graphite is also illustrated by comparison of the thermodynamically calculated APM's. The MgO APM of 69.4 $Å^2$ is slightly lower than the value of 75 $Å^2$ calculated on graphite.

A PES of pyridine on MgO and graphite can be constructed which gives largely different results. Figure 6.3 shows that the PES of pyridine on MgO has one large maxima and minima which indicates one adsorption site. The PES of graphite shows many minima of small energy differences which indicate no preferential adsorption. This is supported by quenching simulations which shows no long-range order and proffered orientation sites.

## 6.7 Benzene

Isotherm data shows one layering transition on graphite and none on MgO at any temperatures. Both systems showed a temperature dependent transition from a non-wetting at low temperatures, to complete wetting at high temperatures. This indicates a strongly temperature dependent A-A interaction which at higher temperatures overcomes the relatively low activation barrier of 2.5 kcal/mol of the quadrupole–quadrupole dimer predominant in bulk benzene. PES calculations of benzene on MgO and graphite (see Figure 6.4) both show multiple energy minimums at different adsorption sites which is indicative of an ill-defined minimum energy configuration which results in a weak interaction with both MgO and graphite.

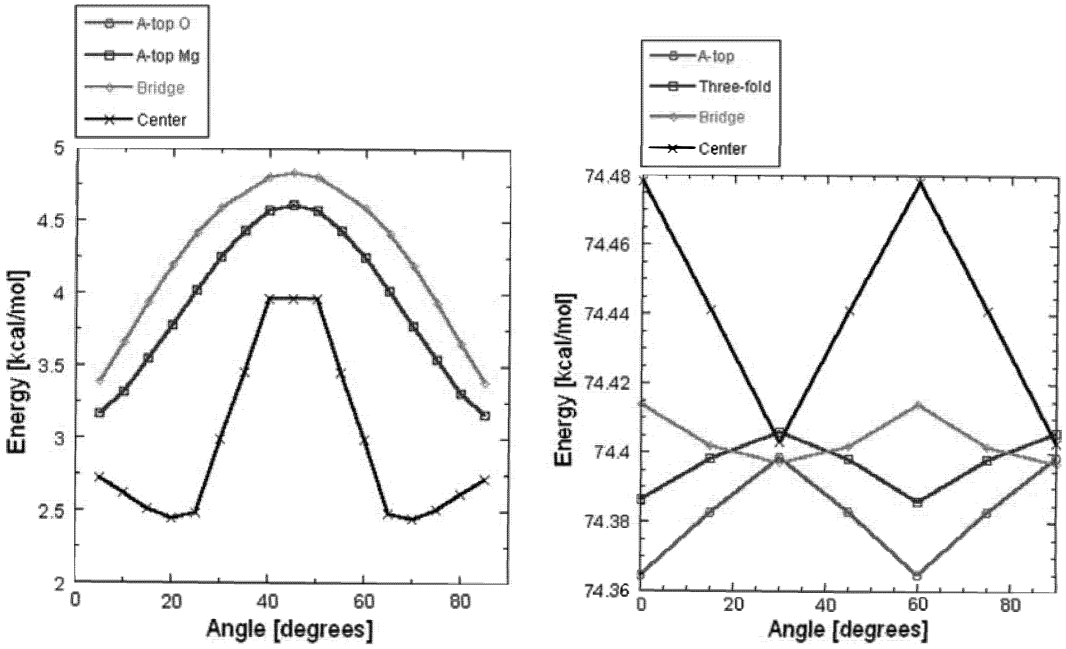


(a) (b)

Figure 6.3: Potential energy surfaces of pyridine on MgO and graphite generated from single molecule geometry optimizations. (a) MgO, (b) graphite.

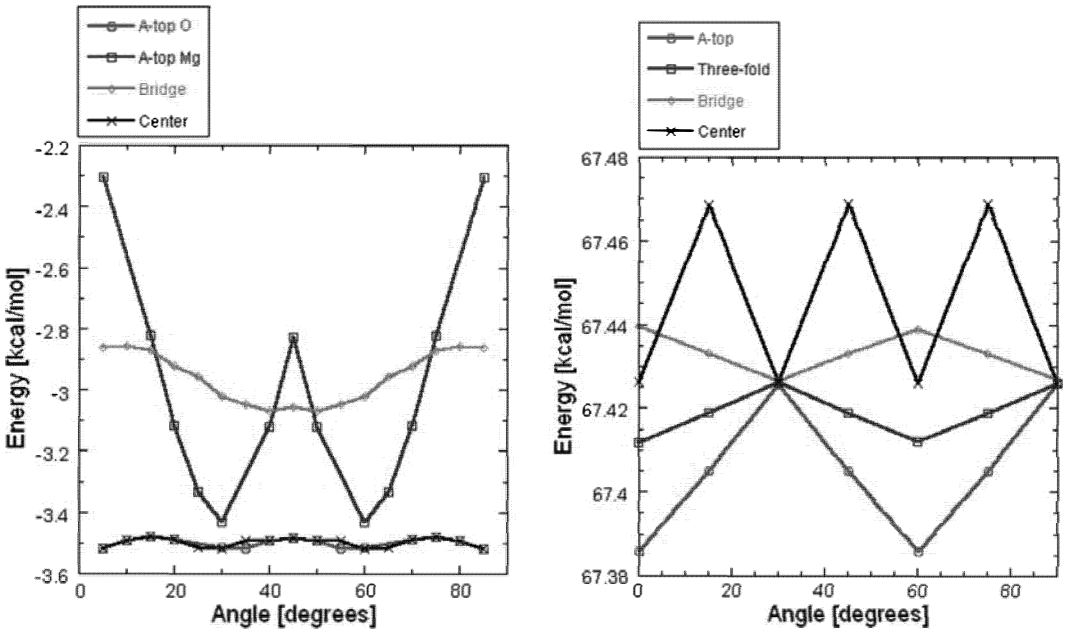


(a) (b)

Figure 6.4: Potential energy surfaces of benzene on MgO and graphite generated from single molecule geometry optimizations. (a) MgO, (b) graphite.

## 6.8 Comparison of *n*-Hexane with Alkanes on MgO

A comparison of *n*-hexane and smaller previously studied alkanes on MgO shows a further weakened A-S interaction. Thermodynamic data shows a continuation of a trend in isosteric heat values and enthalpy values. At this alkane chain length an odd-even alteration in isosteric heats and bulk enthalpy values becomes more pronounced forming a zig-zag type behavior when plotted as in Figure 6.5. Further neutron studies need to be conducted to determine whether the monolayer melting temperatures are affected in the same manner. The surface structure *n*-hexane adopts on MgO seems to continue a similar structural motif found with smaller alkanes on MgO. The structural motif on graphite only breaks down at a chain length of 13 carbons when the lattice strain of the adsorbed layer overwhelms the interaction energy with the surface [Arnold, 2002], [Boese et al., 1999]. At this chain length there is no longer any odd-even dependence and similar surface structures develop. The structural motif on MgO will most likely not endure to such alkane lengths because of the increased lattice strain between MgO and the alkanes. The larger lattice strain on MgO over graphite can also be supported by isotherm data which shows a decreased propensity for multi-layer adsorption on MgO as chain length is increased.

## 6.9 Comparison of Pyridine and Benzene on MgO

A comparison of pyridine and benzene should be made due to the similarities in structure of the two molecules. Thermodynamics and simulations show very different adsorption characteristics which can be solely attributed to the presence of the nitrogen with lone pair of electrons which acts as a Lewis base cite withdrawing electrons from the neighboring hydrogens and allowing for a more favorable interaction with the a-top oxygen adsorption site. Pyridine is an aromatic molecule with its carbon ring comprised of conjugated $\pi$-bonds and consequently has a significant quadrupole moment similar to benzene. This quadrupole moment in pyridine is not as strong as benzene due to the replacement of a carbon with nitrogen. The bulk structure of pyridine shows the formation of dimers where

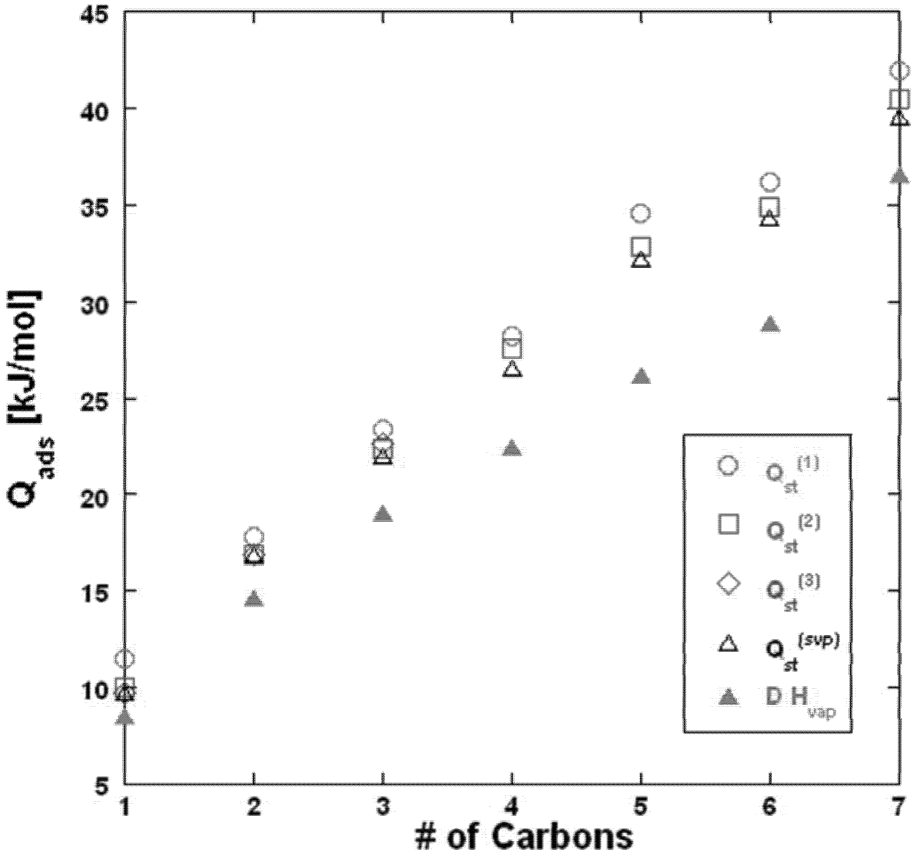


Figure 6.5: A comparison of $Q^{(n)}$ and $\Delta H$ values versus alkane chain length. Starting at a chain length of five carbons a zig-zag behavior forms in the $Q_{st}$ and $\Delta H$ values where odd-numbered molecules show higher values than even-numbered molecules.

the molecules stack on top of each other with nitrogen atoms in the same direction. There is no thermodynamic or simulation data supporting the formation of these dimers indicating a partial wetting of the MgO and graphite surfaces. Other studies support the formation of a pyridinium ion species consisting of two pyridine molecules joined at their nitrogen sites. There is also no thermodynamic or simulation data supporting the formation of these structures. Further structural studies need to be conducted on pyridine to determine how the molecules are oriented on the MgO and graphite as a function of temperature and coverage.

## 6.10 Overall Trends and Results

The layering properties of $n$-hexane on MgO shows a preference for the continuation of herringbone-like structures. The increase in lattice mismatch to the MgO surface is causing deviation from the $P_{2gg}$ herringbone structures to more exotic structures. This will presumably lead to a change in surface structure as alkane chain length is increased and lattice strain of the surface structure is increased.

The moments of inertia of the adsorbed molecule also play a role in the layering and phase characteristics of the system. As a general guide, smaller molecules with equivalent moments of inertia tend to show richer phase transition data. This presumably due to the higher rotational mobility of the atoms which creates a smearing of the molecular PES which facilitates the interactions with the surface and other molecules. In these studies rod-like molecules with $I_B = I_C$, $I_A = 0$, exhibit more liquid-like behavior because the rod-like molecules see a weak enough interaction with the PES because the moments of inertia of the molecule allow for rolling of the molecule to occur via a methyl torsion of its carbon backbone. Simulations show a variety of minimum energy configurations around the same value for all molecules on MgO which increases as the size of the rod-like molecule increases which indicates a possibility for for methyl rotation and translational motion. As coverage

is increased towards monolayer capacity the A-A interactions begin to restrict methyl torsion due to interaction of the hydrogens between molecules methyl torsional translational motion effectively locking the molecule in place. The methyl torsion of molecules at higher coverage would require a concerted 'ratchet-like' motion in order for one molecule to change conformation. On graphite the carbon backbone of the alkanes better match the underlying lattice and therefore creates a slightly more restrictive potential for methyl torsion and lower energies of adsorption than MgO allowing for higher binding energies and improved layering properties. As the rod-like molecules get larger the combination of increased methyl torsion and translational mobility should continue to increase due to the compounding of a slight lattice mismatch of the hydrogens to the surface MgO PES. This effect is less pronounced on graphite but only delays the onset of more liquid-like behavior to a slightly longer alkane chain. The increase of methyl torsion due to a lattice mismatch coupled with the inability of the molecule to properly find a global potential minimum on the surface also allows for more conformational freedom in larger rod-like molecules which could also increase the liquid-like properties of the system.

In disk-like molecules where $I_A < I_B = I_C$ molecules like benzene and pyridine the large barrier to conformational motion restricts accommodation with the surface PES. In the case of benzene on MgO the combination of no conformational freedom and mismatch of of the six-fold symmetry with the four-fold symmetry of the surface and large quadrupole of the molecule due to the conjugated $\pi$-bonding scheme creates little interaction with the surface and is evident in isotherms containing no layering transitions and only a change in the wetting properties form a non-wetting to complete wetting system as temperature is increased. Although the system is completely wetting at high temperatures, the proximity to the bulk triple point inhibits the growth of bulk crystallites and favors the growth of a liquid layer with continuous growth. On graphite, the interaction is only slightly more favorable due to the match of the molecule with the surface however the barrier for any conformational change in a $\pi$-bonded molecule severely prohibits the molecule from finding

the bottom of potential wells on the PES of graphite. This results in only one layering transition but a similar behavior as on MgO in a non-wetting to complete wetting surface.

The case of pyridine is different to benzene due to the presence of a lone pair of electrons at the nitrogen site. Pyridine is also an aromatic molecule with a conjugated $\pi$-bonding scheme. The nitrogen changes the adsorption characteristics of the system and imposes a strong $C_{2v}$ 2-fold symmetry. This symmetry allows for pyridine molecules to more easily explore the PES minima on the respective substrates despite its aromatic properties and mismatch of symmetry with the surface. The ability of nitrogen to attack a specific site due to its $C_{2v}$ symmetry makes it an ideal probe for surface acidity. The interaction of pyridine with graphite does not show a reduction in monolayer capacity due to the lack of ionic character which creates a more homogeneous PES on graphite which has no net ionic character. The lone pair of electrons on the nitrogen atoms therefore cannot find a Lewis acid site on the surface as easily. Previous studies by Lennon et. al. have studied the surface acidity of activated carbon using pyridine as a probe found that carbon is a weak Lewis acid and supports findings using volumetric isotherms [Lennon et al., 2002].

In the case of cyclohexane on MgO and graphite, this tests the interaction of the six-fold symmetric molecule with a low conformation barrier and a four-fold and six-fold surface. This is a particularly interesting system and is a good test of the strength of the interaction with the surface by looking at the strength of the interaction with the surface by looking at the ability of the surface to induce conformational change and could potentially be a good test of the catalytic character of a material. A strong interaction would induce a conformational change to a molecule. A strong interaction would induce a conformational change to better accommodate the molecule. An examination of the torsional component to the final geometries indicates a stronger interaction on graphite than on MgO. The improved layering properties of cyclohexane on graphite is most likely due to the improved match with the underlying lattice and the lack of corrugation due to the surface being

comprised of different atoms. Adsorption on MgO is weaker and results in the isotherms to change from a non-wetting system with one layering transition to an incomplete wetting system with two layering transitions and at higher temperatures a complete wetting system. This is caused by a slight mismatch with the cyclohexane PES and weak interaction which is unable to induce any conformational change and the corrugation of the surface which breaks any symmetry advantages with the surface.

## 6.11 Future Work

Using a combination of volumetric isotherms, neutron diffraction and computer simulations one can determine the thermodynamics associated with the construction of thin films structures on a particular substrate. Results have shown that using a combination of any of the two techniques mentioned perviously, that an intuitive guess can be made about the thermodynamics and structural properties of a thin film physically adsorbed on a particular surface. The use of simulations in conjunction with thermodynamic and structural probes provides a bridge between experiment and theory. The use of improved forcefield models such as COMPASS has drastically reduced the time needed to generate an intuitive guess to a surface structure. This combined with the use of two-dimensional diffraction indexing software like 2Dim allows for a quick and accurate estimate to a surface structure and its theoretical neutron diffraction pattern. A recent addition to the *Material Studio* software package now includes simulation software able to simulate volumetric isotherm data.

This approach described above can allow for the calculation of a proposed surface structure before any experimental structural or thermodynamic experiments have been carried out. Experimental studies can in turn be used to provide a benchmark to these calculations and verify the their validity.

Further neutron scattering information is needed to better understand structural changes at phase transitions and critical points and quantification of dynamics information such

as diffusion. Information about the dynamics of the system can be extracted with the use of inelastic neutron scattering techniques. A neutron spectrometer can be utilized to observe the vibrational modes of the adsorbate molecules. Observing the changes in the various vibrational modes of a molecule as a function of coverage and temperature one can deduce the orientations of the molecules relative to the surface and to each other. Quasi-elastic neutron measurements can be utilized which can give information about the diffusive properties of an adsorbate on a substrate. This can be useful in determining phase transitions of a system by observing the change in the elastic signal as a function of temperature.

Forcite simulations using the COMPASS package have provided a good starting point for more accurate quantum mechanical based calculations. Existing packages such as VASP, PWSCF with quantum espresso, and NWChem 5.0 need to be conducted to obtain a true final energy configuration on the surface which properly accounts for all A-A and A-S interactions. The downside to these calculations are the large amounts of computational time needed to perform them require the use of large-scale computer clusters able to parallelize such calculations.

# Bibliography

[APD, 1988] (1988). *HC-2 Manual*. APD.

[Dow, 2000] (2000). *Vermicular Graphite is a product of the Dow Corporation*. Dow.

[Lar, 2001] (2001). Method for the generation of variable density metal vapors which by-passes the liquidus phase.

[MKS, 2002] (2002). *High-accuracy Pressure Transducer type 120A*. MKS.

[Adamson, 1967] Adamson, A. W. (1967). An adsorption model for contact angle and spreading. *Journal of Colloid and Interface Science*, 27:180.

[Adamson and Gast, 1996] Adamson, A. W. and Gast, A. P. (1996). *Physical Chemistry of Surfaces*. John Wiley and Sons, INC., New York.

[Andersen et al., 2002] Andersen, K., Martin y Marero, D., and Barlow, M. (2002). The osiris diffractometer and polarisation-analysis backscattering spectrometer. *Applied Physics A*, 74:S237.

[Anghel et al., 2002] Anghel, A., Day, G., and Price, S. (2002). A study of the known and hypothetical crystals of pyridine: Why are there four molecules in the asymmetric unit cell? *Crystal Engineering Communications*, 4:348.

[Arnold, 2002] Arnold, T. (2002). *The Adsorption of Alkanes for their Liquids and Binary Mixtures*. Phd, Oxford University, Lincaire College.

[Arnold et al., 2006] Arnold, T., Chanaa, S., Clarke, S., Cook, R., and Larese, J. (2006). The structure of an textitn-butane monolayer adsorbed on magnesium oxide (100). *Physical Review B*, 74:85421–1.

[Arnold et al., 2005] Arnold, T., Cook, R. E., and Larese, J. (2005). Thermodynamic investigation of thin films of ethane adsorbed on magnesium oxide. *Journal of Physical Chemistry B*, 109:8799.

[Atkins and de Paula, 2002] Atkins, P. and de Paula, J. (2002). *Physical Chemistry.* W. H. Freeman, New York.

[Axelrod, 1951a] Axelrod, B. (1951a). Triple-dipole interaction i. theory. *Journal of Chemical Physics*, 19(6):719.

[Axelrod, 1951b] Axelrod, B. (1951b). Triple-dipole interaction ii. cohesion in crystals of the rare gases. *Journal of Chemical Physics*, 19(6):724.

[Bacon, 1977] Bacon, G. E. (1977). *Neutron Scattering in Chemistry.* Buttersworth, London.

[Battezzati et al., 1975] Battezzati, L., Pisani, C., and Ricca, F. (1975). Equilibrium conformation and surface motion of hydrocarbon molecules physisorbed on graphite. *Journal of Faraday Transactions Royal Society Proceedings*, page 1629.

[Beaume et al., 1984] Beaume, R., Suzanne, J., Coulomb, J., Glachant, A., and Bomchil, G. (1984). Neutron diffraction study of the commensurate-incommensurate phase transition in a methane submonolayer adsorbed on graphite. *Surface Science*, 137:L117.

[Bernath, 1995] Bernath, P. F. (1995). *Spectra of Atoms and Molecules.* Oxford University Press, New York.

[Bienfait, 1985] Bienfait, M. (1985). Wetting and multilayer adsorption. *Surface Science*, 162:411.

[Boese et al., 1999] Boese, R., Weiss, H.-C., and Bläser (1999). The melting point alternation in the short-chain $n$-alkanes: Single-crystal x-ray analyses of propane at 30 k and $n$-butane to $n$-nonane at 90 k. *Angew Chemie*, 38(7):988.

[Boinovich and Emelyanenko, 2004] Boinovich, L. and Emelyanenko, A. (2004). On the theory of the stability of dipole molecule solution interlayers in apolar solvents: 3. a formation of adsorption monolayers with dipole orientation normal to the surface. *Colloid Journal*, 66(1):16.

[Boni and Furrer, 2000] Boni, P. and Furrer, A. (2000). *Introduction to Neutron Scattering*, page 1. Frontiers of Neutron Scattering - 1999. World Scientific.

[Bretz et al., 1973] Bretz, M., Dash, J., Hickernell, D., McLean, E., and Vilches, O. (1973). Phases of $he^3$ and $he^4$ monolayer films adsorbed on basal-plane oriented graphite. *Physical Review A*, 8(3):1589.

[Brunauer, 1945] Brunauer, S. (1945). *The Adsorption of Gases and Vapors*. Princeton University Press, Princeton.

[Burkalov, 2006] Burkalov, V. (2006). Ostwald ripening in rareafied systems. *Physical Review Letters*, 97:155703.

[Cañoto and Larese, 2007] Cañoto, D. F. and Larese, J. (2007). To be published. *Langmuir*.

[Che et al., 1977] Che, M., Coluccia, S., and Zecchina, A. (1977). Electron paramagnetic resonance study of electron transfer at the surface of alkaline earth oxides.

[Clarke, 2001] Clarke, S. M. (2001). Neutron diffraction and incoherent neutron scattering from adsorbed layers. *Current Opinion in Colloid and Interface Science*, 6:118.

[Cook and Larese, 2006] Cook, R. and Larese, J. (2006). To be published. *Langmuir*.

[Cook, 2006] Cook, R. E. (2006). *Study of small alkanes adsorbed on MgO nanocubes*. Phd, University of Tennessee.

[Corrsin et al., 1953] Corrsin, L., Fax, B., and Lord, R. (1953). The vibrational spectra of pyridine and pyridine-$d^5$. *Journal of Chemical Physics*, 21:1170.

[Cox, 1958] Cox, E. (1958). Crystal structure of benzene. *Reviews of Modern Physics*, 30(1):159.

[Cox and Hendrich, 1994] Cox, P. A. and Hendrich, V. E. (1994). *The Surface Science of Metal Oxides*. Cambridge University Press, Cambridge, UK.

[Dash, 1977] Dash, J. (1977). Clustering and percolation transitions in helium and other thin films. *Physical Review B*, 15(6):3136.

[Dash and R.D., 1981] Dash, J. and R.D., P. (1981). Phase transitions in heterogeneous films. *Physical Review B*, 24(1):295.

[Dash, 1975] Dash, J. G. (1975). *Films on Solid Surfaces*. Academic Press, New York.

[Delachaume et al., 1983] Delachaume, J., Coulon, M., and Bonnetain, L. (1983). Benzene adsorption on basal planes of boron nitride; comparision with the benzene-graphite system. *Surface Science*, 133:365.

[Diefenderfer and Holton, 1994] Diefenderfer, A. and Holton, B. (1994). *Principles of Electronic Instrumentation*. Saunders, Philiadelphia.

[Do and Do, 2005] Do, D. and Do, H. (2005). Adsorption of benzene on graphitized thermal carbon black: Reduction of the quadrapole moment in the adsorbed phase. *Langmuir*, 22:1121.

[Dollimore et al., 1971a] Dollimore, D., G.R., H., and Martin, D. (1971a). Thermodyanmics of adsorption of a series of related organic molecules on graphite and a carbon black: Part 1. heat of adsorption. *Journal of Faraday Transactions Royal Society Proceedings*, page 832.

[Dollimore et al., 1971b] Dollimore, D., G.R., H., and Martin, D. (1971b). Thermodyanmics of adsorption of a series of related organic molecules on graphite and a carbon

black: Part 2. entropy of adsorption. *Journal of Faraday Transactions Royal Society Proceedings*, page 1784.

[Dutta and Sinha, 1982] Dutta, P. and Sinha, S. K. (1982). Analytic form for the static structure factor for a finite two-dimensional harmonic lattice. *Physical Review Letters*, 47:50.

[Firment and Samorjai, 1978] Firment, L. and Samorjai, G. (1978). Low energy electron diffration study of the surface of thin film crystals and monolayers of normal paraffins and cyclohexane on the ag(111) crystal surface. *Journal of Chemical Physics*, 69(9):3940.

[Fisher and Pandit, 1983] Fisher, M. E. and Pandit, M. (1983). Wetting transitions near bulk triple points. *Physical Review B*, 51(19):1772.

[Fowler and Guggenheim, 1949] Fowler, R. and Guggenheim, E. (1949). *Statistical Thermodynamics: A Version of Statistical Mechanics for Students of Physics and Chemistry.* Cambridge University Press, Cambridge.

[Frank and van der Merwe, 1949] Frank, F. and van der Merwe, J. (1949). Misfitting monolayers. *Proc. Roy. Soc. London*, 198:205.

[Frenkel, 1946] Frenkel, J. (1946). *Kinetic Theory of Liquids.* Clarendon, Oxford, UK.

[Gomez et al., 2001] Gomez, L., Dobry, A., and Diep, H. (2001). Monte carlo simulation of the role of defects as a melting mechanism. *Physical Review B*, 63:224103.

[Gregg and Sing, 1982] Gregg, S. J. and Sing, K. S. W. (1982). *Adsorption, Surface Area and Porosity.* Academic Press, New York.

[Guinier, 1994] Guinier, A. (1994). *X-Ray Diffraction: In Crystals, Imperfect Crystals, and Amorphous Bodies.* Dover, New York.

[Halsey Jr., 1948] Halsey Jr., G. D. (1948). Physical adsorption on non-uniform surfaces. *Journal of Chemical Physics*, 16:931.

[Hansen et al., 1992] Hansen, F. Y., Newton, J., and Taub, H. (1992). Molecular dynamic studies of the melting of butane and hexane monolayers adsorbed on the basal-plane surface of graphite. *Journal of Chemical Physics*, 98:4128.

[Hartmann and Biscof, ] Hartmann, M. and Biscof, C.

[Hendra et al., 1971] Hendra, P., Horder, J., and Loader, E. (1971). The laser-raman spectrum of pyridine adsorbed on oxide surfaces. *Journal Chemistry Society A*, page 1766.

[Herwig et al., 1997] Herwig, K., Wu, Z., Taub, H., and Hansen, F. (1997). Quasielastic neutron scattering and molecular dynamics simulation studies of the melting transition in butane and hexane monolayers adsorbed on graphite. *Journal of Chemical Physics*, 107(13):5186.

[Hill, 1946] Hill, T. L. (1946). Statistical mechanics of multimolecular adsorption ii. localized and mobile adsorption and absorption. *Journal of Chemical Physics*, 14:441.

[Hill, 1949] Hill, T. L. (1949). Statistical mechanics of adsorption vii. thermodynamic functions for the bet theory. *Journal of Chemical Physics*, 17:772.

[Hill, 1986] Hill, T. L. (1986). *An Introduction to Statistical Thermodynamics*. Dover, Mineola, NY, USA.

[http://invsee.asu.edu, 2006] http://invsee.asu.edu (2006). World of carbon.

[http://webbook.nist.gov, 2006] http://webbook.nist.gov (2006). Nist webbook.

[http://www.doe mbi.ucla.edu/, 2006] http://www.doe mbi.ucla.edu/ (2006). Cryocrystallography and data collection.

[Iizuka and Tanabe, 1975] Iizuka, T. and Tanabe, K. (1975). The spectroscopic study on the dimerization of pyridine derivatives on the surfaces of mgo, cao, and sro. *Bulletin of the Chemical Society of Japan*, 48:2527.

[Imry and Gunther, 1971] Imry, Y. and Gunther, L. (1971). Fluctuations and physical properties of the two-dimensional crystal lattice. *Physical Review B*, 3(11):3939.

[IUC, 1952] IUC (1952). *International Tables for X-ray Crystallography*. Kynoch Press.

[Kahn et al., 1972] Kahn, R., Fourme, R., André, D., and Michael, R. (1972). Crystal structures of cyclohexane i and ii. *Acta Crystallographica*, B29:131.

[Kim and Steele, 1992] Kim, H.-Y. and Steele, W. (1992). Computer simulation study of the phase diagram of the $ch_4$ monolayer adsorbed on graphite: Corrugation effects. *Physical Review B*, 45:6226.

[Kiselev and Avgul, 1967] Kiselev, A. and Avgul, N. (1967). *Physical Adsorption of Gases and Vapors on Graphitized Carbon Blacks*, page 1.

[Kjems et al., 1976] Kjems, J. K., Passell, L., Taub, H., Dash, J. G., and Novaco, A. D. (1976). Neutron scattering study of nitrogen adsorbed on basal-plane oriented graphite. *Physical Review B*, 13:41336.

[Klein and Cole, 1985] Klein, J. R. and Cole, M. W. (1985). Adsorption interactions and the two-dimensional critical temperature. *Faraday Discussions of the Royal Chemistry Society*, 80:71.

[Kline Jr. and Turkevich, 1944] Kline Jr., C. H. and Turkevich, J. (1944). The vibrational spectrum of pyridine and the thermodynamic properties of pyridine vapors. *Journal of Chemical Physics*, 12:300.

[Koehler III et al., 2000] Koehler III, C. F., Larese, J. Z., Rodriguez, J., Jirisak, T., Fritag, A., Hanson, A., and Chaturvedi, S. (2000). Cryostat insert with gas loading capabilities for use in neutron diffraction studies. *Review of Scientific Instuments*, 71:324.

[Krim et al., 1985] Krim, J., Suzanne, J., Schecter, H., Taub, H., and Wang, R. (1985). A leed and neutron diffraction study of hexane adsorbed on graphite in the monolayer range: Uniaxial commensurate-incommensurate transition. *Surface Science*, 162:451.

[Krishnan et al., 2003] Krishnan, M., Balasubramanian, S., and Clarke, S. (2003). An atomistic simulation study of a solid monolayer and trilayer of $n$-hexane on graphite. *Journal of Chemical Physics*, 118:5082.

[Land et al., 1989] Land, D. P., Pettiette-Hall, C. L., McIver Jr., R. T., and C., H. J. (1989). Detection of reaction intermediates in the conversion of cyclohexane to benzene on pt(111). *Journal of the American Chemical Society*, 111:5970.

[Langmuir, 1918] Langmuir, I. (1918). The adsorption of gases on plane surfaces of glass, mica and platinum. *Journal of the American Chemical Society*, 40(1):1361.

[Larese, 1998] Larese, J. (1998). Neutron scattering studies of the structure and dynamics of methane adsorbed on mgo(100) surfaces. *Physica B*, 248:297.

[Larese et al., 1988a] Larese, J., Harada, M., Passell, L., Krim, J., and Satija, S. (1988a). Neutron-scattering study of bilayer and trilayer films of methane on graphite. *Physical Review B*, 37(9):4735.

[Larese et al., 1991] Larese, J., Hastings, J., Passell, L., Smith, D., and Richter, D. (1991). Rotational tunneling of methane on mgo surfaces: A neutron scattering study. *Journal of Chemical Physics*, 95(9):6997.

[Larese and Lee, 1997] Larese, J. and Lee, M. (1997). Combined neutron diffraction and adsorption isotherm study of the anomalous wetting properties of $nh_3$ on graphite. *Physical Review Letters*, 79(4):689.

[Larese et al., 1988b] Larese, J., Passell, L., Heidemann, A., and Wicksted, J. (1988b). Melting in two-dimensions: Ethylene-on-graphite system. *Physical Review Letters*, 61(4):432.

[Larher, 1967] Larher, Y. (1967). Transitions du premier ordre en phase adsorbe. i. *Journal Chimique Physique*, 62:974.

[Larher, 1979] Larher, Y. (1979). The critical exponent $\beta$ associated with the two-dimensional condensation in the second adlayer of argon on the cleavge face of cadmium chloride. *Molecular Physics*, 38(3):789.

[Lee and Kosterlitz, 1990] Lee, J. and Kosterlitz, J. (1990). New numerical method to study phase transitions. *Physical Review Letters*, 65(2):137.

[Lennon et al., 2002] Lennon, D., Lundie, D., Jackson, S., Kelly, G., and Parker, S. (2002). Characterization of activated carbon using x-ray photoelectron spectroscopy and inelastic neutron spectroscopy. *Langmuir*, 18:4667.

[Leventis et al., 1997] Leventis, N., Hanna, S. B., and Sotiriou-Leventis, C. (1997). A three-dimensional energy surface for the conformational inversion of cyclohexane. *Journal of Chemical Education*, 74:813.

[Lewis, 1992] Lewis, F.L., P.-H. . (1992). *Applied Optimal Control and Estimation*. Prentice-Hall, New York.

[Lindermann, 1910] Lindermann, F. (1910). The calculation of molecular vibration frequencies. *Physik. Z*, 11:609.

[Lysek et al., 1983] Lysek, M., LaMadrid, M., Day, P., and Goodstein, D. (1983). Heat capacity of multilayer methane on graphite: phase transitions in the first four layers. *Physical Review B*, 47:7389.

[MacPherson and Leung, 1996] MacPherson, C. and Leung, K. (1996). Observation of room temperature dehyrogenation of cyclohexane to benzene and cyclohexene on a common semiconductor surface, si(111)-(7x7). *Surface Science Letters*, 356:L–399.

[Madih, 1986] Madih, K. (1986). Phd, Universite d' Aix-Marsielle.

[Matties and Hentschke, 1996] Matties, M. A. and Hentschke, R. (1996). Molecular dynamics simulation of benzene on graphite: 1. phase behavior of an adsorbed monolayer. *Langmuir*, 12:2495.

[McQuarrie and Simon, 1997] McQuarrie, D. and Simon, J. (1997). *Physical Chemistry, A Molecular Approach*. University Science Books, Sausalito.

[Merck, 2004] Merck (2004). Nist index.

[Mursic et al., 1996] Mursic, Z., Lee, M., Johnson, D., and Larese, J. (1996). A computer-controlled apparatus for performing high-resolution adsorption isotherms. *Review of Scientific Instruments*, 67(5):1886.

[Mutaftschiev, 2001] Mutaftschiev, B. (2001). *The Atomistic Nature of Crystal Growth*. Springer, New York.

[Nakanishi and Fisher, 1982] Nakanishi, H. and Fisher, M. E. (1982). Multicriticality of wetting, prewetting, and surface transitions. *Physical Review B*, 49(21):1565.

[Newton, 1989] Newton, J. C. (1989). *The Structure and Phase Transitions of Linear Chain Hydrocarbons on Graphite*. Phd, University of Missouri-Columbia.

[Ostlund and Halperin, 1981] Ostlund, S. and Halperin, B. (1981). Dislocation-mediated melting of anisotropic layers. *Physical Review B*, 23:335.

[Pan et al., 1998] Pan, H., Ritter, J. A., and Balbuena, P. A. (1998). Examination of the approximations used in determining the isosteric heat of adsorption from the clausius-clapeyron equation. *Langmuir*, 14:6323.

[Pandit et al., 1982] Pandit, R., Schick, M., and Wortis, M. (1982). Systematics of multilayer adsorption phenomena on attractive surfaces. *Physical Review B*, 26(9):5112.

[Partal et al., 2000] Partal, F., Fernandez-Gomez, M., Lopez-Gonzalez, J. J., Navarro, A., and Kearly, G. J. (2000). Vibrational anlysis of the inelastic neutron scattering spectrum of pyridine. *Chemical Physics*, 261:239.

[Phillips and Larese, 1997] Phillips, J. M. and Larese, J. (1997). Microscopic structure and transitions in xenon multilayer films. *Physical Review B*, 56(24):15938.

[Rahman and Ghosh, 1980] Rahman, M. and Ghosh, A. (1980). Surface area of cupric oxide and magnesium oxide by adsorption of stearic acid and pyridine. *Applications of Surface Science*, 5:332.

[Rauch and Waschkowski, 2003] Rauch, H. and Waschkowski, W. (2003). *Neutron Scattering Lengths*, page 1. Neutron Data Booklet. Old City Publishing Science.

[Redhead, 1962] Redhead, P. (1962). Thermal desorption of gases. *Vacuum*, 1:203.

[Reynolds, 1968] Reynolds, W. (1968). *Physical Properties of Graphite*. Elsevier, Amsterdam.

[Richards, 2006] Richards, R. (2006). *Surface and Nanomolecular Catalysis*. Taylor and Francis, New York.

[Rietveld, 1967] Rietveld, H. (1967). Line profiles of neutron powder-diffraction peaks for structure refinement. *Acta Crystallographica*, 22:151.

[Robertson and O'Reilly, 1987] Robertson, J. and O'Reilly, E. (1987). Amorphous carbon. *Physical Review B*, 35.

[Roth and Wexler, 2005] Roth, M.W.and Pint, C. and Wexler, C. (2005). Phase transitions in hexane monolayers physisorbed onto graphite. *Physical Review B*, 71:155427.

[Ruland and Tompa, 1967] Ruland, W. and Tompa, H. (1967). The effect of preffered orientation on the intensity distribution of (hk) interferences. *Acta Crystallographica*, A24(?):93.

[Sands, 1993] Sands, D. E. (1993). *Introduction to Crystallography*. Dover, New York.

[Schick, 1990] Schick, M. (1990). *Introduction to Wetting Phenomena*, page 415. Les Houches, Session XLVIII, 1988. Elsevier.

[Schildberg and Lauter, 1989] Schildberg, H. P. and Lauter, H. J. (1989). Lineshape calculations for two-dimensional powder samples. *Surface Science*, 208:507.

[Schweizer and Dunitz, 2006] Schweizer, W. B. and Dunitz, J. D. (2006). Quantum mechanical calculations for benzene dimer energies: Present problems and future challenges. *J. Chem. Theory Comput.*, 2:288.

[Shriver and Drezdzon, 1986] Shriver, D. F. and Drezdzon, M. A. (1986). *The Manipulation of Air Sensitive Compounds*. John Wiley and Sons, INC., New York.

[Sircar and Cao, 2002] Sircar, S. and Cao, D. V. (2002). Heat of adsorption. *Chemical Engineering and Technology*, 25:945.

[Sivasankar and Vasudevan, 2004] Sivasankar, N. and Vasudevan, S. (2004). Stabilization of a distorted conformation of cyclohexane adsorbed in the voids of silicate-1. *Catalysis Letters*, 97:53.

[Smith et al., 1950] Smith, N., Pierce, C., and Cordes, H. (1950). Adsorption of benzene and cyclohexane by graphite. *Journal of the American Chemical Society*, page 5595.

[Somorjai, 1994] Somorjai, G. A. (1994). *Introduction to Surface Chemistry and Catalysis*. John Wiley and Sons, New York.

[Sprung, 2001] Sprung, M. (2001). *Adsorbed Films of Methyl Halides on Magnesium Oxide and Boron Nitride*. Phd, Christian-Albrechts-Universität zu Kiel.

[Sprung and Larese, 2000] Sprung, M. and Larese, J. (2000). Adsorption isotherms studies of methyl chloride on mgo. *Physical Review B*, 61(19):13155.

[Squires, 1978] Squires, G. L. (1978). *Introduction to the Theory of Thermal Neutron Scattering*. Dover, Mineola, NY, USA.

[Stanley, 1971] Stanley, H. E. (1971). *Introduction to Phase Transitions and Critical Phenomona*. Oxford University Press, Oxford.

[Steele, 1993] Steele, W. (1993). Molecular interactions for physical adsorption. *Chemistry Review*, 93:2355.

[Steele, 1974] Steele, W. A. (1974). The interaction of gases with solid surfaces. volume 3 of *The International Encyclopedia of Physical Chemistry and Chemical Physics*. Pergamon, New York.

[Steele, 1996] Steele, W. A. (1996). Monolayers of linear molecules adsorbed on the graphite basal plane: Structures and intermolecular interactions. *Langmuir*, 12:145.

[Strandburg, 1988] Strandburg, K. J. (1988). Two-dimensional melting. *Reviews of Modern Physics*, 60(1):161.

[Stranski and Krastanow, 1937] Stranski, I. and Krastanow, L. (1937). Zur theorie der orientierten ausscheidung von ionenkristallen aufeinander. *Monatshefte fr Chemie/Chemical Monthly*, 71(1).

[Strzelczyk et al., 1997] Strzelczyk, M., Haak, N., Asmussen, B., Süßenbach, Press, W., and Larese, J. (1997). Structures and phase diagrams of tetramethyltin and tetramethyllead adsorbed on graphite. *Surface Science*, 376:339.

[Sun, 1998] Sun, H. (1998). Compass: An ab initio force-field optimized for condensed phase applications-overview with details on alkane and benzene compounds. *Journal of Physical Chemistry B*, 102:7338.

[Tait et al., 2005] Tait, Stephen L., D. Z., Campell, C. T., and Kay, B. D. (2005). *n*-alkanes on mgo (100). ii. chain length dependence of kinetic desorption parameters for small *n*-alkanes. *Journal of Chemical Physics*, 122(16):164708.

[Telling and Andersen, 2005] Telling, M. T. and Andersen, K. H. (2005). Spectroscopic characteristics of the osiris near-backscattering crystal analyser spectrometer on the isis pulsed neutron source. *Physical Chemistry Chemical Physics*, 7:1255.

[Thomy and Duval, 1990] Thomy, A. and Duval, X. (1990). Stepwise isotherms and phase transitions in physisorbed films. *Surface Science*, 299:415.

[Thouless, 1978] Thouless, D. (1978). Melting of the two-dimensional wigner lattice. *Journal of Physics C*, 11:L189.

[Travert et al., 2006] Travert, A., Vimont, A., Sahibed-Dine, A., Daturi, M., and Lavalley, J.-C. (2006). Use of pyridine ch(d) vibrations for the study of lewis acidity of metal oxides. *Applied Catalysis A*, 307:98.

[Tsai and Muetterties, 1982] Tsai, M.-C. and Muetterties, E. (1982). Coordination chemistry of benzene, tolune, cyclohexadienes, cyclohexene, and cyclohexane on pt(100). *Journal of Physical Chemistry*, 86:5067.

[Vitale et al., 1997] Vitale, G., Mellot, C. F., and Cheetham, A. K. (1997). Localization of adsorbed cyclohexane in the acid form of zeolite y. a powder diffraction and computational study. *Journal of Physical Chemistry B*, 101:9886.

[Volmer and Weber, 1926] Volmer, M. and Weber, Z. (1926). Nucleus formation in supersaturated systems. *Z. Phys. Chem*, 119:277.

[Wade, 1995] Wade, L. (1995). *Organic Chemistry*. Prentice Hall, New York.

[Warren, 1990] Warren, B. (1990). *X-ray diffraction*. Dover, New York.

[Weling and Griffin, 1981] Weling, F. and Griffin, A. (1981). Static structure factor for a finite incommensurate monolayer. *Physical Review Letters*, 46(5):353.

[White et al., 1978] White, J., Thomas, R., Trewern, T., Marlow, I., and Bomchil, G. (1978). Neutron diffraction and inelastic scattering from adsorbed molecules. *Surface Science*, 76:13.

[Wu et al., 2001] Wu, Z., Ehrlich, S., Matthies, B., Herwig, K., P.C., D., Volkmann, U., Hansen, F., and Taub, H. (2001). Growth of *n*-alkane films on a single-crystal substrate. *Chemical Physics Letters*, 348:168.

[Yang et al., 2006] Yang, S., Ouyang, L., Phillips, J. M., and Ching, W. Y. (2006). Density-functional calculation of methane adsorption on graphite (0001). *Physical Review B*, 73:165407.

[Young and Crowell, 1962] Young, D. M. and Crowell, A. D. (1962). *Physical Adsorption of Gases*. Butterworths, London.

[Zecchina and Stone, 1986] Zecchina, A. and Stone, F. S. (1986). Adsorption and reaction of pyridine on alkaline earth oxides as studied by uv-visible diffuse reflectance spectroscopy. *Journal of Catalysis*, 101:227.

# Vita

Peter Nikolaivich Yaron was born in Saõ Paulo Brazil, on June 21, 1977 the son of Nikolai Yaron and Dalva Antoinia Yaron. After graduating in 1995 from Ward Melville High School in Setauket, New York he attended the University of Maryland, College Park where he received a Bachelor of Science degree in Natural Resource Management with a concentration in Biological Resource Engineering, in 2000. During his undergraduate studies he worked at the Remote Sensing and Modeling Laboratory at the USDA, Beltsville research facility. He later joined the workforce as an engineer for Art Preservation Services and Canard Associates Land Surveying and Engineering. In 2001 he returned part-time to the academic world to obtain a Bachelor of Science in Physics at State University of New York at Stony Brook. Concurrently he worked at Brookhaven National Laboratory with the pp2pp group on the Relativistic Heavy Ion Collider. In 2002 he entered graduate school in the Chemistry Department at the University of Tennessee, Knoxville to persue a PhD in Chemical Physics. He joined the Larese group in 2003 where he completed his Doctor of Philosophy degree in 2007.